U.PORTO

FEUP FACULDADE DE ENGENHARIA
UNIVERSIDADE DO PORTO

# Analysis of an Aeronautical Morphing Structure

Sérgio João Monteiro de Barros Moreira

Supervisor:
Doutor Sérgio M. O. Tavares

Co-Supervisor:
Prof. Doutor Paulo M.S.T de Castro

Thesis submitted to
Faculdade de Engenharia da Universidade do Porto
as a requirement to obtain the Master Degree in Mechanical Engineering

Mestrado Integrado em Engenharia Mecânica

Departamento de Engenharia Mecânica
Faculdade de Engenharia da Universidade do Porto

Porto, September 2016

Final Revised Version - Issued 13 October 2016

LyX
FEUP - U.Porto
Sérgio João Moreira
2016

Aos meus pais, António e Glória.

Ao Nuno e ao Gui.

À Inês.

*"Once you have tasted flight, you will forever walk the earth with your eyes turned skyward, for there you have been, and there you will always long to return."*

Leonardo da Vinci

# Agradecimentos / Acknowledgements

Aos meus orientadores, Doutor Sérgio Tavares e Professor Doutor Paulo Tavares de Castro, quero expressar a minha mais profunda gratidão. Sem eles, o presente trabalho não era possível. Pelo apoio incansável, pela compreensão, por tudo o que me ensinam e me fizeram aprender, e por todas as oportunidades e meios que me disponibilizaram, muito obrigado. Citando Newton, "Se vi mais longe, foi por estar de pé sobre ombros de gigantes".

Ao INEGI e à sua unidade LAETA, quero agradecer os meios disponibilizados e, sobretudo, a Bolsa de Investigação Científica que me foi atribuída durante a realização deste trabalho, no contexto do projecto interinstitucional (AeroG/UBI, IDMEC/IST, INEGI/UP*) Damage tolerant structures under mixed mode loading*, DALMAT.

The author kindly acknowleges the clarifications and informations provided by Dr. Martin Radestock and Dr. Markus Kintscher from DLR.

Ao Eduardo Aguiar, agradeço a troca de ideias e de informações.

Um obrigado ao João Filipe, com quem fui partilhando alegrias e desabafos, e ainda ao Marco Alves, ao Tomás Chuaqui, ao Joel Couto e ao Luís Reis.

A todos os que me acompanharam durante os cinco anos de percurso que culminaram neste trabalho, e em particular:

Ao Hugo, por ter sido o meu terceiro irmão, enquanto vivi no Porto. Não há palavras. Obrigado.

À Filipa, por todas as vezes em que tive o prazer de ouvir e acompanhar a tua fantástica voz e que, em retrospectiva, deviam ter sido mais.

À Joana, pela amizade à tua maneira especialmente louca.

À Catarina e à Rita, pela proeza de terem vivido comigo quatro anos e por todas a recordações que daí ficaram.

Ao Rafa e ao Chico, pela não menos heróica proeza neste último ano.

Ao Nuno, pela paciência. Ao Silva, por todas as conversas filosóficas. Ao Mankind, pela magia que tantas vezes fizeste com uma guitarra. À Catarina, por ser um "pequeno unicórnio". Ao Roberto, pelas gargalhadas inconfundíveis. Ao Zé, por me acompanhar na loucura por aviões. Às Marias, porque sem elas o nosso grupo estava incompleto. Ao Zé Diogo por me ter acompanhado na ideia do grelhador. Ao Rui, pela boa disposição constante. A todos vocês: Obrigado por todos os momentos, todos os sorrisos e choros.

Por todas as vezes que me ajudaram na mínima coisa, por tudo o que aprendi convosco e por tudo o que levo destes cinco anos. Muito, muito obrigado.

Aos meus irmão, que melhor do que ninguém sabem lidar com o meu mau feitio, talvez porque sejam eles quem já levou mais com ele.

Aos meus pais, porque lhes devo quem sou e onde estou. Porque têm sido os gigantes que me fazem ir mais longe desde que nasci. Por tudo o que, todos os dias, fazem por mim e pelos meus irmãos. Por terem tolerado as minhas ausências continuadas devido a este trabalho e a distância que provocaram. Por terem estado sempre lá quando eu precisei, mesmo com essa distância. Por me conhecerem e saberem tão bem quando eu preciso deles, mesmo quando tento não os preocupar. Em suma, por todo o amor que só o abraço de uma mãe e de um pai conseguem transmitir.

Finalmente, à Inês. Ninguém teria sabido estar ao meu lado, durante este semestre, melhor do que tu. Devo-te mil obrigados. Por me aturares sempre que o trabalho parecia não se querer deixar fazer. Por me fazeres esquecer esse trabalho e não dar em doido. Por o tentares perceber e, mesmo sem o perceberes bem, me ouvires falar dele vezes sem conta. Por me levantares todas as vezes que quebrei, e por outras tantas vezes não me deixares quebrar. Por todo o carinho, por toda a ternura, pelos sorrisos que tantas vezes fizeram passar o dia de mau a bom. E porque quando eu desapareci do mundo para acabar o trabalho, foste a pessoa mais paciente do mundo e arranjaste forma de me continuares a motivar e apoiar. Esta tese também é tua: se cheguei ao final, devo-o a tudo o que fizeste e fazes por mim. Obrigado, Nessie.

# Abstract

Innovation is a constant in the aeronautics field. The search for more efficient technologies, often inspired by nature, has led to the emergence of novel aircraft structural concepts such as morphing aircraft. These aircraft make use of large scale shape deflections to achieve improved flight performance across significantly different flight regimes and missions. However, such loading conditions may yield unusual crack propagation, and mixed fracture modes may take place. Consequently, morphing concepts require a full understanding of the materials' behaviour in primary or secondary structures in order to reliably withstand unusual and demanding operating conditions. A case study of a morphing leading edge developed for the wings of an UAV was performed. Damage tolerance was taken into consideration. Since leading edges are the most exposed parts of an airfoil, small cracks can be originated from material flaws, unnoticed bird strike, impact with foreign object or other reasons. Therefore, due to the deflections during the morphing structure actuation, these defects can propagate under mixed mode fatigue crack up to a critical size. A preliminary analysis of possible crack propagation scenarios is presented. Finite Element Method analysis were performed to simulate these scenarios, and data retrieved was used to estimate the fatigue life of the wing skin.

**Keywords:** Morphing structure; Fatigue crack growth; Aluminium alloys; Wing leading edge; Computational fracture mechanics.

# Resumo

A inovação é uma constante na aeronáutica. A busca de tecnologias mais eficientes, inspiradas muitas vezes na natureza, levou ao surgimento de novos conceitos estruturais para aeronaves, tais como aeronaves com estruturas adaptáveis (*morphing aircraft)*. Estas aeronaves sofrem mudanças de forma em grande escala para conseguir um melhor desempenho face a regimes de voo e missões significativamente diferentes. No entanto, tais condições de carga podem levar a propagação de fendas fora do comum e à ocorrência de modos mistos de fractura. Consequentemente, o conceito de *morphing* requer um conhecimento completo do comportamento dos materiais das estruturas primárias ou secundárias, de modo a que estas suportem com segurança as condições de funcionamento invulgares e exigentes. Foi estudado o bordo de ataque sujeito a *morphing*, desenvolvido para as asas de um UAV. A tolerância ao dano foi tida em consideração. Uma vez que os bordos de ataque são as partes mais expostas da asa, pequenas fendas podem iniciar, devido a defeitos do material, *bird-strikes* despercebidos, impacto com objectos estranhos ou por outros motivos. Deste modo, devido às deflexões durante a actuação da estrutura, esses defeitos podem propagar-se em modo misto até um tamanho crítico. Uma análise preliminar dos possíveis cenários de propagação de fendas é apresentada. Foram realizadas análises de elementos finitos para simular estes cenários, e os dados obtidos foram usados para estimar a vida à fadiga da pele da asa.

**Palavras-chave:** Estrutura adaptável; Crescimento de fenda de fadiga; Ligas de Alumínio; Bordo de ataque da asa; Mecânica da fractura computacional.

# Contents

# List of Figures

# List of Tables

# List of Acronyms

| | |
|---|---|
| AAWC | Active Adaptive Wing Camber |
| AeroG | Aeronautics and Astronautics Research Center (Covilhã, Portugal); |
| AFTI | Advanced Fighter Technology Integration |
| AFWAL | Air Force Wright Aeronautical Laboratories (US) |
| AHS | American Helicopter Society (US) |
| AIAA | American Institute of Aeronautics and Astronautics (US) |
| ASC | American Society for Composites (US) |
| ASCE | American Society of Civil Engineers (US) |
| ASME | American Society of Mechanical Engineers (US) |
| CFD | Computational Fluid Dynamics |
| CNATRA | Chief of Naval Air Training (US) |
| DLR | Deutschen Zentrum fur Luft- und Raumfahrt |
| DOF | Degree of Freedom |
| EAP | Electroactive Polymer |
| FEM | Finite Element Method |
| FEUP | Faculdade de Engenharia da Universidade do Porto |
| FGM | Functionally Graded Gaterial |
| IDMEC | Instituto de Engenharia Mecânica |
| IMechE | Institution of Mechanical Engineers (UK) |
| INEGI | Instituto de Ciência e Inovação em Engenharia Mecânica e Engenharia Industrial (Porto) |

| | |
|---|---|
| ISBN | International Standard Book Number |
| IST | Instituto Superior Técnico (Lisbon) |
| LE | Leading Edge |
| LAETA | Laboratório Associado de Energia, Transportes e Aeronáutica |
| MAW | Mission Adaptive Wing |
| MIT | Massachusetts Institute of Technology |
| mVCCT | Modified Virtual Crack Closure Technique |
| NACA | National Advisory Committee for Aeronautics (predecessor of NASA) |
| NASA | National Aeronautics and Space Administration (US) |
| OMPI | Organisation Mondiale de la Propriété Intellectuelle (WIPO) |
| PLA | Polylactic acid or Polylactide |
| SIF | Stress intensity factor |
| SMA | Shape Memory Alloy |
| SMP | Shape Memory Polymer |
| SPIE | International Society for Optics and Photonics |
| TE | Trailing edge |
| UAV | Unmanned Aerial Vehicle |
| UBI | Universidade da Beira Interior (Portugal) |
| UCAV | Uninhabited Combat Air Vehicle |
| UK | United Kingdom |
| UP | Universidade do Porto |
| US | United States |
| USAF | United States Air Force |
| WIPO | World Intellectual Property Organization (OMPI) |

# Chapter 1

# Introduction

## 1.1 Contextualization

This work will analyse a concept of morphing leading edge for an Unmanned Aerial Vehicle (UAV) wing. This concept was developed at the German Aerospace Centre (DLR, *Deutsches Zentrum für Luft- und Raumfahrt*) in the context of the EU financed project Change (Combined morphing assessment software using flight envelope data and mission based morphing prototype wing development). This work is described in the papers "Experimental Investigation of a Compliant Mechanism for an UAV Leading Edge", (Radestock et al., 2015), and "Structural Optimization of an UAV Leading Edge with Topology Optimization" (Radestock et al., 2014). Also related to these works are the papers "Design of a smart leading edge device for low speed wind tunnel tests in the European project SADE" (Kintscher et al., 2011) and "Design of a smart leading edge device" (Kintscher and Wiedemann, 2013), focusing on the wing skin.

The base of the concept was an UAV model from TEKEVER[a], with a wing span of 4m and a maximum take-off weight of 25 kg, for which morphing wings were developed. The morphing actions included span extension and independent leading edge and trailing edge camber variation. The above mentioned papers report the leading edge studies in this context. This thesis will focus and analyse the morphing leading edge concept. The paper "Experimental Investigation of a Compliant Mechanism for an UAV Leading Edge" (Radestock et al., 2015) will be used as a guideline to simulate the actuation and morphing of the structure. However, the skin will not be modelled as if it was manufactured in composite materials, but instead in Aluminium alloys, traditional to the aircraft industry.

The design of the morphing wing was based on the premise the UAV spent most of its flight time in observation status. Therefore, the basis wing profile was chosen to be NACA 6510 profile, with a chord length of 60 cm. This means that the unmorphed, original shape of the wing is one with a drooped leading edge, and the morphing action

[a]TEKEVER is a Portuguese product oriented company, founded in 2001 by former students of Instituto Superior Técnico, Lisbon. It focuses in innovative technologies for the enterprise, aerospace, defense and security markets (`www.tekever.com/en/group/about/`).

consists in lifting it. As it will be seen on Chapter 2, this modifies the characteristics of wing, making it more suitable for observation (drooped) or high speed cruise (lifted).

The leading edge morphing was implemented in 30 % of the chord, and its conception used three input profiles (Figure 1.1): NACA 6510 (Green), 2510 (Red) and 3510 (Blue). The maximum deformation occurs between the NACA 6510 and 2510, being needed 11.1 mm vertical displacement to achieve the intended morphing. The NACA 3510 profile was only used as an intermediate state.

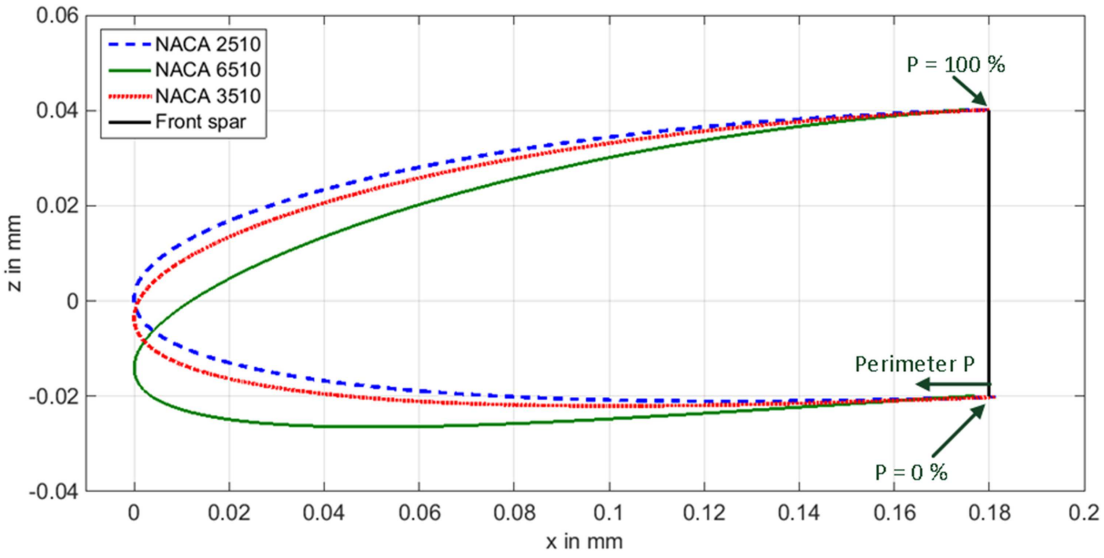


Figure 1.1: Leading edge base profiles (Radestock et al., 2015).

A digital 3D model of the leading edge was obtained and used as base to all computational work done during this thesis. The model comprised the following parts:

1. Skin, following the NACA 6510 profile. Holes for countersunk bolts are visible both in the skin and the spar, leading to the assumption that the skin is to be bolted to the spar in several places. Therefore, the connection was assumed to constraint all degrees of freedom.

2. A Stringer located at about 55% of profile perimeter. Its function is to provide an attachment point, where the skin is actuated. Reinforcement plates were present in the faces that contact with the actuation mechanism. No information was provided, by any source, concerning the connection between this part and the skin, nor concerning the connection between the actuator and this part, and possible gaps between them.

3. Compliant Mechanism, which applies the actuation motion resultant from the rotation of the Servomotor to the skin, and is connected to the Front spar by a fixing

part and connectors (pins, bolts or similar) in both holes. It was assumed that these connections were rigid and without gaps, meaning that all degrees of freedom (DOF) could be considered fixed at this end. This is because the upper rotational DOF's are constrained by the lower connections and vice-versa.
This mechanism relies in the concept of flexure hinge, a zone that, due to its relatively low stiffness, bends and allows the "rotation" of the remaining zones;

4. A Servomotor providing the energy and motion needed to the morphing action, and its fixtures;

5. The front Spar, to which the servomotor and skin are fixed, and is the major structural component of the wing structure, together with rear Spar (not present in the model).

Figure 1.2 shows the *SolidWorks* 3D model with the mentioned parts, the coordinated axis used throughout this text and the main dimensions.

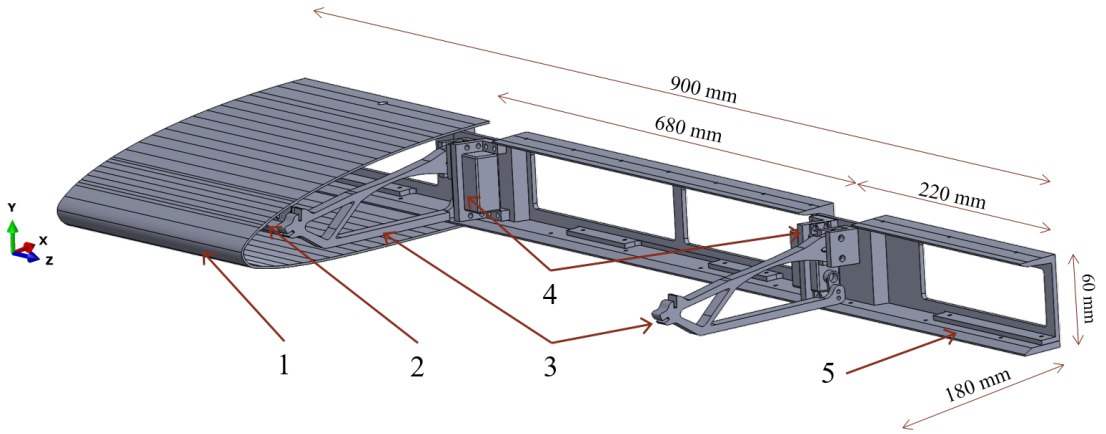


Figure 1.2: 3D model of the analysed structure.

The morphing action will be repeated throughout the life of the UAV, and this implies varying stresses on the components, specially in the compliant mechanism and in the skin. Therefore, and bearing in mind the possible existence of a crack, due to any reasons, it is important to predict any fatigue problems, and make an assessment of the damage tolerance of this design. Also, due to the skin's curvature, the presence of cracks is an interesting problem from the point of view of Fracture Mechanics.

## 1.2 Objectives

The objective of this work is to understand the behaviour of cracks that, for any reason, could be present on the leading edge skin. For that purpose, Linear Elastic Fracture Mechanics (LEFM) concepts and assumptions will be used. Also, and provided that crack behaviour is know, a fatigue life estimate in the light of the Damage Tolerant Design philosophies will be performed.

## 1.3 Structure of the document

This document is divided into 10 Chapters:

1. Introduction, the present one, where the problem in study was presented;
2. Basic Aerodynamics Concepts, in which the reader is briefly informed about airfoils, their behaviour and characterization. In this chapter, high-lift devices are given special attention;
3. Morphing Aircraft. In this Chapter, the evolution and current state-of-art regarding morphing aircraft is addressed;
4. Damage Tolerant Design. This Chapter provides the theoretical background necessary to fully understand this work. Fatigue design philosophies and life prediction techniques are introduced, the most important Linear Elastic Fracture Mechanics concepts are reminded and Computational LEFM techniques are introduced and discussed;
5. Analysis of the Compliant Mechanism, where the behaviour of the actuation mechanism behaviour;
6. Modelling of the Leading Edge. This Chapter describes and discusses the process of modelling the leading edge and the analysis of its behaviour without cracks.
7. Modelling of Longitudinal Cracks. In this Chapter, through cracks parallel to the generatrix of the skin surface are modelled and studied. A discussion of the problems encountered and respective solutions is made.
8. Modelling of Oblique Cracks, where the behaviour of cracks oblique to the aforementioned generatrix is assessed. Again, modelling difficulties are assessed.
9. Estimation of the Fatigue Life, based on the data gathered on Chapters 7 and 8.
10. Conclusions and Future Works.

# Chapter 2

# Basic Aerodynamics Concepts

Since this work is concerned with morphing wings, a brief overview of relevant terminology and concepts is appropriate and will be done in this Chapter. Moreover, it is relevant to present a brief introduction on high lift devices, its types and their influence on wings behaviour This will be completed and illustrated with a number of relevant patents of mechanisms of this type.

## 2.1 Basic Concepts

In this section, a concise summary of important concepts on wing construction and behaviour will be done. Books on aerodynamics, of varying depth and purpose, should be consulted for details. General presentations are found, for instance, in Anderson's "Introduction to flight" (Anderson, 1989), and "Fundamentals of aerodynamics" (Anderson, 2011). Roots of aerodynamic studies of airfoils (NACA, etc.) are found in Abbott and von Doenhoff "Theory of wing sections: including a summary of airfoil data" (Abbott and von Doenhoff, 1959), and a very practical presentation of basic concepts is found in Naval Air Training Command "Fundamentals of aerodynamics" (Naval Air Training Command, 1988).

The shape of a typical airfoil, Figure 2.1, is defined by Leading edge (LE), Trailing edge (TE), Chord line, Camber line (or mean line), Upper and Lower surfaces, leading to an airfoil as schematically presented in Figure 2.2 (Talay, 1975). Basic definitions, as given by Anderson's "Introduction to Flight" (p.179, Anderson, 1989), are:

**Chord line** is the straight line connecting the leading and the trailing edges;

**Mean camber line** is the locus of the points halfway the upper and lower surfaces, as measured perpendicular to the mean camber line itself;

**Camber** is maximum distance between mean camber line and chord, measured perpendicular to the chord line. The camber variation implies variation of aerodynamic forces, as suggested in Figure 2.3.

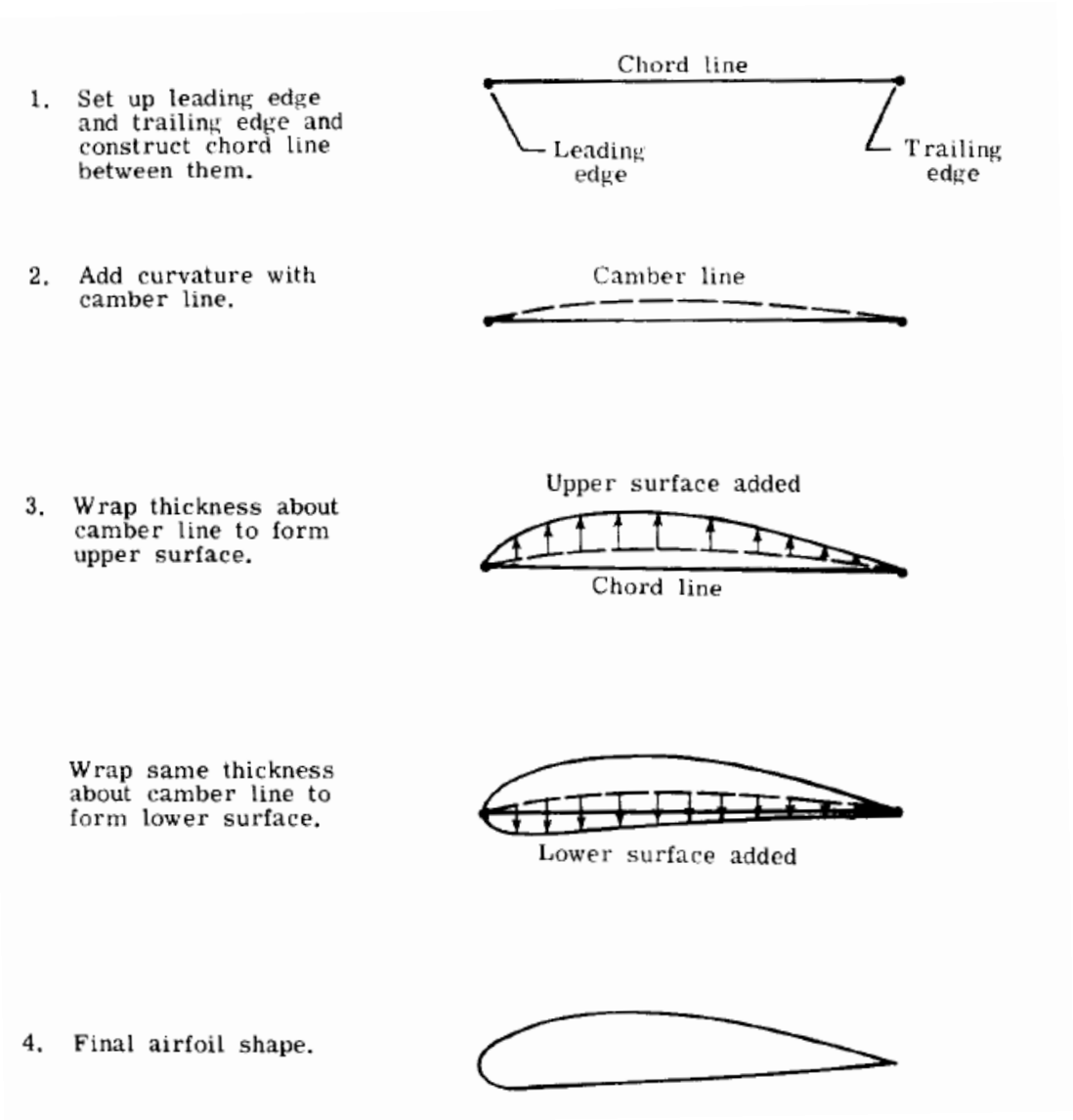


Figure 2.1: Geometric construction of an airfoil (Talay, 1975, p. 60).

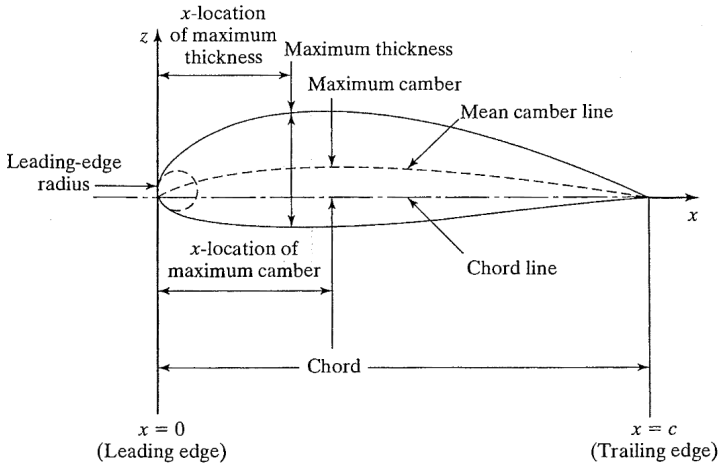


Figure 2.2: Airfoil geometry and nomenclature (p.219, Bertin and Cummings, 2009).

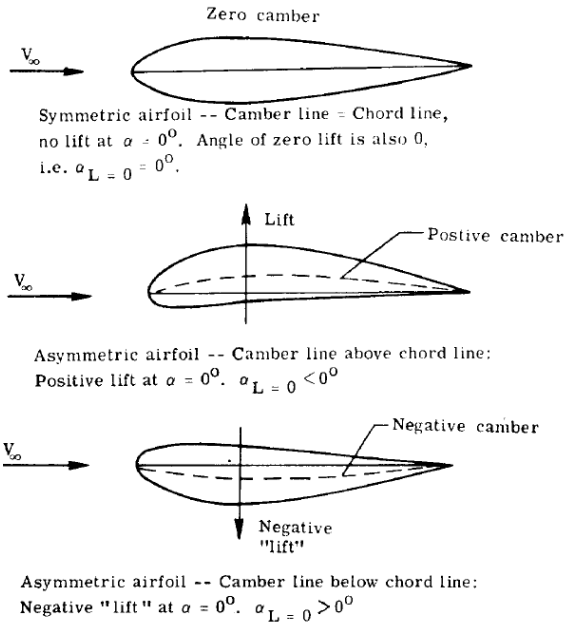


Figure 2.3: Airfoil camber line variation (p.61, Talay, 1975).

2D coefficients are commonly used to characterize aerodynamic loads. Figure 2.4 shows the resultant aerodynamic force acting on an airfoil. The line of action of the aerodynamic force crosses the chord line in the centre of pressure. The aerodynamic force

has two components, lift and drag, Figure 2.4 (b) . Lift is the component perpendicular to relative wind; drag is the component parallel to relative wind. The centre of pressure, lift and drag depend on the angle of attack $\alpha$, angle between relative wind direction and chord line. Since the line of action of the aerodynamic force passes through the centre of pressure, there is no moment there.

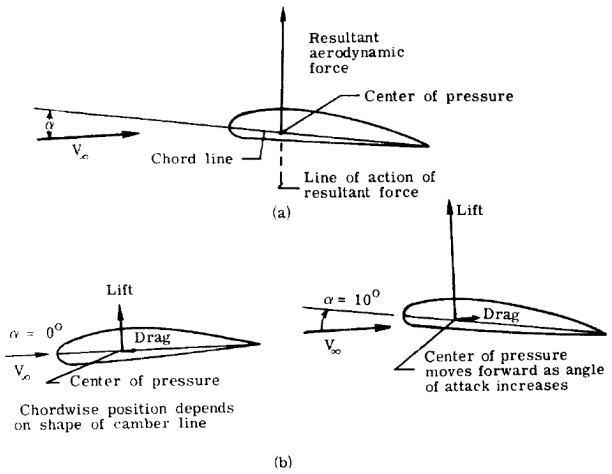


Figure 2.4: Airfoil aerodynamic characteristics (p.66, Talay, 1975).

As in (p.195, Sadraey, 2012), angle of incidence is the angle formed by the wing chord line and the fuselage longitudinal axis, an imaginary line that extends from the nose of the aircraft to the tail. In this sense, 'angle of incidence' is a design constant of each aircraft [a] , whereas angle of attack $\alpha$ is, of course, a variable during each mission [b]. Figure 2.5 shows typical pressure distributions on an airfoil section. for several values of $\alpha$ (angle of attack[c]).

[a] Unless the aircraft is equiped with wings variable incidence wings; this is extremely uncommon (the Vought F-8 Crusader is a rare exemple, as will be seen later), and the reasons are well explained by Sadraey: "A variable wing incidence is not recommended, since there are huge safety and operational concerns. To allow for the wing having a variable setting angle, there must be a single shaft around which the wing is rotated by pilot control. Such a mechanism is not 100% reliable for aviation purposes, due to fatigue, weight, and stress concentration concerns" (p.195, Sadraey, 2012).

[b] For more detail, refer to http://www.aviation-history.com/theory/angle_of_incidence.htm and http://www.aviation-history.com/theory/angle_of_attack.htm

[c] These authors use the designation angle of incidence for $\alpha$, named here as angle of attack, i.e, angle between the chord line of a given airfoil section and the direction of flight or of the undisturbed stream (see p.17, Houghton and Carpenter, 2003). The same usage for 'angle of incidence' is found, for instance, in (p.76 and p.90, Piercy, 1947).

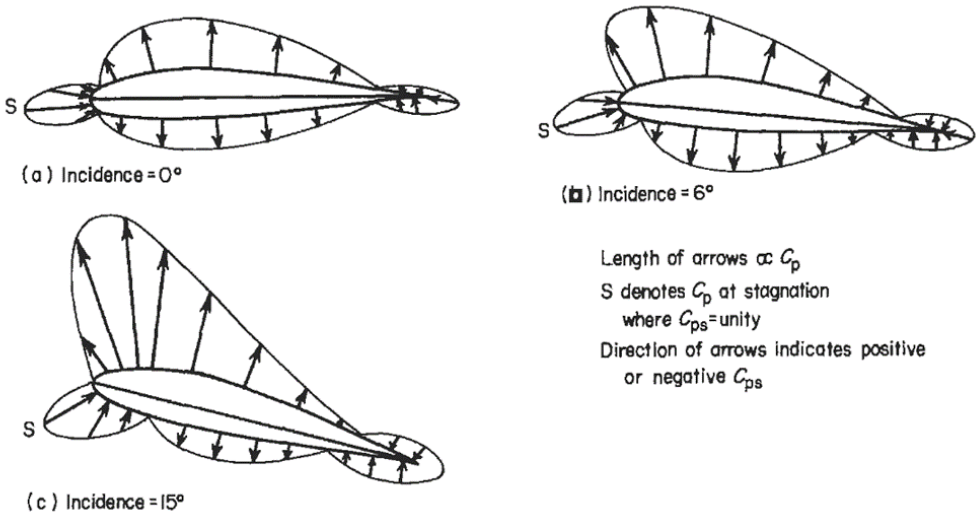


Figure 2.5: Typical pressure distributions on an airfoil for several values of $\alpha$ (angle of attack) (p.29, Houghton and Carpenter, 2003).

Major 2D aerodynamic characteristics, measured in wind-tunnel tests, are the lift coefficient $c_l$, the drag coefficient $c_d$, and moment coefficient $c_m$ about the quarter-chord point and about the aerodynamic centre.

With:

- Chord length of the airfoil: $c$;
- Wing span: $b$;
- Wing area, or planform area: $S = c \times b$;
- Relative airspeed: $v$;
- Air density: $\rho$;
- Dynamic pressure: $q = 0.5\rho v^2$ ;
- Lift acting in on the airfoil, per unit of length: $l$;
- Drag acting in on the airfoil, per unit of length: $d$;
- Moment acting in on the airfoil (at the aerodynamic centre, quarter chord or any other point), per unit of length: $m$;

The non-dimensional coefficients, expressed per unit of length of the airfoil, are:

$$c_l = l/0.5\rho v^2 c \tag{2.1}$$

$$c_d = d/0.5\rho v^2 c \tag{2.2}$$

$$c_m = m/0.5\rho v^2 c^2 \tag{2.3}$$

Considering the total of these actions, namely:

- $L$, the total lift acting on the wing;
- $D$, the total drag acting on the wing;
- $M$, the total lift acting on the wing;

One can arrive to the 3D aerodynamic characteristics of the airfoil are:

$$C_l = L/\rho v^2 S \tag{2.4}$$

$$C_d = D/\rho v^2 S \tag{2.5}$$

$$C_m = M/\rho v^2 c S \tag{2.6}$$

Figure 2.6, taken from Anderson's "Introduction to Flight", compares schematically the dependency of with angle of attack, for cambered and symmetric airfoils.

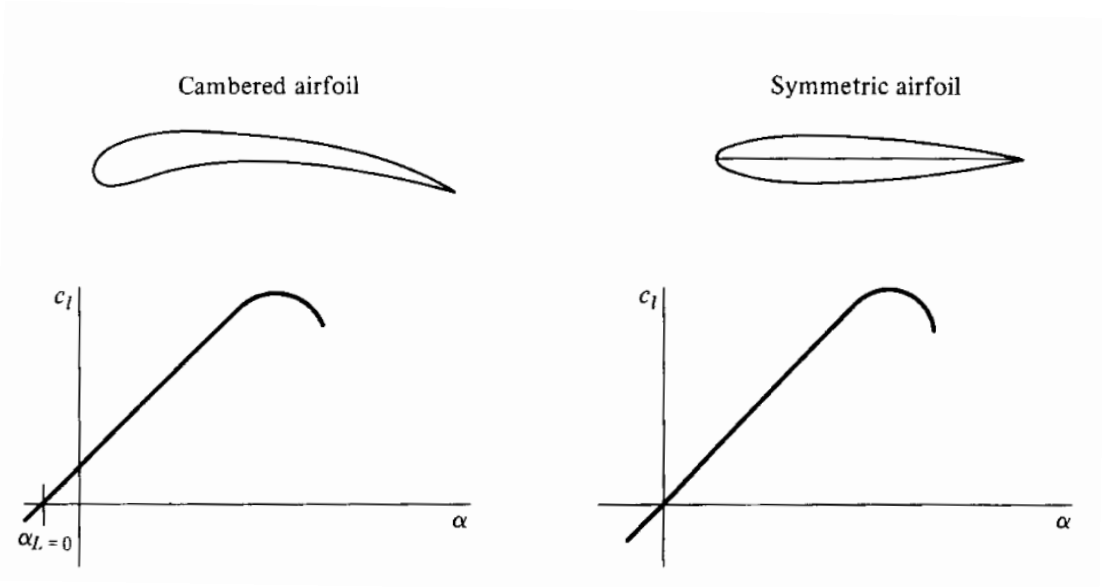


Figure 2.6: Comparison of lift curves: cambered and symmetric airfoils (Anderson, 1989).

## 2.2 High lift devices

High lift devices come in many different shapes and formats. A summary is given in (Loftin, 1985) on Figure 2.7, where a comparison of maximum lift for different types of high lift devices is presented.

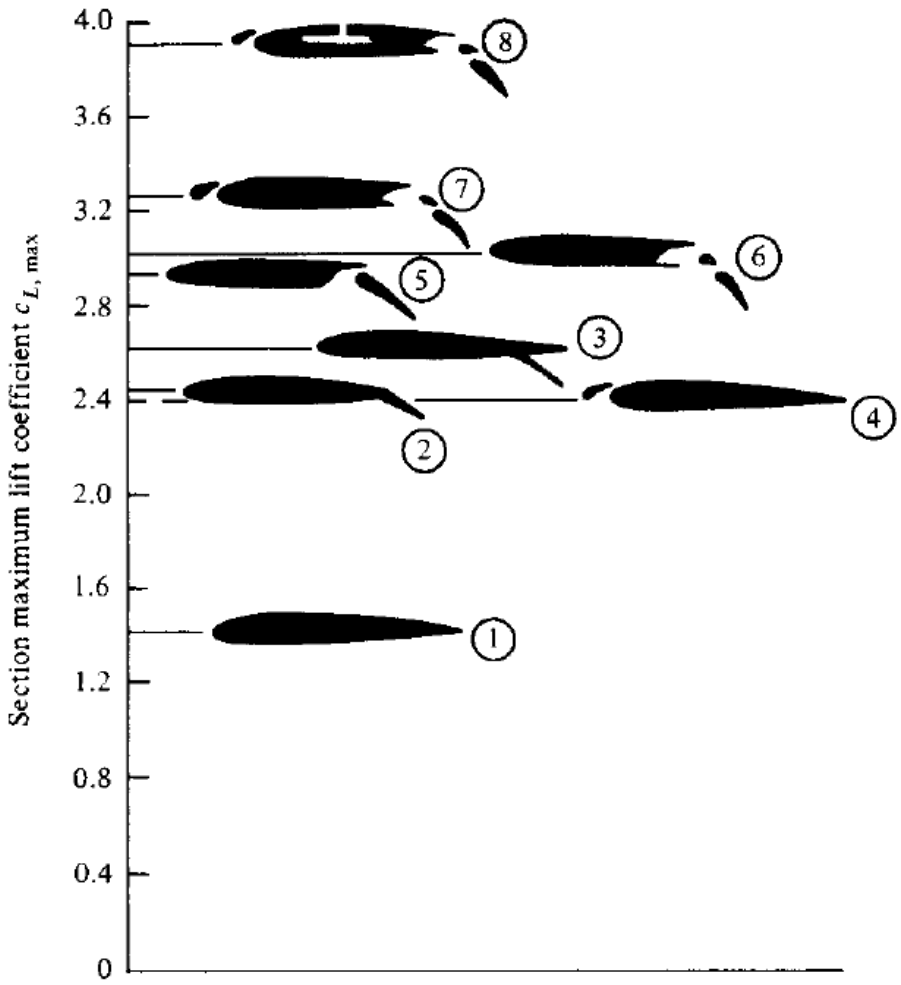


Figure 2.7: Typical values of maximum lift coefficient for various types of high lift devices: 1 – airfoil only; 2 – plain flap; 3 – split flap; 4 – leading edge slat; 5 – single-slotted flap; 6 – double-slotted flap; 7 – double-slotted flap together with a leading edge slat; 8 – addition of boundary layer suction at the top of the airfoil (Loftin, 1985).

An example the influence of these devices are trailing edge flaps, which have a remarkable influence on the lift versus angle of attack curves. This is shown schematically in Figure 2.8, from Anderson's "Introduction to Flight".

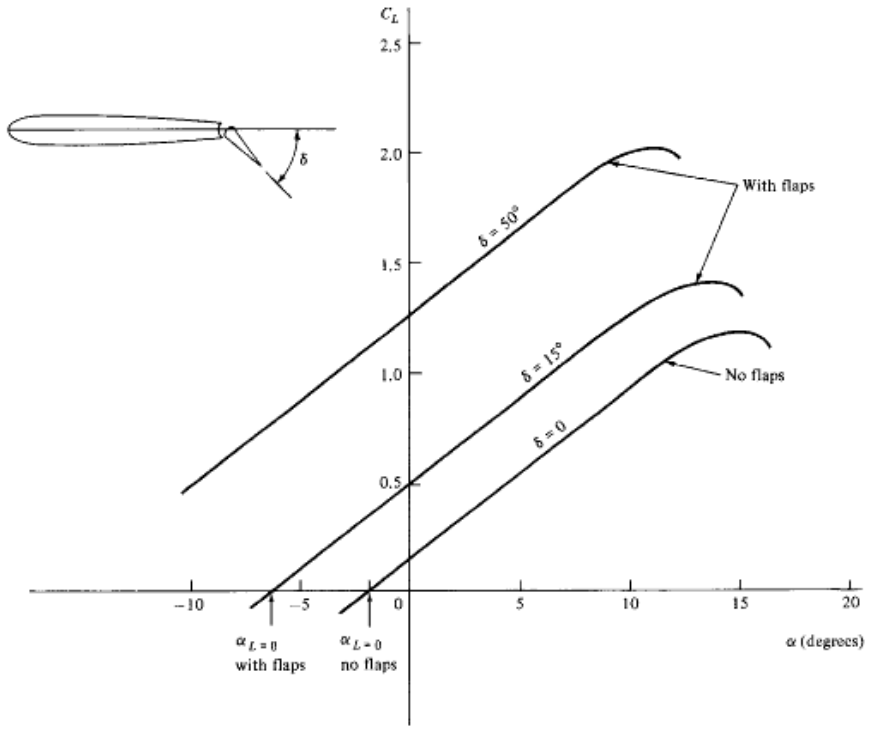


Figure 2.8: Dependency of lift on the flap angle. Curves for typical medium range transport jet (Anderson, 1989).

Leading edge devices such as nose flaps, Kruger flaps, and slats reduce the pressure peak near the nose by changing the nose camber. Slots and slats permit a new boundary layer to start on the main wing portion, eliminating the detrimental effect of the initial adverse gradient (Sforza, 2014; Kroo, 1997). Taken from an AIAA book by Raymer (Raymer et al., 1992), Figure 2.9 shows some leading edge devices whereas Figure 2.10 shows some types of flaps, illustrating the variety of current solutions for control surfaces (and auxiliary control surfaces). Figure 2.11 distinguishes leading edge flaps and Krueger flaps.

Figure 2.12shows the leading edge slats and trailing edge flaps of an Airbus A310-300. A Boeing 747-400 ready for landing shows its Krueger flaps in Figure 2.13, together with triple-slotted trailing edge flaps. Finally, trailing edge flaps of an Airbus A380 are shown in Figure 2.14.

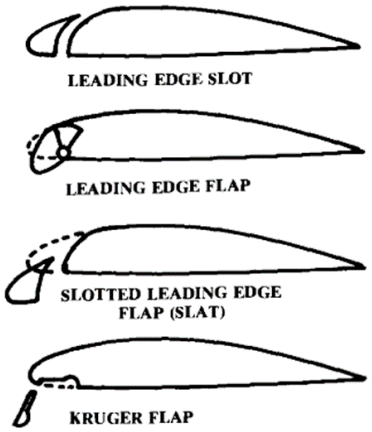


Figure 2.9: Leading edge devices (p.277, Raymer et al., 1992).

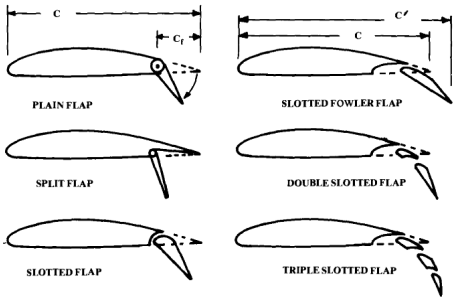


Figure 2.10: Flap types (p.276, Raymer et al., 1992).

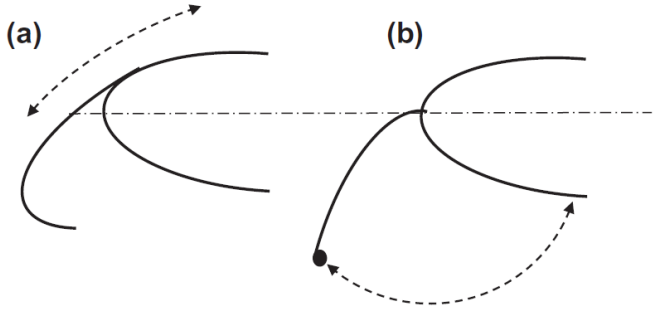


Figure 2.11: Leading edge flap systems: (a) flap; (b) Krueger flap (Sforza, 2014).

Figure 2.12: Leading edge slats and trailing edge flaps on Airbus A310-300, showing fairing for the trailing edge flap mechanisms in the deflected position (Wikipedia, 2016d).

Figure 2.13: Triple-slotted trailing edge flaps and variable camber Krueger flaps on the leading edges of the wings of a Boeing 747-400 in the landing configuration (Wikipedia, 2016b).


Figure 2.14: Airbus A380 with trailing edge flaps deployed (Wikipedia, 2015).

## 2.3 Patents on High lift devices

Steve Olson, citing Richard Miller, an American Professor of Mechanical Engineering, wrote that "(...) engineering is not a body of knowledge. "Engineering is a process. It's a way of thinking, [....]. The aircraft industry started in a bicycle shop. It didn't start with folks who had a PhD in physics"" (Olson et al., 2013).

The innovative folks that are typically interested in aeronautics, and the struggle for market opportunities, imply that there are many patents related with the topic of the present work.

Nowadays the search for patents is made easy using the Internet, using Google or sites such as Free Patents Online[d] where, in an user friendly way, search by topic can be made and .pdf files of original documents can be downloaded. Through these, several aircraft wing topics were searched:

1. Leading edge devices (droop nose, slat, Krueger, ...);

2. Trailing edge devices;

3. Morphing and related aspects;

The third will be addressed later on this work. On the next paragraphs, a few highlights for the first two topics are illustrated.

### 2.3.1 Patents concerning leading edge devices

There are plenty of patents concerning leading edge devices. Table 2.1, while not being fully extensive, cites a number of relevant patents retrieved by the search done, in chronological sequence. This topic includes patents that deal with the wing control surfaces or auxiliary control surfaces, and are very numerous. An early one, by Boeing, is US 3 282 535, 1966, concerning a simple flap (Figure 2.15). Boeing patent US 3 743 219, 1973, also deals with a high lift leading edge device (Figures 2.15 and 2.17). Patent US 4 202 519, 1980 also by Boeing, concerns a leading edge slat (Figure 2.18). A recent example is patent US 8 534 610 B1, 2013, again by Boeing, involving a slat with shape memory alloy (SMA) that deploys a suitable aerodynamic geometry (Figure 2.19).

[d] http://www.freepatentsonline.com

Table 2.1: Patents for leading edge devices.

| | | |
|---|---|---|
| US 3 282 535 | 1966 | Leading edge spoiler and flap wing stall control means |
| US 3 375 998 | 1968 | Leading edge flap and apparatus thereof |
| US 3 743 219 | 1973 | High lift leading edge device |
| US 3 743 220 | 1973 | Leading edge flap mechanism |
| US 3 831 886 | 1974 | Airfoil with extendible and retractable leading edge |
| US 3 910 530 | 1975 | Leading edge flap |
| US 4 189 120 | 1980 | Variable camber leading edge flap |
| US 4 202 519 | 1980 | Airfoil leading edge slat apparatus |
| US 4 285 482 | 1981 | Wing leading edge high lift device |
| US 4 360 176 | 1982 | Wing leading edge slat |
| EP 0 100 775 A1 | 1982 | Wing leading edge slat |
| EP 0 068 737 A1 | 1982 | Leading edge flap for an airfoil |
| US 4 398 688 | 1983 | Leading edge flap for an airfoil |
| US 4 399 970 | 1983 | Wing leading edge slat |
| US 4 422 606 | 1983 | Automatic leading edge slat for aircraft |
| US 5 158 252 | 1992 | Three-position variable camber Krueger leading edge flap |
| US 5 544 847 | 1996 | Leading edge slat/wing combination |
| US 5 839 699 | 1998 | Leading edge slat/wing combination |
| US 6 375 126 B1 | 2002 | Variable camber leading edge for an airfoil |
| US 2006 / 0 000 952 A1 | 2006 | Aircraft leading edge apparatuses and corresponding methods |
| US 2006 / 0 102 803 A1 | 2006 | Leading edge flap apparatuses and associated methods |
| US 7 270 305 B2 | 2007 | Aircraft leading edge apparatuses and corresponding methods |
| EP 1 972 547 A1 | 2007 | Wing leading edge device |
| WO 2008 / 084 260 A2 | 2008 | A leading edge structure for an airfoil |
| US 2009 / 0 072 093 A1 | 2009 | Link mechanisms for gapped rigid Krueger flaps and associated systems and methods |
| US 7 828 250 B2 | 2010 | Leading edge flap apparatuses and associated methods |
| US 2010 / 0 084 515 A1 | 2010 | Leading edge structure for an airfoil |
| US 2011 / 0 024 575 A1 | 2011 | Leading edge flap method |
| US 7 992 826 B2 | 2011 | Leading edge flap method |
| US 8 186 630 B2 | 2012 | Leading edge structure for an airfoil |
| US 8 215 590 B2 | 2012 | Aerofoil with leading edge projection |
| US 8 534 610 B1 | 2013 | Method and apparatuses for a leading edge slat on a wing of an aircraft |
| EP 2 851 285 A1 | 2014 | Leading edge variable camber system and method |
| US 8 622 350 B1 | 2014 | Compound leading edge device for aircraft |
| US 9 169 000 B2 | 2015 | Leading edge rib assembly |

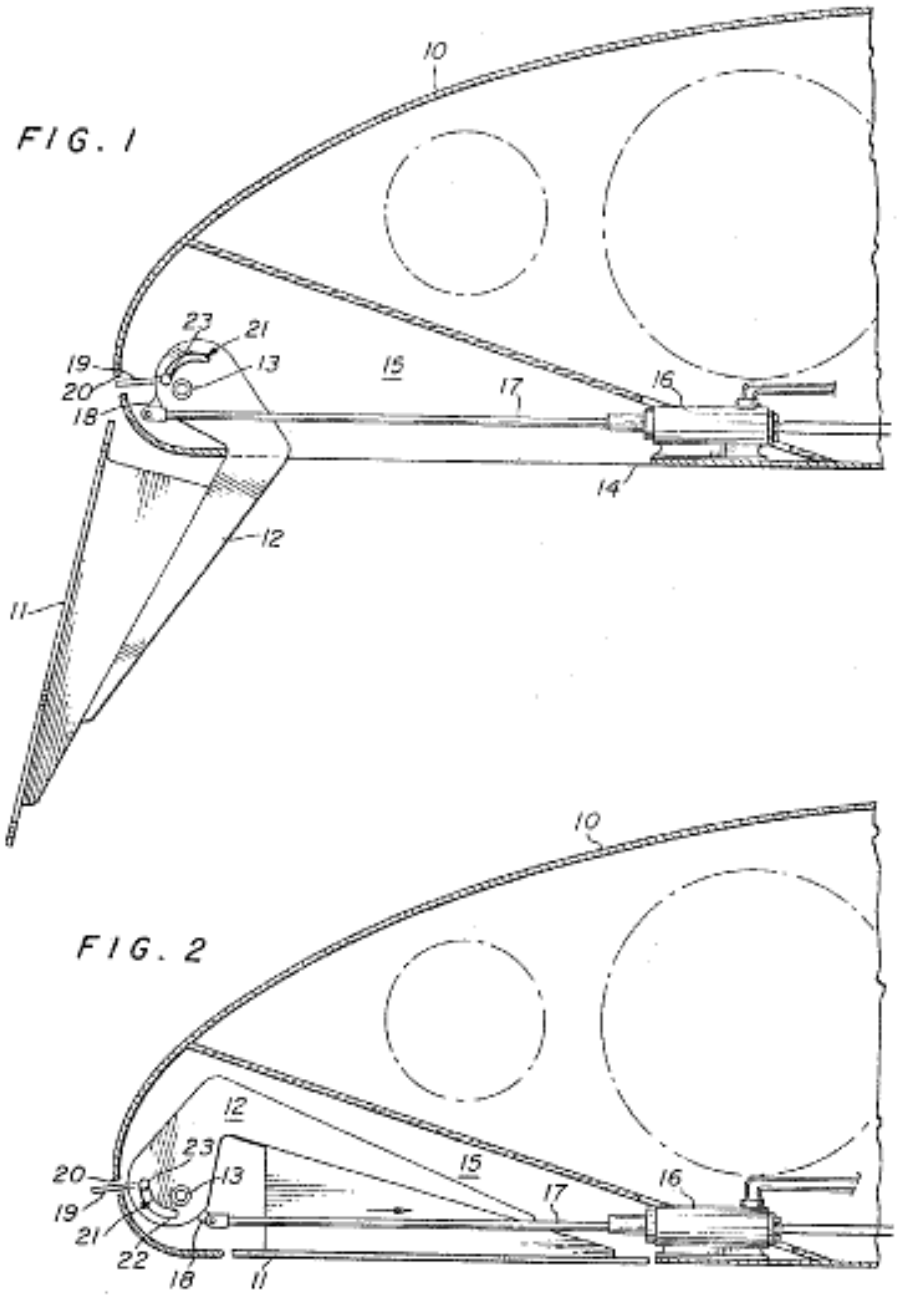


Figure 2.15: Boeing US patent 3 282 535, 1966, "Leading edge spoiler and flap wing stall control means".

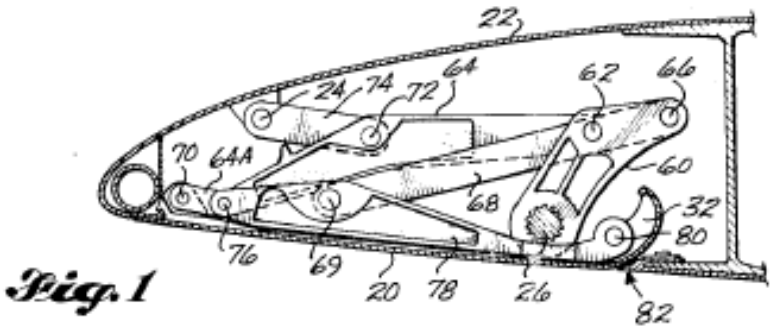


Fig. 1

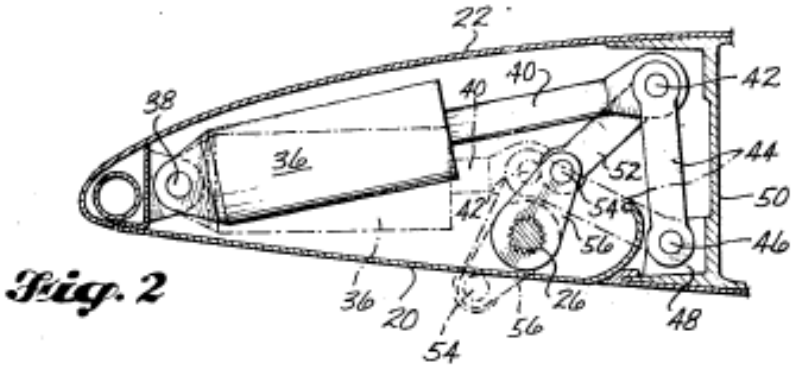


Fig. 2

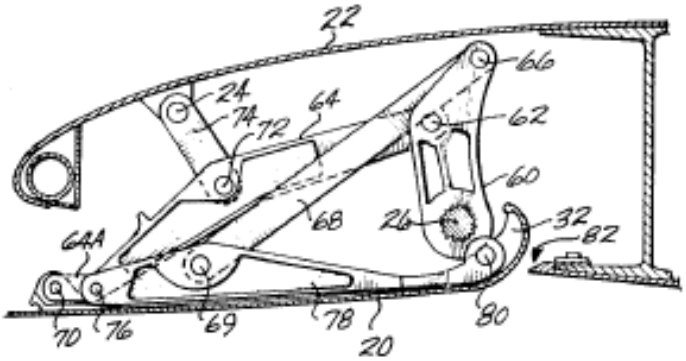


Fig. 3

Figure 2.16: Boeing patent US 3 743 219, 1973: high lift leading edge device.

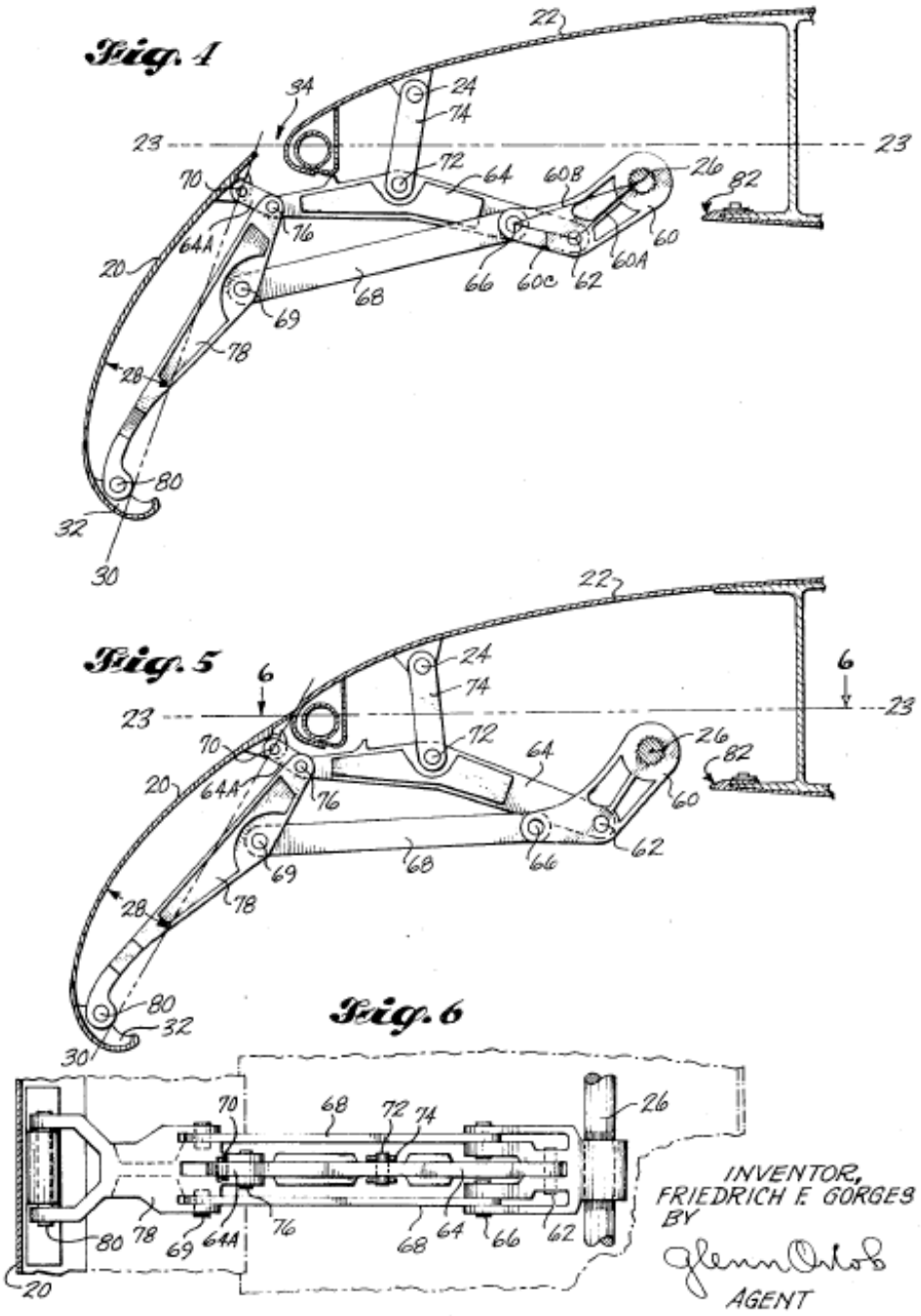


Figure 2.17: Boeing patent US 3 743 219, 1973: high lift leading edge device.

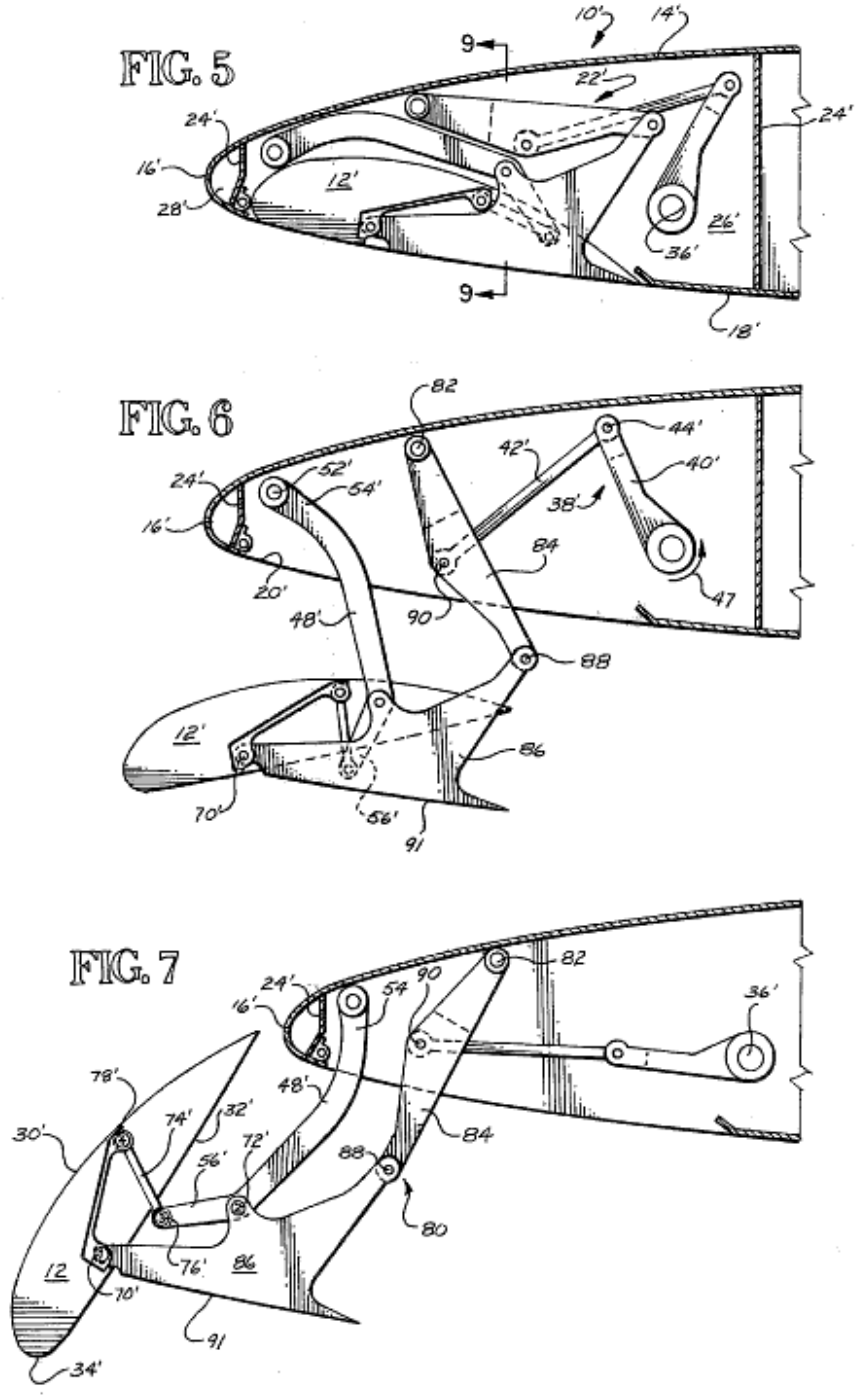


Figure 2.18: Patent US 4 202 519, 1980, Boeing: leading edge slat.

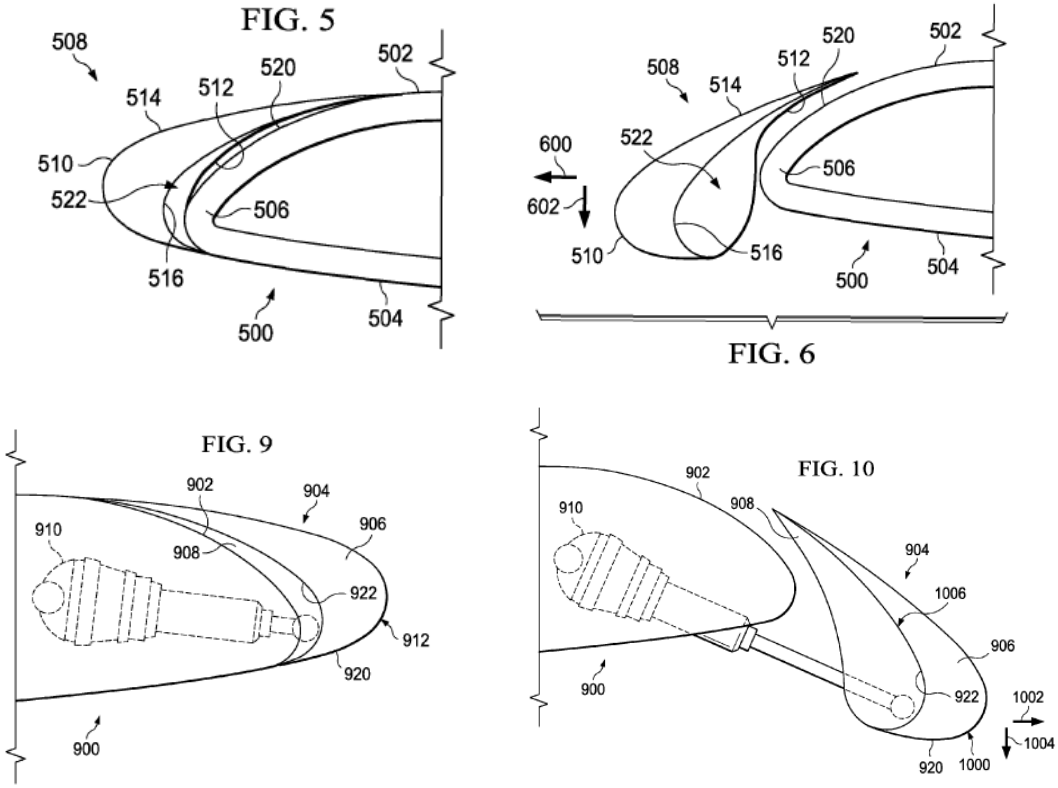


Figure 2.19: Boeing patent US 8 534 610 B1, 2013: slat with shape memory alloy (SMA).

### 2.3.2 Patents concerning trailing edge devices

There is also a number of patents concerning trailing edge devices. Some examples are mentioned on Table 2.2. A Junkers patent, originally published in Germany in 1939, and as US patent (2 282 516) in 1942, concerns an airplane wing structure, Figure 2.20, and is exemplary of the leading edge auxiliary control surfaces that are commonly found.

Table 2.2: Patents for trailing edge devices

| | | |
|---|---|---|
| US 2 282 516 | 1942 | Airplane wing structure |
| US 2 289 704 | 1942 | Aircraft wing |
| US 2 518 854 | 1950 | Wing high lift device |
| US 3 528 632 | 1970 | High lift flaps for aircraft |

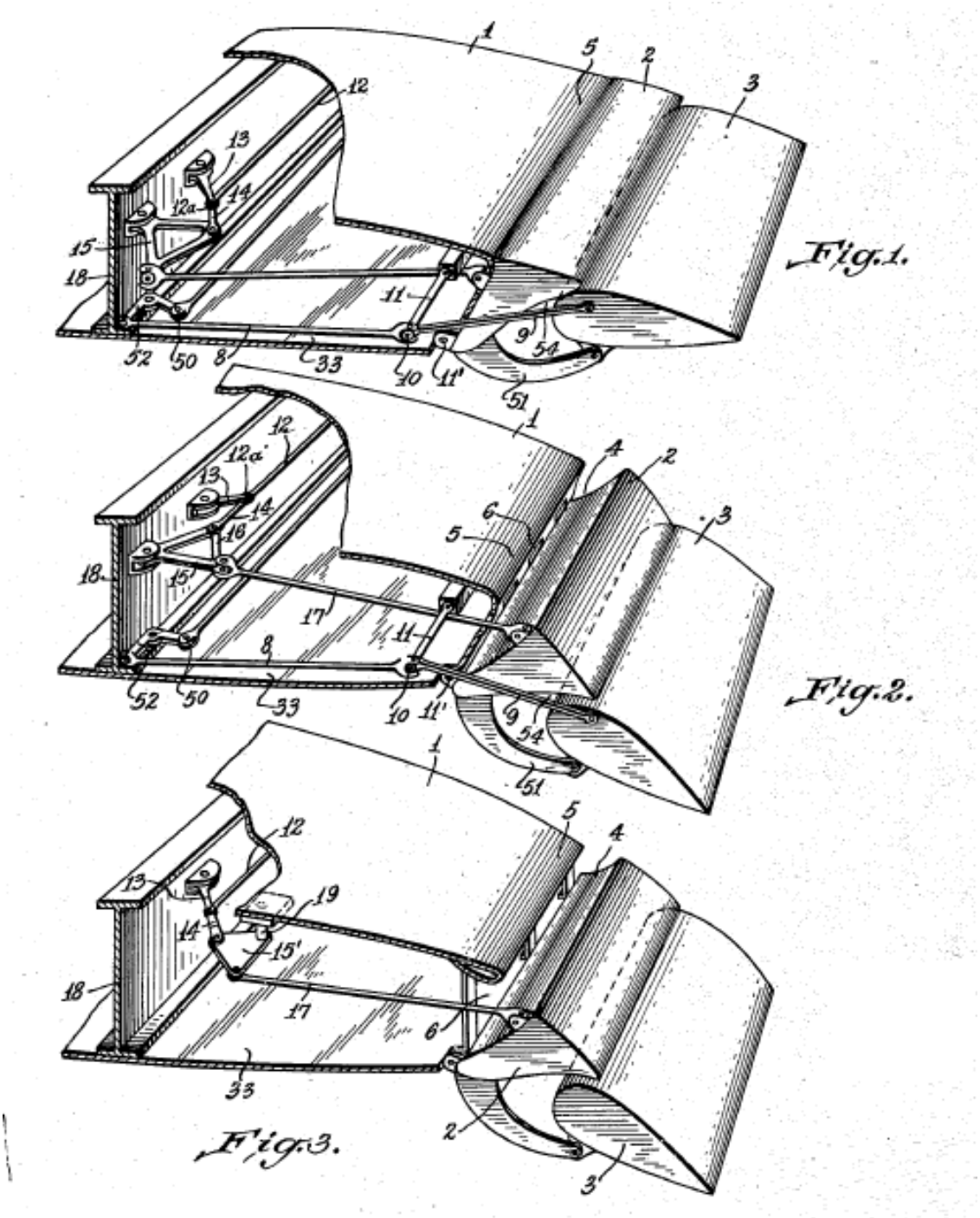


Figure 2.20: US patent 2 282 516 of 1942: airplane wing structure.

# Chapter 3

# Morphing Aircraft

In this chapter, the evolution and current status of morphing aircraft will be addressed. First, the concept of morphing aircraft will be analysed, different classifications will be presented and its inspiration will be mentioned. After that, the evolution of morphing aircraft will be addressed with a on leading edge morphing designs, using patents. Finally, the current trends in research will be addressed.

## 3.1 Morphing Aircraft: Definition and classifications

### 3.1.1 Definition

Independently of their nature (commercial, recreational, military or other), aircraft face different conditions throughout the various stages of a flight. A list of design constraints and requirements for aircraft design is given in the recent textbook (Sadraey, 2012), consisting of 18 topics as type of aircraft (civil, military...), manoeuvrability, pilot control, weight, take off run, amongst others, and each one of them subdivided in several items. As in many other engineering fields, aircraft design is a compromise among the requirements of the various flight conditions: a design can be optimized for certain specific conditions, but not for all conceivable flight conditions. If an aircraft design aims to excel performance at a given condition, another conditions exist in which the performance will be relatively poor (Seigler et al., 2007). Therefore, there is not an ideal single design for all flight conditions, and either aircraft designers achieve a compromise between the requirements of the various flight conditions or the aircraft has the ability to change shape (Falcão et al., 2011). The latter solution has been sought since the beginnings of aviation: the 1903 Wright brothers' airplane changed its shape, since it was controlled by means of twisting its wings (Jha and Kudva, 2004; Rodriguez, 2007).

Aircraft morphing is included among 25 new technologies and operational improvements relevant for "green aviation" (Agarwal, 2012) and emerged as a widely researched topic. Consulting the Merriam-Webster dictionary, to morph is defined as "to change the form or character of", and also "to undergo transformation" (Merriam-Webster Dictionary, 2016). (Barbarino et al., 2011), while citing (Weisshaar, 2006), write that "Morphing

is short for metamorphose and, in the aeronautical field, is adopted to define a set of technologies that increase a vehicle's performance by manipulating certain characteristics to better match the vehicle state to the environment and task at hand".

Other authors also have came up with their definitions:

- According to the above mentioned (Weisshaar, 2006), "Morphing aircraft are multi-role aircraft that change their external shape substantially to adapt to a changing mission environment during flight. Morphing aircraft are also known as variable geometry or polymorphous aircraft";
- (Jha and Kudva, 2004) define a morphing aircraft as "an aircraft that changes configuration to maximize its performance at radically different flight conditions. These configuration changes can take place in any part of the aircraft, e.g. fuselage, wing, engine, and tail.";
- Morphing is defined by (Cesnik et al., 2004) as "a capability to provide superior and/or new vehicle system performance by tailoring the vehicle's state to adapt to the environment and multi-variable mission roles";
- For (Seigler et al., 2007), "Morphing aircraft are flight vehicles that alter their shape to effectuate a change in either mission performance and/or to provide control authority for manoeuvring";
- (Sofla et al., 2010) state that "in the field of aeronautics, "shape morphing" has been used to identify those aircraft that undergo certain geometrical changes to enhance or adapt to their mission profiles";
- (McGowan et al., 2009) advocate a broader definition, which includes air, land and sea vehicles and is based on the work of NATO Research and Technology Organization, Applied Vehicle Technology Technical Team on Morphing Vehicles: "Real-time adaptation to enable multi-point optimized performance".

Clearly, authors in this field are yet to agree on an exact definition. Nevertheless, despite the diversity of definitions the general idea is the same: "increasing the adaptability of the vehicle to enable optimized performance at more than one point in the flight envelope" (McGowan et al., 2009).

### 3.1.2 Classifications

Another important point where there is no agreement yet is the type and extent of the changes needed for and aircraft to qualify as "shape morphing" (Sofla et al., 2010). High-lift devices, such as flaps and slats, and even landing gears are sometimes considered as morphing (Weisshaar, 2006). Also, air-brakes and spoilers are mentioned in this literature current, but with the remark that "these technologies do not necessarily allow an aircraft to perform different types of mission tasks" (Rodriguez, 2007). However, other authors affirm that "the conventional hinged control surfaces or high lift devices, such as flaps or

slats that provide discrete geometry changes cannot be considered as morphing" (Sofla et al., 2010).

The different points of view above can be conciliated with the distinction draw between "Discrete Morphing" and "Continuous Morphing" by (Ajaj et al., 2016), and shown on table 3.1:

Table 3.1: Discrete versus Continuous morphing (adapted from Ajaj et al. 2016).

| Discrete morphing | Continuous morphing |
|---|---|
| Singular functionality | Multiple functionalities |
| Adopted locally on board the aircraft | Adopted distributed over the body of the aircraft |
| Operated at few points of the flight envelope | Operated continuously within the flight envelope |
| Suppress coupling between the aircraft axes | Exploit couplings in morphing schedules and between the aircraft axes |

Analysing the table, it is difficult to give examples of continuous morphing structures. However, flaps, slats or landing gears can be easily classified as Discrete Morphing. As these are traditionally used and well established in aviation, it is understandable why some authors do not consider these as morphing structures. Helping to further differentiate these two variants of morphing structures, the concepts of gapless and seamless surfaces are frequently associated with continuous morphing (Kintscher et al., 2011). Morphing may also be grouped in other forms: how the morphing structure is operated, the extent of the geometry change (small, medium or large morphing) (Sun et al., 2016; Weisshaar, 2013), or the location where it happens within the aircraft (e.g.. engine, fuselage, or wings).

Throughout this text all the conceptual currents mentioned above will be taken into account, and will be tried not favour any of them in particular. Whenever possible, the broader definition or opinion will be used.

### 3.1.3 Wing Morphing

Since wings are by far the most studied location for morphing, and as this work will be focused on a wing leading edge, it is important to present yet another classification. Analysing the nature of the change on the wings, a comprehensive classification arises, which is proposed by several authors (Jha and Kudva, 2004; Sofla et al., 2010; Barbarino et al., 2011; Gomez and Garcia, 2011; Weisshaar, 2013; Sun et al., 2016) and is detailed on Figure 3.1.

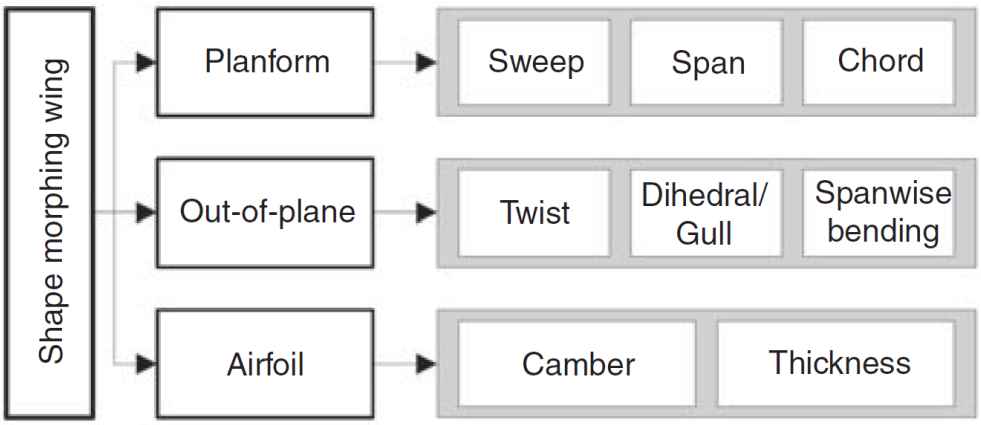


Figure 3.1: Classification of wing morphing concepts (Barbarino et al., 2011).

As morphing main aim is to adapt to the different flight status, it is important to know how changing a certain wing geometric parameter affects the aircraft performance. Figure 3.2 summarizes this information.

| Parameter | Effects of Variability – all other parameters unchanged |
|---|---|
| Wing Plan Area ↑ ↓ | **Increased** lift, load factor capability<br>**Decreased** parasitic drag |
| Wing Aspect Ratio ↑ ↓ | **Increased** L/D, loiter time, cruise distance, turn rates **Decreased**: engine requirements<br>**Increased** maximum speed; **Decreased** parasitic drag |
| Wing Dihedral ↑ ↓ | **Increased** Rolling moment capability, lateral stability<br>**Increased** maximum speed |
| Wing Sweep ↑ ↓ | **Increased** critical Mach no., dihedral effect **Decreased** high-speed drag<br>**Increased** $C_{Lmax}$ |
| Wing Taper Ratio | Wing efficiency (spanwise lift distribution); Induced drag |
| Wing Twist Distribution | Prevents tip stall behavior; Spanwise lift distribution |
| Airfoil Camber | Zero-lift angle of attack, airfoil efficiency, separation behavior |
| Airfoil Thickness/Chord Ratio ↑ ↓ | **Improved** low-speed airfoil performance<br>**Improved** high-speed airfoil performance |
| Leading Edge Radius ↑ ↓ | **Improved** low-speed airfoil performance<br>**Improved** high-speed airfoil performance |
| Airfoil Thickness Distribution | Airfoil characteristics, laminar/turbulent transition |

Figure 3.2: Influence of wing geometric parameters on aircraft performance (Jha and Kudva, 2004).

## 3.2 Nature as inspiration for Morphing Aircraft

Mankind's dream of flight has been inspired by birds and other flying animals. Like aircraft, these also encounter different flight stages, and are able to adapt accordingly. The eagle's flight (Figure 3.3) is a good example of this adaptation, which has been studied since the advent of aviation, in order to optimize aircraft designs.


Figure 3.3: Eagle adapting to different flight phases (Ajaj et al., 2016).

In 1889, Otto Lilienthal[a], wrote the book "Birdflight as the Basis of Aviation", where he describes the problem of flight as "processing the surrounding air with properly shaped wings in a proper way" (Lilienthal, 2001). This implied that the basis of constructing an aircraft is to design a proper shape-adaptable structural system (Barbarino et al., 2011). Lilienthal design several gliders, based on his studies of bird flight mechanics. An illustrative example if these studies is given on Figure 3.4. The work of Lilienthal is a good example of biomimetics: "the study of biological mechanisms and their application to science and engineering" (Thill et al., 2008).

An early and interesting example of aircraft design mimicking nature is the Etrich Taube ("dove" in German) series of designs by Ignaz Etrich[b]. Although they used the now traditional engine and propeller arrangement, Etrich designs resembled much to birds, as one can see in Figure 3.5.

[a]Otto Lilienthal (23 May 1848 – 10 August 1896) was a German pioneer of aviation who focused his work on gliding flights, dying in an accident while flying one of his concepts (Wikipedia, 2016f).

[b]Ignaz "Igo" Etrich (25 December 1879 - 4 February 1967) was Austrian flight pioneer, pilot and fixed-wing aircraft developer (Wikipedia, 2016c).

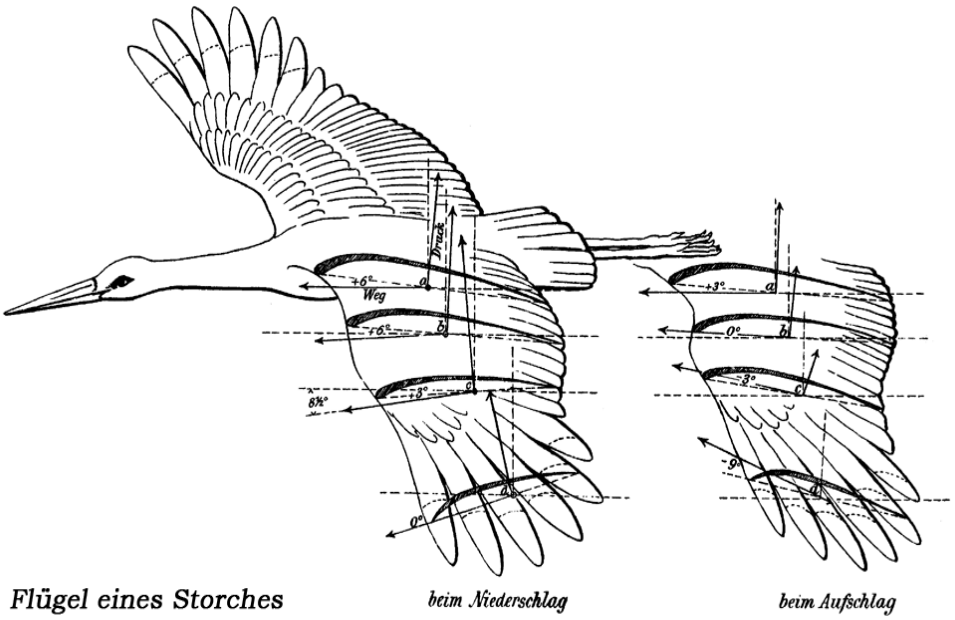


Figure 3.4: Illustration of the flight of a white stork by Otto Lilienthal (Lilienthal, 2001).

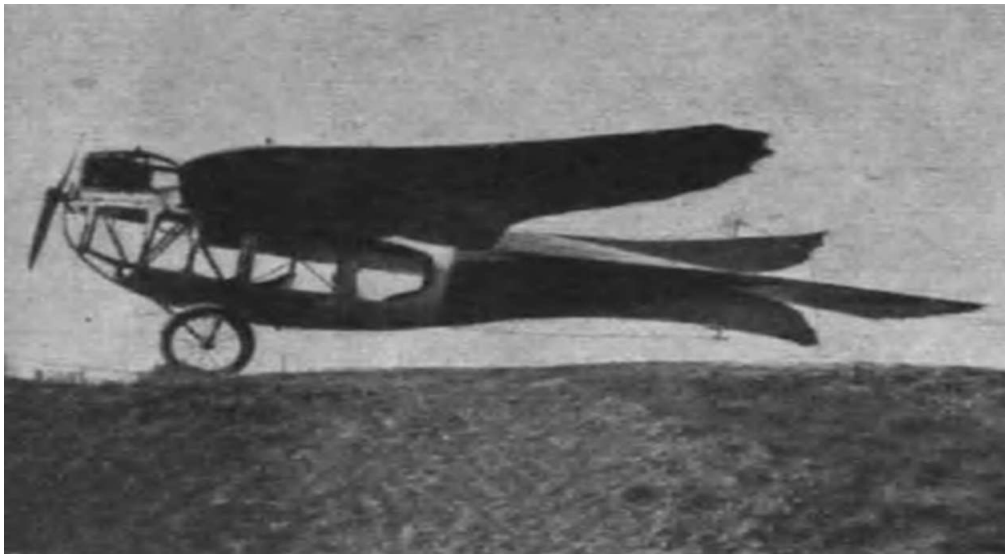

Figure 3.5: Etrich Luft-Limousine / VII four-seater passenger airplane of 1912 (Valasek, 2012)

While Liliental focused his attention on gliding and bird-like flapping wing tips, he was not the only one who recognized the importance of morphing to achieve controlled flight (Valasek, 2012). As said before, the 1903 Wright brothers' airplane did not resemble much of a bird, but featured lateral and directional control by warping. The concept of structural flexibility of airframes was explored by other aviation pioneers, but quickly fell in disuse from aviation. Increased flying speeds and vehicle weights meant that more rigid wings were needed, as they could withstand greater forces associated. (Weiss, 2003). Hinged control surfaces, such as ailerons and rudders, were added to to aircraft in order to control them, and by the time of the First World War, the standard for high performance aircraft was to use conventional hinged control instead of warping (Valasek, 2012). This was coupled with the growing use rigid metallic structures towards the 1930´s. Therefore, aircraft morphing was to be achieved using (now conventional) mechanisms such as hinges, pivots, and rails (Valasek, 2012). This meant that the paradigm changed from Continuous Morphing to Discrete Morphing (see Table 3.1), and morphing became less similar similar to birds behaviour. However, since the 1990's investigators directed again their focus to nature and biomimetics. For instance, a study by (Abdulrahim and Lind, 2006) presents feasible morphing solutions similar to those found on seagulls and pigeons and simulates their implementation in small UAVs. More attention will be given to the aspect of UAVs later in this text.

## 3.3 Evolution of Morphing Aircraft

### 3.3.1 Important marks during the XX century

The adoption of more rigid airframes and the paradigm of discrete changes did not discouraged aircraft developers from achieving adaptive designs. Throughout the XX century, and many times impelled by military needs, several concepts and designs were proposed and built. The following chronological list is not extensive, but aims to demonstrate marks on morphing aircraft, specially wing morphing.

**1920:** Parker Variable Camber Wing (Figure 3.6), a concept for bi- and tri-planes that consisted of a flexible wing portion between the front and rear spars, and adapted its shape according to the aerodynamic forces it was subjected (Jha and Kudva, 2004).

**1931:** Westland-Hill Pterodactyl IV (Figure 3.7). The Pterodactyl IV was one of a series of tailless designs by Geoffrey Hill and built by the English company Westland Aircraft (Barbarino et al., 2011). It relied on a wing whose sweep angle in order to allow longitudinal trim (Weisshaar, 2006).

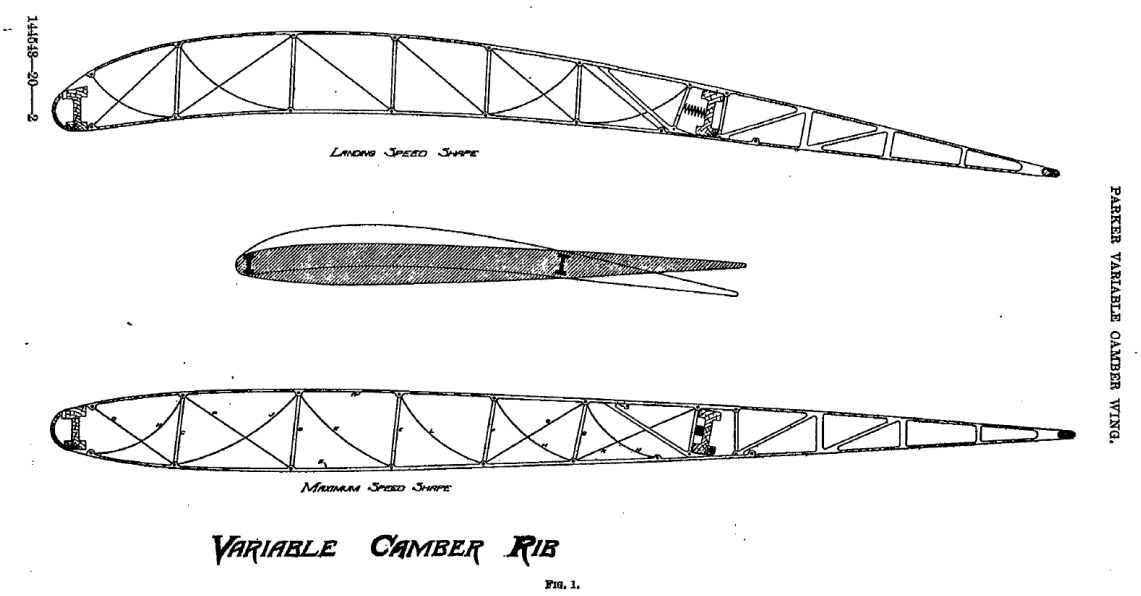


Figure 3.6: Parker Variable Camber Wing (Parker, 1920).

Figure 3.7: Pterodactyl IV in flight (Weisshaar, 2006).

**1931-47:** Ivan Makhonine MAK-10: airplane with pneumatically actuated telescopic wings, which enabled it to increase wing span by 162% (Figure 3.8). The design was followed by several iterations, culminating on the MAK-123 of 1947, successfully demonstrated extension and retraction of telescoping wings with no adverse effects (Jha and Kudva, 2004).

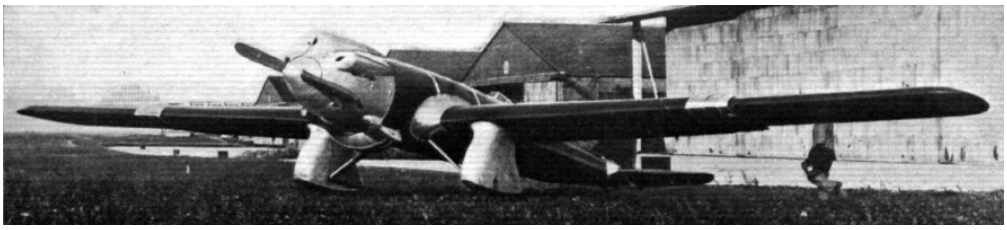

Figure 3.8: MAK-10 aircraft with wings completely extended (Wikipedia, 2014).

**1932-41:** Nikitin-Shevchenko IS series (from *Istrebitel Skladnoi* – folding fighter, Figure 3.9) was one of the first applications of variable dihedral wings, and was capable of out-of-plane morphing from a bi-plane to a monoplane to operate at high speed (Barbarino et al., 2011). The project resulted on IS-1 to IS-4 designs (although IS-3 design was not materialized) (Gordon et al., 2000).

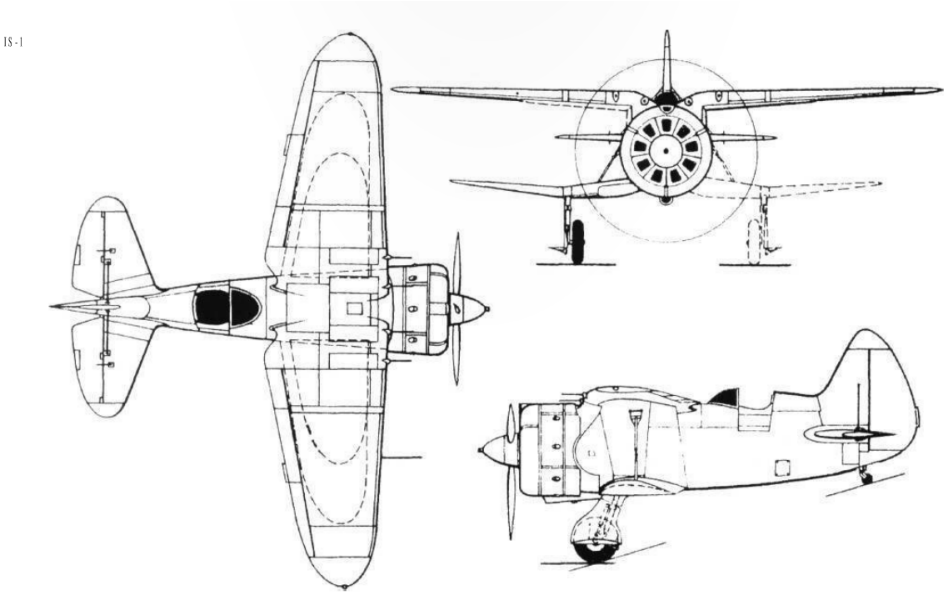


Figure 3.9: Nikitin-Shevchenko IS-1 (Gordon et al., 2000)

**1933:** Vincent Burnelli Variable Camber and Area Wing patent (Figure 3.10), which was fitted to the Burnelli GX-3 The main portion of the wing was fixed, while the leading and trailing edge moved outward and downward in order to change the area and the camber of the wing (Jha and Kudva, 2004).

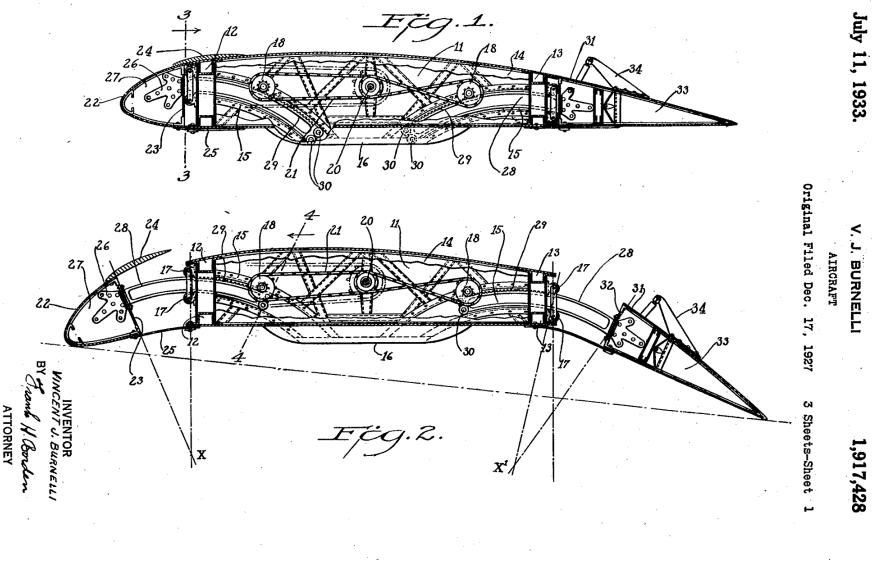


Figure 3.10: Burnelli patent for the mechanism fitted on GX-3 (Burnelli, 1933).

**1937-41:** NIAI RK and RK1, also know as LIG-7 and RK-800 respectively and shown on Figure 3.11 Designed in the USSR by Grigorii Baksayev, these were probably the first aircraft featuring wing chord extension capabilities (Weisshaar, 2006).

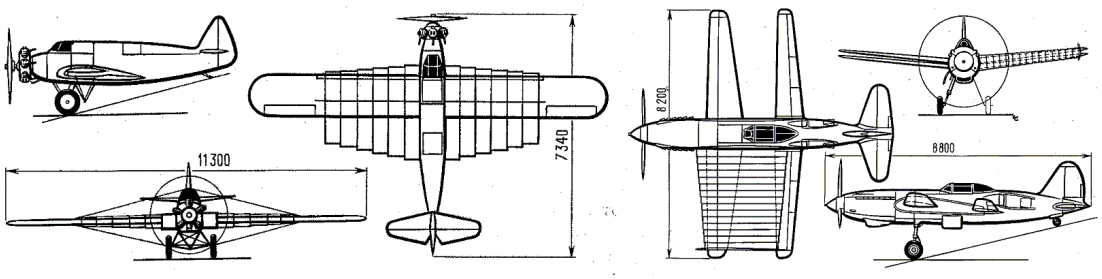


Figure 3.11: NIAI RK (left) and RK-1 (right) (adapted from Jha and Kudva, 2004; Weisshaar, 2006).

**1945-57:** Sir Barnes Wallis, a British aircraft designer, worked on several swing-wing, supersonic concepts. He presented the Wild Goose and the Swallow (Figure 3.12) designs, but these never passed from the sub-scale mock-ups. However, his ideas were influential on the development of later aircraft such as the F-111 (Valasek, 2012).

Figure 3.12: Sir Barnes Wallis with a model of the Swallow, wings at low sweep (Valasek, 2012).

**1949:** Republic XF-91 "Thunderceptor" (Figure 3.13) was prototype interceptor aircraft, equipped with variable incidence wings, changing the angle of attack during flight. A high angle-of-attack was used for take-off and landing and low angle-of-attack configuration was used for high-speed flight (Jha and Kudva, 2004).

Figure 3.13: Republic XF-91 "Thunderceptor". Notice the polished surface where the wing slides (United States Air Force, 2015).

**1951:** Bell X-5, a prototype (hence the X designation), was the first jet powered aircraft with variable geometry wings (Figure 3.14) to connect efficient low speed flight with efficient high speed flight (Weisshaar, 2006).

Figure 3.14: Bell X-5 showing variable sweep wing positions (Valasek, 2012).

**1953:** Short SB.4 Sherpa (Figure 3.15), an aircraft that had all-moving wing tips that offered greater control power than conventional ailerons (Jha and Kudva, 2004). It was a experimental aircraft, intended to test the "aero-isoclinic wing: a wing in which the incidence remains constant throughout the span under varying loads and deflections" (1954).


Figure 3.15: Shorts SB.4 Sherpa (Jha and Kudva, 2004).

**1955:** Vought F-8 Crusader, shown on Figure 3.16, was a production jet aircraft incorporating, amongst other technologies, variable incidence wings (Jha and Kudva, 2004).

Figure 3.16: Vought F-8 during flight (Wikipedia, 2009b).

**1964:** The prototype North American Aviation XB-70 Valkyrie used a form of three dimensional wing morphing (Figure 3.17) that hinged the outer wing panel upwards/downwards in order to control the lift-to-drag ratio (Barbarino et al., 2011; Weisshaar, 2006, 2013).

Figure 3.17: XB-70 various wing geometries (adapted from Weisshaar, 2006).

**1964:** The General Dynamics F-111 Aardvark, a supersonic multi-task military aircraft, was the first production aircraft with swing wing capability, shown on Figure 3.18 (Barbarino et al., 2011). This aircraft was later used as a test bed for other morphing concepts, as will be discussed on section 3.3.2.

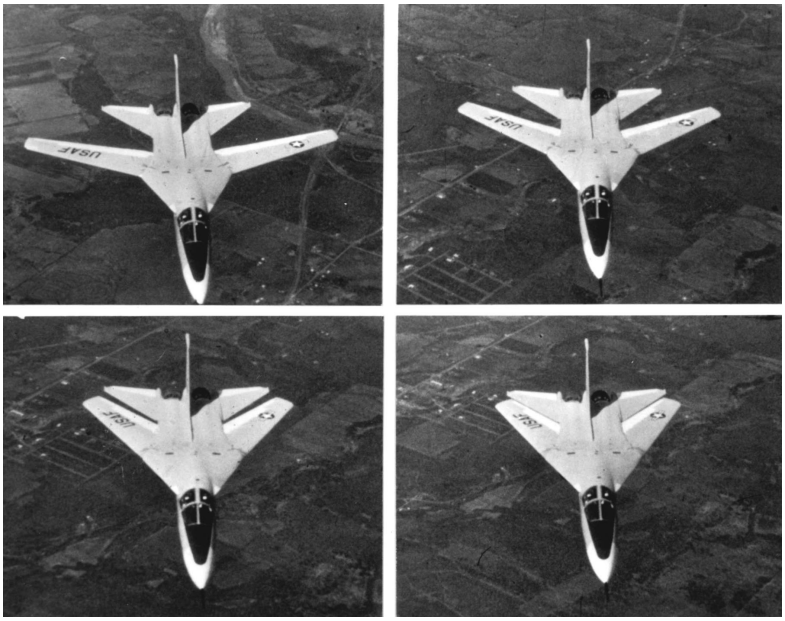

Figure 3.18: Four-photo series showing the F-111A wing sweep sequence (Wikipedia, 2009a).

**1966-69:** Russian military aircraft start to employ variable sweep wings. The first example was the Sukhoi Su-17, followed by the Mikoyan-Gurevich MiG-23 (Figure 3.19) and MiG-27, the the Su-24 and the Tupolev Tu-22M (Barbarino et al., 2011).

Figure 3.19: Mechanism used to change the sweep angle on the MiG-23 (Wikipedia, 2006).

**1970:** The South-African experimental J-5 sailplane by Fritz Johl was able to change wing area, chord and camber in order to improve its soaring performance. It achieved a chord change of 100% using an internal "lazy-tongs" mechanism, shown on Figure 3.20 (Jha and Kudva, 2004).

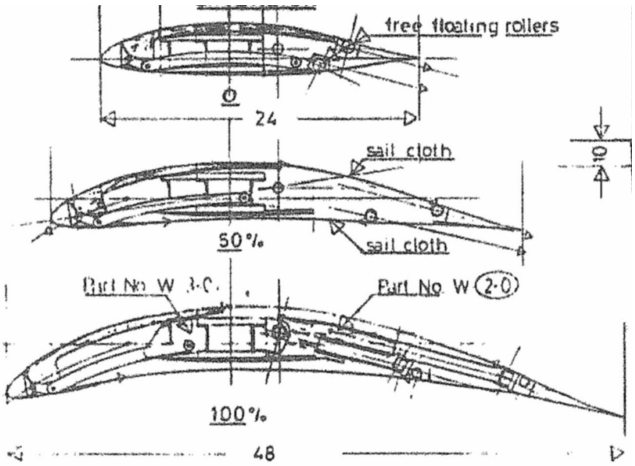


Figure 3.20: J-5 Mechanism (Jha and Kudva, 2004).

**1972:** The telescopic wing (Figure 3.21) of the German FS-29 sailplane was another example of morphing technology used in order to improve soaring performance. (Weisshaar, 2006, 2013).

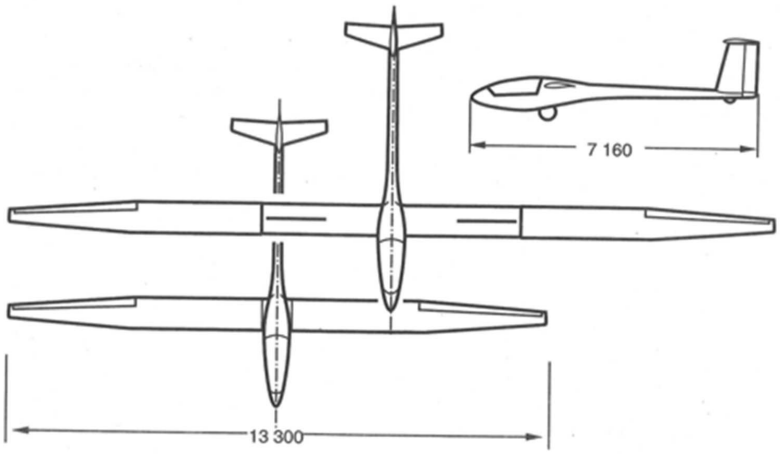


Figure 3.21: FS-29 sailplane (Weisshaar, 2006).

**1974:** The Panavia Tornado (Figure 3.22) was the first European variable sweep combat aircraft to reach the production phase (Weisshaar, 2013).

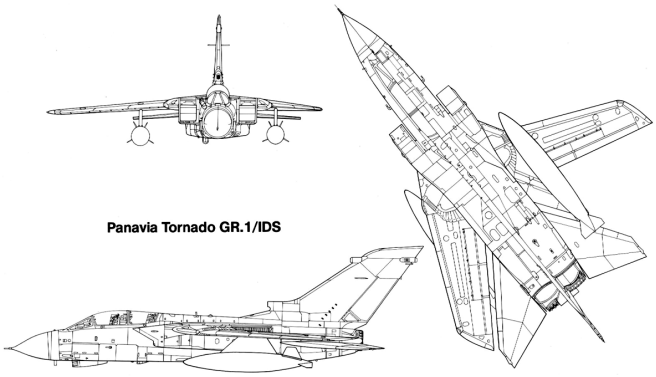


Figure 3.22: Panavia Tornado different views (Blueprints, 2016).

**1974:** General Dynamics F-16 Fighting Falcon uses leading edge flaps to change the camber of its wings (Barbarino et al., 2011; Jha and Kudva, 2004).

**1979:** The Ames-Dryden 1 (AD-1) was a test aircraft for a unique wing morphing concept, the oblique wing, which was designed to rotate on centre pivot, so that one tip is swept forward while the opposite tip is swept aft (Figure 3.23). This is a variation on the classic swing-wing design, intended to simplify construction and retain the centre of gravity as the sweep angle is changed (Jha and Kudva, 2004).

Figure 3.23: AD-1 with its oblique wing in action (Wikipedia, 2016e).

**1985:** NASA/USAF Advanced Fighter Technology Integrator (AFTI) was a F-111 with Mission Adaptive Wings (MAW), a device built by Boeing and capable of controlling the wing curvature by means of an automated control system (Barbarino et al., 2011). This flight research program was highly successful and served as a vital stepping stone toward the realization of a fully morphing aircraft (Valasek, 2012). Therefore, it will be further discussed on the next section.

### 3.3.2 The Advanced Fighter Technology Integrator F-111

Nowadays almost of the research on morphing wings concerns UAVs. The AFTI F-111 is a case of manned aircraft with adaptive wings, of most interest for this text as it changed the camber if its wings.

In the early 1980s the wings on a F-111A aircraft were replaced with Mission Adaptive Wings, which were able to adapt themselves "by means of configuration and/or shape variation, to changes of flight conditions during the mission, so as to maximize some performance indices" (Ricci et al., 2006). These were built by Boeing in a joint NASA and US Air Force project: Advanced Fighter Technology Integration. Figure 3.24 shows a modified General Dynamics AFTI/F-111A Aardvark with MAWs installed, flying over the El Paso Mountains. The four dark bands on the right wing are the locations of pressure orifices used to measure surface pressures and shock locations on the MAW.


Figure 3.24: Modified General Dynamics AFTI/F-111A Aardvark with super-critical mission adaptive wings (MAW) installed (NASA, 2009).

The project is described in numerous publications. (Cesnik et al., 2004) discuss a framework and process for assessing vehicle morphing capability in the context of objective missions, performance needed, and the state changes and potential technology advancements required to enable that vehicle performance. (Bonnema and Smith, 1988)

contrast, in Figure 3.25, the traditional and novel approaches to changing lift, and present in Figure 3.26 the resulting schematic drag polar curves and resulting minimum drag envelope.

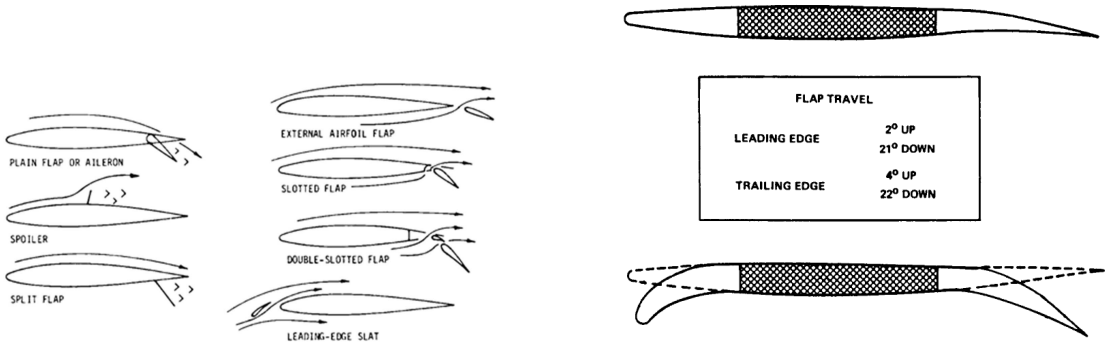


(a) Lift altering surfaces (b) Variable camber concept

Figure 3.25: The comparison made by (Bonnema and Smith, 1988).

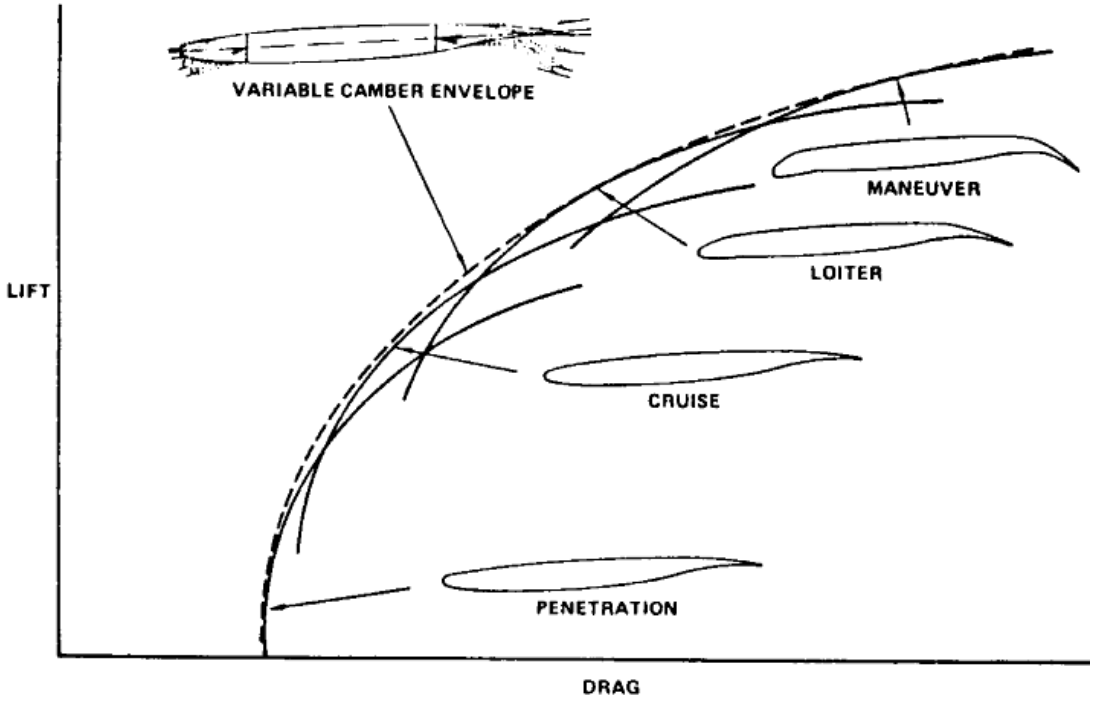


Figure 3.26: Minimum drag envelope (Bonnema and Smith, 1988).

(Gilbert, 1981) is a most informative article, with details of the morphing mechanisms involved (Figure 3.27).

(a) Leading edge

(b) Trailing edge

Figure 3.27: The AFTI leading and trailing edge mechanisms (Gilbert, 1981).

Figure 3.28 gives a schematic representation of the full envelope performance, indicating the variety of combinations of LE and TE configurations possible to optimize this multi-objective design.

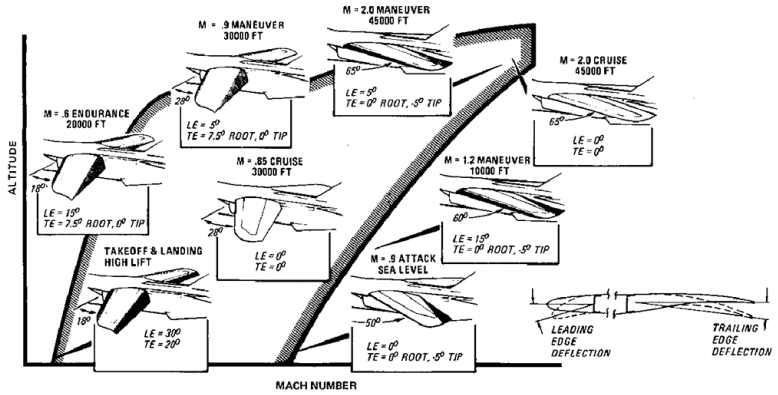


Figure 3.28: Full envelope performance (Bonnema and Smith, 1988).

(AFWAL-TR-88-3082, 1988) gives more details, such as the leading edge, see Figure 3.29. The skin material seems to be a epoxy/fibreglass composite, and "closure panel" should be noticed.

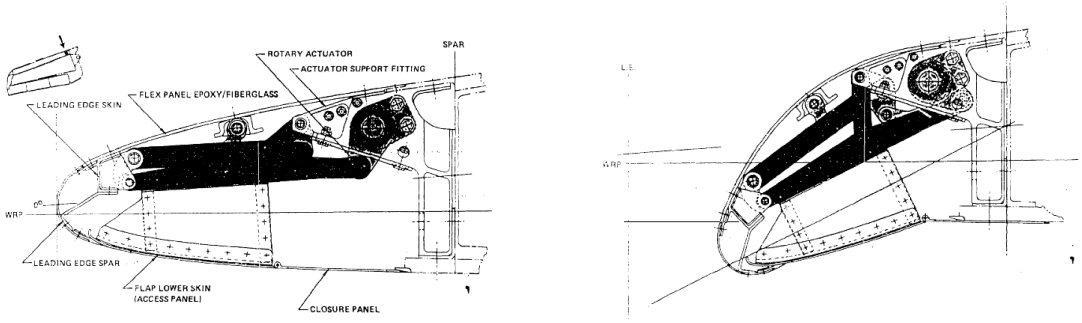


(a) LE undeflected (b) LE fully deflected

Figure 3.29: Inboard LE deflection (AFWAL-TR-88-3082, 1988).

### 3.3.3 Patents

As it was conveyed on section 2.3, patents are a valuable source to understand the evolution of concepts on the field of Engineering. Therefore, research of patents concerning morphing wings (mainly leading and trailing edge) was performed. Table 3.2 summarizes the results retrieved.

Table 3.2: Patents concerning morphing concepts

| | | |
|---|---|---|
| US 3 711 039 | 1973 | Pneumatic leading edge flap for an aircraft wing |
| DE 29 07 912 A1 | 1980 | Quertriebskörper mit veränderbarer Profilierung, insbesondere Flugzeugtragflugel |
| US 4 200 253 | 1980 | Aircraft wing drooping leading edge device |
| US 4 247 066 | 1981 | Airfoil variable cambering device and method |
| US 4 553 722 | 1985 | Variable camber airfoil |
| US 4 986 493 | 1991 | Convertible fixed wing aircraft |
| US 6 213 433 B1 | 2001 | Leading edge for an aircraft |
| EP 0 103 038 A1 | 2002 | Continuous skin, variable camber airfoil edge actuating mechanism |
| US 8 534 611 B1 | 2013 | Movable leading edge device for a wing |
| EP 2 915 741 A1 | 2014 | Morphing airfoil leading edge |
| US 8 925 870 B1 | 2015 | Morphing wing leading edge |
| US 9 233 749 B1 | 2016 | Variable camber adaptive compliant wing system |
| US 2016 / 0 009 372 A1 | 2016 | Morphing airfoil leading edge |

Concerning morphing, patents seeking to emulate a droop nose airfoil are numerous. Boeing patent US 3 711 039, of 1973, presents an extendable inflatable nose, visible on Figure 3.30. A German patent by Dornier, frequently mentioned in current DLR technical literature, is DE 29 07 912 A1, 1980, concerning a droop nose (Figure 3.31). The concept behind this patent is again found in a British Aerospace patent, US 4 200 253, 1980, see Figure 3.32.

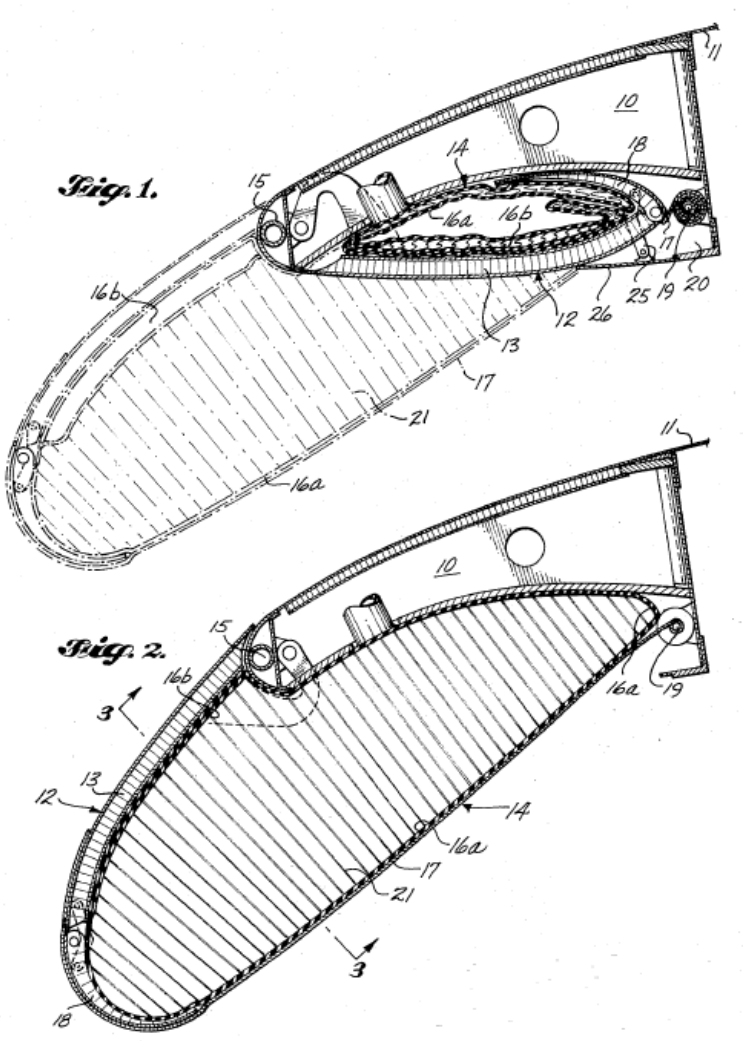


Figure 3.30: Pneumatic leading edge flap for an aircraft wing, US 3 711 039, 1973.

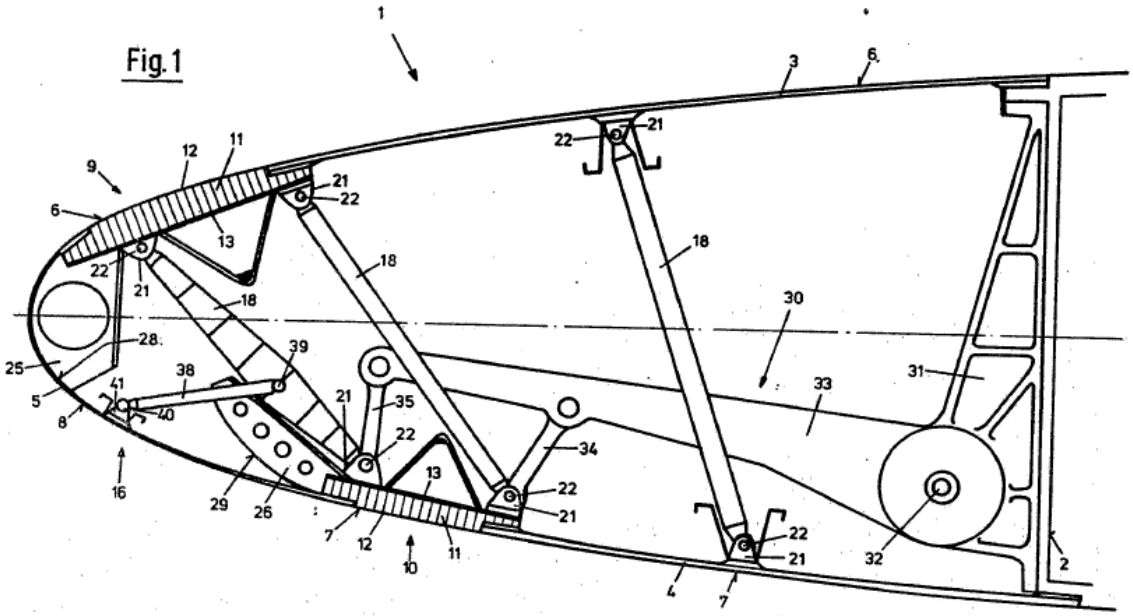


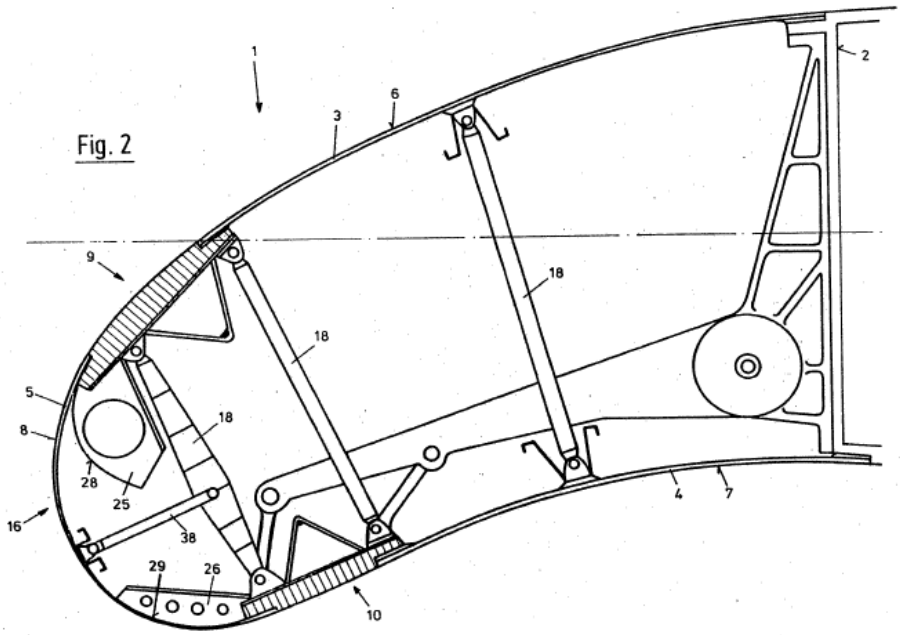


Figure 3.31: German patent DE 29 07 912 A1, 1980.

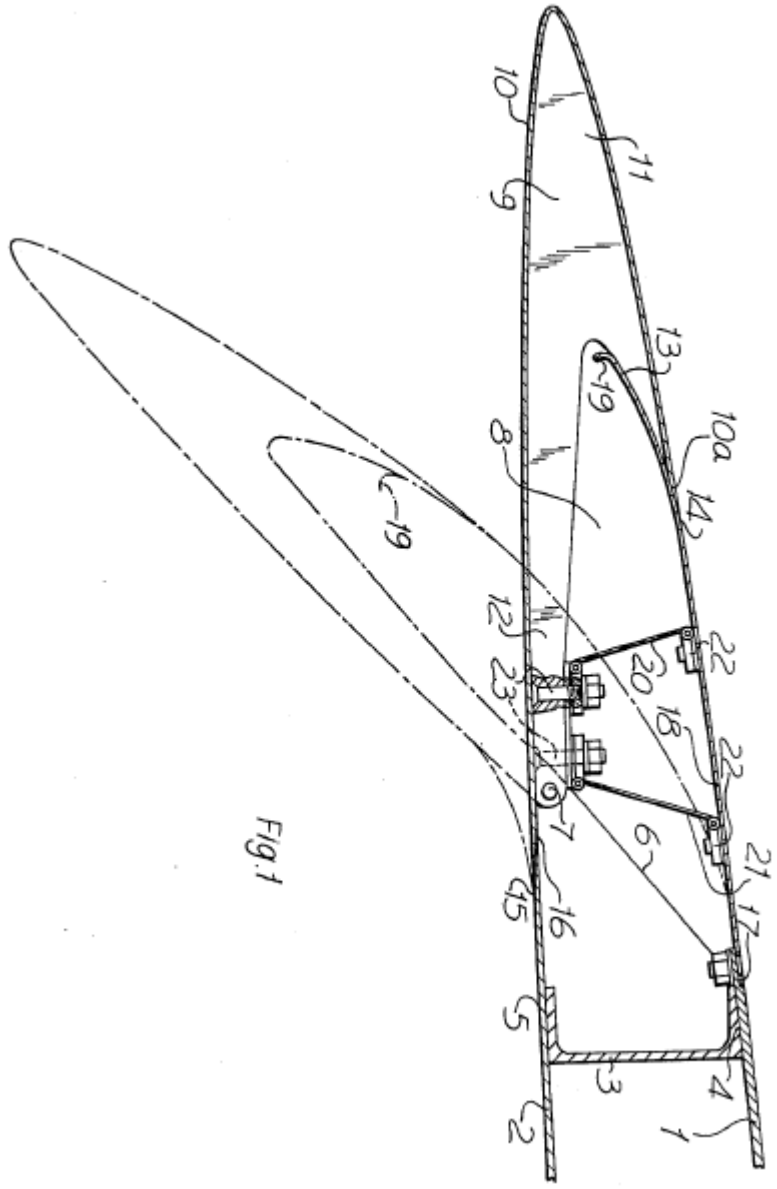


Figure 3.32: British Aerospace patent, US 4 200 253, 1980.

The patents mentioned above concern leading edge. Naturally, trailing edge is also object of patents. See, for instance, US 4 247 066, 1981, by General Dynamics Corp.,

Figure 3.33. Another patent frequently mentioned in DLR reports is Boeing patent US 4 553 722, 1985 (Figure 3.34).

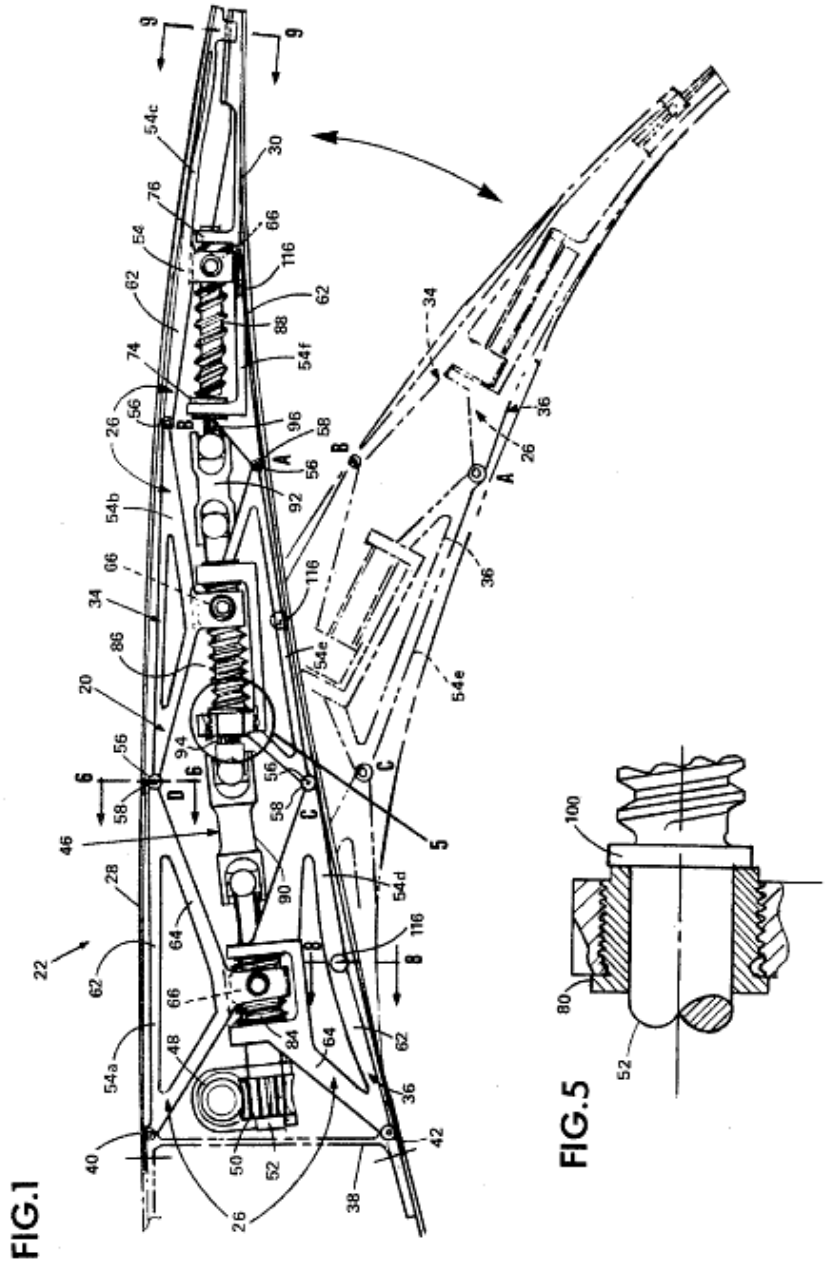


Figure 3.33: Morphing trailing edge, US 4 247 066, 1981, by General Dynamics Corp.

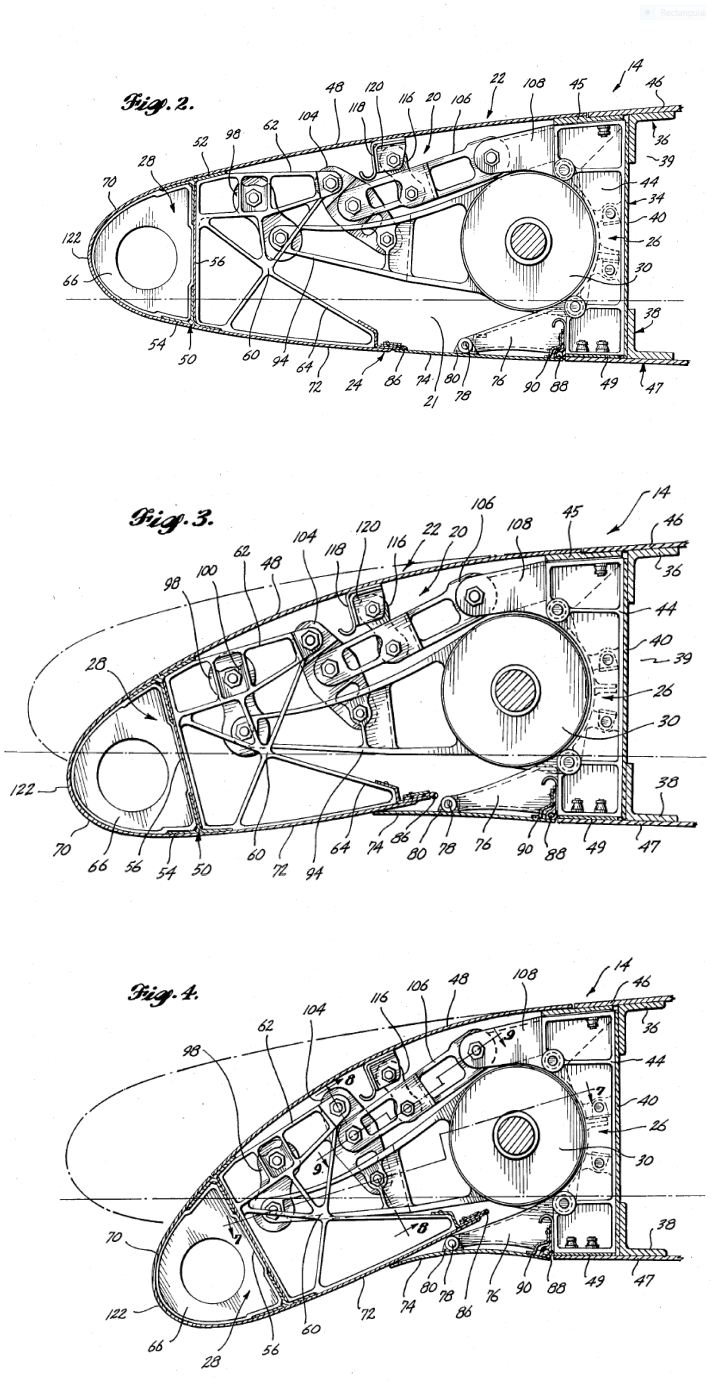


Figure 3.34: Boeing patent US 4 553 722, 1985

According to (Falcão et al., 2011), "morphing thus serves two main purposes: to maximize efficiency at all stages of the flight; and/or to allow a single aircraft to perform dissimilar missions that would otherwise require different specialized aircraft". A radical case of morphing, in the sense of " perform dissimilar missions". is US patent 4986493 of 1991 (Figures 3.35 (a) to (e)).

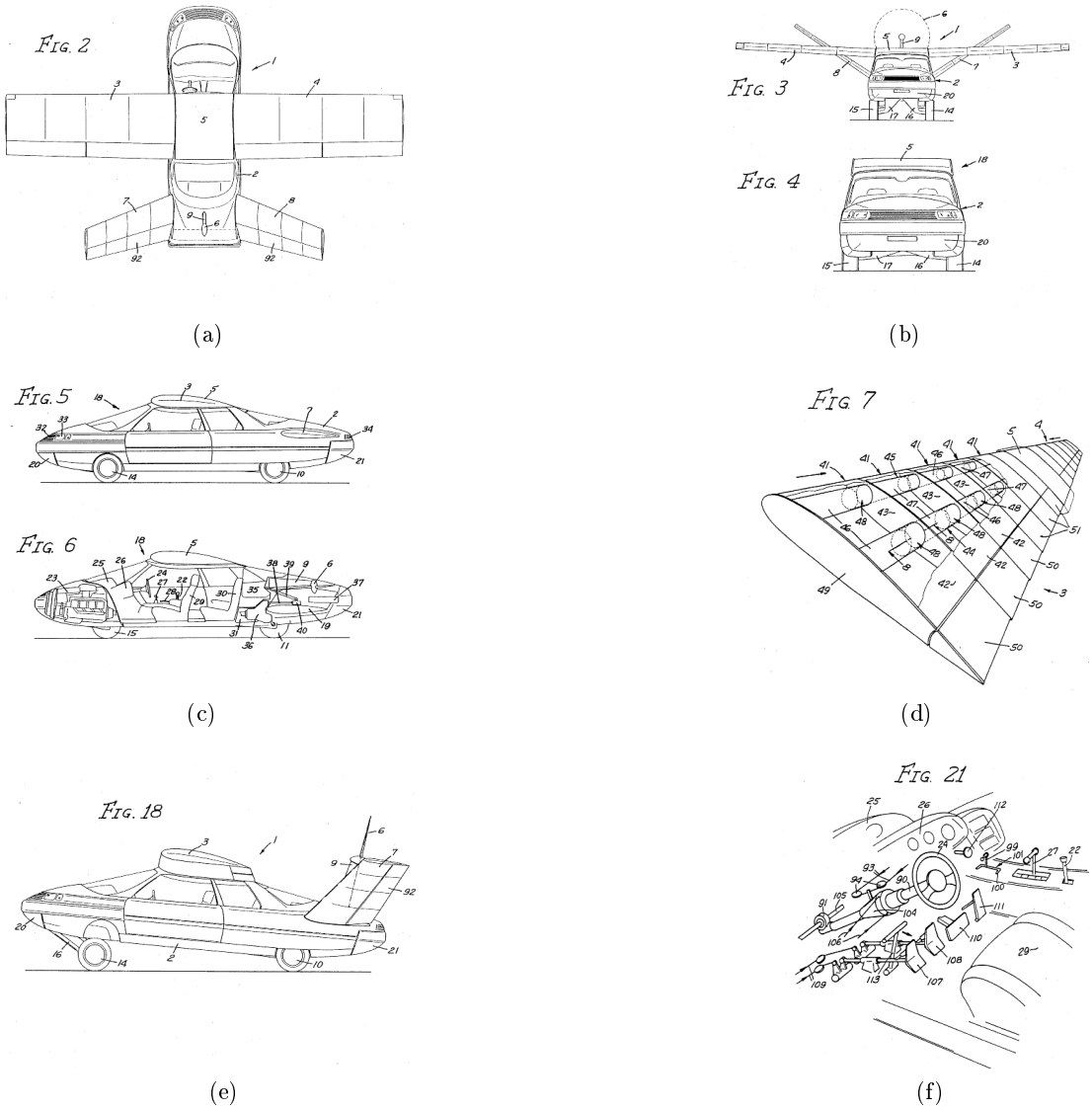


(a) (b) (c) (d) (e) (f)

Figure 3.35: US patent 4986493 of 1991: "Convertible fixed wing aircraft".

Another patent worth commenting is Boeing patent US 8 534 611 B1, 2013, consisting of a "movable leading edge device for a wing". Figure 3.36 is self-explanatory, the novelty consisting of some flexible connection between the leading edge and the continuation of the airfoil, that once deployed gives an adequate smooth geometry. Clearly, in this case there is a non constant perimeter of the leading edge.

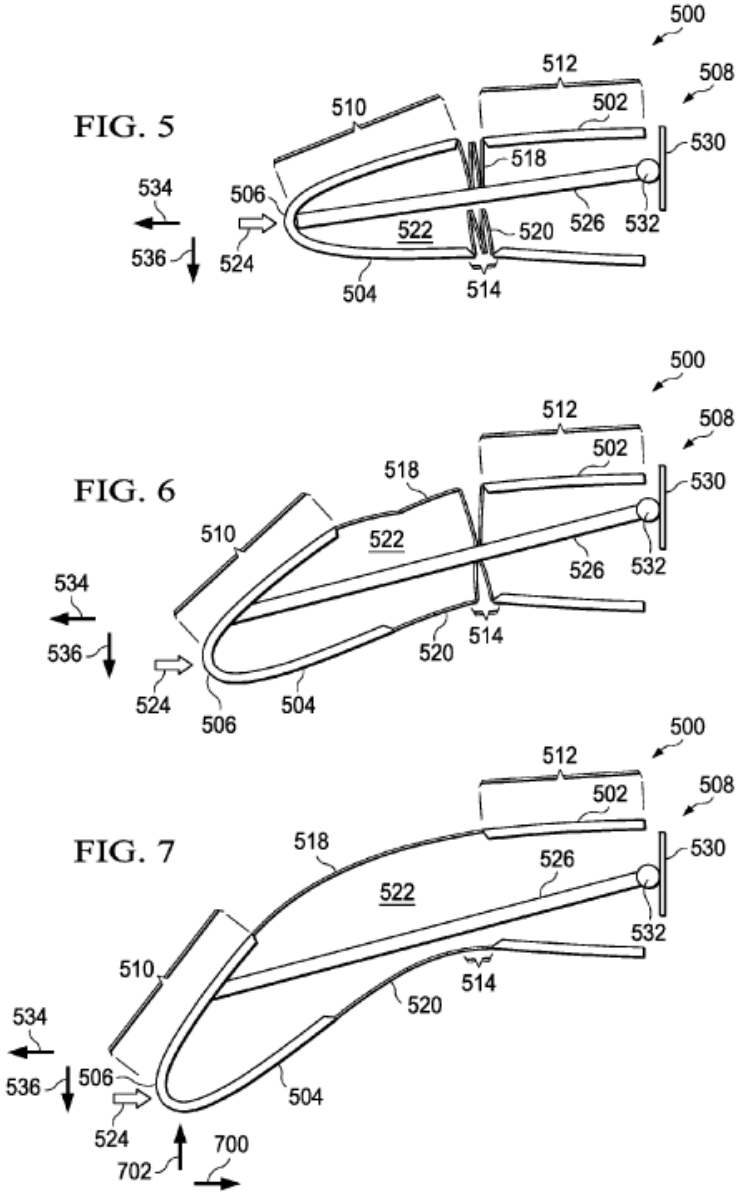


Figure 3.36: Patent US 8 534 611 B1, 2013

## 3.4 Current Status of Morphing Aircraft Research

The present work concentrates on the morphing leading edge of an UAV wing. Therefore, from now on, the biggest focus will be on morphing wing edge surfaces and its research on UAVs. However, where needed or of interest, manned aircraft will be mentioned.

(Gomez and Garcia, 2011) give a review of morphing unmanned aerial vehicles (UAVs). These authors state that UAVs are ideal platforms for experimenting with novel concepts and testing new structural solutions, because of the lower certification and safety constraints as compared with other sectors of aviation. Furthermore, the small scale of many UAVs implies that experimentation at this scale is affordable even by low budget university groups that in many parts of the world embrace this type of research. An example in Portugal is Universidade da Beira Interior (UBI), which managed to gain international visibility in this field of research. With a variety of morphing alternatives currently being tested, it is reasonable to affirm that a solution will probably emerge in due course.

Complementing the more traditional aircraft materials as aluminium alloys, the current explosion of interest in morphing aircraft is also fuelled by the increasing diversity and availability of prospective materials, such as shape memory alloys (SMAs), shape memory polymers (SMPs), electroactive polymers (EAPs), composites or rubbers, amongst others. Frequently, these novel materials have properties tailored, along the volume, to the part's application. Functionally graded materials (FGMs) are a good example of this.

A morphing wing study may include, among others, the following aspects:

- Cross section ("airfoil") - constant (rectangular planform) or varying from fuselage to wing tip;
- 2D or 3D modelling;
- Leading edge morphing *versus* high-lift devices (slats, Krueger flaps);
- Trailing edge morphing *versus* change by flaps;
- Morphing concerning airfoil cross section and/or wing extension (span);
- Aerodynamic pressure over wing:
  - Modelled with CFD software, XFOIL or other tools;
  - Interaction with wing geometry, and iterative refinement of modelling;
- Wing torsion and bending:
  - complete modelling: aerodynamic loading and skin, reinforcement structure and mechanism;
  - or separate modelling of those components;
- Morphing:

- kinematics and power needed to actuate the system;
- optimization of morphed skin geometry:
  - including local variation of skin thickness, so as to change local radii;
  - including stress analysis to evaluate stress for complex geometry and varying skin thickness;

### 3.4.1 Main trends on current research

As seen in previous sections, the traditional approach (compromise between requirements) involves the use of control surfaces (or auxiliary control surfaces) like flaps or slats, promoting adaptability to various circumstances. Aerodynamic lift and drag are affected by traditional control surfaces, but may certainly be affected by morphing solutions, particularly those changing camber as briefly discussed before.

(Kintscher et al., 2011) presents a comparison of weight for several high lift solutions (Figure 3.37) in the context of a study of a morphing leading edge structure. Figure 3.37 conveys the message that the droop nose solution is the one with lower weight, and therefore the one leading to lower energy consumption. Figure 3.38, from the same paper, provides some relevant nomenclature for the present work, which concerns a droop nose morphing device and its damage analysis.

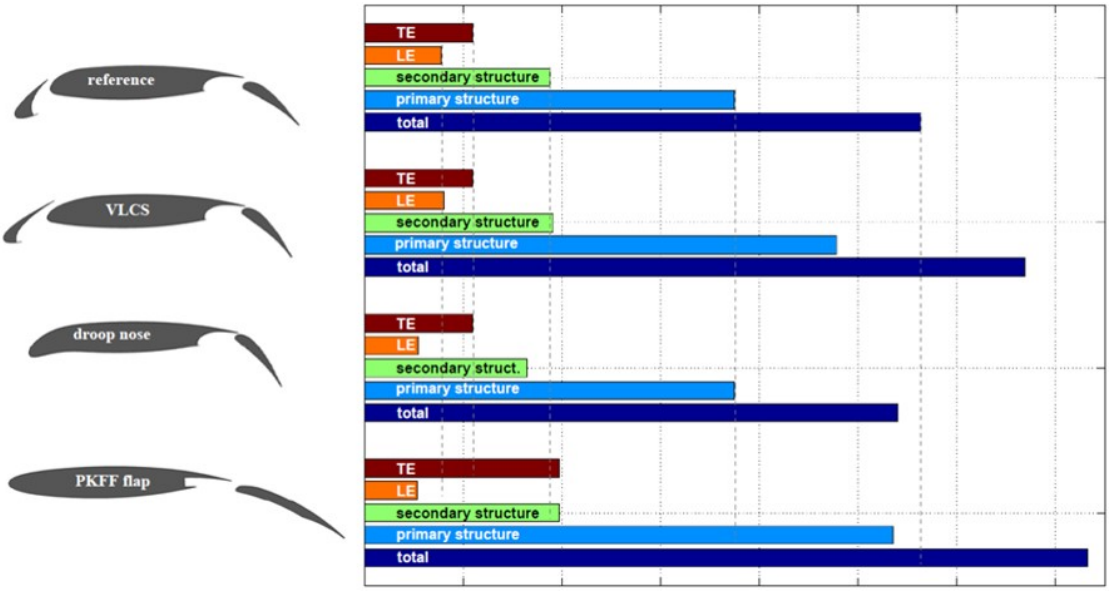


Figure 3.37: Weight comparison of several high lift solutions, (TE – trailing edge; LE – leading edge). (Kintscher et al., 2011).

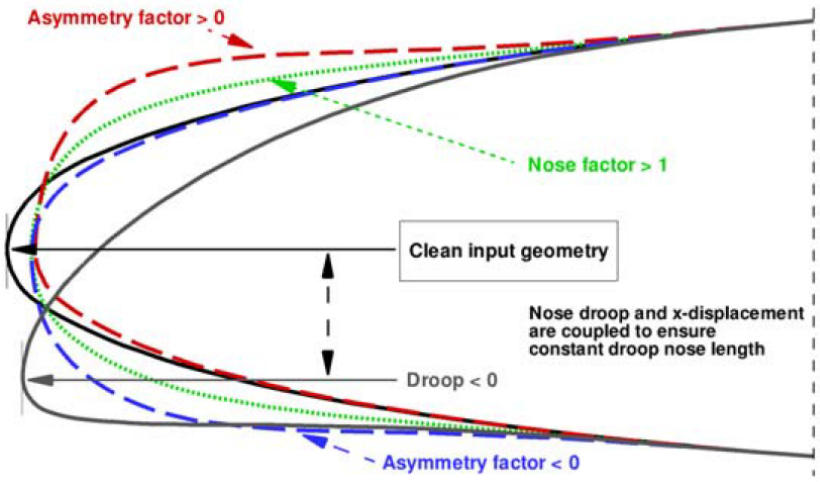


Figure 3.38: Smart droop nose device, (Kintscher et al., 2011).

(Bolonkin and Gilyard, 1999) give a schematic representation of a drag polar diagram, Figure 3.39, illustrating the benefits of variable-geometry wing camber control for transport aircraft.

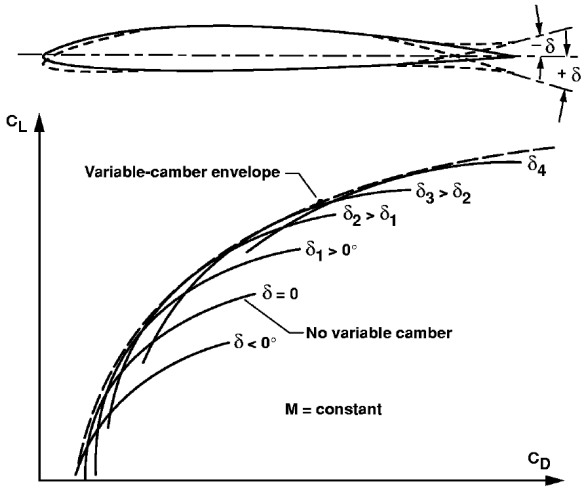


Figure 3.39: Variation of drag polar as a function of trailing edge deflection (schematic). Constant Mach number. (Bolonkin and Gilyard, 1999).

SMAs are potential materials for morphing applications. (Strelec et al., 2003) discusses the design of a SMA actuated re-configurable airfoil, whereas (Elzey et al., 2003)

discuss bio-inspired actuators for shape morphing, pointing out that structures such as lightweight beams and panels (Figure 3.40) should be capable of generating sufficiently high forces and moments to actuate and maintain shape in the presence of external forces: "Cellular metals concepts, such as honeycomb, tetrahedral truss and corrugated layer architectures, are ideally suited for the core structures of stiff, strong yet lightweight sandwich beams and panels, with relative densities as low as 2-3%. Replacing the conventional metallic or polymeric face sheets of cellular metal sandwich structures with smart material actuators, e.g. SMAs, offers the potential for high performance shape morphing structures for aerospace and other demanding applications".

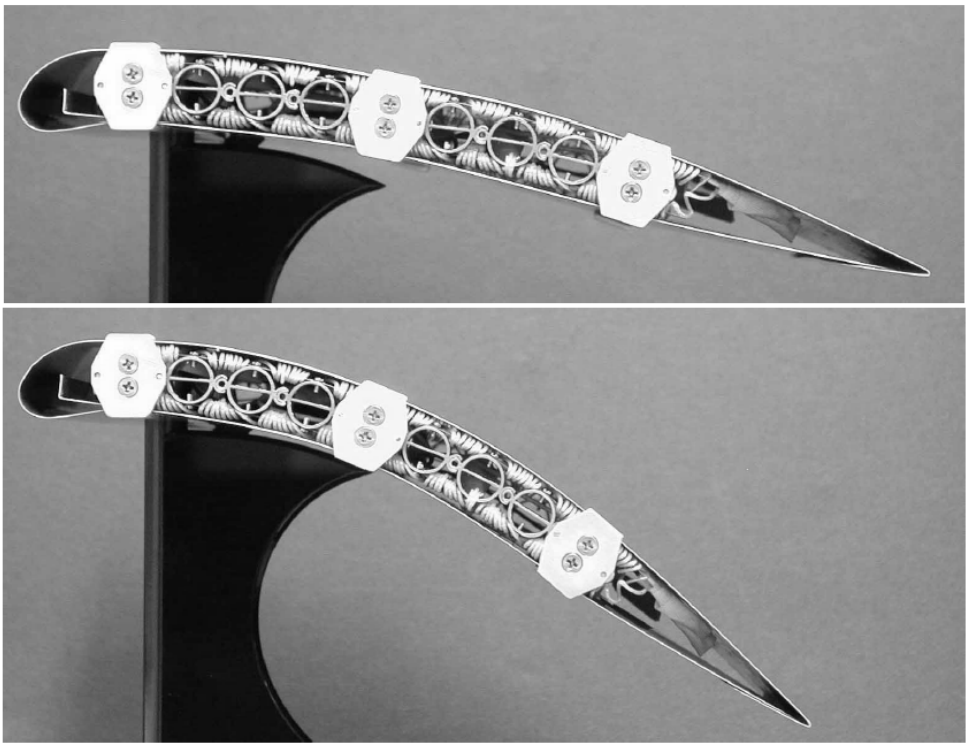

Figure 3.40: Shape morphing aero control surface (Elzey et al., 2003).

Corrugation is a simple mean of forming lightweight anisotropic structures stable under buckling load and with energy absorption capability (Dayyani et al., 2014, 2015). Morphing structures, seeking to exploit the anisotropy of a corrugated panel to allow a structure's shape to change, is shown by these authors in Figure 3.41.

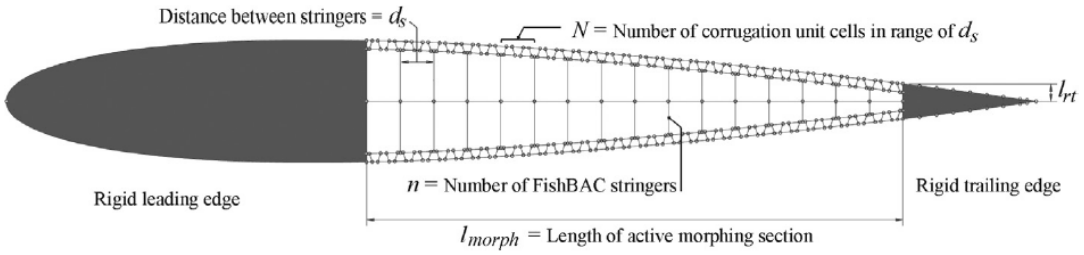


Figure 3.41: Corrugated skin (Dayyani et al., 2014, 2015).

Mechanisms can also be used for morphing purposes: (Perera et al., 2010; Perera and Guo, 2009) present a wing morphing solution based upon the use of an eccentric curved beam, which converts an actuated rotation motion into a vertical displacement along the beam. The output end of the curved tube is in contact with the upper and lower skins of the trailing edge which can be deflected up or down depending on the direction of the input rotation, Figure 3.42.

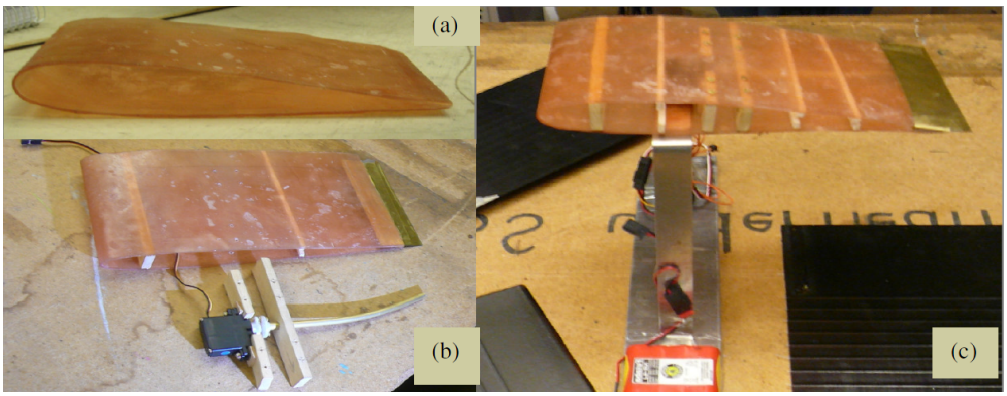


Figure 3.42: Eccentric curved beam (tube) as actuator; a) skin; b) curved tube; c) assembled model (Perera and Guo, 2009).

The curved tube actuator is also found in work presented by (Bartley-Cho et al., 2004), in an application for an uninhabited combat air vehicle (UCAV), Figure 3.43.

(Vos et al., 2010) present a structural solution based upon an open airfoil section at the tip of the trailing edge, allowing for wing twisting through warping displacement between the lower and upper wing skins at the trailing edge. The principle is schematically depicted in Figure 3.44.

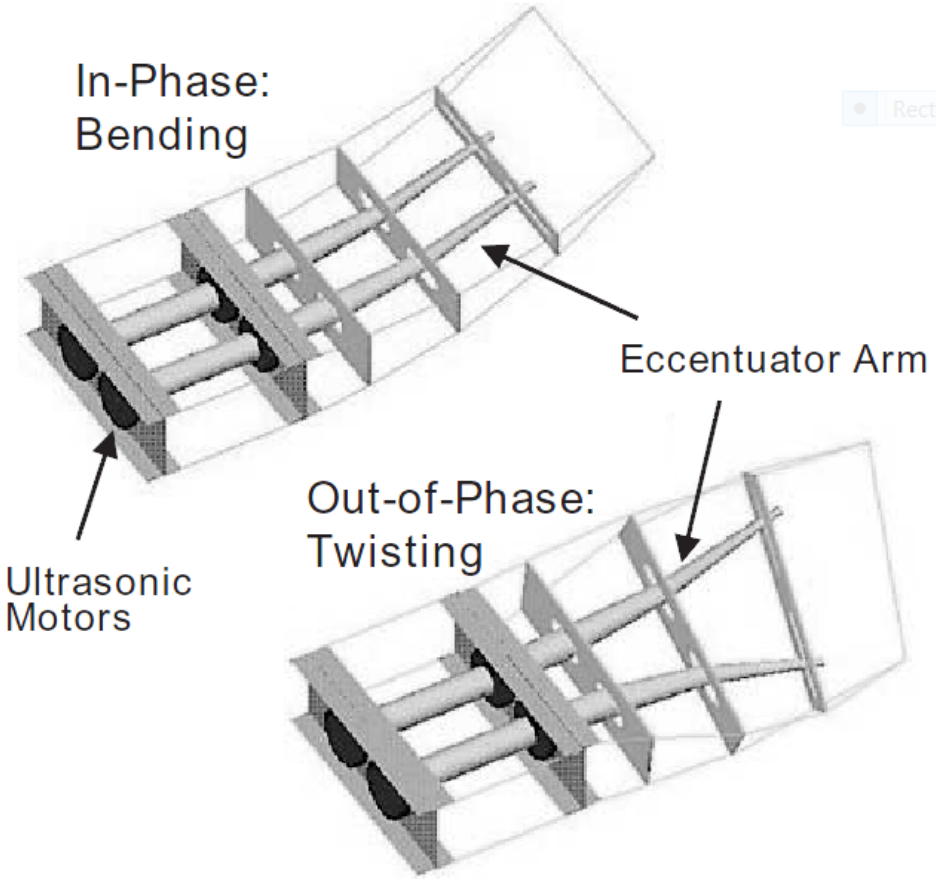


Figure 3.43: Actuation using curved tube (Bartley-Cho et al., 2004).

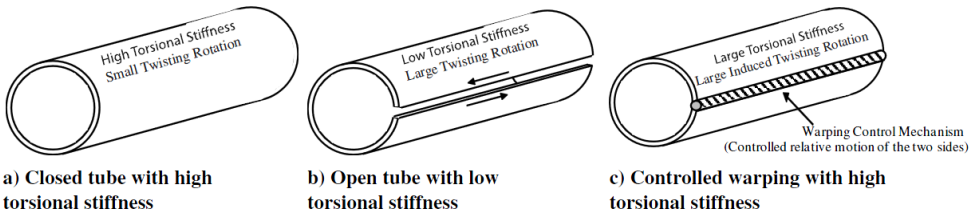


Figure 3.44: Basic principle of the warping mechanism (Vos et al., 2010).

Not all research on morphing wing involves exotic materials. Common Aluminium alloy 2024 is employed by (Ricci et al., 2006), presenting the Active Adaptive Wing

Camber (AAWC) concept, related to the concept of Mission Adaptive Wing (MAW). The device, presented by (Ricci et al., 2006) and shown on Figure 3.45, is based on a modification of the original idea proposed by Hans Peter Monner from DLR, Germany.

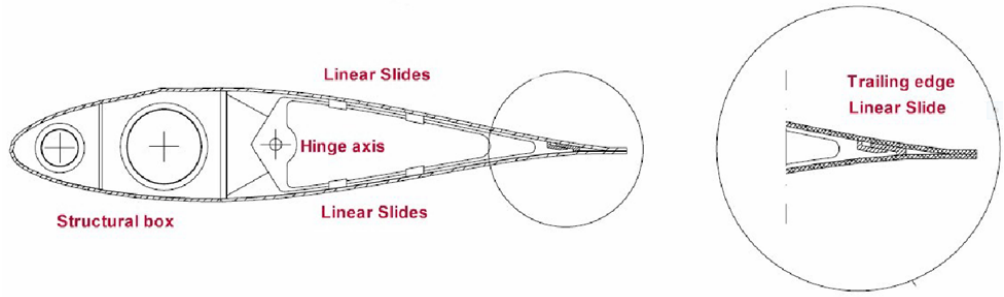


Figure 3.45: The rotating rib concept (Ricci et al., 2006).

### 3.4.2 Fatigue

Since this work concerns a damage analysis of a droop nose morphing solution, a specific reference to fatigue is now made. Searching the sites of scientific literature publishers (such as SAGE, publisher of the Journal of Intelligent Material Systems and Structures, relevant for this area) , the terms “morphing” AND “fatigue” returns relevant literature.

(Dayyani et al., 2014) recognizes that there may exist a fatigue problem, but candidly adds that "other constraints may be added, based on manufacturing requirements or structural integrity and fatigue, although these are rarely considered in current morphing aircraft design".

(Wereley and Gandhi, 2010), in the editorial of a special issue of the Journal of Intelligent Material Systems and Structures dedicated to "Flexible Skins for Morphing Aircraft", state that "such material considerations as toughness, resistance to erosion (e.g., to sand, dust, and ice), chemicals, fatigue, and weather, high strain rate capability, and ability to easily recover from high strain rates must be thoroughly evaluated for any practical flexible skin application".

It is observed that most papers only mention fatigue cursorily, stating, as in an afterthought, that “by the way, this deserves a fatigue analysis”. Examples of this situation are found in (Barbarino et al., 2011), (Mcknight et al., 2010), (Bubert et al., 2010) and (Vocke et al., 2011). Other authors observe that composites present a good fatigue performance: (Mattioni et al., 2006),(Wildschek et al., 2010). (Barbarino et al., 2011) states that “SMA fatigue behaviour shall be verified by appropriate experimental campaigns”, and (Sun et al., 2016) remarks, ominously, that “SMA, SMP, and EAP have poor anti-fatigue ability”.

### 3.4.3 Aerodynamic Loads

The structural analysis of a morphing wing may or may not consider the influence of the aerodynamic forces upon the stress state. If these aerodynamic forces are low, it may seem reasonable to simplify the problem not considering that interaction, otherwise a coupled complex problem must be solved, where aerodynamic forces modify the airfoil geometry, thus changing its aerodynamic performance, leading to an iterative solution, (Strelec et al., 2003). Several softwares for computational fluid dynamics (CFD) are available (e.g.. FLUENT[c]). For airfoil analysis, a free of charge software originated at the MIT, developed by Mark Drela is available: XFOIL (Drela, 1989). This software has been used recently at UBI (Universidade da Beira Interior) in papers such as (Morgado et al., 2016, 2015)). Several publications report the use of XFOIL: van der Horst et al. (2016); Sruthi et al. (2015); Gabor et al. (2015); Grigorie et al. (2012); Lafountain et al. (2012); Previtali and Ermanni (2012); Lafountain et al. (2009); Strelec et al. (2003).

(Raither et al., 2014) studies a variable skin stiffness concept, Figure 3.46, and states that "The performed analyses have also shown that the aeroelastic coupling of the considered airfoil is weak as the aerodynamic loads have only a small influence on the deformation. (...) Accordingly, a direct aeroelastic coupling in the numerical model has been dispensed with".

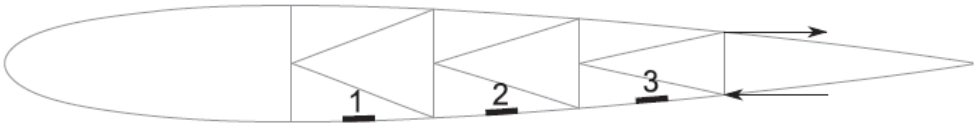


(a) Concept of variable camber morphing airfoil

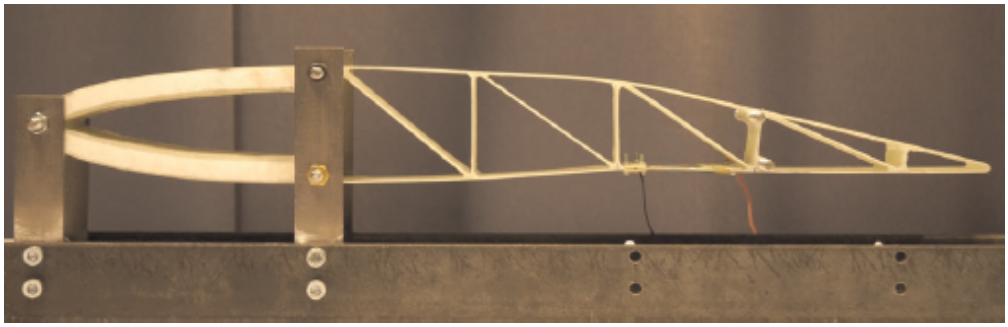

(b) Experimental airfoil in the cambered state

Figure 3.46: Work by (Raither et al., 2014).

[c] http://www.ansys.com/Products/Fluids/ANSYS-Fluent

Nevertheless, work reported in (Ricci et al., 2006) show substantial differences in actuation torques, considering or not aerodynamic loads.

(Dayyani et al., 2014) studies a corrugated skin for a camber morphing airfoil, Figure 3.47, and in the context of the finite element method (FEM) analysis observes that "The predicted aerodynamic pressure loads would allow the out-of-plane deformations of the skin to be estimated, and these deformations would be constrained so that their effect on the aerodynamics, particularly drag, is negligible. This step is not trivial and may require analysis of the fluid–structure interaction, particularly if unsteady effects are considered".

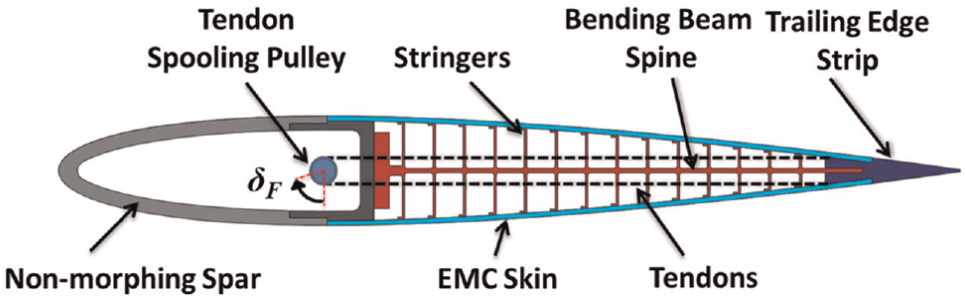


Figure 3.47: Morphing airfoil concept. (Dayyani et al., 2014).

### 3.4.4 Aluminium alloys for the skin

Materials used in morphing structures include shape memory alloys, composites, rubbers, etc., but traditional Aluminium alloys as 2024 as well (Ricci et al., 2006). As far as skin is concerned, thickness of the Al alloy chosen is relevant, since a droop nose morphing device should need a limited power for actuation, and a compromise with mechanical strength must be reached. Thicknesses greater or equal to 0.3mm for Aluminium alloys of aeronautical use (such as 6xxx) are available out of the shelf [d], and it is possible to obtain thinner sheet[e] in tempers from annealed through full hard.

It may be interesting to have locally varying thickness, particularly for local variation of the stiffness facilitating or enabling compliance with some desired geometry for the profile. In aeronautics it is common to use high speed machining, but since the thickness of the aluminium alloy skin of interest in this project is very small, possibly an alternative process is Chemical Milling (Stiffler and Tershin, 1967).

[d] http://www.mingtai-al.com/Products/alloyseries/2015EcQ7hlfFhe.html
[e] http://www.allfoils.com/single-product/aluminum-sheet/

# Chapter 4

# Damage Tolerant Design

This chapter will cover the evolution of damage tolerant design and demonstrate its necessity. Also, it will cover the principles of Fatigue and Fracture Mechanics in which that study will be based. Finally, it will explain the computational methods used to obtain the parameters needed to complete the present structure analysis.

## 4.1 Fatigue Design Philosophies

Over the years, engineering has constantly evolved, and design philosophies have followed suit. Based and aided by new developments in fields ranging from materials science to computational mechanics, the design of any structure is, nowadays, an complex, iterative and continuous process. A crucial aspect to structural integrity that must be taken into account is the possibility of damage, and the structure's capacity to withstand it to some extent. This concept is called damage tolerance, and is defined by (Grandt, 2003) as "the ability to resist to a specified amount of damage for a given period of service". Given its nature, aircraft structure designs are a chief example of this philosophy.

The damage mentioned above can be of various kinds. A radical example is the case of the USAF bomber Boeing B-17F Flying Fortress named *All American III,* which survived, with its tail section severely damaged, a mid-air collision with a German fighter Messerschmitt Bf 109. The bomber, nearly cut in half by the collision and with the left horizontal stabilizer torn completely off (Figure 4.1), flew another 90 minutes before landing safely. This happened over Tunisia, on February 1, 1943, during the Second World War (The Aviation History Online Museum, 2013; Wikipedia, 2016a).

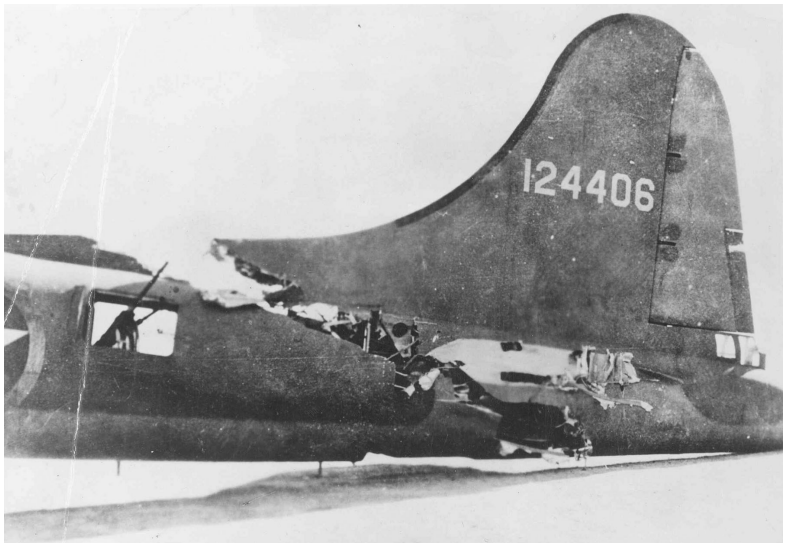


Figure 4.1: Close-up of the damage to Boeing B-17F-5-BO (S/N 41-24406) *All American III* (United States Air Force, 1943).

A comment must be made on this example. This kind of damage was certainly not taken into account by Boeing engineers from the 1930's and 1940's. Although it is used to emphasize the concept of damage tolerance, it is a exaggerated example, and one must bear in mind that concerns with damage tolerance saw development mainly after the 1950's and 1960's, as it will be later shown.

Common damage is, for instance, pre-existent to manufacture, such as material abnormalities, damage due to manufacturing problems like poor workmanship or incorrect design, or to service-induced damage, such as fatigue cracks (p.4, Grandt, 2003). Another sources, such as (p. 1.0.1, Miedlar et al., 2002), refer these problems in aviation, mentioning that "from the standpoint of flight safety, it was found prudent to assume that new airframe structures could contain initial damage (e.g. scratches, flaws, burrs, cracks, etc.)". Other cause of possible damage to aircraft are bird-strikes (collision of a bird with any aircraft surface or part), most of which result in detectable damage (rupture, permanent deformation). This problem has been widely studied (Hedayati and Sadighi, 2015; Smojver and Ivančević, 2010; Wang and Yue, 2010; Georgiadis et al., 2008, are some examples), and is known to have caused at least 42 fatal accidents between 1912 and 2002, resulting in 231 deaths (Thorpe, 2003). However, not all bird-strikes are catastrophic occurrences and light, unnoticed bird-strike can occur.

Fatigue problems mentioned on the last paragraph have various roots. Amongst those are the pressurization-depressurization cycles, the load changes due to different manoeuvres, atmospheric and aerodynamic phenomena, or the morphing actions of the aircraft (as mentioned on Chapter 3, Section 3.4.2). Design and manufacture flaws also play a role and can have disastrous consequences: three de Havilland Comet 1 (the first passenger jetliner), suffered fatal structural failures that led to explosive decompression and mid-air break-up, during the 1950's. It was found that the square design of the

windows caused high stress concentrations which, in conjunction with inadequate riveting technique, lead to the formation and propagation of cracks (Atkinson et al., 1962). To address this problem, engineers have employed several criteria, which have evolved along the years.

### 4.1.1 Infinite-Life Design

The more traditional approach is the Infinite-Life Design. Early designers sought that stress levels on the component did not exceed the material's fatigue limit, commonly a stress level that prevents failure after $10^7$ loading cycles. This approach is still used in machinery design, for instance, but is not suitable for the aviation field, as it leads to excessive weight of aircraft and low cost effectiveness (p. 23, Stephens et al., 2000). Also, many components and structures are not suitable to be designed within this approach, as it would be impractical (p. 19, Grandt, 2003). Therefore, other approaches, considering finite fatigue life, have appeared.

### 4.1.2 Safe-Life Design

Another approach to fatigue design is the Safe-Life Design. This approach sees fatigue as a crack nucleation problem, assuming that failure occurs when a crack first appears (p. 19, Grandt, 2003). The mean fatigue life is determined with comprehensive testing, simulated or on field, and as test results are often scattered, a safety factor is applied (Figure 4.2). This approach is used, nowadays, in the design of bearings, gun barrels or pressure vessels (commonly known as "leak before break") (p. 25, Stephens et al., 2000). It was also used in aviation during the 1960's, but resulted in inadequate designs and several failures of American military aircraft (p. 20, Grandt, 2003). For instance, a F-111 fighter lost a wing while on a training flight, having flown about 100 hours (Barter et al., 1993; Schijve, 2009). The failure, located on the lower wing pivot[a], was due to a crack (Figure 4.3, note the light grey band where the fatigue crack growth occurred) initiated by a undetected forging defect (Rudd et al., 1979; Barter et al., 1993; Schijve, 2009). These episodes showed that the Safe-Life designs did not took into account defects originated during manufacturing or in service (p. 1.0.1, Miedlar et al., 2002).

[a] F111 has a swing-wing design (refer to Chapter 3, Section 3.3.1).

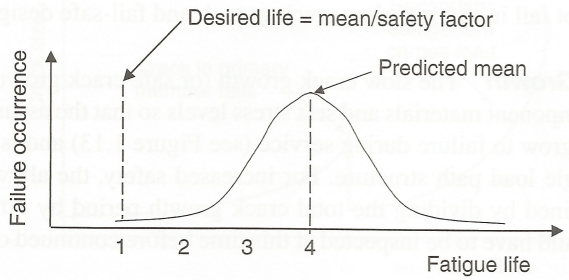


Figure 4.2: Safe-life design philosophy (p. 19 of Grandt, 2003).

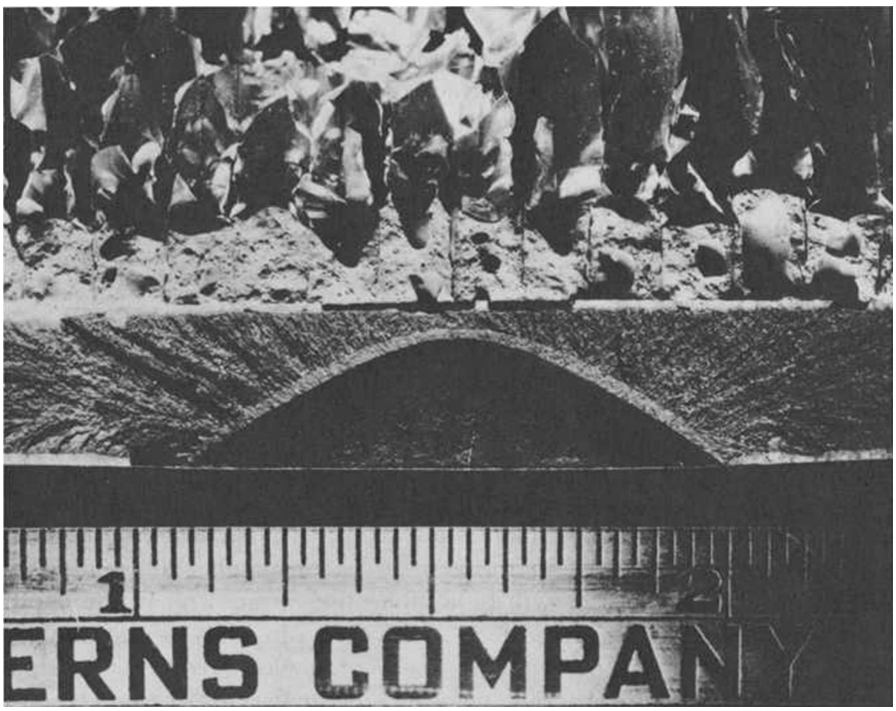


Figure 4.3: F-111 Wing Defect. Length unit: inches (Rudd et al., 1979).

### 4.1.3 Damage Tolerant Design

The lessons learned from these accidents led to a new design philosophy: the Damage Tolerant Design. This philosophy is based in the assumption that small initial flaws are present in new aircraft (Schijve, 2009), and therefore its propagation must be considered, applying Fatigue and Fracture Mechanics concepts. Within this design philosophy, two major approaches may be followed: the Fail-Safe Design, and the Slow Crack Growth approach.

#### 4.1.3.1 Fail-Safe Design

A Fail-Safe Design admits the appearance of fatigue cracks and aims to prevent failure of the structure before cracks are detected. This means that designers accept that an aircraft can fly "even though it contains cracks or, indeed failed components" (Barter et al., 1993). This is ensured by employing multiple load-bearing paths and crack stoppers built at intervals into the structure. If any single component fails, the loads are distributed by the remaining (Figure 4.4). However, the Fail-Safe designs must be accompanied with thorough routine inspections with periodicity based on crack propagation estimated time or number of cycles. It is important that damaged parts are readily detected and repaired, as the extra load will shorten the fatigue life of the remaining intact components (p. 21, Grandt, 2003). Failure to do so has led to some accidents, the most notable being the explosive decompression of a Boeing 737-200 from Aloha Airlines on April 28, 1988. The failure was caused by a large number of undetected cracks that started at many rivet holes in the same lap joint. There, corrosion was promoted by disbonding of doublers and exacerbated by the marine environment in which the aircraft operated. Boeing had given instructions to inspect the zone but they were not yet carried out (Schijve, 2009). Fortunately the aircraft, carrying 95 people, landed safely with only one fatality, a flight attendant who was swept overboard.

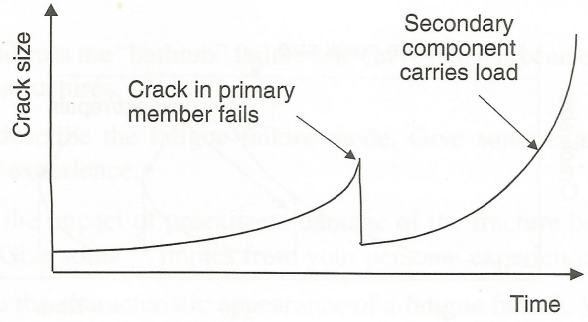


Figure 4.4: Fail-Safe Design (p.21, Grandt, 2003).

#### 4.1.3.2 Slow Crack Growth Design

In Slow Crack Growth Design concepts, cracks are not allowed grow to the critical size. Consequently, there is no unstable crack propagation, and structural integrity is not degraded below a specified limit (p. 1.3.3, Miedlar et al., 2002). Usually, the allowable life depends on the degree of inspectability of the structure in question, and is often obtained by dividing the total crack growth time by a safety factor of 2 (Figure 4.5). By this time, the component has to be inspected to assess its serviceability (p. 21, Grandt, 2003).

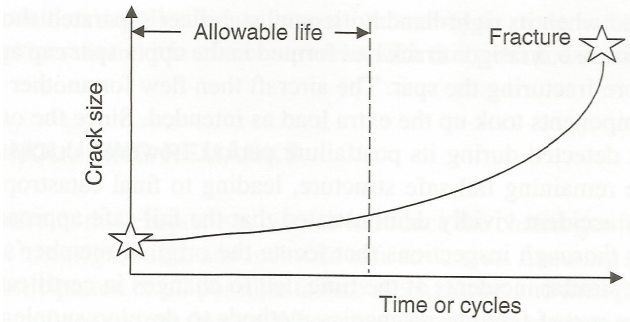


Figure 4.5: Slow Crack Growth approach (p.21, Grandt, 2003).

## 4.2 Fatigue and Fracture Mechanics Principles

The approaches mentioned in the last section are based on the possible existence of cracks in the aircraft structures, and in the determination of its propagation life. Therefore, some Fracture Mechanics concepts will be briefly reviewed. For detailed presentations, books on the subject should be consulted, such as Broek's "Elementary engineering fracture mechanics" (Broek, 1986), Janssen's "Fracture Mechanics" (Janssen et al., 2004), Anderson's "Fracture mechanics: fundamentals and applications"(Anderson, 2005), Miannay's "Fracture Mechanics" (Miannay, 1997) or Knott's "Fundamentals of fracture mechanics"(Knott, 1973). For those readers who wish a concise and fast-reading introduction, Smith's "An introduction to fracture mechanics for engineers", divided in three parts, is recommended (Smith, 1978, 1979a,b).

### 4.2.1 Strain Energy Release Rate

The first important concept for this work is the concept of Strain Energy Release Rate. Griffith showed (Griffith, 1921) that, for a infinite plate with a central crack of length $2a$, and subjected to a remote tensile stress $\sigma$, the Strain Energy Release was (p.6, Miannay, 1997) :

$$\Delta U = -\frac{\sigma^2 \pi a^2}{2E^*} \tag{4.1}$$

This equation is presented by many books on Fracture Mechanics (see, for instance, Chapter 2 of Anderson, 2005).

The Strain Energy Release Rate is obtained by deriving equation 4.1 in order to the crack length:

$$G = -\frac{\partial U}{\partial a} = \frac{\sigma^2 \pi a}{E^*} \tag{4.2}$$

where

$$E^* = \begin{cases} E & for\ plane\ stress \\ \frac{E}{1-v^2} & for\ plane\ strain \end{cases}$$

As it will be seen later, Strain Energy Release Rate is key in the computational Fracture Mechanics techniques used during this work.

### 4.2.2 Crack Propagation Mode

Another relevant concept to this study is crack propagation mode. There are three crack propagation modes (Figure 4.6), depending on the loading conditions:

- Mode I is the opening mode, generated by a tensile stress normal to the plane of the crack. This is the most common and studied mode;
- Mode II is the sliding mode, caused by an in-plane shear stress (acting on the crack plane and perpendicular to the crack front);
- Mode III is the tearing mode, due to a out-of-plane shear stress (acting parallel to the crack plane and to the crack front).

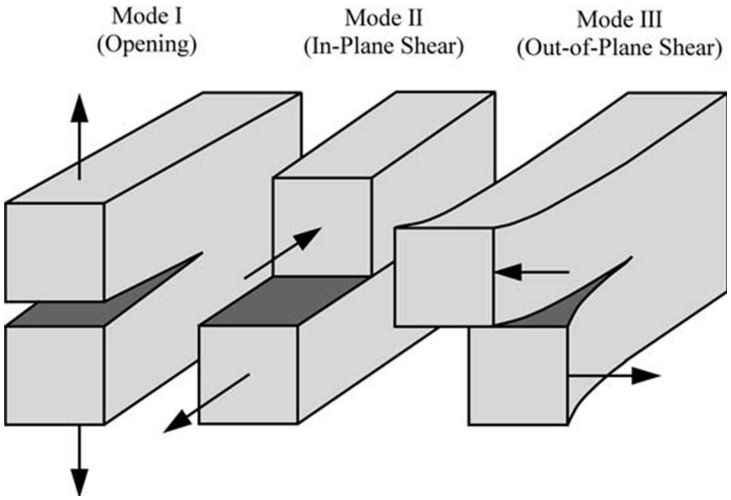


Figure 4.6: Loading conditions and resultant crack modes (p. 43, Anderson, 2005).

Although each mode may occur isolated, it is common to have mixed mode loading conditions, involving two or even the three modes.

### 4.2.3 Stress Intensity Factor

The third fundamental concept for this work is the Stress Intensity Factor. This a measure of the magnitude of the stress components in the region near to the crack tip (Smith, 1978). The Stress Intensity Factor, from now on abbreviated SIF, is represented

by the symbol $K_{I,II\,or\,III}$ (depending on the crack mode it refers to). It depends on the length of the crack, but also on its shape, on the geometry of the cracked body and on the type of loading. A general formula for the SIF in a crack loaded with a remote stress $\sigma$ is:

$$K = Y\sigma\sqrt{\pi a} \tag{4.3}$$

where $Y$ is a dimensionless calibration function of the geometry, and $a$ the half-crack length. For example, the Mode I SIF for a central crack of length $2a$ on a infinite plate subjected to a remote tensile stress $\sigma$ is given by:

$$K_I = \sigma\sqrt{\pi a} \tag{4.4}$$

Details on the derivation of this factor can be found in the literature mentioned above, and in the "Compendium of Stress Intensity Factors" (Rooke et al., 1976), presenting SIF formulas for diverse geometries and loading conditions.

Recalling equation 4.1, and using equation 4.4, one arrives to a very important relationship between the Stress Intensity Factor and the Strain Energy Release Rate ((P.59, Anderson, 2011):

$$G_I = \frac{K_I^2}{E^*} \tag{4.5}$$

where

$$E^* = \begin{cases} E & for\,plane\,stress \\ \frac{E}{1-v^2} & for\,plane\,strain \end{cases}$$

This relationship will also play a major role on the computational Fracture Mechanics techniques used during this work.

The concept of Stress Intensity Factor is of great importance in the design of structures assumed to contain cracks. For a certain material, a limit exists for the Stress Intensity Factor value, and above which the unstable propagation of the crack, and consequent rupture of the part, occurs. This limit is called the material's Fracture Toughness, and for isotropic materials such as metals, its symbol is $K_c$ (or $K_{Ic}$ in the case of plane strain). Values for this material property are found in several databases and books.

Being in the knowledge of this property and the correct calibration of the SIF, and based on equation 4.3, a designer has the necessary tool to follow two paths:

- Calculate the maximum remote stress $\sigma$ that the part can withstand without rupture in the presence of a crack with a (known) certain length $2a$ (this length is normally the minimum size detectable by the inspection techniques available, and/or is determined by Standards);

- Calculate the maximum crack length $2a$ permissible to a part remotely loaded with a (known) certain stress $\sigma$.

### 4.2.4 Estimation of Fatigue Life

The approaches mentioned on Section 4.1 rely on knowledge of the estimated fatigue life of the structure. This estimate may be experimentally determined, or calculated based on known data, namely the Crack Growth Rate:

$$Crack\,Growth\,Rate = \frac{Crack\,lenght\,increase}{cycle} = \frac{da}{dN} \tag{4.6}$$

As mentioned before, Fatigue problems occur in the presence of variable loads. In solids that contain a crack, this means that the remote stress $\sigma$ loading the crack also varies between $\sigma_{max}$ and $\sigma_{min}$. Consequently, we have:

$$K_{max} = Y\sigma_{max}\sqrt{\pi a} \tag{4.7}$$

$$K_{min} = Y\sigma_{min}\sqrt{\pi a} \tag{4.8}$$

$$\Delta K = K_{max} - K_{min} \tag{4.9}$$

The relationship between t$\sigma_{max}$ and $\sigma_{min}$ is usually expressed by the ratio $R$ :

$$R = \frac{\sigma_{min}}{\sigma_{max}} = \frac{K_{min}}{K_{max}} \tag{4.10}$$

Crack growth can be described by a plot of $\log da/dN$ versus $\log \Delta K$, which exhibits a sigmoidal variation (Figure 4.7). This curve is divided in three region:

1. Region 1, due to the existence of a threshold stress intensity factor range $\Delta K_{th}$. Below this threshold, cracks grow at undetectable rates and are characterized as non propagating cracks, and above it there is a sudden increase in crack growth.

2. After that, crack propagation enters Region 2, known as steady-state growth or the Paris regime. It shows a linear variation $\log da/dN$ versus $\log \Delta K$, governed by equation 4.11, the Paris Law (Paris et al., 1961):

$$\frac{da}{dN} = C(\Delta K)^m \tag{4.11}$$

   $C$ and $m$ (the slope of the line, in the log-log plot) are constants for each material. For metals, m values are between 2 to 4 (Smith, 1979a). Depending on the $R$ ratio, the same material may present different Paris Law curves. Therefore, when searching for $C$ and $m$ value on literature, $R$ should be taken into consideration.

3. When $K_{max}$ gets closer to $K_c$, crack growth rates increase rapidly, causing the fracture of the part.

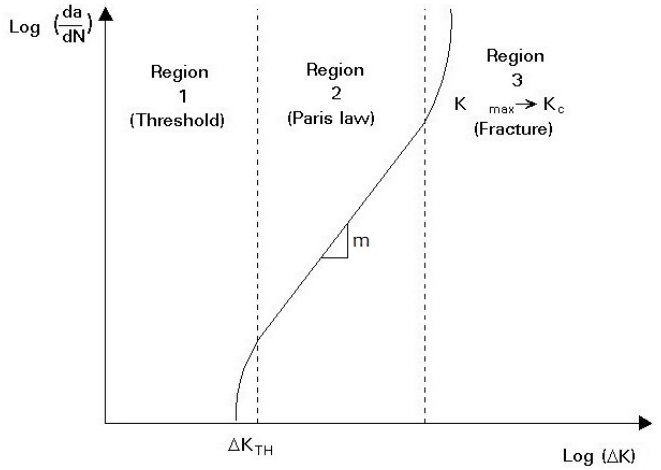


Figure 4.7: Fatigue Crack Growth Rate Curve (adapted from Može, 2016).

Based on the Paris Law (equation 4.11) it is possible to estimate the fatigue life of the part. Assuming an initial crack with and half-crack length $a_o$ (already on the steady-state growth region), the number of cycles until it reaches a certain half-crack length $a_f$ can be calculated by integration of that differential equation.

Rearranging equation 4.11, one obtains:

$$dN = \frac{1}{C(\Delta K)^m} da \tag{4.12}$$

Integration of both members yields:

$$N = \frac{1}{C} \int_{a_o}^{a_f} \frac{1}{(\Delta K)^m} da \tag{4.13}$$

Is is usual to further develop equation 4.13 using equations 4.3 and 4.9. However, as it will be later seen, the stress intensity factors will be computationally determined, and will not resemble equation 4.3. Therefore, further development will not be done by now.

A final note about this process is needed. It was stated that a limit to the crack length should be imposed. This limit may be based on design considerations (such as values given by relevant Standards). It can also be calculated with the knowledge of the Fracture Toughness $K_c$and the maximum remote Stress $\sigma_{max}$. In this case, the limit is called the critical half-crack length, $a_c$, and is obtained using a rearranged form of equation 4.3:

$$a_c = \left( \frac{K_c}{\sigma_{max} Y \sqrt{\pi}} \right)^2 \tag{4.14}$$

The process described above is one of many possible. Many other models of crack growth can be found on literature (see, for instance, pp.169-172, Grandt, 2003). Moreover, several databases of Crack Growth Rate data, collected experimentally, are available, and are used by Fatigue and Fracture Mechanics softwares. Examples are NASGRO[b], which was initially developed and released in the 1980's for fracture control analysis of NASA space hardware, or AFGROW (Air Force Grow), a Damage Tolerance Analysis framework developed by the United States Air Force Research Laboratory.[c].

## 4.3 Extraction of the Stress Intensity Factors

As shown on the previous sections, the knowledge of the Stress Intensity Factors is of chief importance. To obtain these, several techniques exist. During this work, two will be employed: the use of the J-Integral and the Modified Virtual Crack Closure Technique. These will be covered in the next sections

### 4.3.1 J-Integral

The J-Integral is a contour integral developed by J.R. Rice in 1968, and presented in the paper "A path independent integral and the approximate analysis of strain concentration by notches and cracks" (Rice, 1968). As the title reveals, this characterizes the Strain Energy Release Rate for elastic materials. It is defined by the following equation:

$$J = \int_{\Gamma} \left( W dy - \overrightarrow{T} \frac{\partial \overrightarrow{u}}{\partial x} ds \right) \tag{4.15}$$

where $\overrightarrow{T} = \sigma \overrightarrow{n}$ is the traction vector, $\Gamma$ is an arbitrary counter clockwise contour around the tip of the crack, $\overrightarrow{u}$ is the displacement vector and $W$ is the Strain Energy Density:

$$W = \int \sigma_{ij} d\varepsilon_{ij}$$

Figure 4.8 illustrates these concepts.

[b] http://www.swri.org/4org/d18/mateng/matint/nasgro/
[c] http://www.afgrow.net/

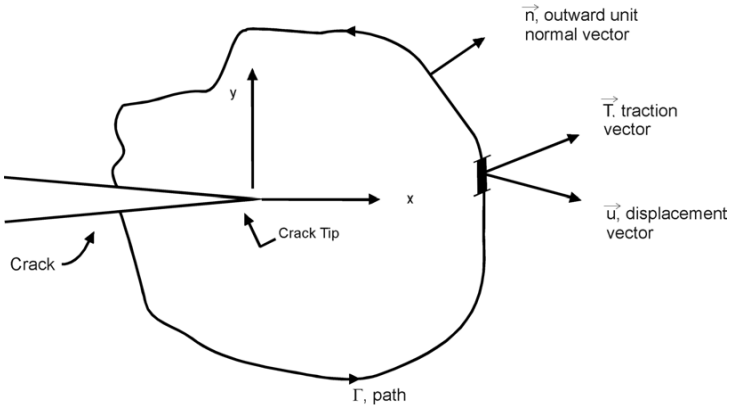


Figure 4.8: J-Integral Contour definition and parameters illustrated (adapted from p.2.1.17, Miedlar et al., 2002)

Rice proved that this contour is independent from the path, a demonstration that can be found in the original paper or in several books (see, for instance, section 3.2 of Anderson, 2005, or section 6.2 of Miannay, 1997). These textbooks also infer another very important property of the J-Integral:

$$J = -\frac{\partial U}{\partial a} = G \tag{4.16}$$

This equation, along with the relationship shown by equation 4.5, provides the engineer with a simple energy-based method for obtaining stress-intensity factors.

### 4.3.2 Stress Intensity Factors Extraction using *Abaqus*

#### 4.3.2.1 J-Integral Calculation

The J-Integral technique is implemented on several Finite Element Method codes. *Abaqus*, on its Theory Guide, states that the J-Integral can be extended to three dimensions by considering a crack with a tangentially continuous front (Figure 4.9). Considering that, when $r \to 0$, the conditions for path independence apply on any contour in the $x_1 - x_2$ plane (perpendicular to the crack), *Abaqus* writes J-Integral as a pointwise energy release rate along the crack front:

$$J(s) = \lim_{\Gamma \to 0} \int_{\Gamma} \vec{n} \left( W\boldsymbol{I} - \boldsymbol{\sigma} \frac{\partial \vec{u}}{\partial \boldsymbol{x}} ds \right) \vec{q}\, d\Gamma \tag{4.17}$$

where $\Gamma$ is a contour beginning on the bottom crack surface and ending on the top surface. The limit $\Gamma \to 0$ indicates that $\Gamma$ shrinks onto the crack tip. $\vec{q}$ is a unit vector in the virtual crack extension direction, which is perpendicular to the local crack front and lies in the crack plane.

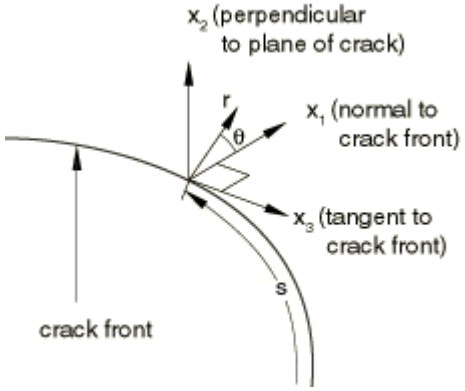


Figure 4.9: Definition of local orthogonal Cartesian coordinates at the point s on the crack front; the crack is in the $x_1 - x_3$ plane (Dassault Systèmes, 2016).

The calculation of the energy release rate is then made considering a virtual crack advance $\lambda(s)$ in the plane of a three-dimensional crack, and calculating a domain integral:

$$\overline{J} = \int_L J(s)\lambda(s)ds = \lim_{\Gamma \to 0} \int_\Gamma \lambda(s)\overrightarrow{n} \left( W\boldsymbol{I} - \boldsymbol{\sigma}\frac{\partial \overrightarrow{u}}{\partial \boldsymbol{x}}ds \right) \overrightarrow{q}\, dA \tag{4.18}$$

where $L$ denotes the crack front under consideration; $dA$ is a surface element on a vanishingly small tubular surface enclosing the crack tip (i.e. $dA = dsd\Gamma$); and $\overrightarrow{n}$ is the outward normal to $dA$. For each node set $P$ along the crack front, $\lambda(s)$ is discretized with the same interpolation functions as those used in the finite elements along the crack front, so that $J^P$ is calculated.

#### 4.3.2.2 Stress Intensity Factors Extraction

Consulting *Abaqus* Theory Guide (Dassault Systèmes, 2016), it is stated that "although the energy release rate is calculated directly in Abaqus/Standard, it is usually not straightforward to compute stress intensity factors from a known J-integral for mixed-mode problems. Abaqus/Standard provides an interaction integral method to compute the stress intensity factors directly for a crack under mixed-mode loading". This interaction integral method is based on the work of (Shih et al., 1986), and details in its implementation are found there.

*Abaqus* uses the following equation to relate the J-Integral value with the Stress Intensity Factors:

$$J = \frac{1}{8\pi}\boldsymbol{K}^T\boldsymbol{B}^{-1}\boldsymbol{K} \tag{4.19}$$

where $\boldsymbol{K} = \begin{bmatrix} K_I & K_{II} & K_{III} \end{bmatrix}^T$ and $\boldsymbol{B}$ is called the pre-logarithmic energy factor matrix (Shih et al. 1986; Barnett and Asaro 1972; Gao et al. 1992; Suo 1990). For homogeneous, isotropic materials, $\boldsymbol{B}$ is diagonal . Therefore, equation 4.19 simplifies to:

$$J = \frac{1}{E^*}(K_I^2 + K_{II}^2) + \frac{1}{2G}K_{III}^2 \tag{4.20}$$

In general, the J-integral equation 4.19 can be written as:

$$J = \frac{1}{8\pi}\left[K_I B_{11}^{-1} K_I + 2K_I B_{12}^{-1} K_{II} + 2K_I B_{13}^{-1} K_{III} + (terms\, not\, involving\, K_I)\right] \tag{4.21}$$

Here, $I, II, III$ correspond to $1, 2, 3$ when indicating the components of $\boldsymbol{B}$. Defining an auxiliary, pure Mode I, crack-tip with stress intensity factor $k_I$, the J-integral for this field comes:

$$J_{aux}^I = \frac{1}{8\pi}k_I B_{11}^1 k_I \tag{4.22}$$

Combining equations 4.21 and 4.22 yields:

$$J_{total}^I = \frac{1}{8\pi}\left[(K_I + k_I)B_{11}^{-1}(K_I + k_I) + 2(K_I + k_I)B_{12}^{-1}K_{II} + 2(K_I + k_I)B_{13}^{-1}K_{III} + (terms\, not\, involving\, K_I\, or\, k_I)\right] \tag{4.23}$$

The terms not involving $K_I$ or $k_I$ in $J_{total}^I$ and $J$ are equal. Consequently, the interaction integral can be defined as:

$$J_{int}^I = J_{total}^I - J - J_{aux}^I = \frac{k_1}{4\pi}(B_{11}^{-1}K_I + B_{12}^{-1}K_{II} + B_{13}^{-1}K_{III}) \tag{4.24}$$

Repeating the process for mode II and III, a linear system of equations is obtained:

$$\begin{cases} J_{aux}^I = \frac{k_1}{4\pi}(B_{11}^{-1}K_I + B_{12}^{-1}K_{II} + B_{13}^{-1}K_{III}) \\ J_{aux}^{II} = \frac{k_2}{4\pi}(B_{21}^{-1}K_I + B_{22}^{-1}K_{II} + B_{23}^{-1}K_{III}) \\ J_{aux}^{III} = \frac{k_3}{4\pi}(B_{31}^{-1}K_I + B_{32}^{-1}K_{II} + B_{33}^{-1}K_{III}) \end{cases} \tag{4.25}$$

Making $k_1$,$k_2$,$k_3$equal to 1, the solution of this system is:

$$\boldsymbol{K} = \begin{bmatrix} K_I & K_{II} & K_{III} \end{bmatrix}^T = 4\pi \boldsymbol{B} \cdot \boldsymbol{J}_{int} \tag{4.26}$$

being $\boldsymbol{J}_{int} = \begin{bmatrix} J_{int}^I & J_{int}^{II} & J_{int}^{III} \end{bmatrix}^T$.

The calculation of the interaction integrals by *Abaqus* is done in the same fashion as the J-Integral, creating three auxiliary pure Mode I, Mode II, and Mode III crack-tip fields and respective auxiliary interaction integrals. Further details can be found on section 2.16 of *Abaqus* Theory Guide (Dassault Systèmes, 2016, from where the section above was adapted). The interested reader is also advised to consult Chapter 12 of (Anderson, 2005), for instance.

### 4.3.3 Remarks regarding the J-integral calculation using *Abaqus*

On *Abaqus* documentation referring to J-integral calculation and Stress Intensity Factor extraction several remarks and warnings are made to the user. On Section 11.4.2 of *Abaqus* Analysis User's Guide, concerning Contour Integral Evaluation, it is stated that to evaluate contour integrals using the conventional Finite Element Method "detailed focused meshes are generally required", requiring the user "to conform the mesh to the cracked geometry, to explicitly define the crack front, and to specify the virtual crack extension direction". Also, the user is warned that "obtaining accurate contour integral results for a crack in a three-dimensional curved surface can be quite cumbersome".

Regarding the evaluation of the value of the Contour Integral, this document mentions that "several contour integral evaluations are possible at each location along a crack." It explains that these evaluation "can be thought of as the virtual motion of a block of material (...) surrounding each node along the crack line (in three dimensions). Each block is defined by contours, where each contour is a ring of elements completely surrounding (...) the nodes along the crack line from one crack face to the opposite crack face. These rings of elements are defined recursively to surround all previous contours".

Abaqus automatically forms each ring of elements, based on the user's definition of the crack tip or crack line, and performs and evaluation of the contour integral for each contour. The user must specify the number of contours he desires, being this the number of evaluations performed.

Concerning the path independence of the J-Integral, it is stated in this document that "the J-integral should be independent of the domain used provided that the crack faces are parallel to each other". Nevertheless, it is said that "estimates from different rings may vary because of the approximate nature of the finite element solution."

This manual also gives information on some problems that can occur. It mentions that strong variations of the estimated values "typically indicate an error in the contour integral definition", whereas "gradual variation in these estimates may indicate that a finer mesh is needed". Attention is also drawn to the fact that "the first few contours may be inaccurate", and it is recommended to "request more contours and determine the value of the contour integral that appears approximately constant from one contour to the next", discarding the outlying. It is added that "In linear elastic problems the first and second contours typically should be ignored as inaccurate". Regarding three-dimensional models, it is reminded that "the J-integral estimates may be inaccurate from the node sets at the crack front ends", due to the "skewness of the outmost layer of elements". However "this accuracy loss (...) has no effect on the accuracy of the contour integral values at the neighbouring node sets along the crack front".

It should be mentioned that, when modelling a crack on *Abaqus,* it is necessary to specify the virtual crack extension direction. About this matter, the documentation refers that "*Abaqus* will calculate the normals automatically to correct any inadequate virtual crack extension directions" specified for the crack surfaces nodes and for external surfaces at the ends of a crack front line.

Concerning the use of J-Integral and *Abaqus,* the interested reader is advised to consult (Brocks and Scheider, 2001), where the reliability of J-Integral values is discussed.

### 4.3.4 Modified Virtual Crack Closure Technique

The Virtual Crack Closure Technique (VCCT) is a method of calculating the Strain Energy Release Rate $G$. It establishes a relation between the Strain Energy variation due to an infinitesimal increment $\Delta a$ on crack length, and that increment:

$$G = \frac{\partial U}{\partial a} \simeq \frac{U_{a+\Delta a} - U_a}{\Delta a} \tag{4.27}$$

This technique was proposed by Rybicki and Kanninen in 1977 (Rybicki and Kanninen, 1977), based on the assumption that the energy needed to open the crack is the same as the energy needed to close the same crack. Although it is called Virtual Crack Closure, the method requires the crack to be actually opened or closed by $\Delta a$ , resulting in the need for two finite elements analysis. In the first step, the crack is considered closed and the nodal forces needed to keep it closed are obtained. In the second step, the crack is opened by $\Delta a$, and the displacements due to that opening are registered. In possession of this information, the strain energy release rate for a specific crack length is calculated.

Due to the need of these two steps, this technique was not widely adapted. However, a modified Virtual Crack Closure Technique (mVCCT) was developed. Along with the assumptions made by Rybicki and Kanninen, in this technique it is further assumed that the state of crack tip does not suffer a substantial variation when the crack is increased by a increment $\Delta a$ small enough. This can be easily explained, considering Finite Element Method model of a crack modelled with two-dimensional, four-noded elements (Figure 4.10). The virtual displacements of the node at the crack tip (node i) are approximately equal to the displacements to those of the node of the original virtual crack tip (in the model, the first node of the cracked region, node l).

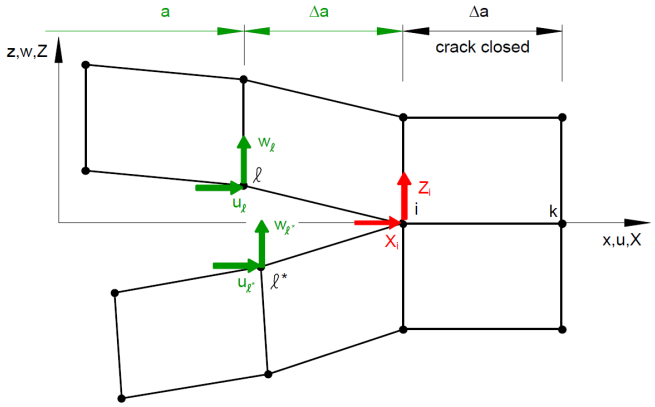


Figure 4.10: Modified Crack Closure Method (mVCCT) (Krueger, 2002).

For the example of Figure 4.10, the energy $\Delta E$ required to close the crack along one element side can be calculated by the equation (Krueger, 2002):

$$\Delta E = \frac{1}{2}\left[X_i \cdot \Delta u_l + Z_i \cdot \Delta w_l\right] \tag{4.28}$$

where $X_i$ and $Z_i$ are the nodal forces at node i, and $u_l$ and $w_l$ are the displacements of node l . This proves that all the data necessary the calculation of the energy variation results from a single finite elements analysis.

Knowing the energy variation, the energy release rate can be calculated by:

$$\Delta G = \frac{\Delta E}{\Delta A} = \frac{\Delta E}{\Delta a \cdot b} \tag{4.29}$$

where $\Delta A$ is the surface area created by the $\Delta a$ crack extension, and the $b$ the thickness of the cracked body.

Using the corresponding displacements and nodal forces, it is possible to calculate the strain energy release rates corresponding to each opening mode. For the example of Figure 4.10, and assuming unitary thickness (Krueger, 2002):

$$G_I = \frac{-Z_i(w_l - w_l^*)}{2\Delta a} \tag{4.30}$$

$$G_{II} = \frac{-X_i(u_l - u_l^*)}{2\Delta a} \tag{4.31}$$

Within this thesis, three-dimensional models will be used. This method is easily generalized to 3D 8-noded or 20-noded elements. Considering the first case (refer to 4.11), the extrapolation is simple. For an unitary thickness, one obtains the following expressions (Krueger, 2002):

$$G_I = \frac{-Z_{li}(w_l - w_l^*)}{2\Delta a} \tag{4.32}$$

$$G_{II} = \frac{-X_{li}(u_l - u_l^*)}{2\Delta a} \tag{4.33}$$

$$G_{III} = \frac{-Y_{li}(v_l - v_l^*)}{2\Delta a} \tag{4.34}$$

For the case of 20-noded elements, corner nodes and midside nodes must have a different treatment due to their different positions. For corner nodes (refer to Figure 4.12), the values of Strain Energy Release Rate are given by:

$$
\begin{aligned}
G_I &= -\frac{1}{2\Delta A_L}\left[\frac{1}{2}Z_{Ki}(w_{Kl}-w_{Kl^*})+Z_{Li}(w_{Ll}-w_{Ll^*})+Z_{Lj}(w_{Lm}-w_{Lm^*})\right.\\
&\qquad\left.++\frac{1}{2}Z_{Mi}(w_{Ml}-w_{Ml^*})\right]\\
G_{II} &= -\frac{1}{2\Delta A_L}\left[\frac{1}{2}X_{Ki}(u_{Kl}-u_{Kl^*})+X_{Li}(u_{Ll}-u_{Ll^*})+X_{Lj}(u_{Lm}-u_{Lm^*})\right.\\
&\qquad\left.++\frac{1}{2}X_{Mi}(u_{Ml}-u_{Ml^*})\right]\\
G_{III} &= -\frac{1}{2\Delta A_L}\left[\frac{1}{2}Y_{Ki}(v_{Kl}-v_{Kl^*})+Y_{Li}(v_{Ll}-v_{Ll^*})+Y_{Lj}(v_{Lm}-v_{Lm^*})\right.\\
&\qquad\left.++\frac{1}{2}Y_{Mi}(v_{Ml}-v_{Ml^*})\right]
\end{aligned}
\tag{4.35}
$$

For midside nodes (refer to Figure 4.13), the equations are:

$$
\begin{aligned}
G_I &= -\frac{1}{2\Delta A_M}\left[\frac{1}{2}Z_{Li}(w_{Ll}-w_{Ll^*})+\frac{1}{2}Z_{Lj}(w_{Lj}-w_{Lj^*})+Z_{Mi}(w_{Ml}-w_{Ml^*})\right.\\
&\qquad\left.+\frac{1}{2}Z_{Ni}(w_{Ni}-w_{Ni})+\frac{1}{2}Z_{Nj}(w_{Nj}-w_{Nj})\right]\\
G_{II} &= -\frac{1}{2\Delta A_M}\left[\frac{1}{2}X_{Li}(u_{Ll}-u_{Ll^*})+\frac{1}{2}X_{Lj}(u_{Lj}-u_{Lj^*})+X_{Mi}(u_{Ml}-u_{Ml^*})\right.\\
&\qquad\left.+\frac{1}{2}X_{Ni}(u_{Ni}-u_{Ni})+\frac{1}{2}X_{Nj}(u_{Nj}-u_{Nj})\right]\\
G_{III} &= -\frac{1}{2\Delta A_M}\left[\frac{1}{2}Y_{Li}(v_{Ll}-v_{Ll^*})+\frac{1}{2}Y_{Lj}(v_{Lj}-v_{Lj^*})+Y_{Mi}(v_{Ml}-v_{Ml^*})\right.\\
&\qquad\left.+\frac{1}{2}Y_{Ni}(v_{Ni}-v_{Ni})+\frac{1}{2}Y_{Nj}(v_{Nj}-v_{Nj})\right]
\end{aligned}
\tag{4.36}
$$

Recalling equations 4.5 and 4.20, the value for the Stress Intensity Factors are readily obtained.

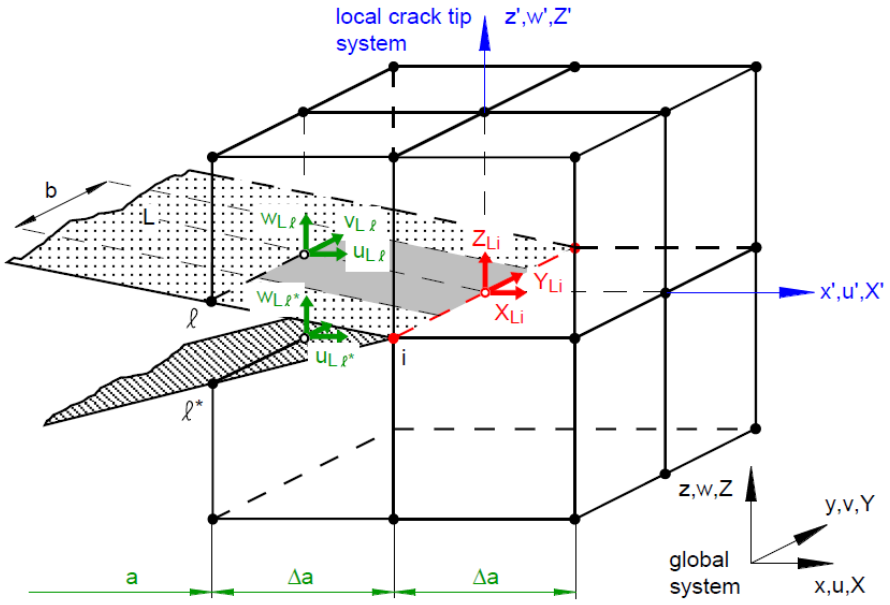


(a) 3D view

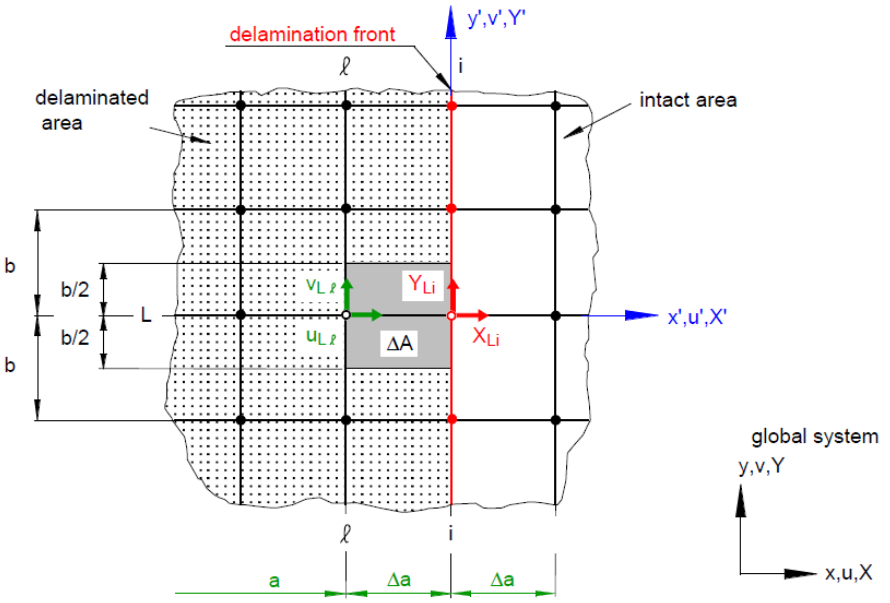


(b) Top view of upper surface

Figure 4.11: Modified Virtual Crack Closure Technique for 8-noded solid elements (Krueger, 2002).

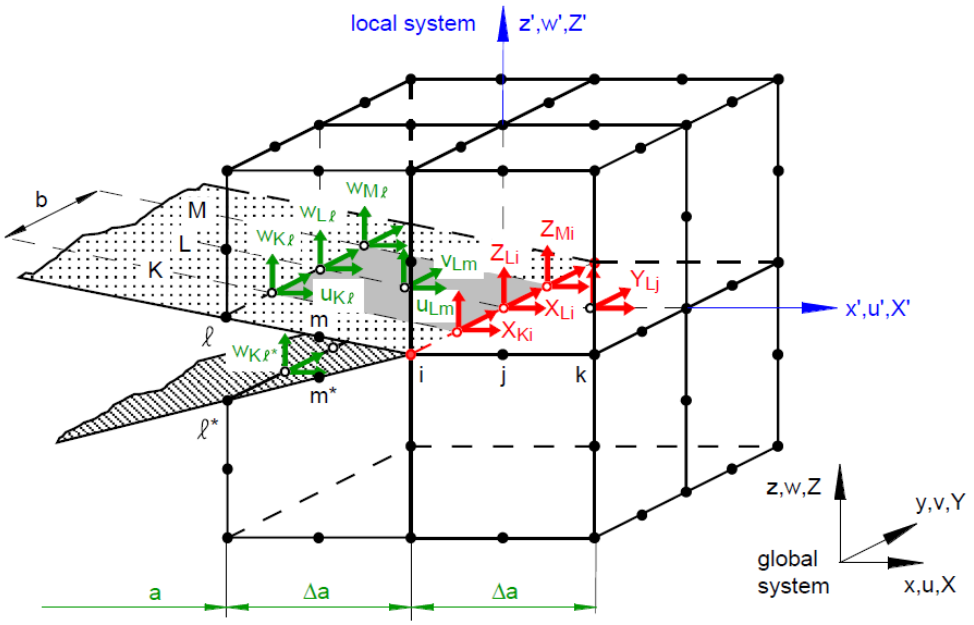


(a) 3D view

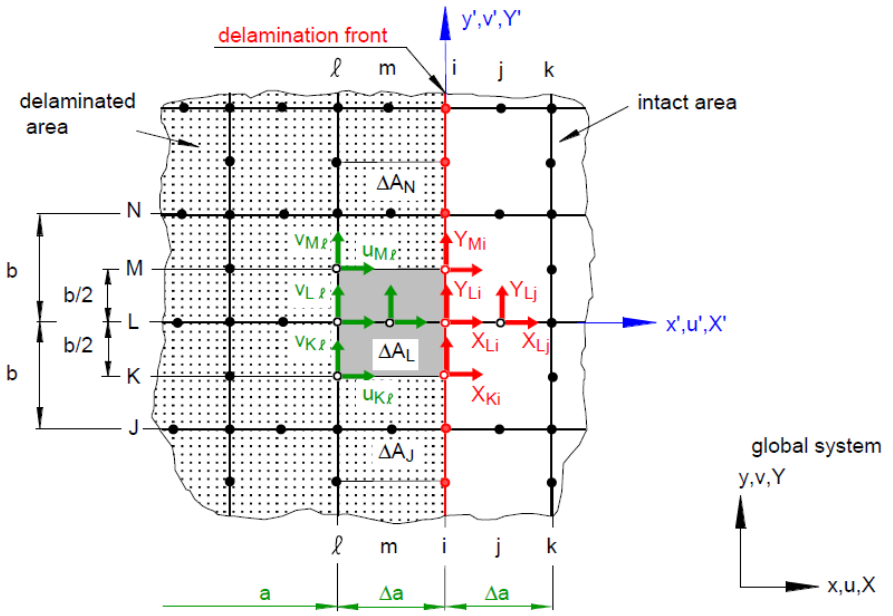


(b) Top view of upper surface

Figure 4.12: Modified Virtual Crack Closure Technique for corner nodes in 20-noded solid elements (Krueger, 2002).

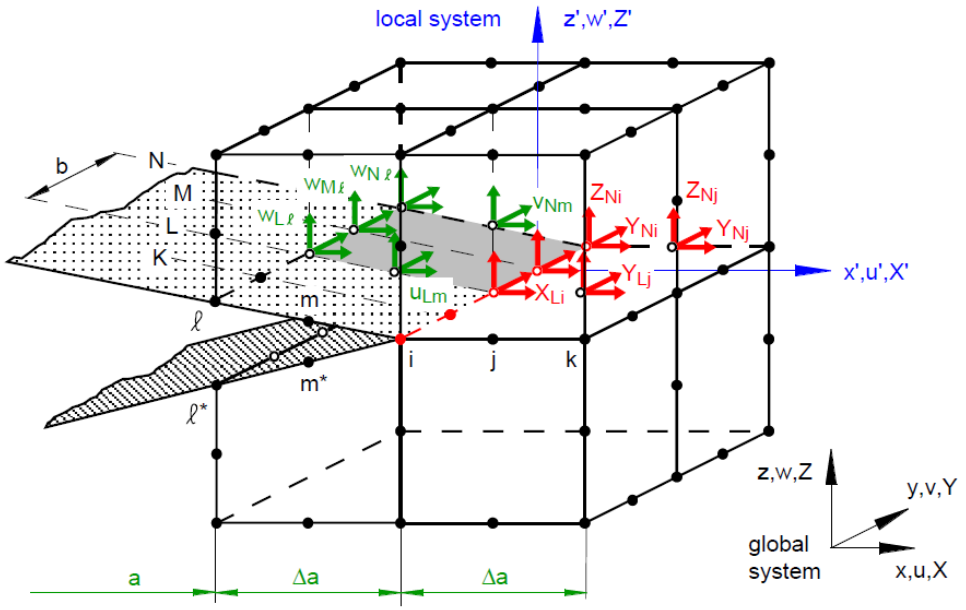


(a) 3D view

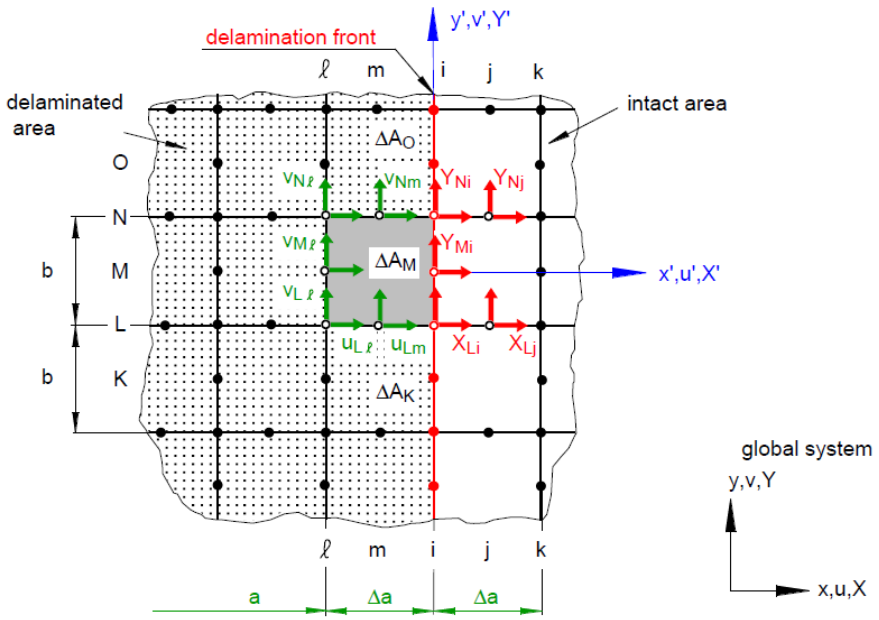


(b) Top view of upper surface

Figure 4.13: Modified Virtual Crack Closure Technique for midside nodes in 20-noded solid elements (Krueger, 2002).

# Chapter 5

# Analysis of the Compliant Mechanism

This chapter will report the first step on the study of the leading edge morphing structure: the analysis of the compliant mechanism.

## 5.1 Benchmarking

The Compliant Mechanism, developed by (Radestock et al., 2015), is depicted on Figure 5.1. It uses a flexure hinge to achieve the intended morphing. This flexure hinge is located in the upper arm, in the zone were the part section is diminished due to the arm's curved design. The part is actuated in the lower arm right (reader's viewpoint) end (actuator connection). In the upper arm right ends, all Degrees of Freedom are considered constrained.

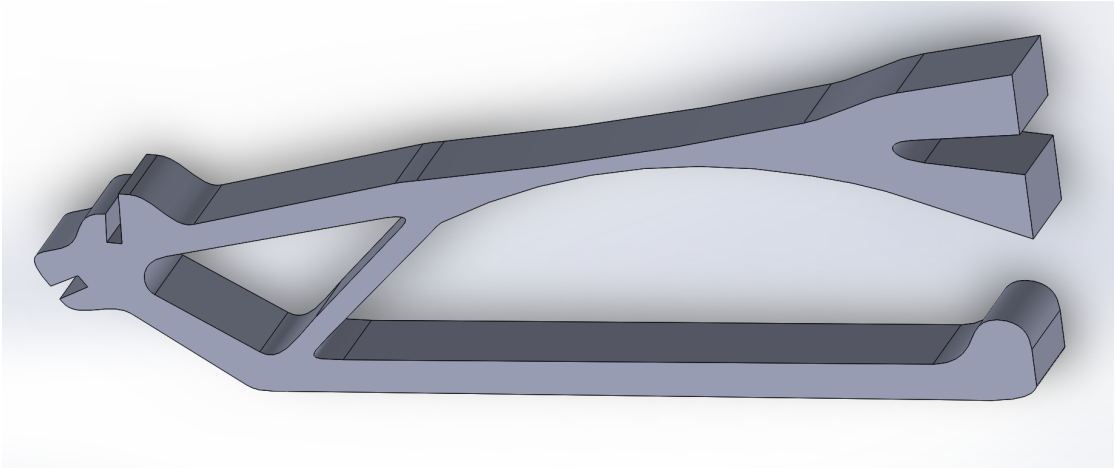

Figure 5.1: Compliant mechanism studied.

In order to benchmark the results, the actuation of the mechanism was simulated mimicking the work of (Radestock et al., 2015). The cited paper is unclear about the properties of the material used, citing another paper, (Mathew et al., 2005), which studies the mechanical properties of Polylactic acid (PLA) reinforced with microcrystalline cellulose up to 25% of weight percentage (*wt%*). However, since the latter paper does not directly state the mechanical properties of the studied materials, *CES EDUPACK* software was used to obtain the mechanical properties of unreinforced PLA, compiled on table 5.1[a]. Unreinforced material was chosen as no reference to any specific composition is made by (Radestock et al., 2015). The average values were used for the Young Modulus and Poisson Ratio, and the thickness was 10 mm.

Table 5.1: Mechanical Properties of PLA

| Material | PLA (Polylactic acid) |
|---|---|
| Young Modulus | 3.3-3.6 GPa |
| Poisson Ratio | 0.38-0.40 |
| Ultimate Tensile Strength | 47-70 MPa |
| Yield Strength | 55-72 MPa |

The part was modelled after the 3D model obtained, extracting the external contours from *SolidWorks* and creating a corresponding part using on the commercial finite element software, *Abaqus*. Several 2D meshes were created, using free and structured meshing to study mesh influence on the results. Shell quadrangular 8 node elements with reduced integration (S8R) were used. Meshes 1 and 2 were created as a preliminary study, which evolved to meshes 3 to 6. A seventh mesh was created, using 3D, 20-node quadratic brick elements with reduced integration (C3D20R): This Mesh, based on Mesh 6, was meant to understand if the 2D approach was reasonable. The meshes used are summarized on table 5.2.

Table 5.2: Used Meshes Summary

| Mesh | Type | Approximated element edge size [mm] | Number of Elements |
|---|---|---|---|
| 1 | Free | 4 | 454 |
| 2 | Free | 2 | 801 |
| 3 | Structured | 2 | 875 |
| 4 | Structured | 1.5 | 1557 |
| 5 | Structured | 1 | 3547 |
| 6 | Structured | 0.8 | 5653 |

[a] *CES EDUPACK* software indicated a yield strength greater than the tensile strength. Since this was, seemingly, an error, the values on table 5.1 were accordingly changed.

Table 5.3 shows the results of the convergence study.

Table 5.3: Convergence study

| Mesh | 1 | 2 | 3 | 4 | 5 | 6 | 7 |
|---|---|---|---|---|---|---|---|
| $U_2^{max}$[mm] | 18.01 | 18.01 | 18.00 | 18.03 | 18.03 | 18.01 | 18.13 |
| $\sigma_{Mises}^{max}$[MPa] | 43.48 | 43.26 | 43.53 | 43.51 | 43.46 | 43.68 | 43.95 |
| $\epsilon_{principal}^{max}$ | 1.27% | 1.25% | 1.26% | 1.26% | 1.26% | 1.27% | 1.28% |

The results of the simulations using the six 2D meshes were very similar, and Mesh number 7 results were also within 1% from the 2D results. There are not many more benefits from mesh refinement other than better resolution. Since the 3D problem is computationally heavier with no significant benefit, the 2D Mesh number 6 (Figure 5.2) was considered the reference for all the comparisons drawn below.

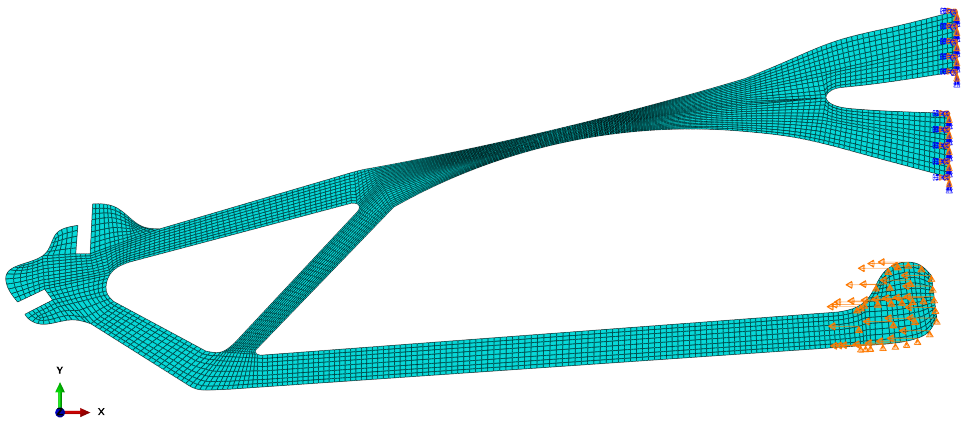


Figure 5.2: Mesh number 6 with boundary conditions.

### 5.1.1 Horizontal Displacement

Firstly, a 7 mm horizontal displacement was imposed on the actuator connection (Figure 5.2 shows the application nodes). Note that, to obtain a plausible deformed shape, the vertical DOF on the application nodes was fixed.

The maximum vertical displacement was of about 18.0 mm in the stringer connection, and the maximum strain was 1.26% at the flexure hinge. These results are illustrated on Figure 5.3.

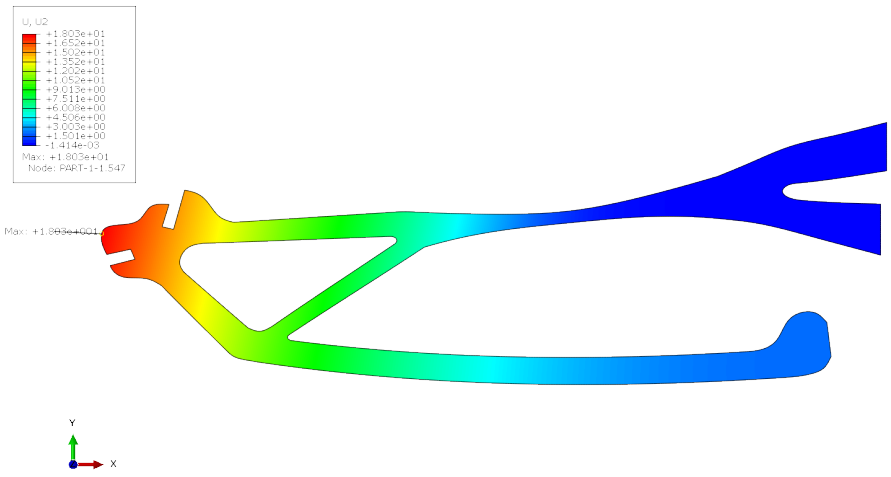


(a) Vertical displacement of the mechanism

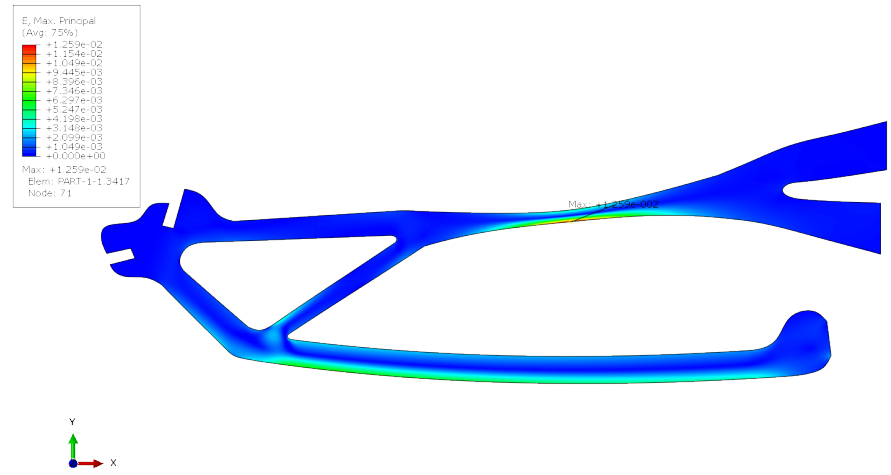


(b) Strain on the mechanism

Figure 5.3: Displacement and Strain on the mechanism due to the horizontal input.

These results are close to those obtained by (Radestock et al., 2015): 18.7 mm of vertical displacement and about 1% of strain (Figure 5.4), and the variation can be

explained by differences between the geometry of the mechanism studied by the cited authors and that used in this study: for example, the upper arm bifurcations are slightly longer than those from the 3D model obtained. Also, the uncertainty about the mechanical properties of the material have influence on these results. The boundary conditions prescribed also deserve a comment: in the *SolidWorks* model, the part is fixed used pins located at some distance from the upper arm bifurcation vertical edges. As explained in section 1.1, this can be though as a built-in joint. However, in the *Abaqus* model, the boundary conditions were prescribed for the vertical edges, moving the encastre to the left. This simplification may have affected the results, but it also may have reduced the differences on the mechanism geometry. Several attempts were performed, only to achieve minor variations. The best results are those presented. It can be said that these results validate the simulations performed.

The stress field was also studied (Figure 5.5). The maximum von Mises Stress was obtained in the flexure hinge, as expected, and its value was of 43.45 MPa, which is below the yield stress of PLA.

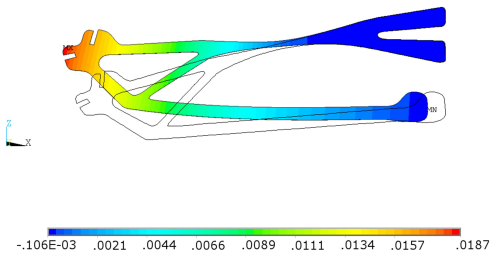


(a) Vertical displacement obtained by (Radestock et al., 2015).

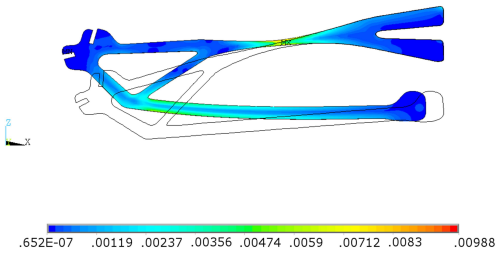


(b) Strain Field obtained by (Radestock et al., 2015)

Figure 5.4: Results obtained by (Radestock et al., 2015)

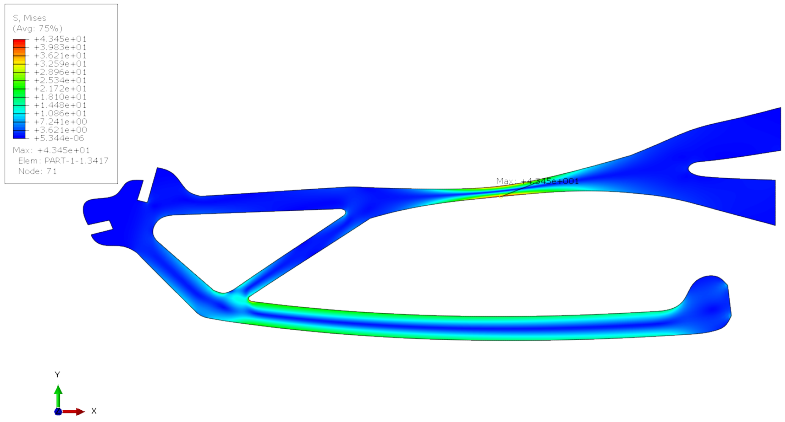

Figure 5.5: von Mises Stress field on the mechanism.

To access if the part had a linear behaviour, a step by step simulation was performed. With an imposed horizontal displacement varying from 0 to 7 mm with 1 mm steps, the maximum vertical displacement was measured and a plot drawn (Figure 5.6). It can be concluded that the part has a linear response to this imposed displacement. Also, it is concluded that the vertical displacement set as requirement by (Radestock et al., 2015) is achieved with a horizontal displacement input between 4 and 5 mm.

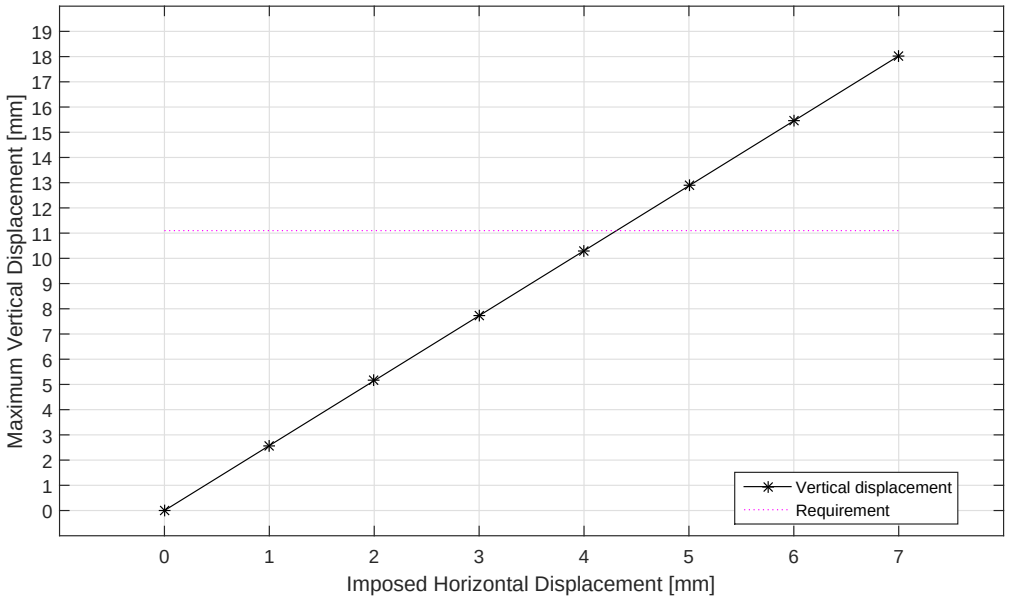


Figure 5.6: Maximum vertical displacement versus imposed horizontal displacement.

### 5.1.2 Actuation by servomotor

Secondly, the mechanism was simulated as being actuated by a servomotor, as depicted in Figure 9 of (Radestock et al., 2015). Since this image can be interpreted in many ways, 3 cases of connection between the mechanism and the servomotor rod: a connector (pin, bolt or similar) in both holes, or only on the top or bottom hole (Figure 5.7). It was simulated a rotation of the servomotor between -20° (drooping the leading edge) and 30° (lifting the leading edge).

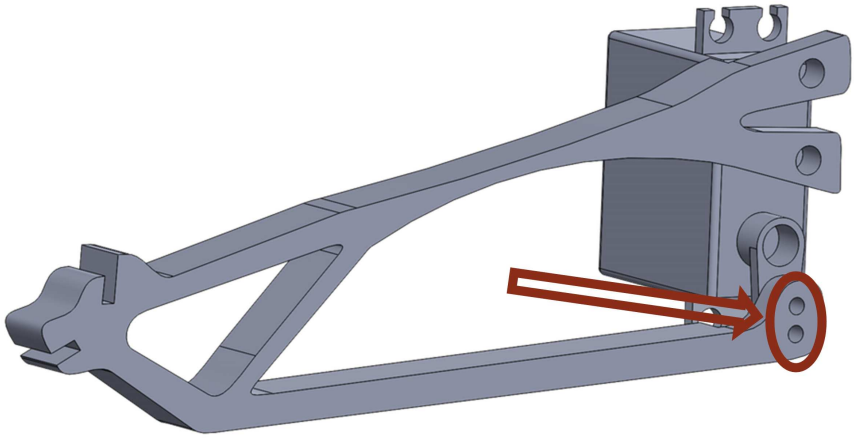

Figure 5.7: Connection between the servomotor and the mechanism.

To model the pivot point for the rotation and holes, the location of these was obtained from *SolidWorks*, and Reference Points were inserted on the Finite Element Model on these locations. Reference Point referring to the pivot point was connected to the others (upper, lower or both, depending on the case studied) using the *Abaqus "Tie"* constraint, creating a rigid link between them. The Reference Points concerning the holes were then tied to the nodes of the lower arm right end zone.

Due to the same differences about the geometry mentioned above, and to the process of relating coordinates from *SolidWorks* to *Abaqus*, some inaccuracy may arise between the results from this work and those of the consulted paper. However, this should not be of an order of magnitude that prevents comparisons to be done.

The first case imposes a rotation of the actuator connection and inferior arm. This yields the stress field below (Figure 5.8), plotted on the deformed shape of the part. The maximum von Mises stress value was of about 144 MPa, corresponding to approximately 4.2% of strain. This results mean that the part would break if subjected to such an

actuation in real life. Also, the obtained maximum displacement is not close to the expected. Therefore, it can be concluded that this is not the actuation method used by (Radestock et al., 2015).

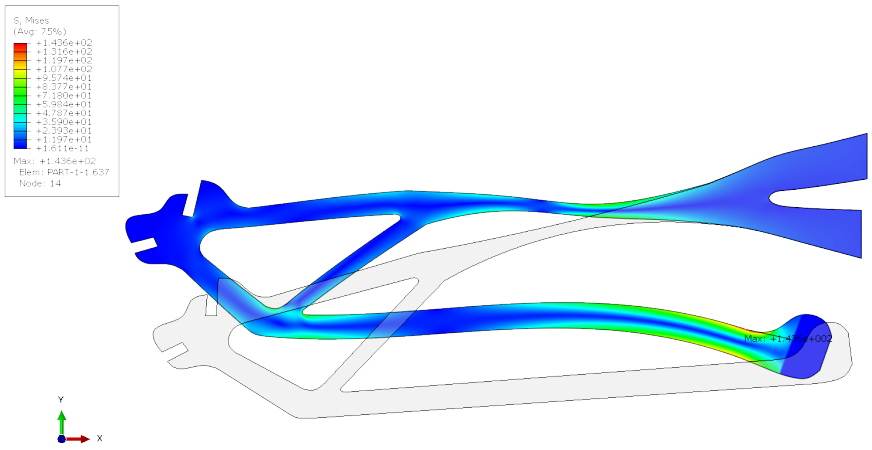


Figure 5.8: Stress field generated by the first load case, plotted over the deformed shape.

Next, a connection using only one pin in the bottom hole was simulated, which results in the deformation illustrated in Figure 5.9.

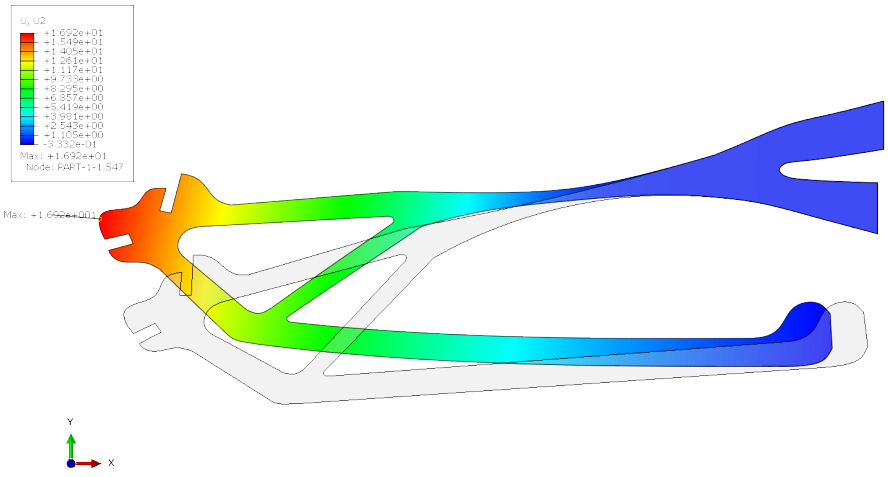


Figure 5.9: Vertical displacement generated by the second load case.

The maximum displacement was 16.9 mm on the stringer connection, corresponding to a 30° rotation of the servomotor. The most stressed zone of the part was the flexure hinge, with a maximum von Mises stress of 40.85 MPa and a corresponding strain of 1.18% (Figure 5.10).

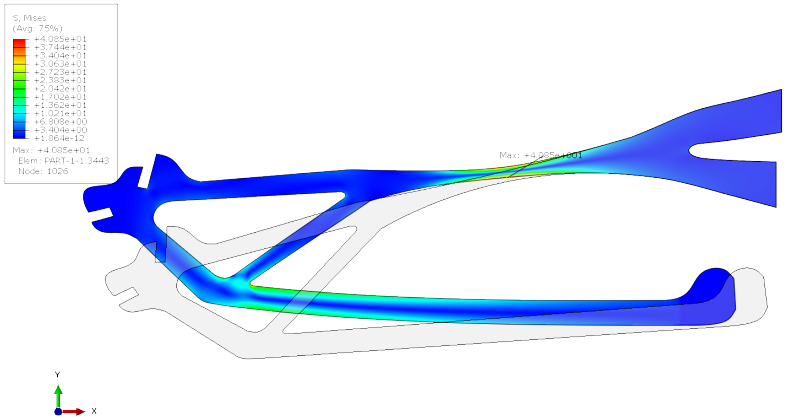

(a) Stress Field on the mechanism

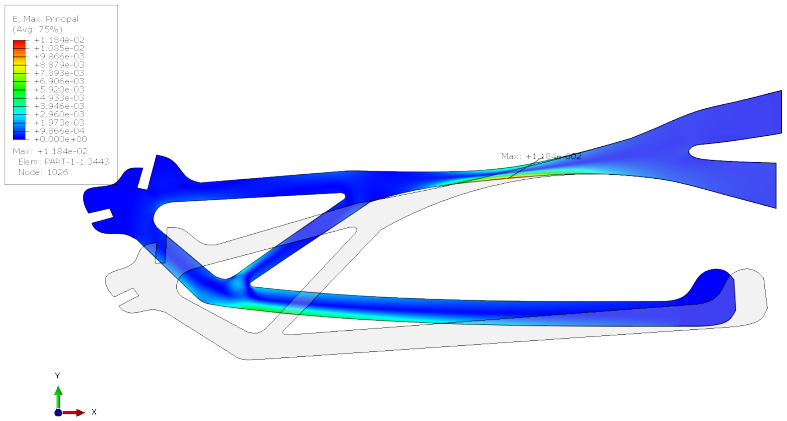

(b) Strain Field on the mechanism

Figure 5.10: Displacement and Strain on the mechanism due the second load case.

Although these results are within the mechanical limits of the material, they do not reflect those obtained in the paper consulted. Hence, the third case was studied, and the actuation of the part on the top hole was simulated. It was obtained a maximum vertical displacement of 11.7 mm when lifting the leading edge, and the required displacement of 11.1 mm was met between 25° and 30°. This is in accordance with what was obtained

by (Radestock et al., 2015), meaning that this is probably the actuation method use by those authors. The deformed shape of the part is illustrated on Figure 5.11, with the vertical displacement plotted in colour map.

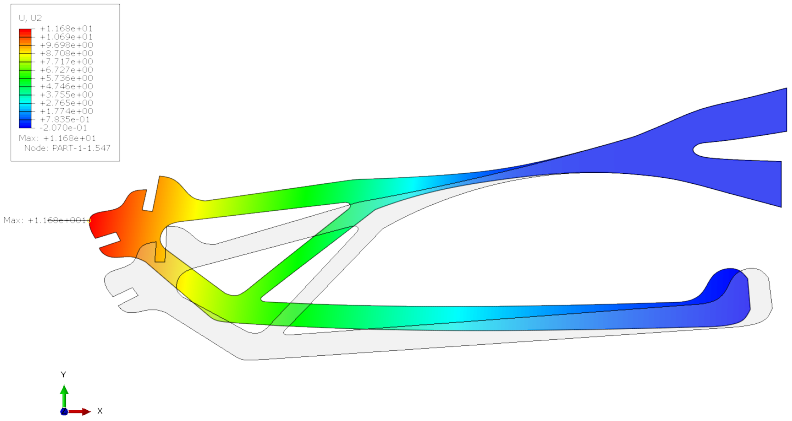

Figure 5.11: Vertical displacement generated by the third load case.

In order to compare the second and third cases, a plot of the vertical displacement versus the actuator angular position is given in Figure 5.12.

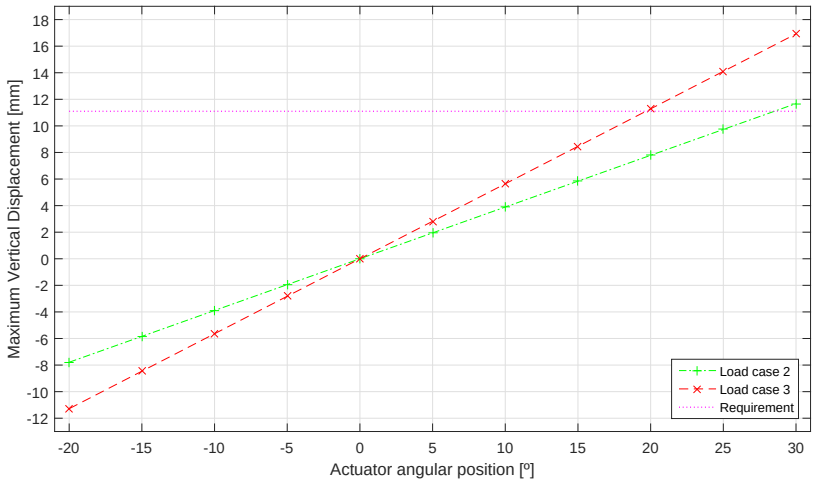


Figure 5.12: Vertical displacement vs. actuator angular position, for the second and third cases.

It was also concluded that this case yields a less intense stress field on the part. The maximum von Mises stress is 28.08 MPa, corresponding to 0.81% of strain on the flexure hinge. Figures 5.13 (a) and (b) show the results of the simulation.

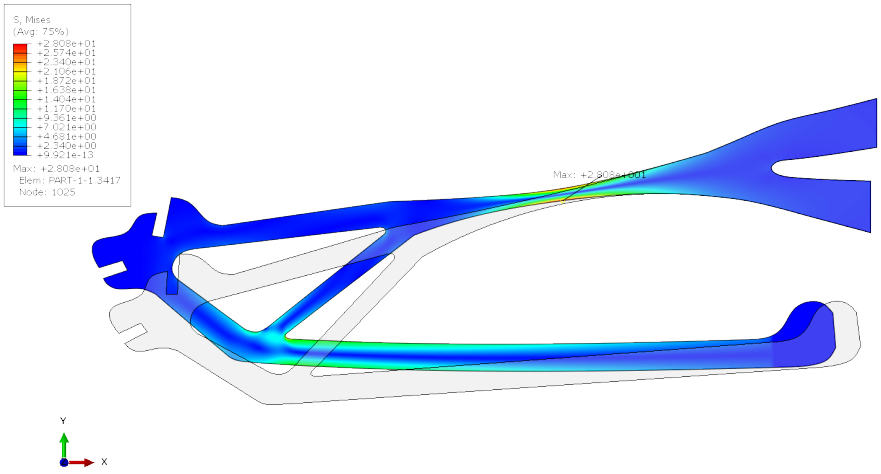


(a) Stress Field on the mechanism

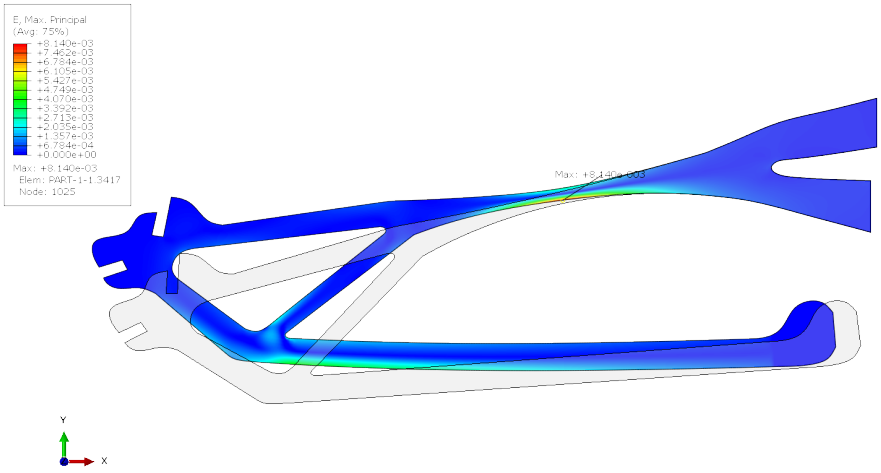


(b) Strain Field on the mechanism

Figure 5.13: Stress and Strain on the mechanism due the third load case.

Due to the uncertainty about the actuation method used by (Radestock et al., 2015), as well as that concerning the Reference Points, it was chosen to use as input a horizontal

displacement, as in section 5.1.1 for the remainder of the work (except where stated otherwise). Also, a plot of the trajectory of the point with higher vertical displacement ("Point M"), until the requirement is met, shows that the two actuations are similar (Figure 5.14).

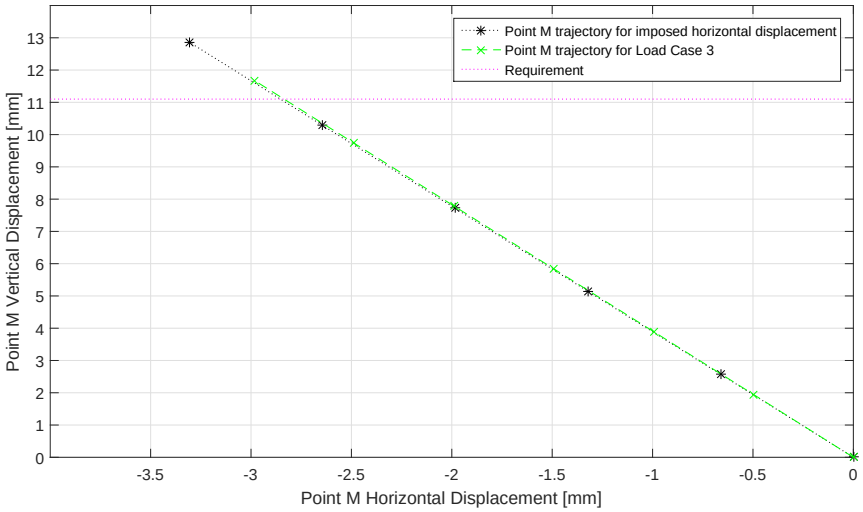


Figure 5.14: Trajectory comparison for Point M.

## 5.2 Analysis of the mechanism while actuating the skin

While benchmarking was important to understand if the work being done was in accordance with that used as a guideline, it did not took in account the outer skin that gives the shape to the airfoil. Therefore, simulations were run to access the effect of the skin rigidity on the behaviour of the mechanism.

Further details concerning the modelling will be given later. However, it is important to mention the parameters used for the skin simulation, table 5.4.

Table 5.4: Material properties of the skin.

| Material | Aluminium |
|---|---|
| Young Modulus | 70000 MPa |
| Poisson Ratio | 0.3 |
| Thickness | 0.5 mm |

For this simulation, 8-node quadratic shell elements with reduced integration (S8R) were used for both skin and actuator. The mesh depicted on Figure 5.2 for the mechanism was retained.

It was determined (Figure 5.6) that the required vertical displacement was obtained with an actuation between 4 and 5 mm. Therefore, two simulations were ran: the first with an input of 7 mm, to act as a comparison with the results obtained in the previous sections, and the second with an input of 5 mm.

### 5.2.1 7 mm horizontal input

Figure 5.15 represents the deformed shape of the assembly in the first case. These results cannot be considered realistic if one takes into consideration the interference between the skin and the lower arm of the mechanism. However, they are only meant to assess the influence of the skin rigidity on the mechanism, and for that purpose they are perfectly acceptable.

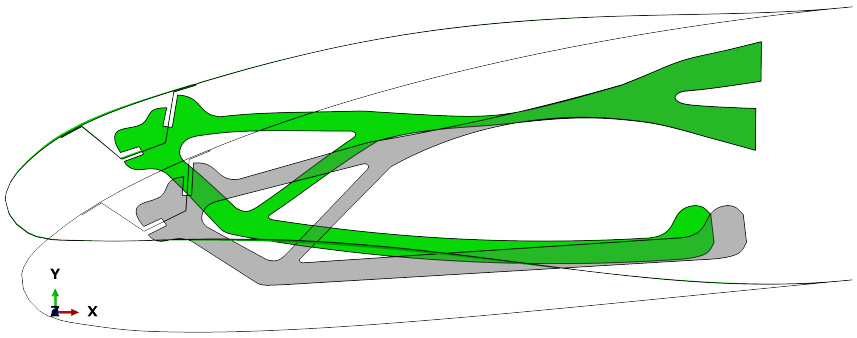


Figure 5.15: Assembly's deformed and undeformed shapes comparison, 7 mm horizontal input.

The influence of the shell rigidity is reflected on the results. For an input of 7 mm, the maximum vertical displacement was of about 16.1 mm, which is 1.9 mm less than without the skin. Figure 5.16 shows the vertical displacement field, plotted over the deformed shape of the mechanism.

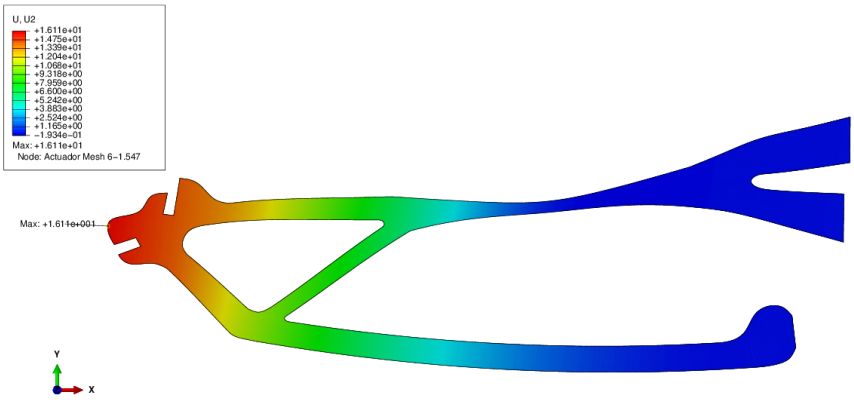


Figure 5.16: Vertical displacement of the mechanism due to the 7 mm horizontal input.

Also, the Strain and Stress levels are, as expected, influenced by the presence of the skin, with an increase on their maximum values. However, besides the increase due to the rigidity of the shell, some local stress concentrations are found. These are due not only to the geometry of the part, but also to the modelling of the connections between the mechanism and the skin stringer. This was achieved with ties between the nodes of

the surfaces where the parts were considered to make contact. Therefore, this creates some artificial stress concentrations, illustrated on Figure 5.17 (note the edges of the connection slots).

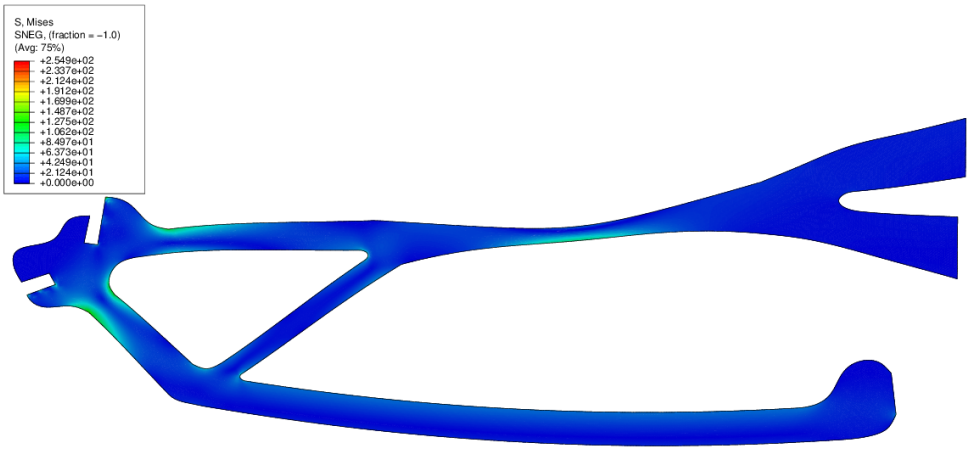


(a) Stress Field on the mechanism

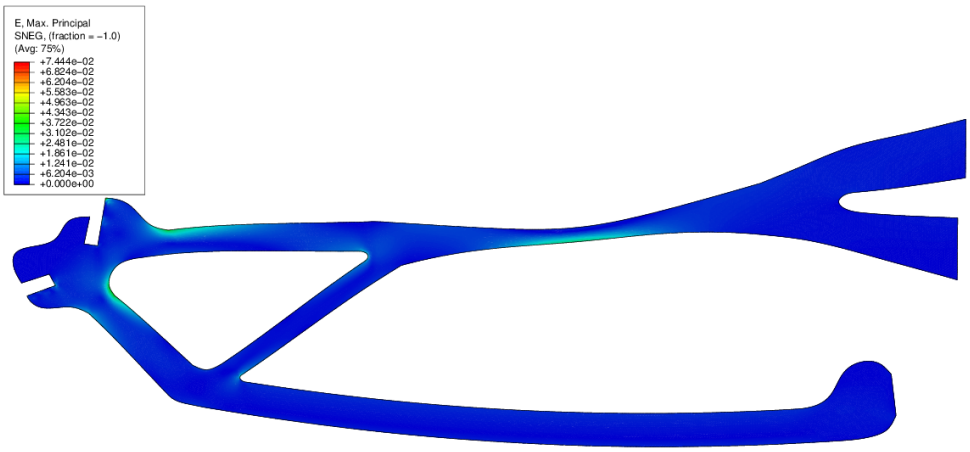


(b) Strain Field on the mechanism

Figure 5.17: Stress and Strain on the mechanism due the 7 mm horizontal input.

To achieve a better comparison, the flexure hinge zone was isolated, Figure 5.18. The maximum von Mises stress of 92.4 MPa and a corresponding Strain of 2.68%.

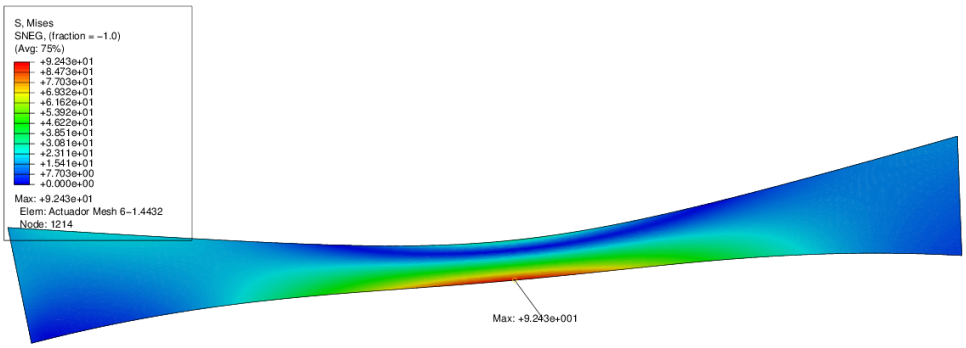


(a) Stress Field on the flexure hinge

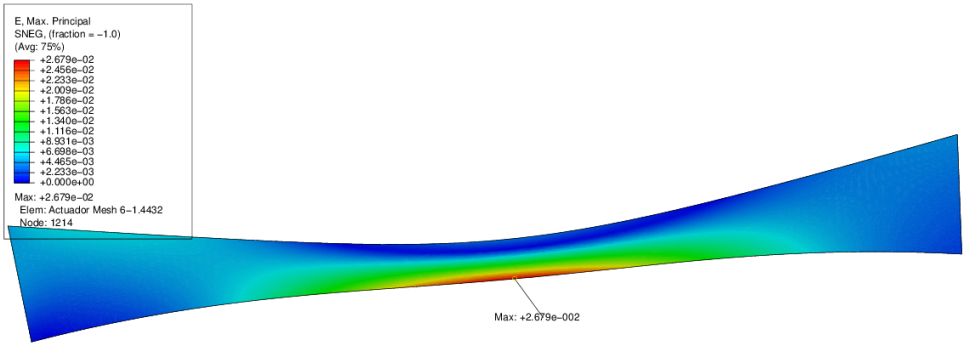


(b) Strain Field on the flexure hinge

Figure 5.18: Stress and Strain on the flexure hinge due the 7 mm horizontal input.

Table 5.5 illustrates the differences between results without and with skin. The percentage difference was calculated using the following formula:

$$\%\,difference = \frac{Parameter_{with\,skin} - Parameter_{without\,skin}}{Parameter_{without\,skin}} \times 100$$

Table 5.5: Influence of the skin on the behaviour of the mechanism for a 7 mm horizontal input.

| Parameter | Without Skin | With Skin | % Difference |
|---|---|---|---|
| $U_2^{max}$[mm] | 18.01 | 16.1 | -11.8 % |
| $\sigma_{Mises}^{max}$[MPa] | 43.5 | 92.4 | 52.9 % |
| $\epsilon_{principal}^{max}$ | 1.26% | 2.68% | 53.0% |

It should be noted that, even not taking into account the stress concentrations, the maximum von Mises stress exceeds the material's Tensile and Yield Strengths, meaning the failure of the mechanism. However, before further considerations are made, let us analyse the results of 5 mm input.

### 5.2.2 5 mm horizontal input

In the second case there is not interference between the mechanism and the skin, meaning that the results for this simulation are realistic and completely acceptable. The deformed shape of assembly is depicted on Figure 5.19.

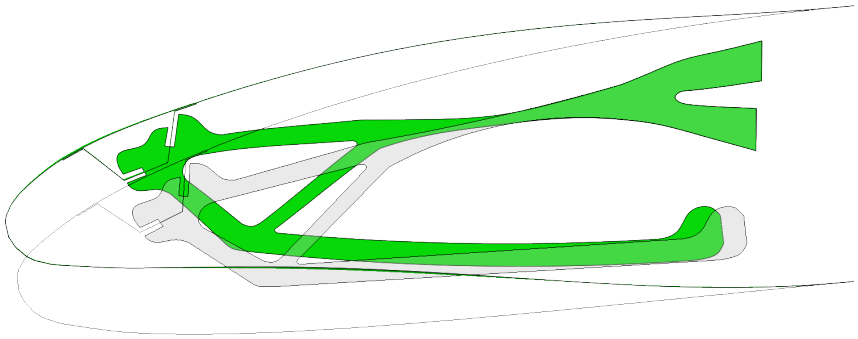

Figure 5.19: Assembly's deformed and undeformed shapes comparison, 5 mm horizontal input.

The maximum vertical displacement was of about 11.5 mm, meaning that the 5 mm input is the correct option to achieve the vertical displacement intended by (Radestock et al., 2015). Figure 5.20 shows the vertical displacement field, plotted over the deformed shape of the mechanism.

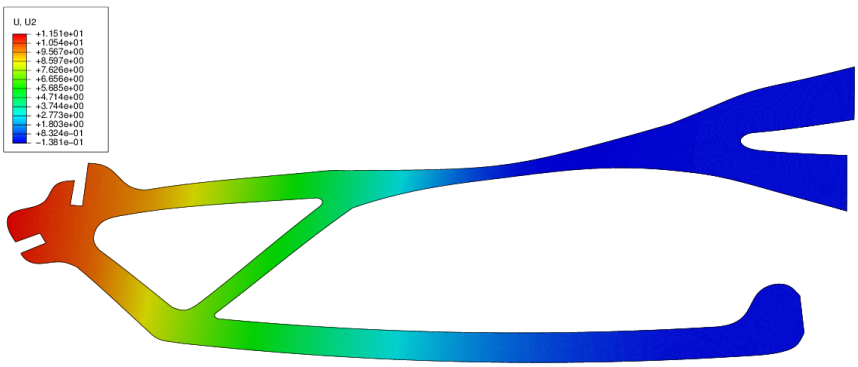


Figure 5.20: Vertical displacement of the mechanism due to the 5 mm horizontal input

As in the previous section, stress concentrations were found in several locations of the mechanism. Figure 5.21 shows the von Mises Stress field and the Strain field.

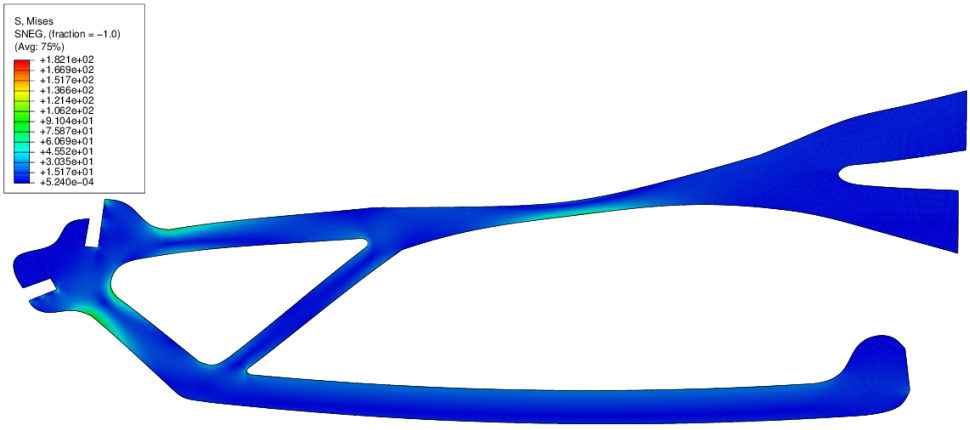


(a) Stress Field on the mechanism

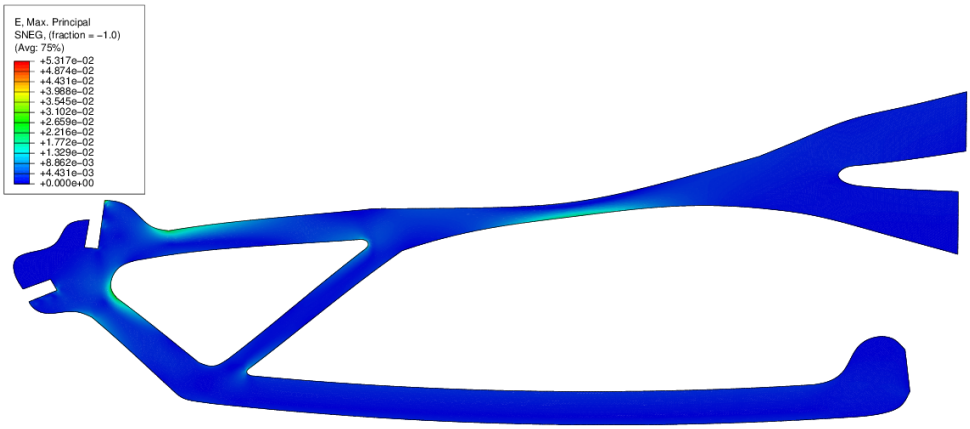


(b) Strain Field on the mechanism

Figure 5.21: Stress and Strain on the mechanism due the 7 mm horizontal input.

Again, the flexure hinge was zoomed, and the maximum von Mises stress of 66.0 MPa was observed, corresponding to a Strain of 1.91% (Figure 5.22).

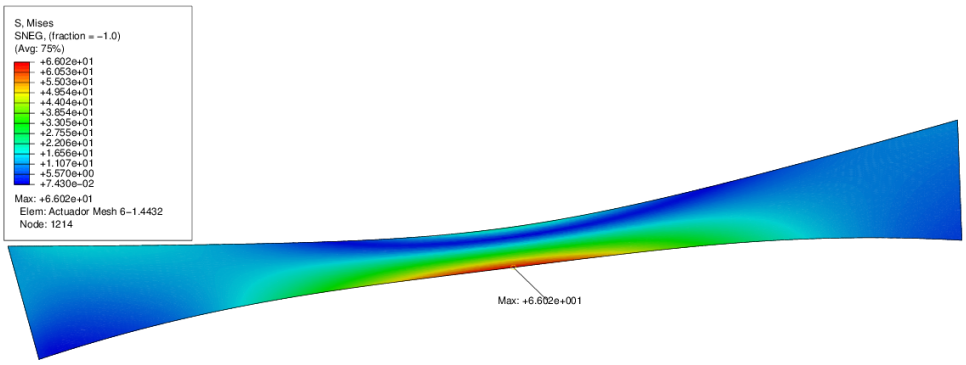


(a) Stress Field on the flexure hinge

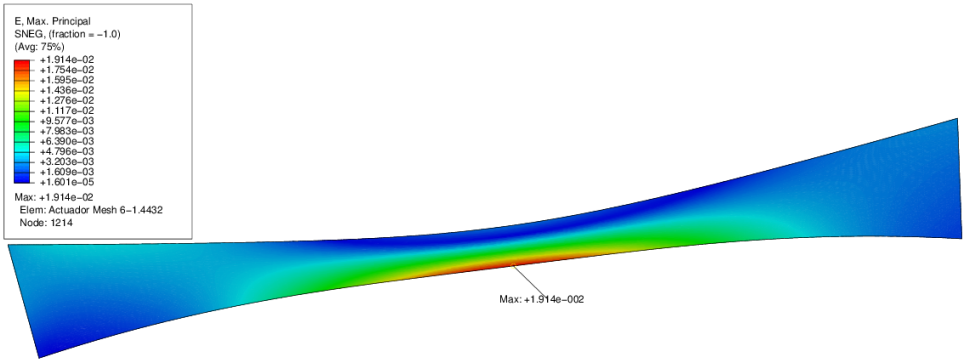


(b) Strain Field on the flexure hinge

Figure 5.22: Stress and Strain on the flexure hinge due the 5 mm horizontal input.

Excluding the stress concentrations, and recalling, from Table 5.1, the Yield Strength of PLA (47-70 MPa), it can be affirmed that this stress field does not necessarily mean the failure of the mechanism. However, this statement can be disputed taking into consideration the values given by (Mathew et al., 2005) for the Yield Strength, ranging from 38.2 to 49.6 MPa. These values also come along with Young Modulus ranging from 3.6 to 6.3 GPa, meaning that stiffness is also affected by the material composition, and that can yield even higher stresses.

Nevertheless, consulting more recent sources, higher values for Tensile Strength (which should also mean superior Yield Strength) are found. (Faruk et al., 2014) report Tensile

Strengths up to 95 MPa to PLA reinforced with man-made cellulose, and (Pickering et al., 2016) give examples of Tensile Strengths of 101 MPa and even 223 MPa, for PLA reinforced with natural fibres. Bearing in mind this data, it can be concluded that PLA may be a suitable material for this mechanism. Therefore, with some redesign addressing stress concentration, the structural integrity should not be a problem.

To complete this analysis, a step by step simulation was performed, with inputs from 0 to 7 mm, and the maximum vertical displacement was registered. It was concluded that, although the presence of skin reduced the vertical displacement for each input, the behaviour of the mechanism was still linear. To compare both situations, the results of these simulations were added to the graphic of Figure 5.6, resulting on Figure 5.23.

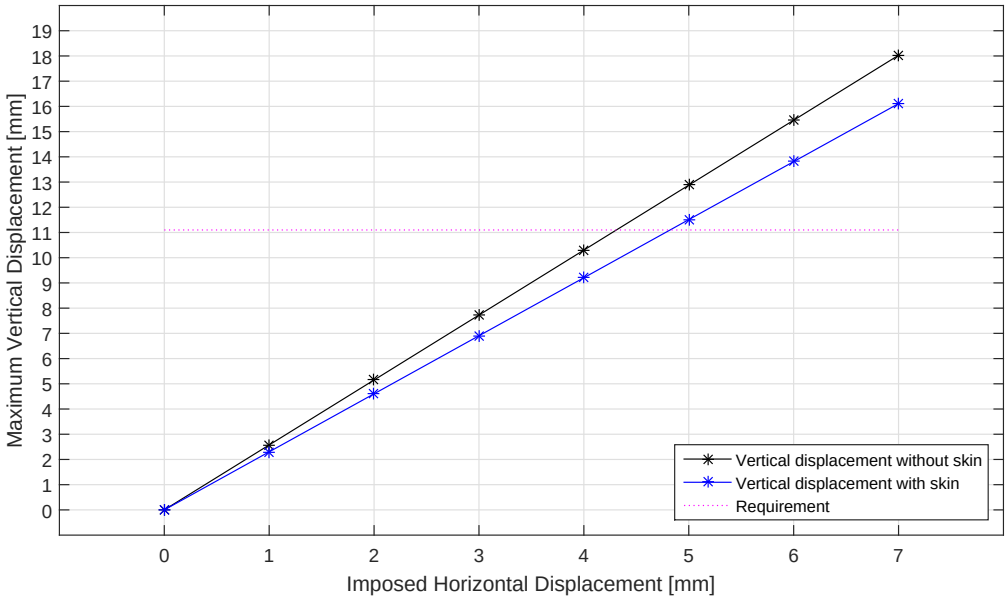


Figure 5.23: Maximum vertical displacement versus imposed horizontal displacement.

## 5.3 Study of the mechanism in Aluminium

PLA is not a traditional material in the aeronautical industry. Also, as it was briefed discussed on section 5.2.2, its properties are quite variable in function of, for instance, the type and quality of the fibres used on the reinforcement or the manufacture process used (Pickering et al., 2016; Faruk et al., 2014). Consequently, it may be suitable for building a quick prototype, but it is not the best choice for a generalized used.

On the other hand, Aluminium alloys are one of the most common materials in aeronautics. Therefore, the possibility of building the compliant mechanism in Aluminium alloy was considered and studied. The material properties were those of 5.4.

### 5.3.1 Horizontal Displacement

Firstly, the mechanism was studied without the skin and using an 7 mm horizontal displacement input, as done on section 5.1.1 for PLA. The mesh used was Mesh number 6, and Figure 5.24 shows vertical displacement field plotted over the deformed shape, with the original shape in grey.

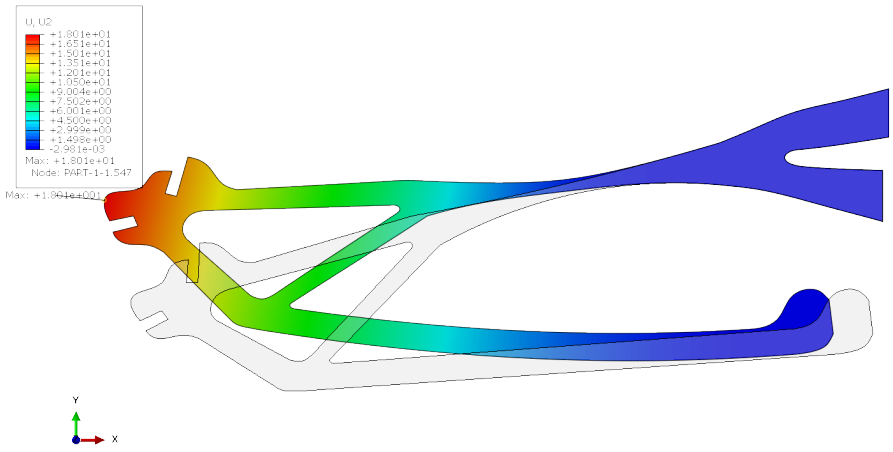


Figure 5.24: Vertical displacement of the Aluminium alloy mechanism for a 7 mm horizontal input.

The maximum value of the displacement was of 18.0 mm, just as that of PLA. At first this may seem incorrect, since Aluminium is much more rigid than PLA, but one must not forget that the input is a displacement and not a force. Also, plasticity was not considered in this model, since it was of no interest to have plastic regions on the mechanism. Therefore, it is expectable to have the same displacement for both materials.

The same is not valid in terms of Stress and Strain Fields (Figure 5.25). For the mechanism in Aluminium, the maximum von Mises Stress was found to be 886.3 MPa

with a corresponding maximum Strain of 1.27%, This level of Stress is unacceptable, meaning that the part would break long before reaching this deformed shape, or, if high strength Aluminium was to be used, Fatigue problems would soon appear.

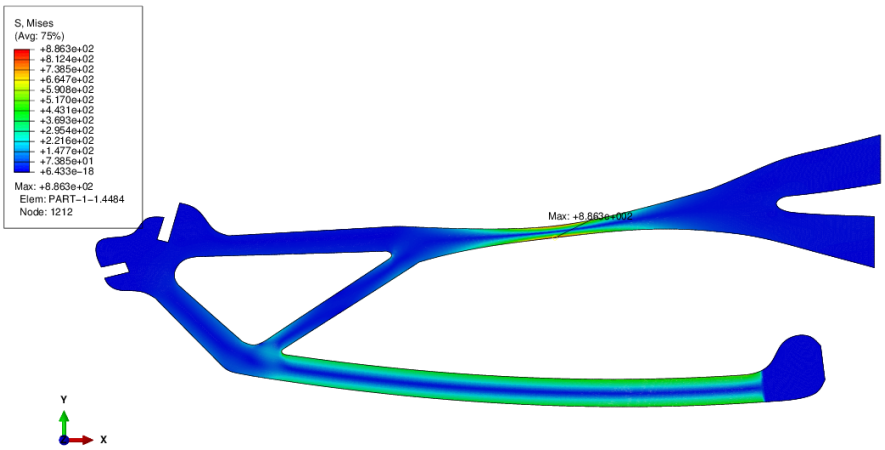


(a) Stress Field on the Aluminium mechanism

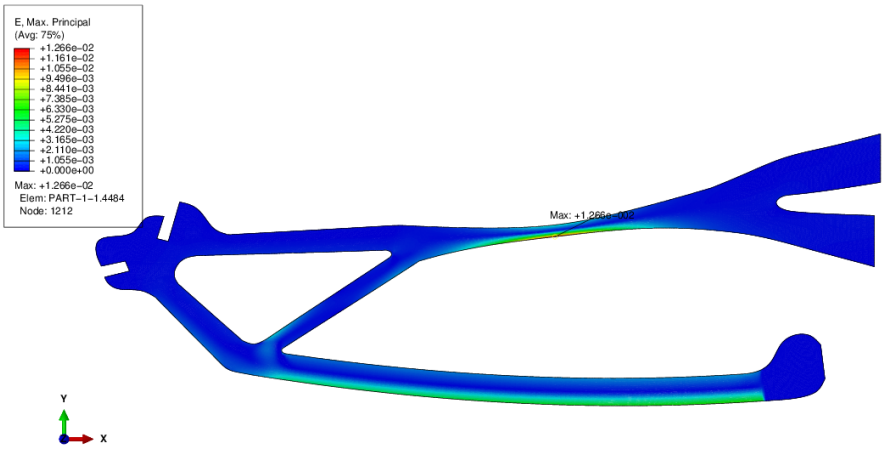


(b) Strain Field on the Aluminium mechanism

Figure 5.25: Stress and Strain on the Aluminium alloy mechanism due the 7 mm horizontal input.

Given that the necessary horizontal input to achieve the target vertical displacement is 5 mm, this situation was simulated. The results were again unsatisfactory: a maximum von Mises Stress of 633.0 MPa (Figure 6.6).

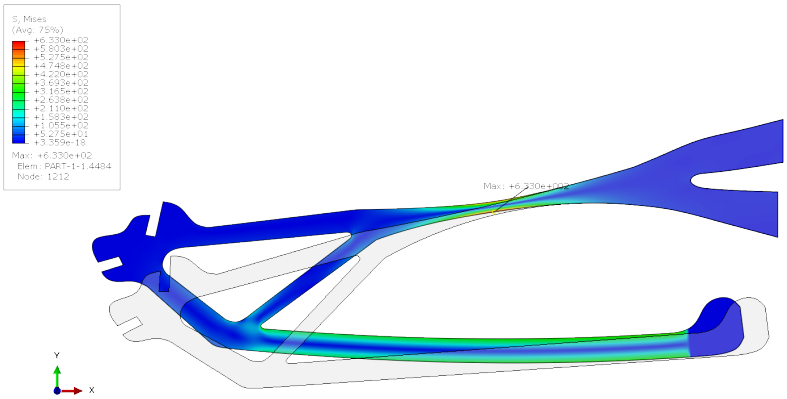

Figure 5.26: von Mises Stress field in the Aluminium alloy mechanism for a 5 mm horizontal input.

The results of these two simulations are clear and show that this design is unsuitable to be materialized in Aluminium. However, a final tentative was made, simulating the actuation of the servomotor, as it was concluded that it yielded less intense Stress fields (end of section 5.1.2).

### 5.3.2 Actuation by servomotor

A simulation was run considering the last load case studied on section 5.1.2: connection on the top hole. For a 30° rotation of the servomotor, which gave the required vertical Displacement, the maximum von Mises Stress was 569.8 MPa (Figure 5.27).

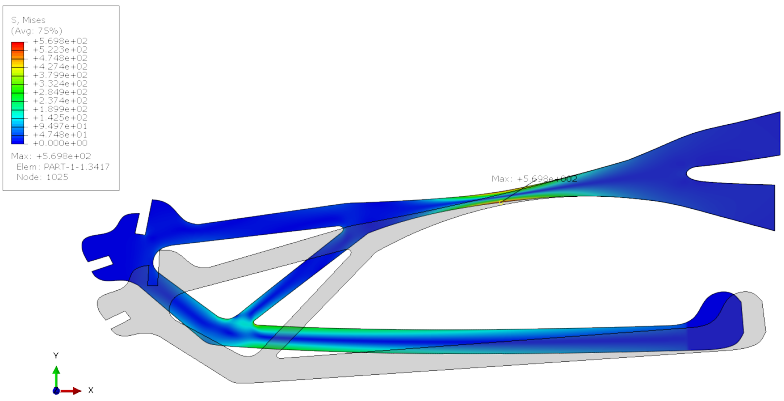

Figure 5.27: Stress Field on the Aluminium alloy mechanism for a 30° servomotor rotation.

Although this value is about 10% less than that obtained due to the 5 mm horizontal Displacement, it still is very high for an Aluminium alloy, especially considering that this a part that will endure load cycles leading to serious fatigue problems. Therefore, if the part is to be made of Aluminium, a redesign is needed.

### 5.3.3 Redesign attempts

The process of adapting the mechanism to Aluminium is an optimization problem which, itself, could be the subject of a Master Thesis. Therefore, and since this was not the aim of the present Thesis, only some attempts, on the trial-and-error basis, were made, and the designs presented do not intend to be a final solution, but suggestions to a possible future assessment of the mechanism.

Despite being a trial-and-error process, it was not a random one, but based in some considerations. To decrease the total stiffness of the mechanism, the thickness (dimension perpendicular to the paper) was reduced by 60%, to 4 mm. However, the effect of this change was not significant. Also, the stiffness of the flexure hinge was reduced, by reducing the width (in-plane "vertical" direction) of the rectangular section of that zone. Other strategies were followed, such as changing the length of the flexure zone to have a more distributed Stress field, or shortening the distance between flexure hinge and the lower arm in order to reduce the bending moment applied on the upper arm. The general size and main features of the original design were preserved as far as possible.

The different designs were discretized in 3D to have a better perception of the effect of thickness. 20-node, quadratic brick elements with reduced integration were used (C3D20R). Meshes were not structured since this process, being time-consuming, did not bring tangible differences on the results (refer to table 5.3). The results of the different design iterations are represented in Figures 5.28 to 5.37, where the von Mises Stress fields are plotted over the deformed shape. Figure 5.28 represents the original design, but with 4 mm thickness. The Figures after represent the following redesigns, bearing in mind the considerations mentioned above. The actuation was a rotation of the servomotor linked to the top pin. The rotation was adjusted case to case, starting on the sixth redesign.

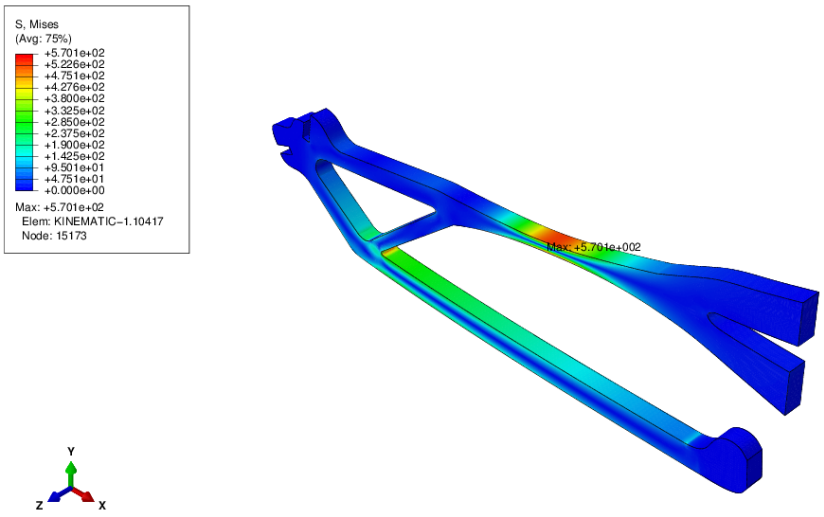


Figure 5.28: von Mises Stress field on the mechanism. Original shape with 4 mm thickness.

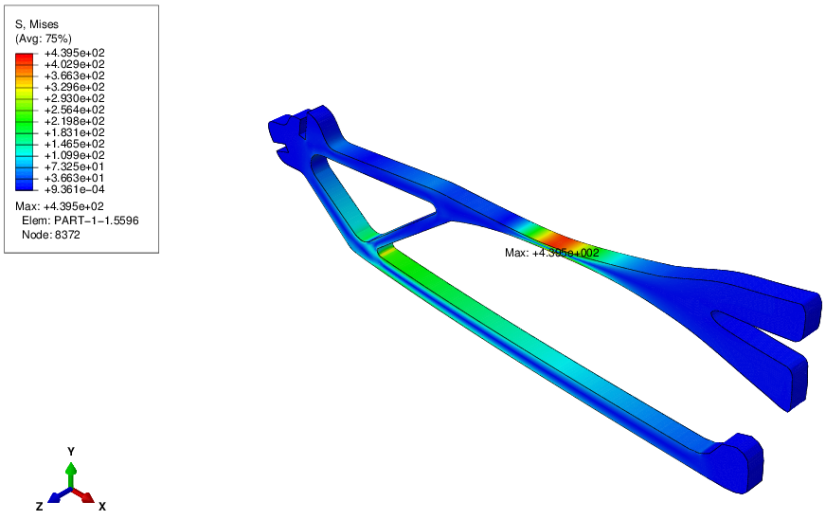


Figure 5.29: von Mises Stress field on the mechanism. First redesign.

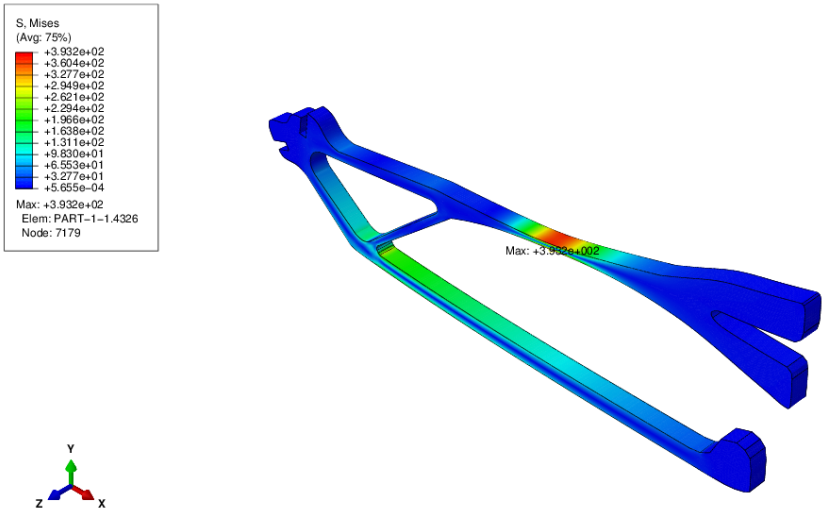


Figure 5.30: von Mises Stress field on the mechanism. Second redesign.

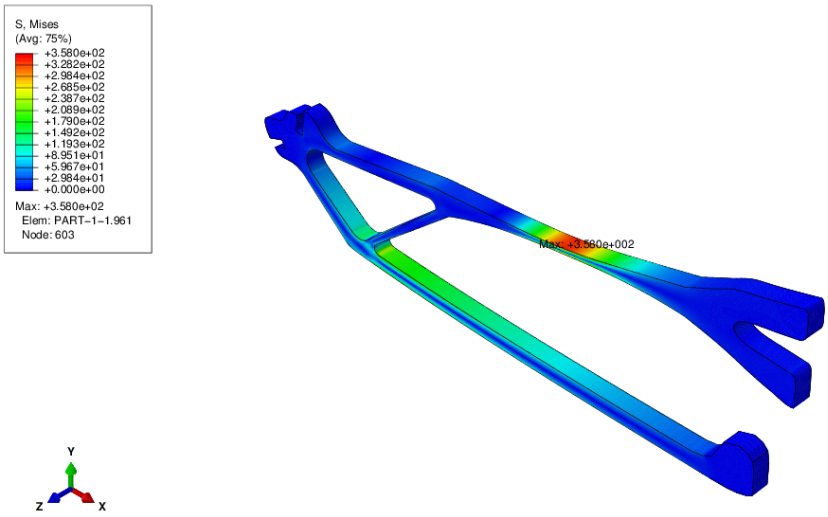


Figure 5.31: von Mises Stress field on the mechanism. Third redesign.

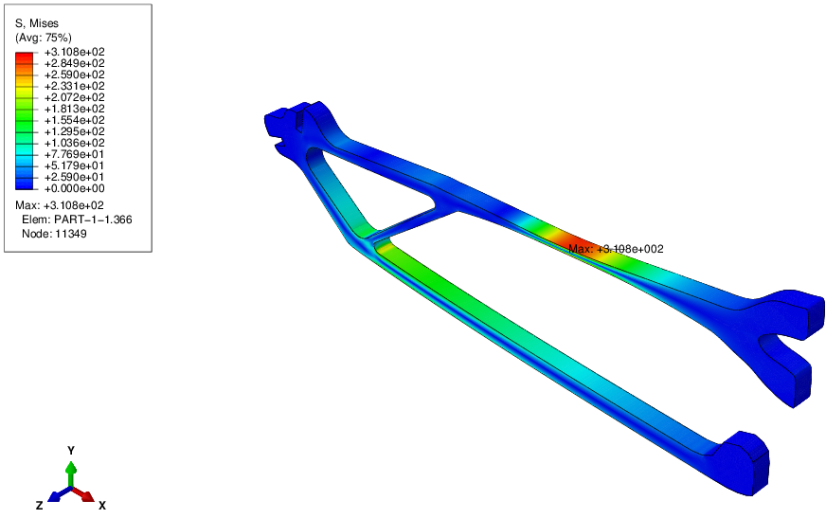


Figure 5.32: von Mises Stress field on the mechanism. Fourth redesign.

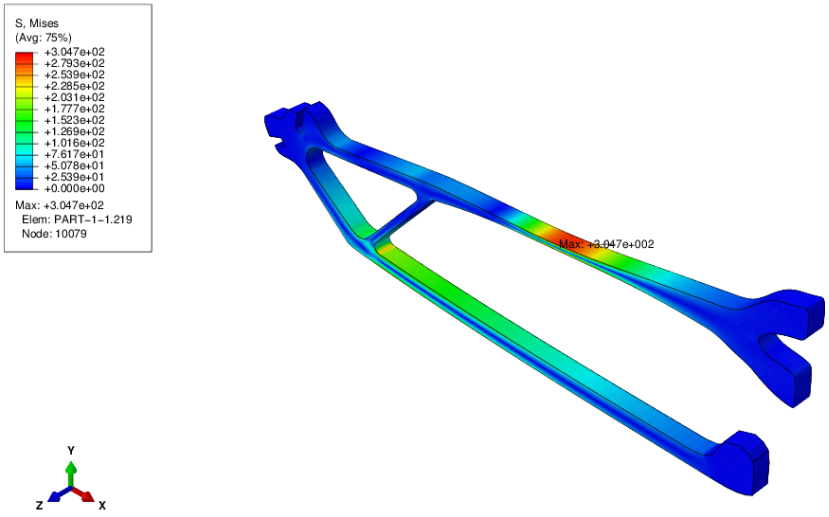


Figure 5.33: von Mises Stress field on the mechanism. Fifth redesign.

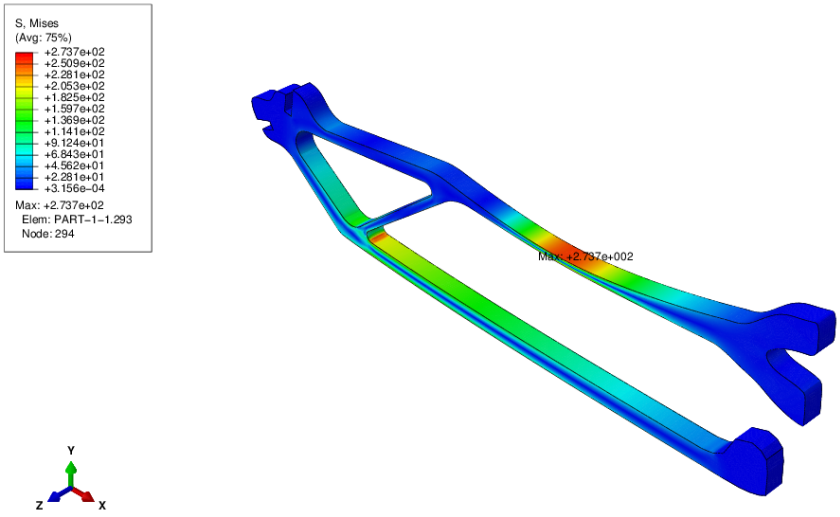


Figure 5.34: von Mises Stress field on the mechanism. Sixth redesign.

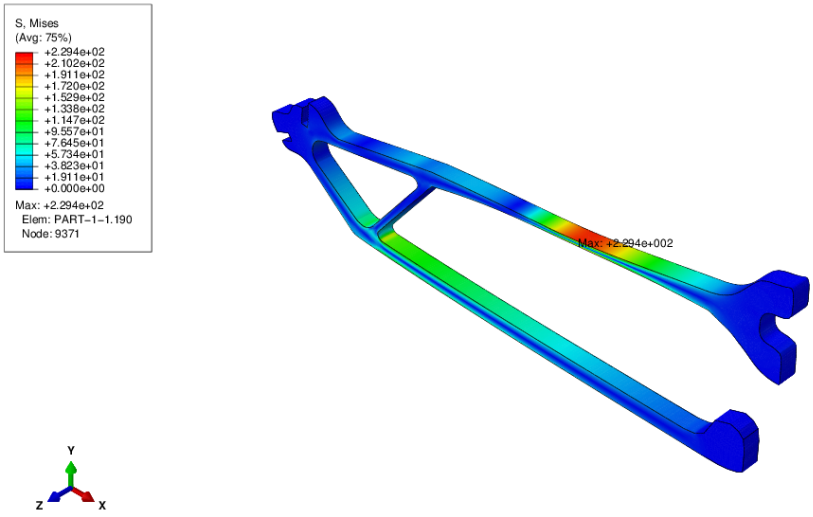


Figure 5.35: von Mises Stress field on the mechanism. Seventh redesign.

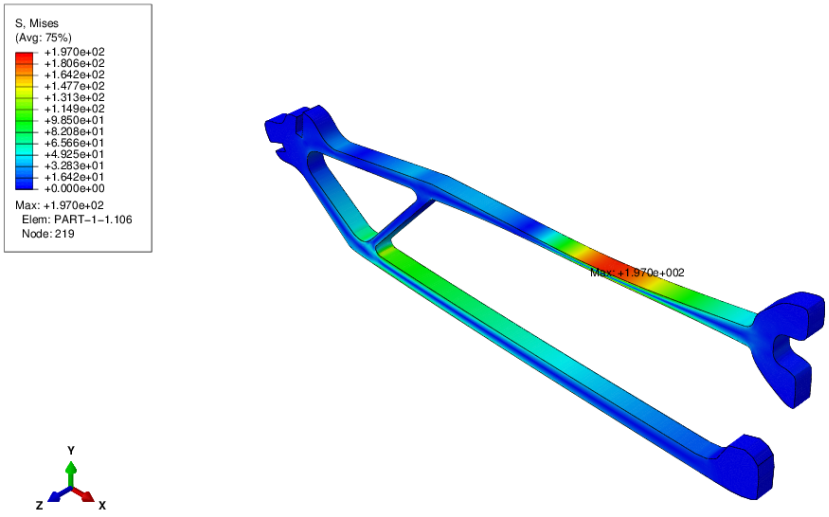


Figure 5.36: von Mises Stress field on the mechanism. Eighth redesign.

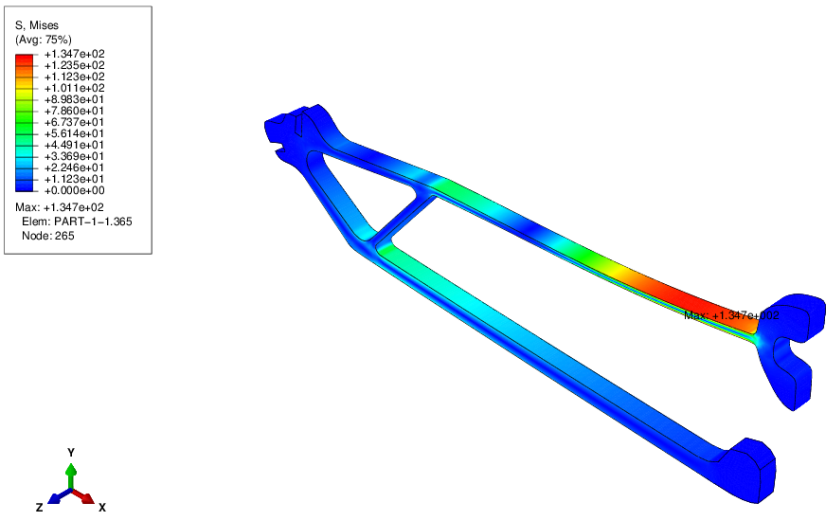


Figure 5.37: von Mises Stress field on the mechanism. Final redesign.

The evolution of the results is summed up in Table 5.6.

Table 5.6: Results of the different redesigns.

| Design | Rotation [°] | $U_2^{max}$[mm] | $\sigma_{Mises}^{max}$[MPa] |
|---|---|---|---|
| Original (4 mm) | 30 | 11.7 | 570.1 |
| 1 | 30 | 11.8 | 439.5 |
| 2 | 30 | 11.7 | 393.2 |
| 3 | 30 | 12.1 | 358.0 |
| 4 | 30 | 12.4 | 310.8 |
| 5 | 30 | 12.3 | 304.7 |
| 6 | 25 | 12.4 | 273.7 |
| 7 | 25 | 11.7 | 229.4 |
| 8 | 22.5 | 11.1 | 197.0 |
| 9 | 20 | 11.6 | 134.7 |

The results show that the Stress levels on the mechanism were significantly lowered. Decreases of 65.4%, if the eight iteration is considered, and 76.4%, considering the final iteration, were achieved. The last solution presented, with a maximum von Mises Stress of about 135 MPa, while not yet within the fatigue limits[b] for most Aluminium alloys, indicates a possible way to achieve stress level below that limit. However, it is a radical solution, where the maximum Stress is located very close to the fastening points and is there is not a real distinction between the flexure hinge and the rest of the upper arm. Nevertheless, and given the constraints to this process, this design proves that the strategy proposed to achieve a practical mechanism built using an Aluminium alloy is valid.

Since this redesign is just a concept, and to follow closely the guidelines adopted for this project, the PLA original actuator will be used from now on.

[b] By fatigue limit, the author means a stress level that yields a fatigue life between $10^6$ and $10^7$ cycles. Aluminium alloys do not present the same fatigue behaviour of steels, for instance, for which a fatigue limit is clearly identifiable.

# Chapter 6

# Modelling of the Leading Edge

In this Chapter, the process of creating several Finite Element models of the Leading Edge will be reported. The different discretizations will be explained and compared. Also, comparisons will be made concerning the achieved morphed shape, in comparison with the theoretical goal, and the influence of the different skin thicknesses will be assessed.

## 6.1 Modelling using Shell Elements

The first models were created using Shell elements. From a computational point of view, Shell elements are a relatively inexpensive form of modelling, and served the purpose of comparing the achieved morphed form with the desired one. Also, shell based parts are easier to create, as the user is only required to define the top, middle or bottom surfaces, and the part's thickness.

The skin was modelled after the 3D model obtained, extracting the middle surface line from *SolidWorks* and creating a corresponding sketch on *Abaqus*. This sketch was used to create a Shell based part, by extruding it perpendicularly to the sketch plan. The same was done for the Stringer, the Compliant Mechanism being already modelled.

### 6.1.1 Modelling of the Stringer and its connections

The Stringer is the part providing connection between the actuation mechanisms and the skin. It transmits to the skin the displacements from the mechanisms, located at a distance of 220 mm on the Z axis from the ends of the model. Also, it ensures that this distribution is even, preventing to some extent, torsion on the Z axis and bending about the X and Y axis, due to its stiffness.

The Stringer was firstly modelled as rigid part, a feature provided by *Abaqus*. Using this makes part that much stiffer than the rest of the model, thus neglecting its deformation. However, since one of the aims of this work is to assess the feasibility of the concept in Aluminium, and as the thicknesses of the skin and the stringer (as present on the *SolidWorks* model) were similar, this approach was discarded. Therefore, the stringer was modelled with generic Aluminium alloy properties (table 6.1).

Table 6.1: Material properties of the skin.

| Material | Aluminium |
|---|---|
| Young Modulus | 70000 MPa |
| Poisson Ratio | 0.3 |

As mentioned on Section 1.1, reinforcement plates were present in the faces that contact with the actuation mechanism. These plates had 1 mm thickness, whereas the stringer had 0.5 mm thickness. The part was modelled as one, and to accommodate the difference, the part was partitioned, and the corresponding thickness was assigned to each partition according to its position (0.5 mm for unreinforced, and 1.5 mm for reinforced).

The connection between the stringer and its adjacent part was not described on the paper used as guideline (Radestock et al., 2015). Contacts were made with Dr. Martin Radestock, who kindly informed that he had modelled the connection between the skin model and the compliant mechanism using two beam elements, extremely stiffer than the skin or the mechanism, and key-points from skin and mechanism near to each other. Concerning the doubts on the existence of any gap between the stringer and the compliant mechanism, Dr. Radestock informed that no gap existed between stringer and mechanism.

Based on this information, the connections between Stringer and both the Compliant mechanism and the skin were modelled using the *"Tie"* constraint. This created a rigid link between the nodes of the locations where the connection was considered to happen. To define these locations, partitions were used both on the stringer and the skin.

Figure 6.1 shows the location of the tie constraints (Yellow circles), and the section assignments:

- Grey for Mechanism in PLA, t=10 mm;
- Blue for reinforced Stringer in Aluminium alloy, t=1.5 mm;
- Red for Stringer in Aluminium alloy, t=0.5 mm;
- Green for Skin (will be addressed later);

The rest of the skin was omitted for clarity. Note that, although gaps seem to exist between the stringer and the connection slots on the compliant mechanism, only the middle surface of each section is plotted. Moreover, bearing in mind the constraints imposed, the existence of those gaps and, for that matter, the penetration of the stringer by the mechanism, only exists visually, and not present on the model. The only concern here is to correctly place the different parts, which was done in close observance of the *SolidWorks* 3D model.

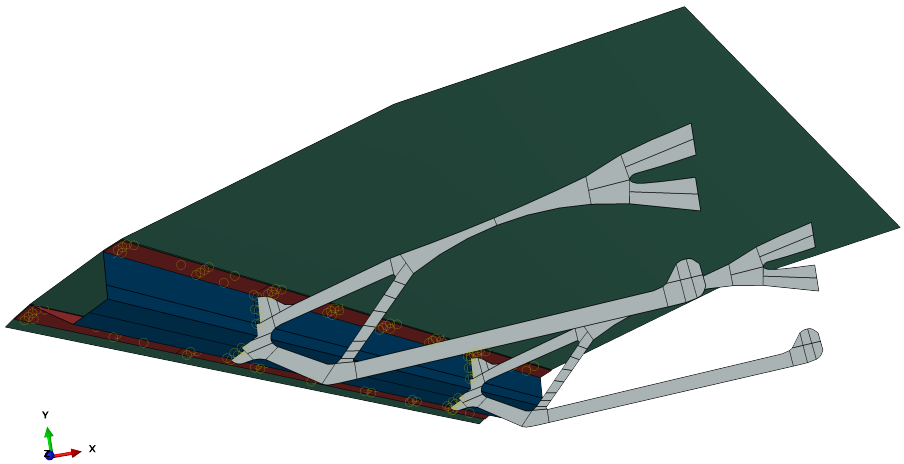

Figure 6.1: Location of the tie constraints and section assignments.

To understand the mesh effect on the Stringer, a brief study was conducted. The main aim was to understand the effect of mesh refinement on the displacements, since these affect the skin. For both 4-noded linear (S4R) and 8-noded quadratic (S8R) shell elements with reduced integration, a coarse and a rather fine mesh were used. Reduced integration was used, and the a 5 mm horizontal displacement was simulated.

The resultant Displacement $U_{resultant} = \sqrt{U_1^2 + U_2^2}$ and the maximum von Mises Stress were recorded. In the finer meshes, an artificial stress concentration was found, due both to tie constraints and excessive refinement of the mesh. Using *Abaqus* value probing functionality, the Stress values corresponding to the zones where the maximum values were indicated for the coarser meshes were also registered. Results are summarized on table 6.2.

Table 6.2: Stringer mesh study. ⋆Values ignoring stress concentrations.

| Mesh | Element type | Number of Elements | $U^{min}_{resultant}$ [mm] | $U^{max}_{resultant}$ [mm] | $\sigma^{max}_{Mises}$ [MPa] | $\sigma^{max}_{Mises}\star$ [MPa] |
|---|---|---|---|---|---|---|
| 1 | S4R | 252 | 10.27 | 12.65 | 78.1 | - |
| 2 | S8R | 252 | 10.28 | 12.62 | 150.1 | - |
| 3 | S4R | 37800 | 10.27 | 12.62 | 167.1 | ≈138 |
| 4 | S8R | 37800 | 10.27 | 12.62 | 550.4 | ≈145 |

Based on the results, it can be concluded the mesh does not have an great influence on the results, specially on displacements, were on negligible differences were found. Although the coarse linear mesh (mesh 1) yielded Stress values about half of those obtained with the refined meshes, this was not considered a problem: the other meshes proved that the Stress level on the part its acceptable, and Stresses are not a major concern in this specific part. Therefore, in order to keep the model as light as possible, the coarse mesh will be used for the rest of the work.

Concluding the stringer study, the results for mesh 4 are presented on Figure 6.2. Note that the grey zones on Figure 6.2 are the zones where artificial stress concentrations were considered.

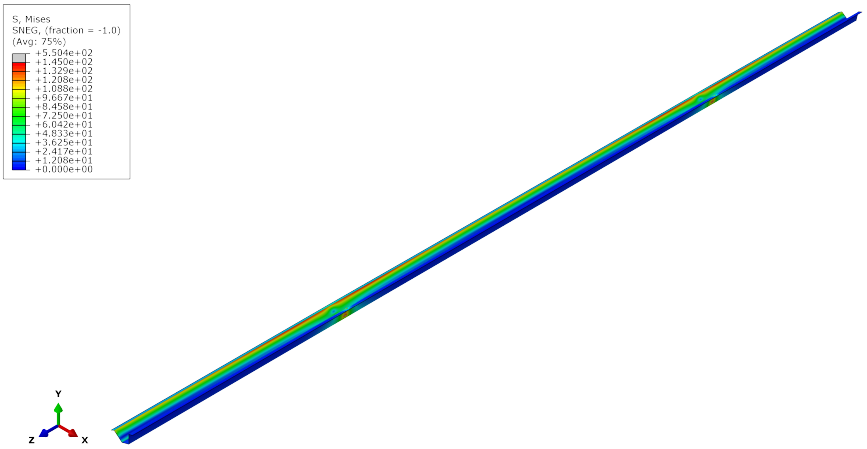


(a) Resultant Displacements of the Stringer

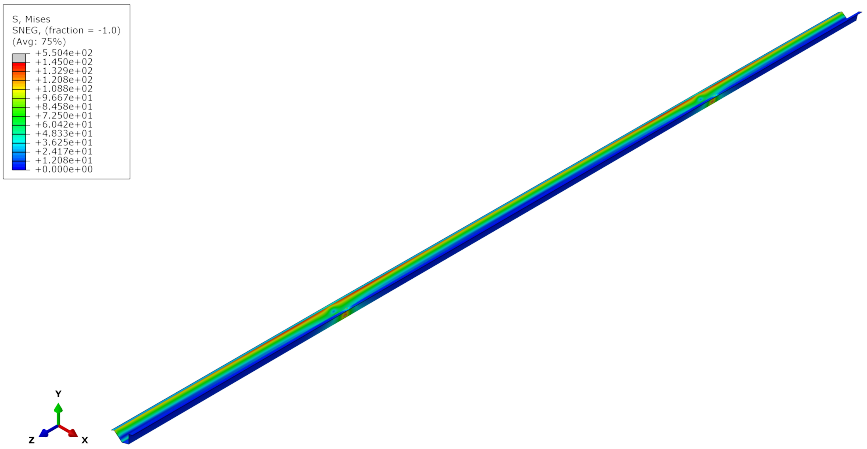


(b) von Mises Stress field on the Stringer

Figure 6.2: Results for mesh 4

### 6.1.2 Modelling of the Skin

The Skin is the part of the leading edge which will receive most attention during this study. Therefore, it is important not only to understand the mesh effect, but also the effect of the skin thickness on the deformed shape.

Following what was concluded on Section 1.1, all degrees of freedom were fixed on both top and bottom skin edges (edges along the Z axis).

The modelling of the Skin as a shell feature was done using using the same type of elements used for the Stringer (4-noded linear (S4R) and 8-noded quadratic (S8R) shell elements). For a 0.5 mm thickness, 8 meshes were created, and are resumed on Table 6.3.

Table 6.3: Skin meshes summary

| Mesh | Element Type | Approximated element edge size [mm] | Number of Elements |
|---|---|---|---|
| 1 | S4R | 25 | 1260 |
| 2 | S4R | 10 | 4770 |
| 3 | S4R | 5 | 15300 |
| 4 | S4R | 2.5 | 54000 |
| 5 | S8R | 25 | 1260 |
| 6 | S8R | 10 | 4770 |
| 7 | S8R | 5 | 15300 |
| 8 | S8R | 2.5 | 54000 |

Note that the stated size of the element edge is approximated. It does not always hold true for the edges contained on the XY Plane, since this plane contains the airfoil profile lines, which were partitioned on several locations to locate the stringer constraints and to better accommodate the profile. This was due to an error when importing the middle line from *SolidWorks*: only the line points were transferred, and were connected using a sequence of lines, not a continuous one. This error has not affected the present mesh study, so it was only found later, and corrected. This will will be further discussed later on this text.

The maximum vertical Displacement and maximum von Mises Stress were recorded, and the percentage errors relative to the values obtained with Mesh 8 were calculated. Results are presented on Table 6.4.

Table 6.4: Skin mesh study.

| Mesh | $U_2^{max}$ [mm] | Relative Error | $\sigma_{Mises}^{max}$ [MPa] | Relative Error |
|---|---|---|---|---|
| 1 | 14.23 | -3.1% | 240.8 | -11.3% |
| 2 | 14.41 | -1.8% | 221.8 | -18.3% |
| 3 | 14.45 | -1.6% | 220.1 | -18.9% |
| 4 | 14.67 | -0.1% | 247.0 | -9.0% |
| 5 | 14.63 | -0.3% | 268.6 | -1.1% |
| 6 | 14.67 | -0.1% | 266.9 | -1.7% |
| 7 | 14.68 | 0.0% | 270.3 | -0.4% |
| 8 | 14.68 | - | 271.5 | - |

Observing the results from Table 6.4, conclusions similar to those drawn from the previous mesh studies arise. The refinement of the mesh does not have an important influence on the convergence of the displacement values, but there is some difference on the values of the Stresses. Based on this, coarse meshes will be used in the zones where the Stress values are not the concern, and local refinement will be carried out where deemed necessary. This does not have a significant influence on the results of the refined zones because, as it was just proven, the Displacements transmitted to those areas are not significantly affected my mesh refinement or element order. These parameters only affect the results from post-processing, justifying the local refinements.

To fully report the behaviour of the skin, the results above, and the displacements $U_1$ and $U_3$ are presented in Figures 6.3 to 6.6, plotted over the morphed configuration, for Mesh 8.

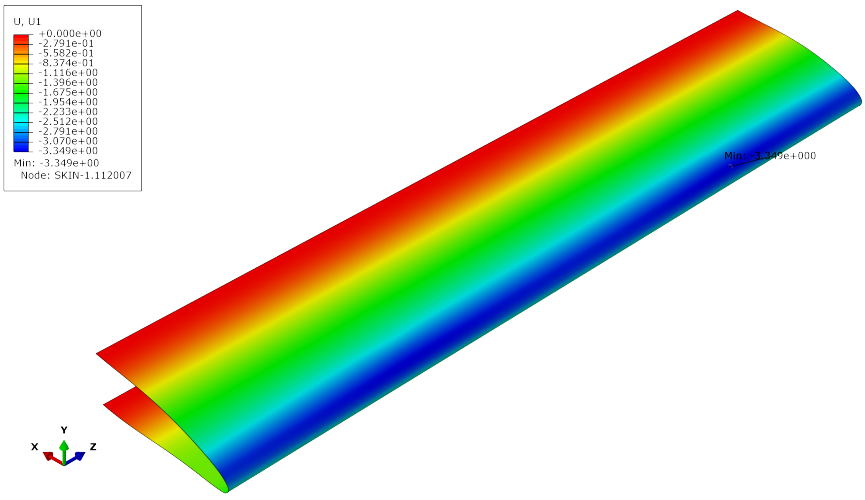


Figure 6.3: $U_1$ displacement field.

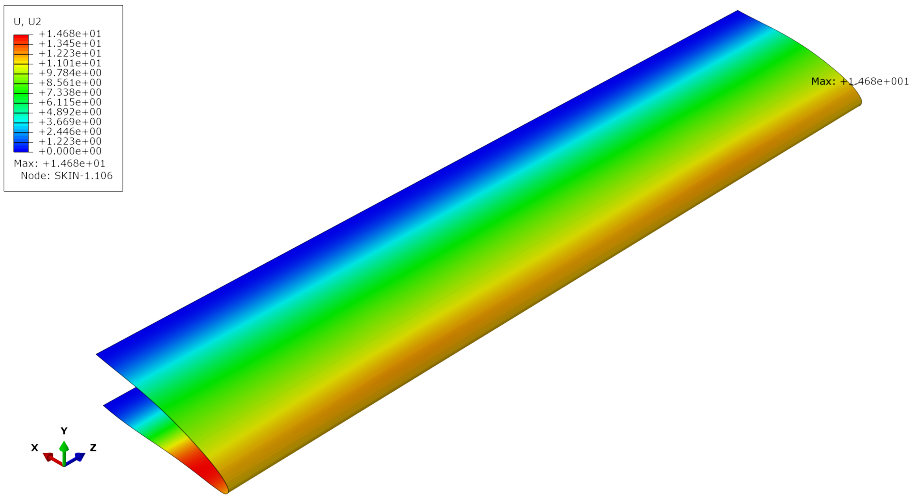


Figure 6.4: $U_2$ displacement field.

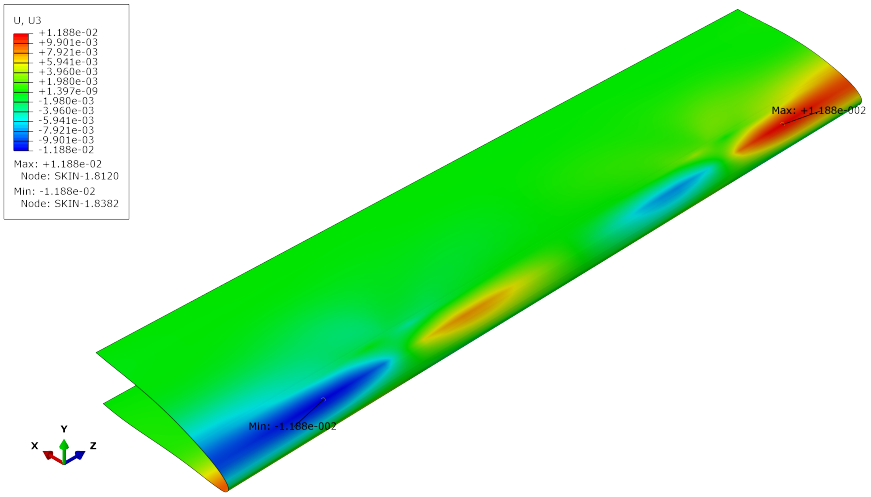


Figure 6.5: $U_3$ displacement field.

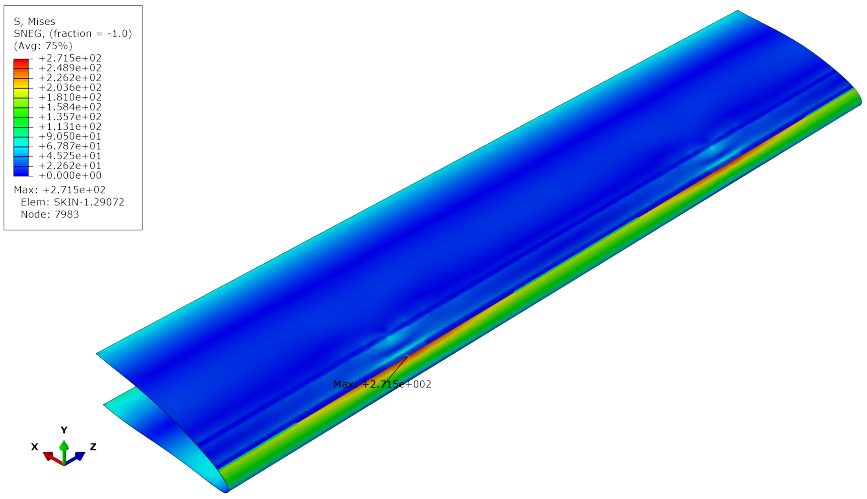


Figure 6.6: von Mises Stress field.

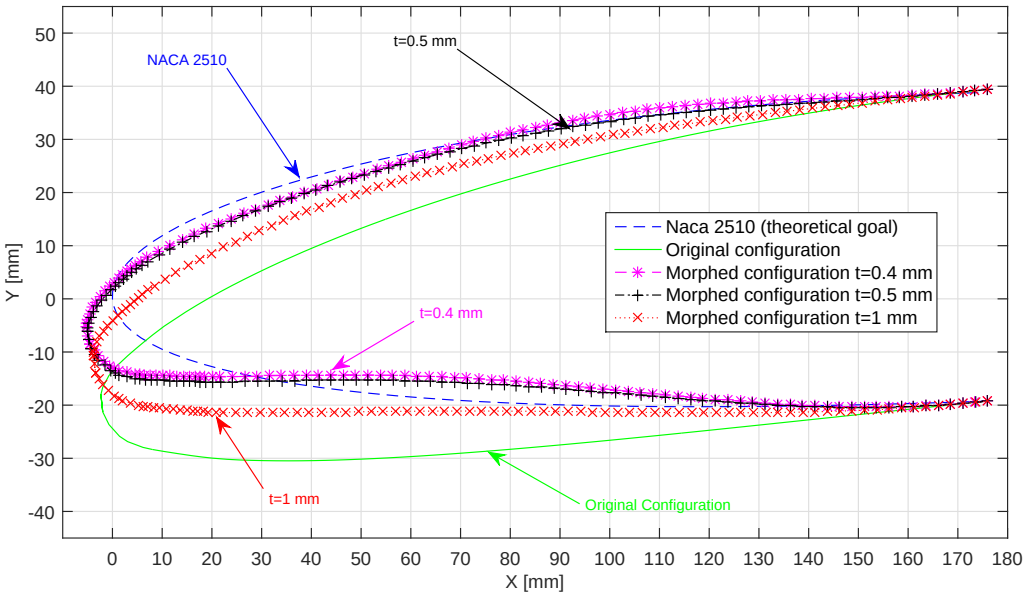


Figure 6.7: Influence of thickness on morphed configuration.

The results mentioned were obtained with a 5 mm horizontal displacement actuation and a shell thickness of 0.5 mm. However, the deformed shape does not resemble the

NACA 2510 profile, which was the intended final form. This can be related to several aspects: the magnitude of actuation input, the shell thickness and the fact that aerodynamic loads were not simulated. It was chosen not to change the input, as it had been the basis for the all the previous work done. Also, aerodynamic loads were not simulated as several data needed to this simulations was unknown, such as the speed and altitude ranges for the UAV studied, and also as it would lead to complex analysis, out of the scope of this work. As mentioned in section 3.4.3, some authors have dispensed aerodynamic loads, as they "have only a small influence on the deformation" (Ricci et al., 2006). Therefore, it was chosen to do the same.

With thickness remaining a variable, its influence was assessed, by running simulations with different thickness assignments. The deformed shape was then retrieved, by obtaining the displacements on XY plane at half span of the model (so that any errors caused by Z–axis displacements were minimized). Thicknesses of 0.4 mm, 0.5 mm and 1 mm were considered. The results are presented in Figure 6.7.

Observing the results, it can be concluded an increase in thickness also increases the differences between the intended and achieved shape. This was expectable, as it also increases the skin stiffness, thus making it less deformable. Another conclusion drawn is that for t=0.4 mm and t=0.5 mm, there are not many differences, but t=0.4 mm yields a more "wavy" surface. This was considered inadequate, and thickness was chosen to be 0.5 mm for the remainder of this work.

The differences between the theoretical and simulated results deserve a final mention. On the contacts made with Dr. Martin Radestock, he kindly provided a image of his results, and mentioned that he had considered the aerodynamic loads (details were not provided). Based on this image (Figure 6.8), and although Dr. Radestock's results show $U_2^{max} = 16.06$ mm (about 9% difference), it can be concluded that the morphed shaped achieved in this work is substantially similar to that obtained at DLR.

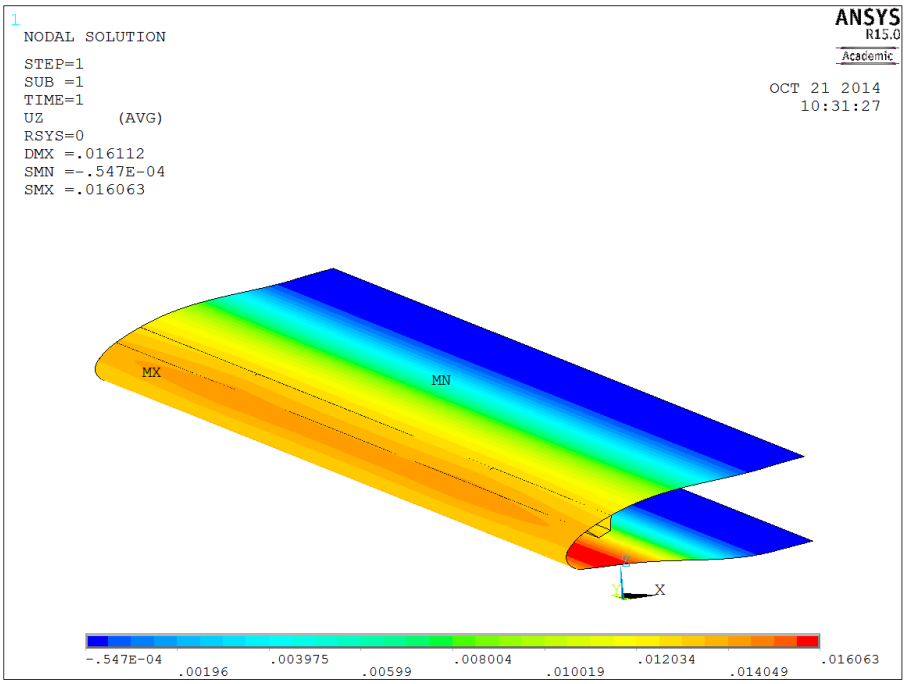


(a) Vertical displacement obtained by DLR. Kindly provided by Dr. Martin Radestock.

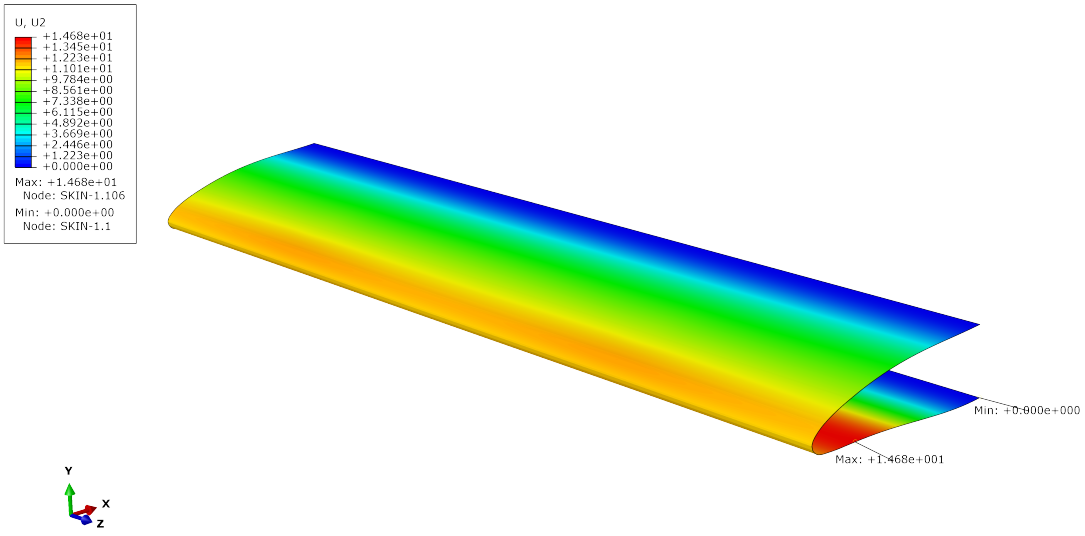


(b) Vertical displacement obtained on this study.

Figure 6.8: Comparison between Dr. Radestock and current results.

## 6.2 Modelling using Solid Elements

Shell elements are computationally lighter than Solid elements, but they have limitations, since Shell theories only consider in-plane stresses. Therefore, the use of 3D solid elements was considered, and models were created for the skin accordingly.

The skin was modelled using again the middle surface line extracted from the *Abaqus* model, and offsetting this line to the desired thickness. This time, the continuity of this line was ensured. To accommodate the skin's curvature, special attention was given to the mesh creation, and zones with bigger curvature were assigned finer mesh size.

Mesh influence was again studied. For this purpose, two meshes were created, using 8-node linear brick elements (C3D8R) and 20-node quadratic brick elements (C3D20R), both with reduced integration. Three elements were used along the thickness, and the general element edge size, for the less curved skin edges was 5 mm. Other zones, where skin has considerable curvature, were assigned edge sizes according to their geometry, as explained before. These meshes had 50220 elements each.

The deformed shape was accessed, and the results are shown on Figure 6.9. It can be concluded that, as happened before, the order of the element resulted only in slight differences. For the exterior surface, von Mises and Normal Stress $\sigma_{11}$, which is the stress in the circumferential direction (tangent to the airfoil line, in a similar fashion the hoop stress on a cylinder), where also registered. In contrast to the Displacement values, Stress values were dissimilar, as seen on Figures 6.10 and 6.11. Due to this, a more refined linear mesh was created, with a general element edge size of 1 mm (982800 elements), and the results were added to the Figures mentioned.

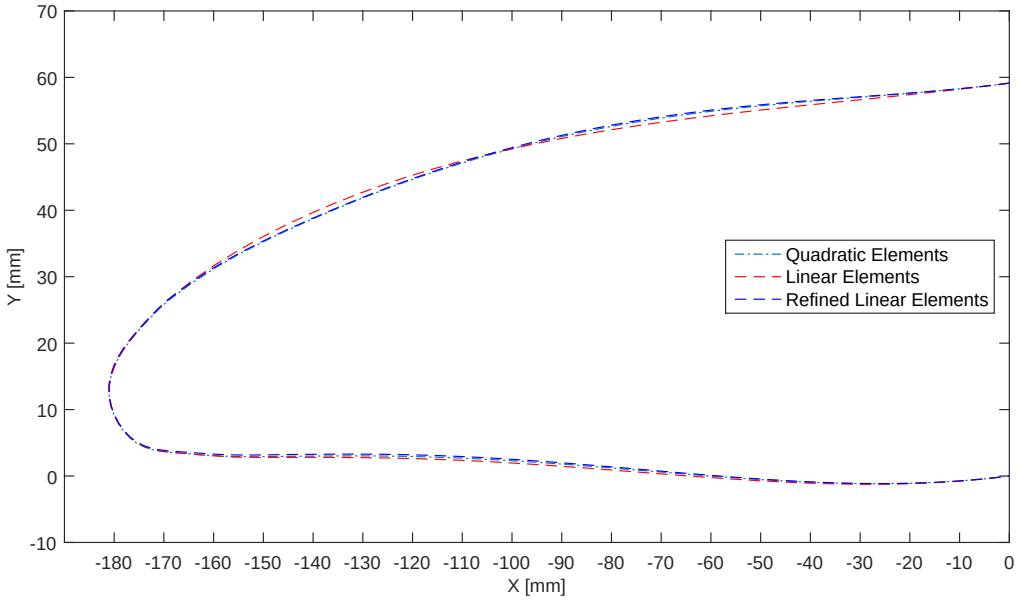


Figure 6.9: Deformed Shape for the 3 meshes used.

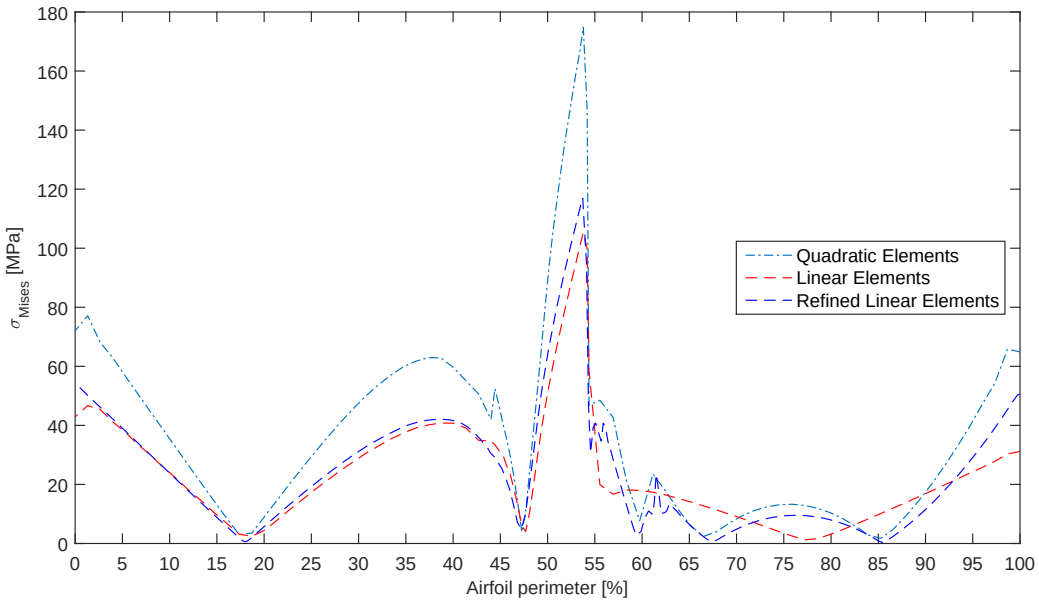


Figure 6.10: von Mises Stress for the 3 meshes used.

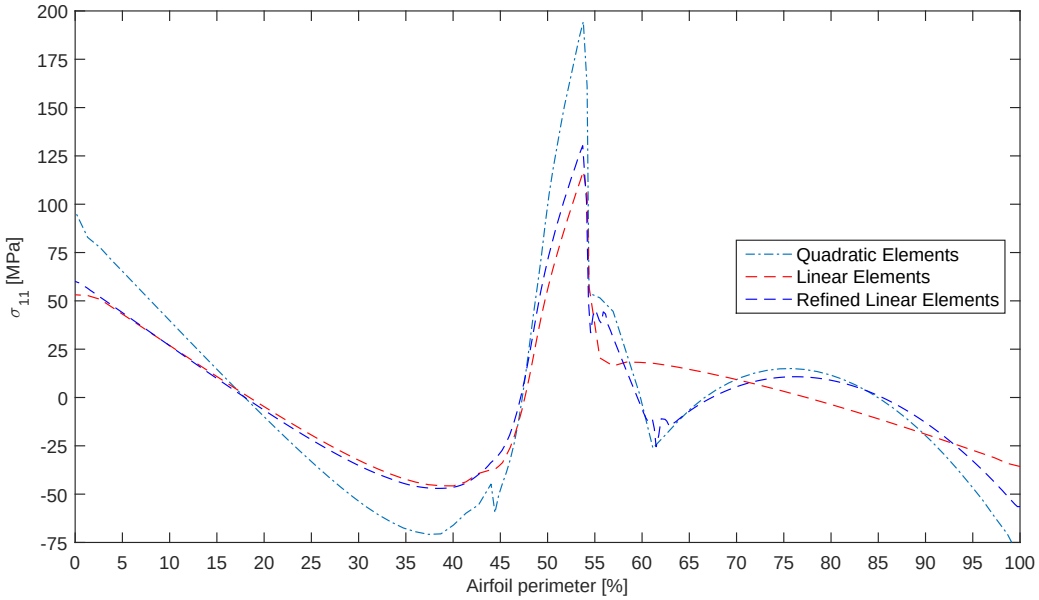


Figure 6.11: $\sigma_{11}$ Stress for the 3 meshes used.

Observing the graphics, it can be concluded that increasing the number of elements on the faces of the skin, for the linear mesh, approximates the results to a certain degree. However, this only happens the skin portion after the stringer, which is around 54% of the airfoil perimeter. Before that, although following the same patterns, the stress values for quadratic and linear elements have some differences. The presence of the stringer also accounts for the peaks of the graphics at that position.

To understand the if the number of elements along the thickness improved the results, it was increased to six on the first two meshes, and von Mises and $\sigma_{11}$ Stresses were registered (Figures 6.12 and 6.13).

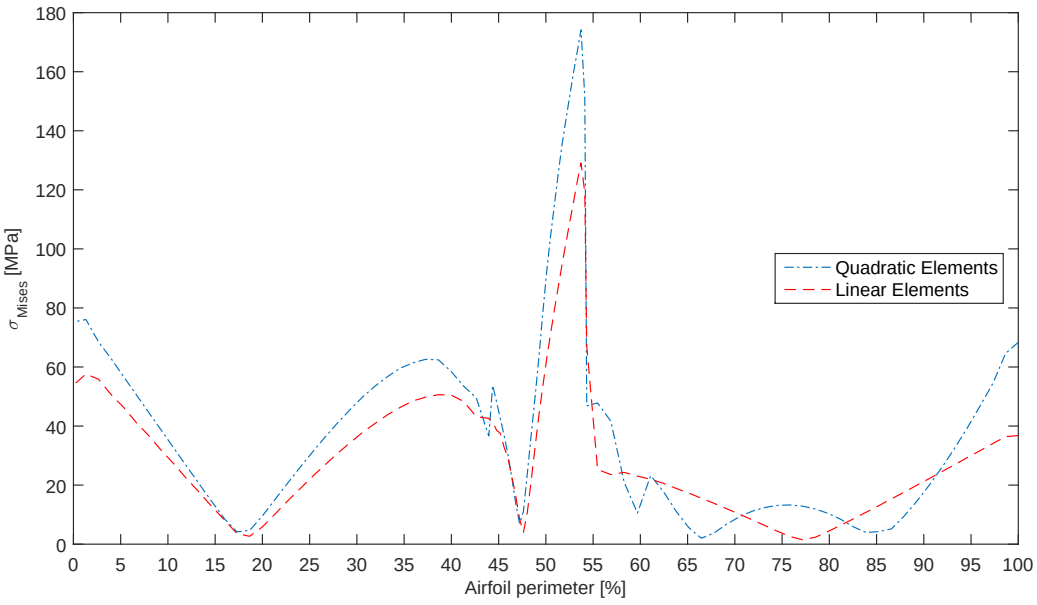


Figure 6.12: von Mises Stress for the 2 meshes used with 6 elements along the thickness.

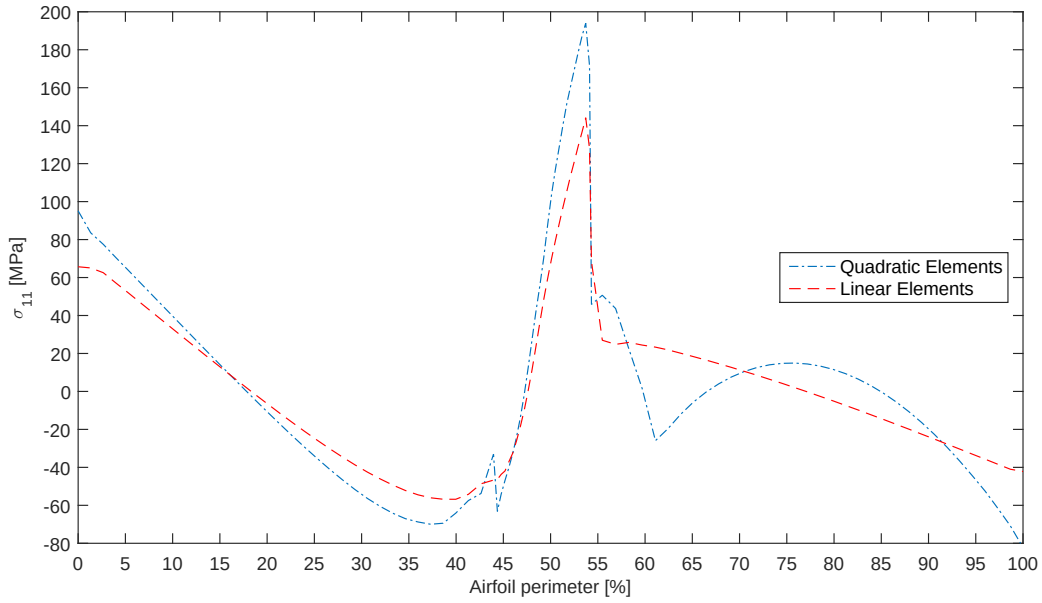


Figure 6.13: $\sigma_{11}$ Stress for the 2 meshes used with 6 elements along the thickness.

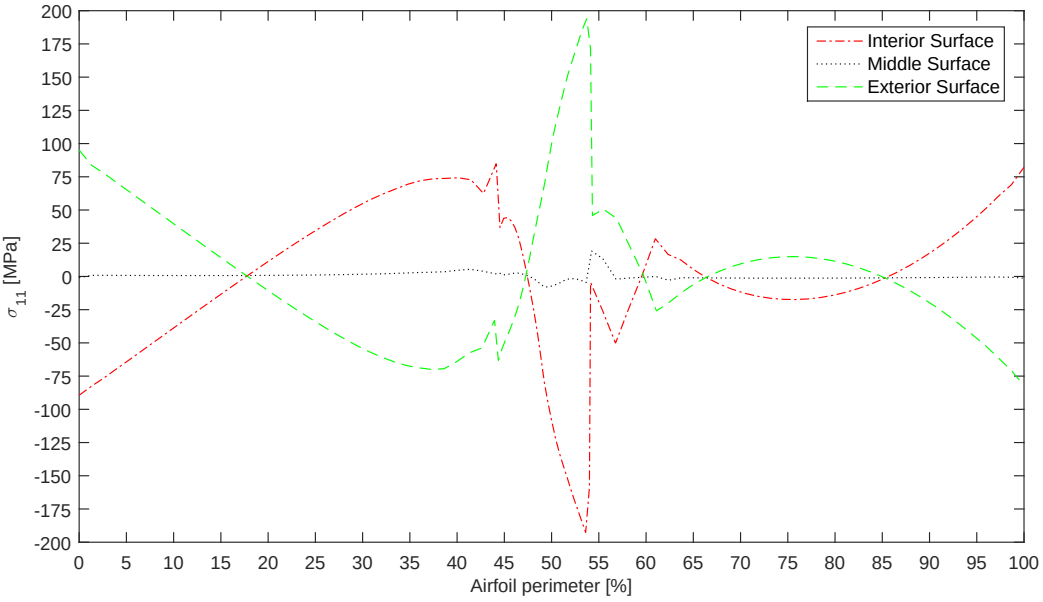


Figure 6.14: $\sigma_{11}$ Stress on the exterior, middle and interior surfaces.

The graphics from Figures 6.12 and 6.13 resemble closely those from Figures 6.10 and 6.11, leading to the conclusion that the increased number of elements does not have a significant effect on the results. However, it is advisable to keep this increased number, since it provides better results resolution along the thickness of the skin. This is important since it was found that the skin is under bending. Plotting the $\sigma_{11}$ stresses on the exterior, middle and interior surface, its visible that, for each point, stresses exterior and interior surface have opposite signs (one being a tensile stress, the other compressive), whereas stresses on the middle surface are very low. This is shown by Figure 6.14.

This work will be focused on the most curved part of the leading edge, which is located between 45% and 54% of the perimeter of the studied airfoil. This is where stresses rises rapidly, but also where is seems to exist a better correlation between the stresses yielded be linear and quadratic elements. To quantify this, the linear element results error (when comparing to their quadratic counterpart) was calculated for this portion of the airfoil (Figures 6.15 and 6.16).

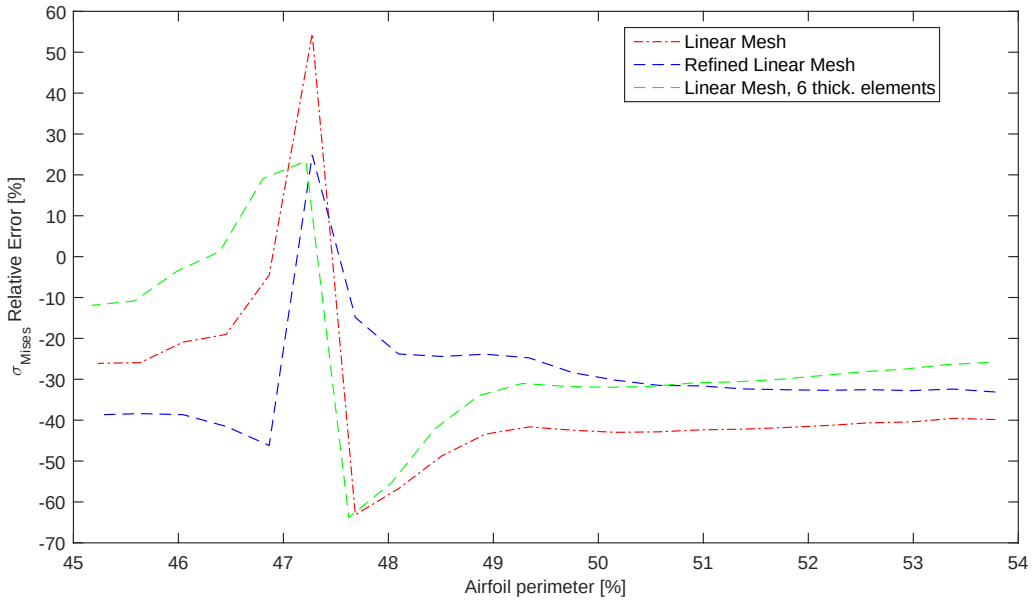


Figure 6.15: von Mises Stress Relative error for the different meshes.

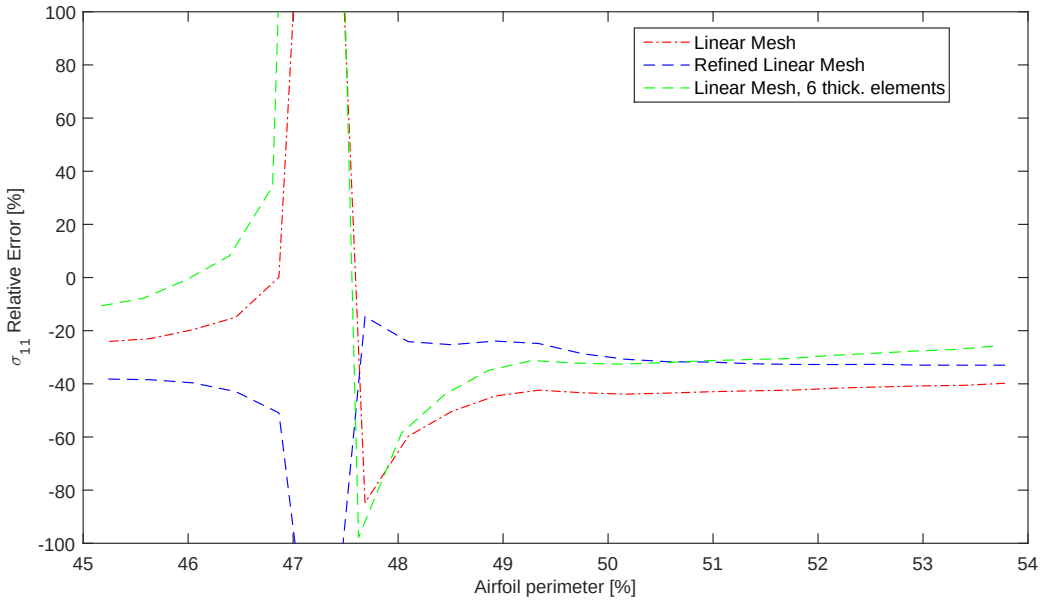


Figure 6.16: $\sigma_{11}$ Stress Relative error for the different meshes.

As expectable, increasing the number of elements led to lower error, especially if that increase is along the thickness. Nevertheless, errors are much higher than desirable or acceptable, from an engineers point of view. Peaks and rapid changes of sign were also found in the plots, caused by stress values approaching zero or transitioning between negative and positive values in slightly different locations. These peaks were also affected by the number of thickness elements, specially on what concerns the $\sigma_{11}$ stress error, whose signal changes. Overall, it was concluded that the linear mesh refined along the thickness yielded lower errors, except on the transition zones. This could be because refined meshes are more sensitive to stress variations and concentrations.

The errors above were calculated considering values obtained from quadratic meshes as those closest to reality. They were calculated using the formula:

$$Relative\,error\,(\%) = \frac{Stress_{lin\,mesh} - Stress_{quad\,mesh}}{Stress_{quad\,mesh}} \times 100$$

However, these stresses are calculated following the Finite Element Method procedures. Thus, they are first calculated at the integration points. Only after that, on post-processing, is the calculation of the nodal values (those retrieved from *Abaqus*) done, using the interpolation functions associated to the each element type and/or other techniques. Due to lower order of the linear elements, less integration points, in different locations, are used per element. This means that previously plotted stresses, extrapolated to surfaces, are based on possibly different values, from different positions. As the skin is bending, thus creating a stress gradient along the thickness, the positions where

values are computed, for linear and quadratic elements, are at different distances from the bending neutral surface. This may explain the magnitude of the errors found. Other post-processing techniques, such as averaging nodal values and smoothing the result plots, may also account for this.

Based on this conclusions it was decided that, when modelling cracks, local refinement would be done, both through thickness and along the surface edges, and that quadratic elements would be used at these zones, when possible. The use of quadratic or linear elements will be further discussed on Chapter 7.

## 6.3 Development of a Mixed Element Model

Running the simulations described on the previous section was, computationally, quite time consuming, in comparison to the shell elements. Bearing in mind the need for both solid elements and mesh refinement, but also the need to keep the complexity of the model as low as possible (from the computational point of view), a solution using both solid and shell elements to model the skin was considered.

Since this study will be focused on the most curved zone of the skin, located between 45% and 54% of the airfoil perimeter, it was considered to use Solid elements to model it, and Shell elements for the remainder of the skin. *Abaqus* provides a type of constraint named "Shell-to-Solid Coupling", described on its User's Guide as "a surface-based technique for coupling shell elements to solid elements". This technique is "intended to be used for mesh refinement studies where local modelling requires a relatively fine through-the-thickness solid mesh coupled to the edge of a shell mesh" (Dassault Systèmes, 2016).

The first approach was to use a small patch of Solid elements for each zone where a crack was to be modelled. In these zones, the mesh would be composed of refined solid elements, and the remaining zones, of less interest, would modelled with coarser shell meshes.

To test this approach, a central location was chosen. Some problems appeared when modelling this situation. If the change from a coarse mesh to a fine one happens without transition, only some nodes are shared between meshes. Therefore, variables from the coarse mesh are concentrated only on some nodes from the refined mesh. To address this, two solutions were considered.

The first consisted on creating a transition mesh, using, for instance, triangular elements. This approach has some issues: triangular elements are affected by their relationship with it the meshed geometry. Furthermore, obtaining good quality meshes manually is time consuming, cumbersome and requires special attention. Software to perform better meshing exist, such as *Femap*[a]. Since only an outdated version is available at FEUP, and as the author lacked experience on the use of software of this kind, a second solution was considered.

[a]Femap is the acronym for Finite Element Modeling and Postprocessing. It is an engineering analysis program sold by Siemens PLM Software.
For more information, consult https://www.plm.automation.siemens.com/en_gb/products/femap/

The second solution was to conform the coarser mesh to the finer one. The latter is done by using partitions within the zones with coarser mesh, and making this mesh as fine as the refined one, along the edges serving as interface between meshes. However, this yields elements with high aspect ratio, which is not advisable as it can negatively influence results. Nevertheless, this is not a big problem in this case, as these zone are not those in study.

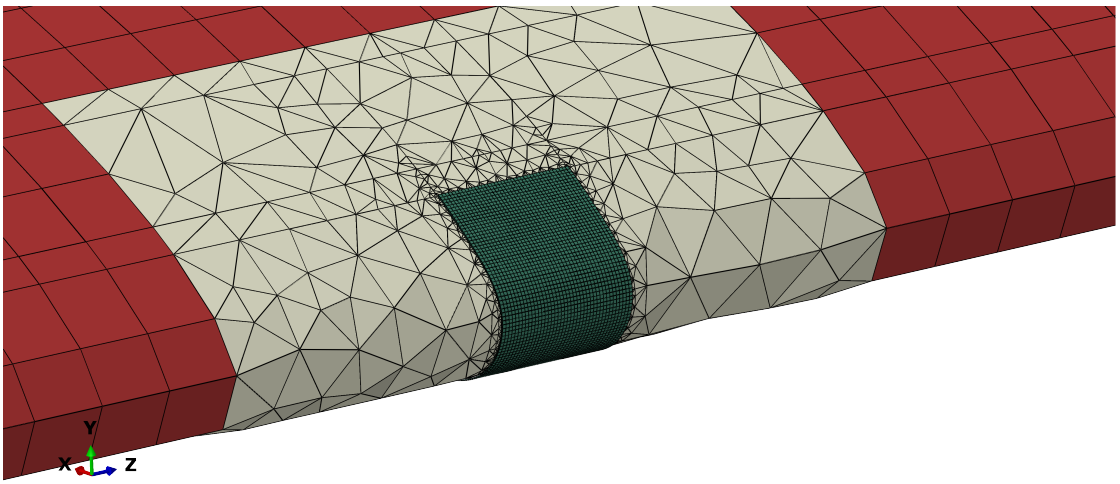


(a) First Solution: the mesh irregularity is difficult to eliminate manually.

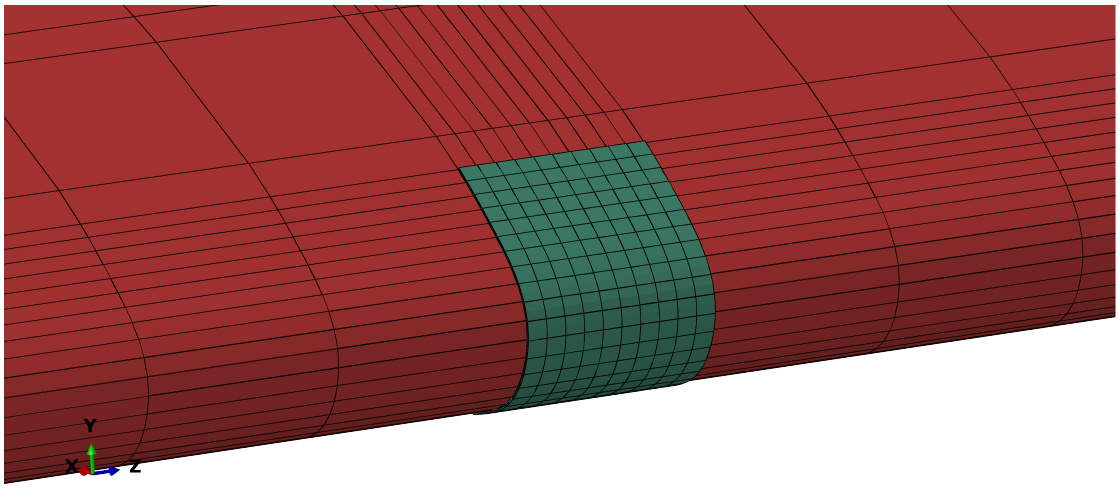


(b) Second Solution

Figure 6.17: First approach to the mixed element model (Red: Shell quadrangular elements; White: Shell Triangular elements; Green: Solid brick elements).

Figure 6.17 shows examples of these two solutions, for which several simulations were run. It was verified that the first solution was unpractical, and that the second still could not achieve a smooth transition of results between shell and solid elements, on the interface edges contained on the XY plane (airfoil plane). Therefore, a second approach was developed, extending the patch along the total length of the span, and using the second solution mentioned. The one of the resulting meshes is show on Figure 6.18.

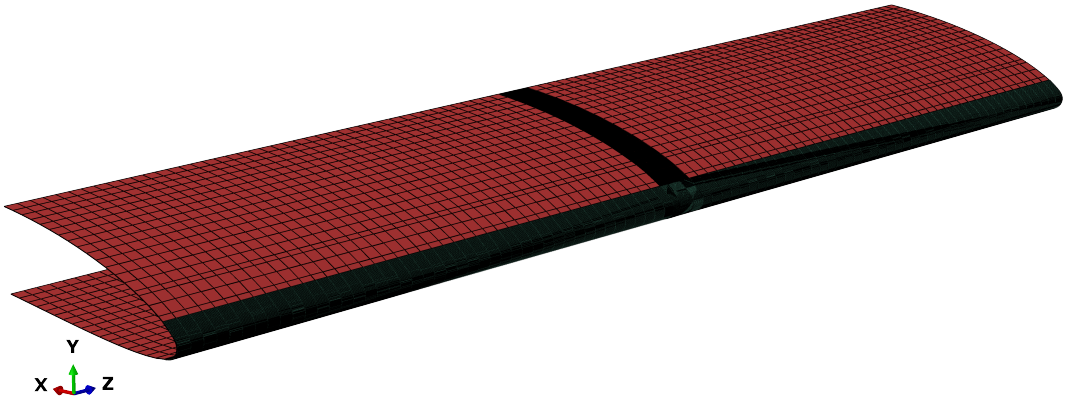


(a) Second approach: the patch covers the entire span.

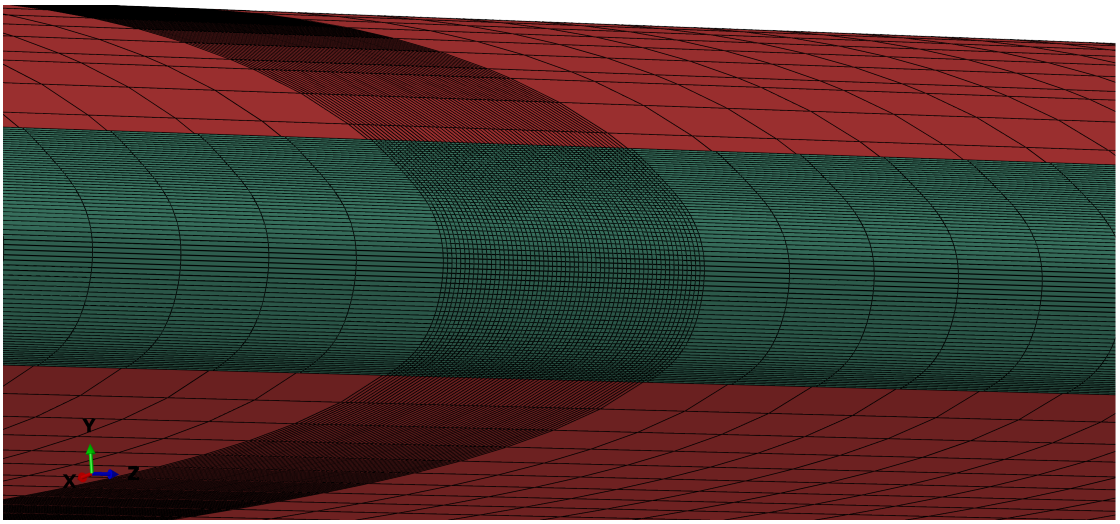


(b) Second approach: zoom

Figure 6.18: Second approach to the mixed element model (Red: Shell elements; Green: Solid Elements).

To understand if distinct types of elements affected the results, the deformed shape and von Mises Stress of the exterior surface of the Solid elements patch were registered along a path contained on its symmetry plan. 20-noded quadratic elements (C3D20R) were used, with 6 elements along thickness. The plots of Figure 6.19 (a) and (b) and show the results for the region of interest only.

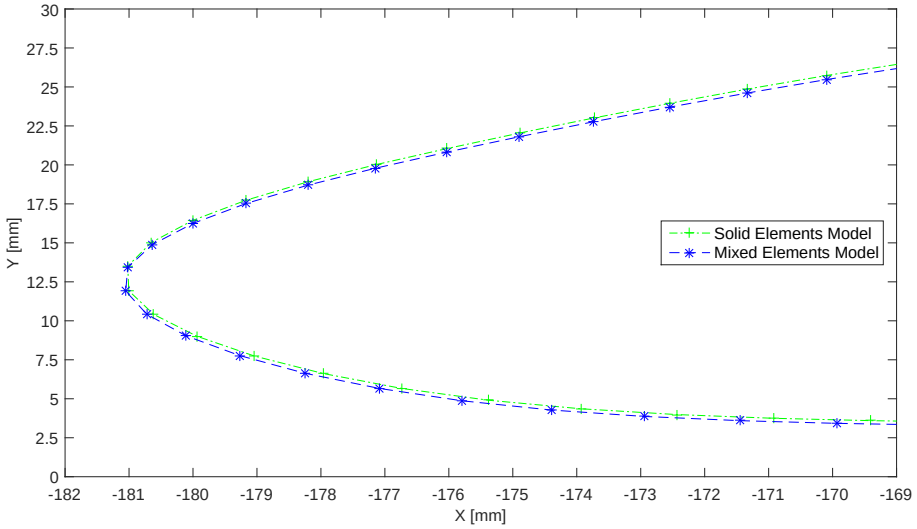


(a) Deformed Shape comparison (Region of interest only).

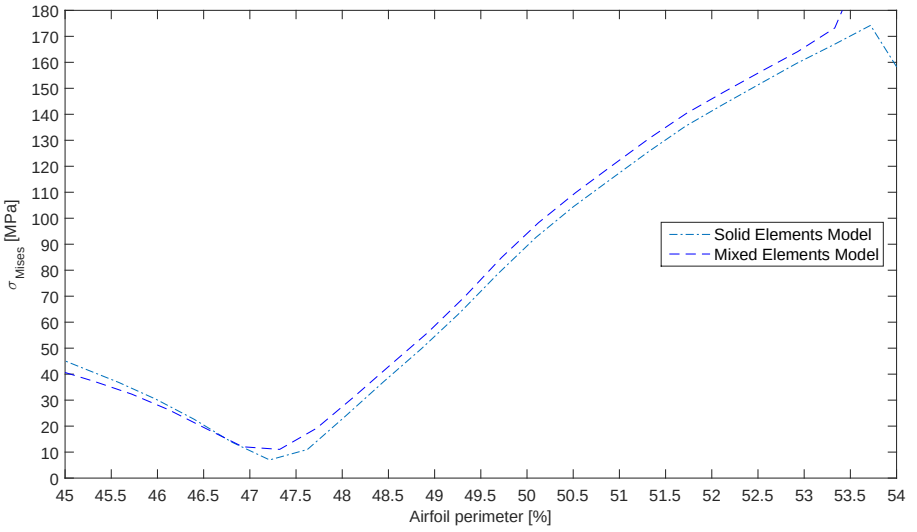


(b) von Mises Stress Comparison

Figure 6.19: Results for the patch zone compared with those of Solid Elements model.

These results show that, concerning the displacements, there are no noticeable differences. Concerning the Stress values, although there is a small difference, it is perfectly acceptable, since the relative error (Figure 6.20) is comprehended between -1% and 3.5%. This error and the difference increase at about 53.5%, but this is due to the coupling between the Shell and the Solid elements, and also due the nearby presence of the stringer.

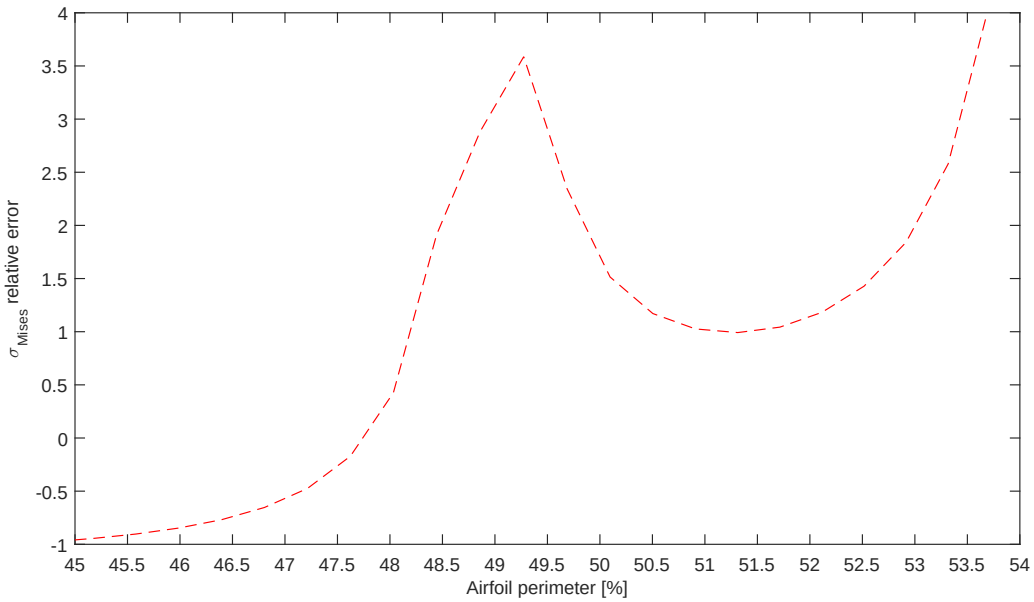


Figure 6.20: $\sigma_{Mises}$ relative error.

These graphics prove that the Mixed Elements model has the same behaviour of the Solid Elements model, validating it. Since this model is computationally lighter, it will be used instead.

# Chapter 7

# Modelling of Longitudinal Cracks

This chapter will address the modelling of longitudinal cracks in the leading edge of the wing skin (i.e. cracks parallel to the generatrix of the wing curved surface). The modelling of cracks using the previous studied finite element models will be discussed, as well as the problems faced and solutions adopted. The extraction of the Stress Intensity Factors will be covered, and results from simulations will be presented and analysed.

## 7.1 Crack modelling using Shell Element Models

The first model containing a crack was done using the initial Shell Elements models. As mentioned in the previous Chapters, this model has some limitations, but was used due to the ease of modelling and to the fast obtention of results. However, during the creation of this model minor mistakes were made, which were only found during the extraction of the Stress Intensity Factors (SIFs): *Abaqus* J-integral approach was used to obtain the SIF values, but *Abaqus* only retrieved diverging and erroneous values. The reason was found to be the crack location, which was being defined using one of the "artificial" longitudinal edges. This line, located at about 49% of the airfoil perimeter, resulted of the use of straight lines while sketching the airfoil shape. This prevented *Abaqus* from achieving a correct definition of the contours used for J-Integral evaluation.

While still using the skin part based on that flawed sketch, a second attempt of SIF extraction using Shell Elements. Several cracks parallel to the Z-axis (horizontal) were modelled on a skin portion centred at half-span a and between two "artificial" longitudinal edges These cracks were located at about 50.5% of the airfoil perimeter. This crack location, although being a fallback solution, was unfortunate. As will be seen on the next sections, it prevents direct comparisons with the models presented on the next sections. Nevertheless, results will be presented and discussed. Later in this chapter, some comparisons will still be drawn (Section 7.4.2).

Crack length was 10 mm for the shortest crack, and then ranged from 25 mm to 200 mm, in 25 mm steps. *Abaqus* partitioning functionalities were used to locate the crack and define its geometry (crack line and crack tip). The seam feature was used to enable crack faces separation. A seam "defines an edge or a face (...) that is originally closed

but can open during an analysis. *Abaqus* places overlapping duplicate nodes along a seam when the mesh is generated." (Dassault Systèmes, 2016). Virtual crack extension direction was defined using the line which defined the crack on the shell (same direction and point outwards the crack). *Abaqus* J-integral approach was used to obtain the SIF values. It was chosen since it is included in this software code, eliminating the need for further manual post-processing. Also, this approach is regularly used, and mentioned by different authors (for instance: Courtin et al. 2005; Chen and Pan 2013).

As mentioned on section 4.3.3, a mesh adapted to the crack geometry is need when using the J-Integral approach. Therefore, further partitions were used locally to perform mesh refinement, and globally to ensure a coherent mesh. 4-noded shell elements with reduced integration (S4R) were used, since convergence was only achieved using this type of elements.

Several simulations were run to determine the SIF as a function of crack length. Figures 7.1 and 7.2 illustrate the crack location and deformed shape for a crack length of $2a = 100$ mm. Note that Figure 7.2 is a cut using the XY plane at half-crack, which clearly shows the existence of a bulging effect.

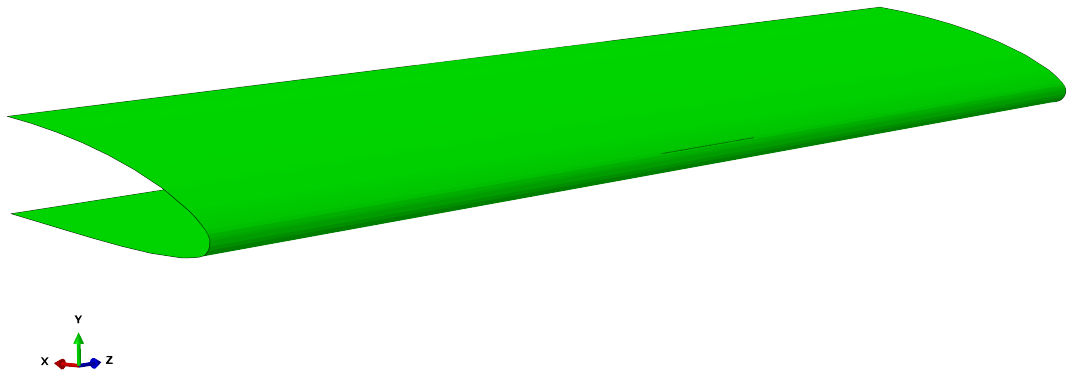


Figure 7.1: Location of the crack on the shell model.

Figures 7.3 to 7.5 show the relevant stress fields on the crack tip. S11 is the normal stress in the "circumferential" direction, and S12 is the in-plane shear stress. These were obtained using a crack length of $2a = 25$ mm, and show the stress fields for the exterior and interior surfaces. The coordinate system used is as follows: 1-axis is the axis tangent

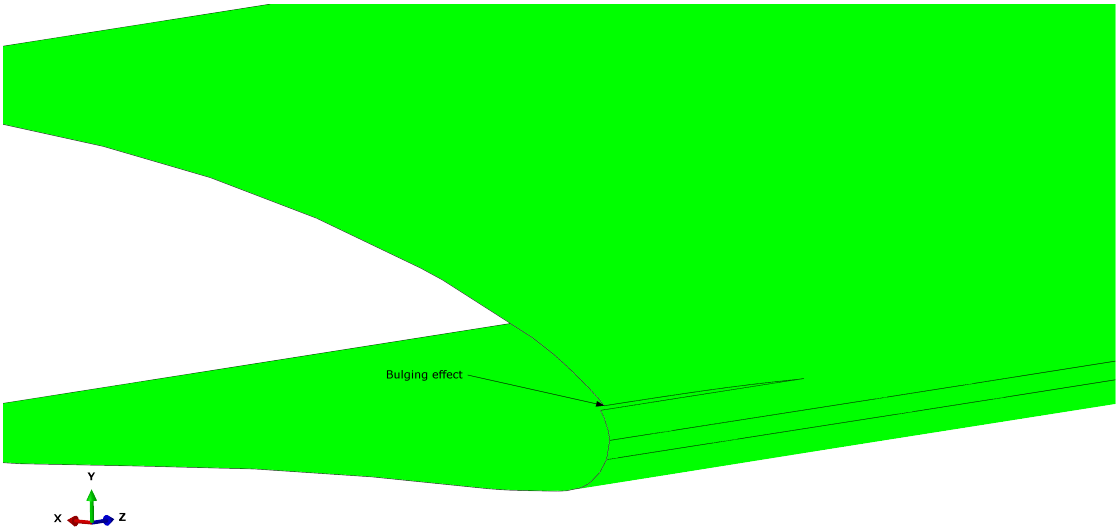


Figure 7.2: Deformed shape of the crack on shell model.

to the shell surface, 2-axis is the longitudinal one, and 3-axis is normal to the surface. These are *Abaqus* default axis for shell elements. Note that the stress fields are plotted over the middle surface and, although seen from the same point of view, do reflect the different surfaces. This was done using *Abaqus* results visualisation capabilities.

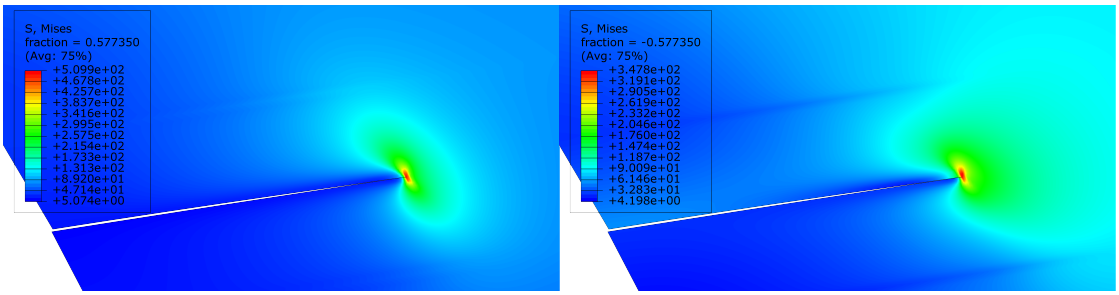


(a) Exterior surface. (b) Interior surface.

Figure 7.3: von Mises stress field on the crack tip.

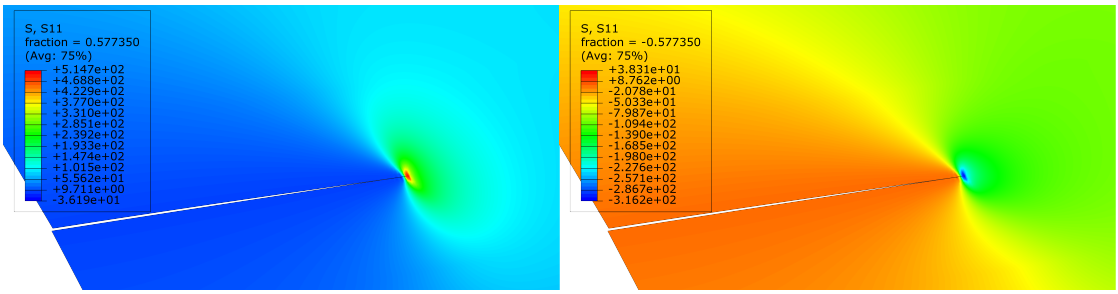


(a) Exterior surface. (b) Interior surface.

Figure 7.4: S11 stress field on the crack tip.

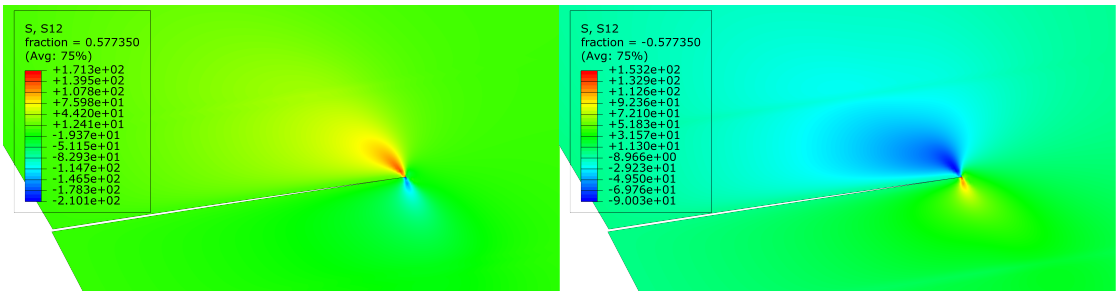


(a) Exterior surface. (b) Interior surface.

Figure 7.5: S12 stress field on the crack tip.

From the previous plots, it can be concluded that the crack zone is under bending. The normal stresses are tensile on the outer surface, but compressive on the interior. Therefore, and considering the skin thickness ($t = 0.5$ mm, which shell elements do not visually represent), the crack is under compression on its interior end and tensioned on the exterior one. This mean that the mode I intensity will change along the thickness, and by itself justifies a 3D study. Also, the in-plane shear stress appears to change not only sign, but absolute value, across the skin thickness. This may be related with the bulging effect, and will be further discussed on section 7.4.1. Therefore, the most important conclusion from these plots is the importance of the solid elements model.

As mentioned before, *Abaqus* built-in J-integral approach was used to extract the Stress Intensity Factors. Figure 7.6 illustrates one of the node rings used by Abaqus to define the J-Integral Contours. The displacements have been amplified by a factor of 10, to provide better visualization of the crack opening and so that the contour zones lying on the crack free surface are clearly noticed.

Due to the shell elements nature, only the values of mode I and II SIFs were retrieved, and only for the middle surface were extracted by *Abaqus*, and are plotted on Figure 7.6. These two curves show an interesting behaviour, with $K_I$ starting to decrease after a certain value of $2a$, while the absolute value of $K_{II}$ increases steadily for longer cracks.

This leads to an increasing predominance of mode II. However, these results should be seen as preliminary. On the following sections, a more thorough evaluation of the several cracks will serve to provide a more consolidated understanding of the crack behaviour on this leading edge.

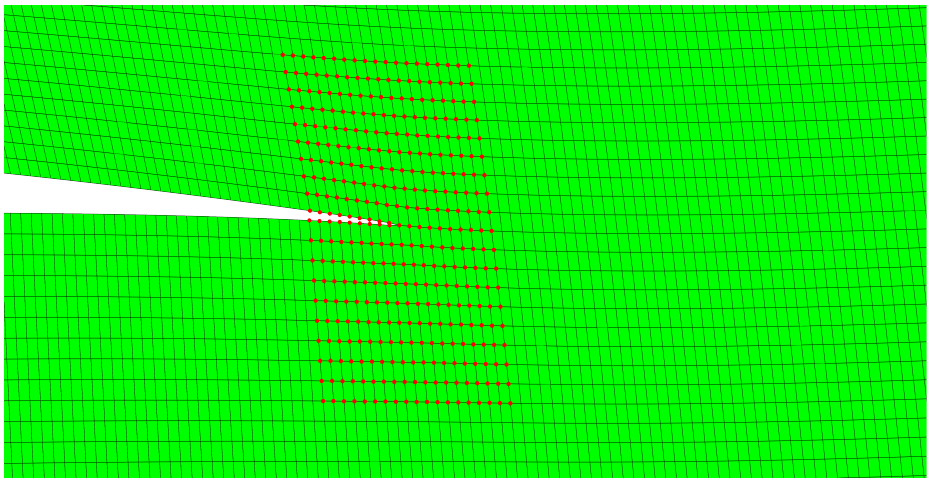

Figure 7.6: Example of a J-Integral contour defined by *Abaqus*.

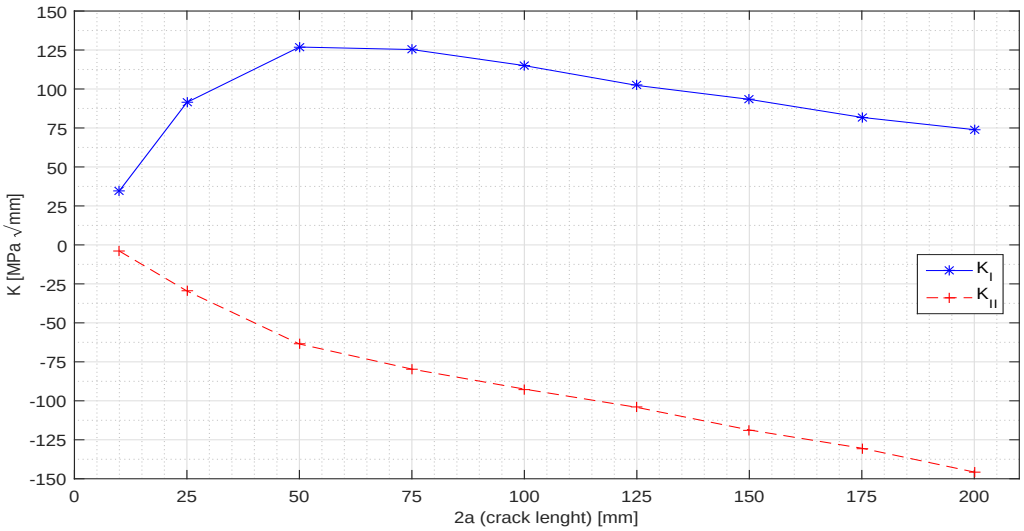


Figure 7.7: $K_I$ and $K_{II}$ versus crack length.

## 7.2 Crack Modelling using Mixed Element Models

To better understand the crack behaviour along the foremost zone of the leading edge, three crack locations, within the solid element patch previously created, were chosen: 52%, 49% and 46% of the total airfoil perimeter (Figure 7.8). The crack centres were again defined at half distance between the actuation mechanisms (680 mm from one mechanism to the other). This coincides with the centre of the structure, which is symmetric in geometry and loading. Therefore, only one crack front will be studied. Cracks were modelled as trough thickness, perpendicular to the skin surface and with their free edges parallel to the Z-axis (horizontal). The same crack lengths as on the previous section were used: 10 mm for the shortest crack, and then 25 mm to 200 mm, in 25 mm steps.

Partitioning was again used to locate and define crack geometry, namely the crack surfaces, to which a seam was assigned, and crack front. Virtual crack extension direction was defined using the crack edges on the surface of the skin (same direction and point outwards the crack). SIF values were once more extracted via *Abaqus* J-integral approach. Local mesh refinement and conformation to the crack geometry lead to the use of further partitions. This was done on a case by case basis, depending on the convergence of the SIF values extracted. To ensure a coherent mesh, not only was the solid elements patch partitioned, but also the shell elements skin where necessary.

Both 8-noded linear (C3D8R) and 20-noded quadratic (C3D20R) brick elements with reduced integration were used. Linear elements were primarily used in the partitions not adjacent to the crack location (which were not covered by the J-Integral contours), but sometimes also in these zones. It was found that, although these two types of elements yielded different results when modelling[a] the full solid model, the SIF values extracted did not show major differences. It was also found that convergence was influenced by the element type, for each case. Therefore, for each case, the best parameters were found and results extracted using them. These adjustments will be further discussed with an exemplifying comparison.

As final introductory note, a consideration about the coordinate systems used: unless stated otherwise, the axis used for the solid element patch , and to which the stresses plotted are referred, are those shown on Figure 7.9: 1-axis is tangent to the surface, 2-axis perpendicular, and 3-axis is parallel to the Z-axis.

[a] remember section 6.2

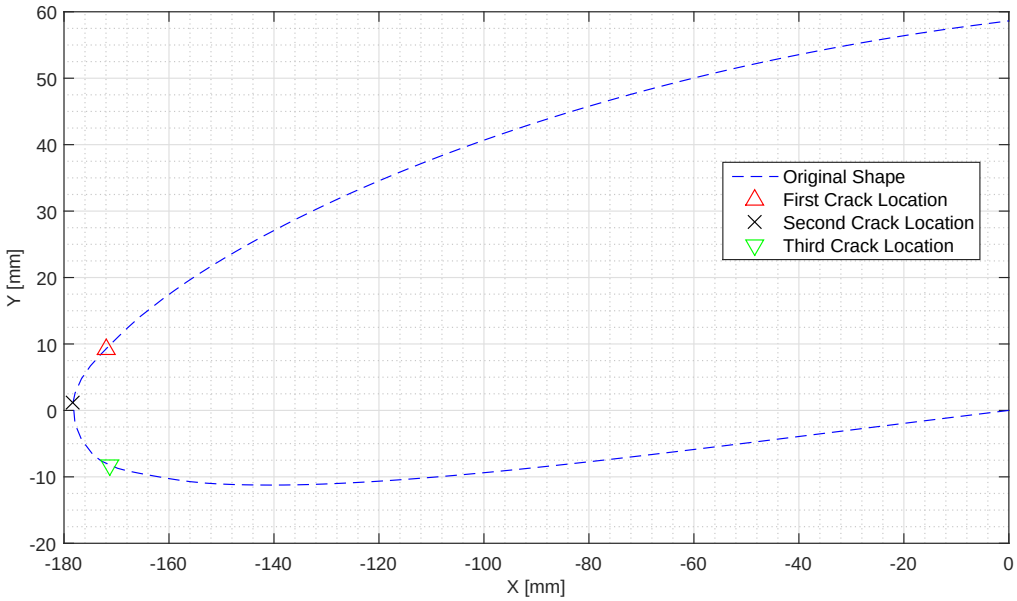


Figure 7.8: Crack locations.

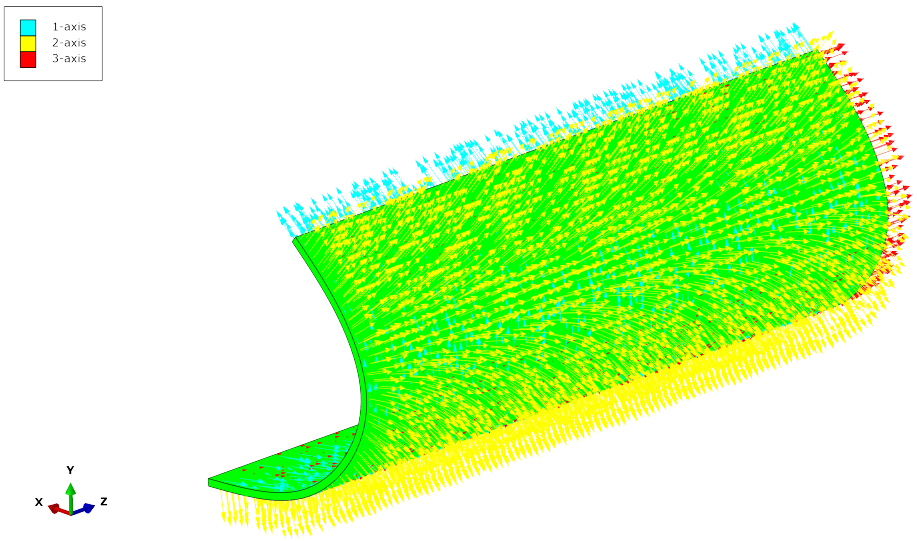


Figure 7.9: Axis system used.

## 7.3 First Crack Location

The first crack simulated was located at 52% of the perimeter (Figure 7.10), and served as basis to several studies. An assessment of the influence of the type of element on the values of the extracted SIFs was conducted, as well as extraction of the SIF values for the crack length range previously mentioned. Additionally, is it was considered interesting to evaluate the SIFs values not only for the final morphed configuration, but also for the intermediate states (using unitary steps from 0 to 5 mm).

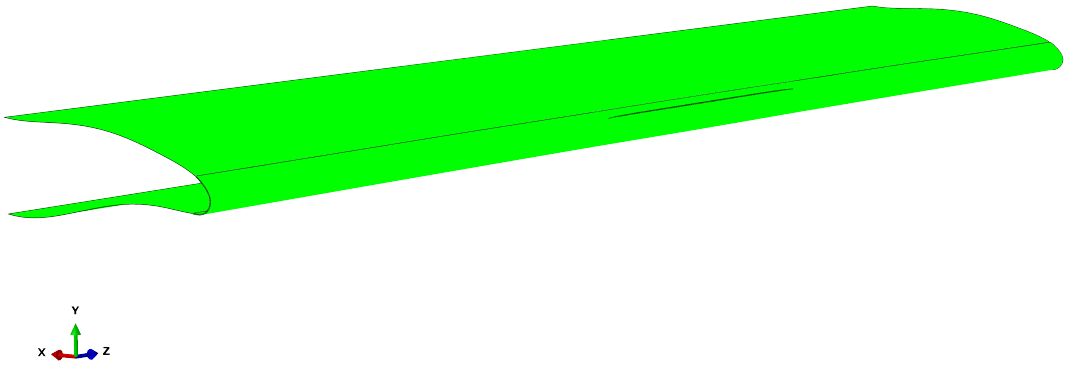


Figure 7.10: First crack location. Amplified deformed shape (2x) for $2a = 200$ mm.

### 7.3.1 Stress Intensity Factor along Thickness and Element Type Influence

To understand if linear and quadratic elements yielded significantly different values of the SIF and, if so, to evaluate the difference, a model containing a crack with length $2a = 25$ mm was used. The deformed shape of the leading edge cracked zone is shown in Figures 7.11a and 7.11b, both using a XY plane view and the latter being a cut by half of the crack. Notice the interpenetration of the crack surfaces, and the existence of a bulging effect of the skin in both upper and lower crack vicinities.

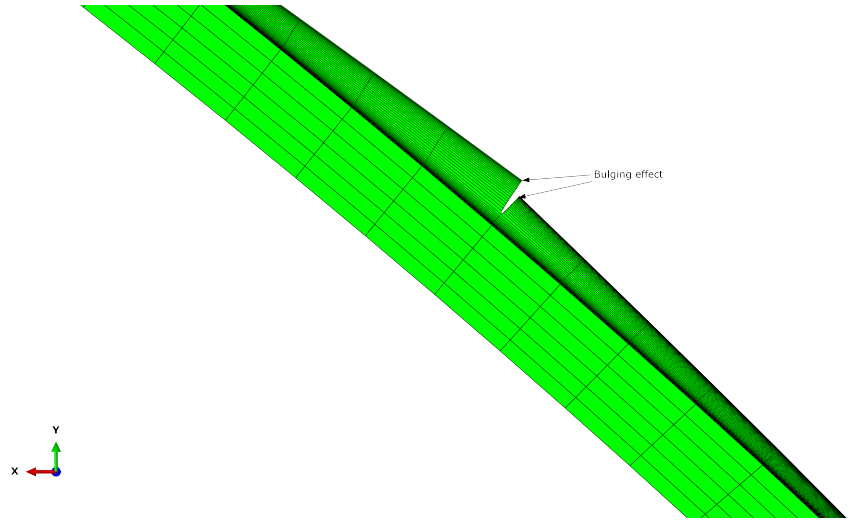


(a)

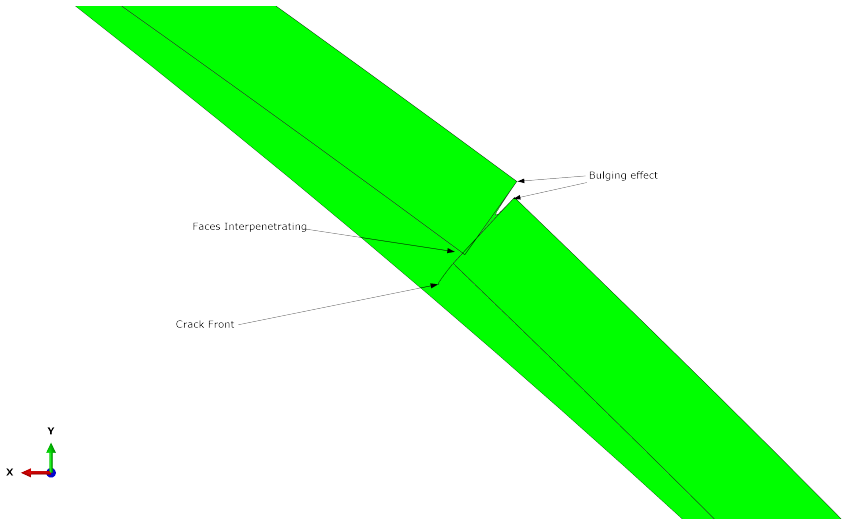


(b)

Figure 7.11: Deformed shape of the crack zone.

Simulations were run using both linear and quadratic elements above mentioned. 6 elements along the thickness ($t = 0.5$ mm) and mesh was refined until acceptable convergence was achieved. This deserves a comment: originally, and considering the results from section 6.2, quadratic elements were being used. However, a very fine mesh was needed to achieve convergence, and this led to greater computation times. Linear elements usually yield shorter calculation times, so it was tried to assign these elements to the mesh in use and understand if this solution was valid. The validity of the solution

will be discussed in the next paragraphs, but it is important to mention that linear elements led to computation times 50% lower, if not more.

The values of the SIF along the thickness of the skin were recorded. Since *Abaqus* J-Integral approach does not provide reliable values for SIF on the crack line extremities, these values were not considered. Therefore, 5 values were registered for linear elements (C3D8R), and 11 for quadratic ones (C3D20R). The values were recorded from the exterior to the interior of the skin. Percentage difference was calculated using as reference the values obtained from the quadratic mesh. Table 7.1 details the values obtained, and from it, several conclusions can be drawn.

First of all, several negative $K_I$ values arise. These are due to the bending of the skin, resulting in compressive normal stresses on the crack front from about middle thickness to the interior as seen on Figure 7.13 (S11 is the stress normal to the crack plane, responsible for crack mode I). This bending effect forces the interior part of the top surface of the crack to penetrate the lower face, as seen in the cuts of Figures 7.11a and 7.11b. These results have no physical meaning. Therefore, negative $K_I$ values will be only used for curve fitting, and otherwise disregarded.

Concerning modes II and III, values of $K_{II}$ and $K_{III}$ are not of the same magnitude order of $K_I$. They also show varying signs, but this depends on the distribution of the corresponding shear stresses on the crack plane. Remembering the axis from Figure 7.9, S13 (Figure 7.14) is the shear stress on the crack plane and perpendicular to the crack front, relevant for crack mode II. This stress field plot is symmetric about the skin's middle surface, but with different signs. This explains the approximate absolute value of the mode II SIFs for thickness points at the same distance from the middle surface. For mode III, relevant stress is S12 (Figure 7.15), the shear stress on the crack plane and acting perpendicular to the crack front. This stress field does not present visible changes of along the thickness. However, SIFs values extracted present significant variation but not a tendency, as will be later shown. For this reason, the average value was presented and used for comparison.

The analysis of Table 7.1 alone, specially taking into account the error values, can lead to the conclusion that great discrepancies exist between the results obtained using linear or quadratic elements. However, further analysing the values retrieved, patterns are found: for mode I and II, SIF values show the same evolution as their respective relevant stresses. This does not hold true for mode III, as it shows fluctuating SIF values, more visible for the values obtained used quadratic elements.

Before further discussion of results, von Mises stress field and other relevant stress fields on crack vicinity are shown on Figures 7.12 to 7.15. These results were obtained with quadratic elements, and the plots show a zoom on the crack, cut by a plane perpendicular to crack at its half-length.

Table 7.1: SIFs obtained from both linear and quadratic elements

| Thickness Point [mm] | $K_I$ $[MPa\sqrt{mm}]$ | | $Diff.$ | $K_{II}$ $[MPa\sqrt{mm}]$ | | $Diff.$ | $K_{III}$ $[MPa\sqrt{mm}]$ | | $Diff.$ |
|---|---|---|---|---|---|---|---|---|---|
| | C3D8R | C3D20R | | C3D8R | C3D20R | | C3D8R | C3D20R | |
| 0.000 | | | | | | | | | |
| 0.042 | | 508.1 | | | 31.8 | | | 8.0 | |
| 0.083 | 370.0 | 370.6 | -0.2% | 29.5 | 42.1 | –30.0% | 32.3 | 43.4 | -25.7% |
| 0.125 | | 321.1 | | | 19.6 | | | 16.8 | |
| 0.167 | 211.6 | 217.5 | -2.7% | 12.0 | 20.4 | -41.3% | 41.2 | 126.6 | -67.4% |
| 0.208 | | 139.4 | | | 6.0 | | | 19.4 | |
| 0.250 | 52.5 | 47.7 | 10.0% | -4.4 | -1.7 | 163.4% | 23.9 | 58.4 | -59.0% |
| 0.292 | | -40.2 | | | -7.5 | | | 18.1 | |
| 0.333 | -106.9 | -124.9 | -14.4% | -20.3 | -21.8 | -6.9% | 41.8 | 123.6 | -66.2% |
| 0.375 | | -222.4 | | | -21.5 | | | 11.8 | |
| 0.417 | -266.6 | -278.2 | -4.2% | -38.3 | -46.9 | -18.3% | 16.4 | -54.7 | -130.0% |
| 0.458 | | -410.3 | | | -34.0 | | | -0.3 | |
| 0.500 | | | | | | | | | |
| | | | | | | Average | 31.1 | 33.73 | -7.7% |

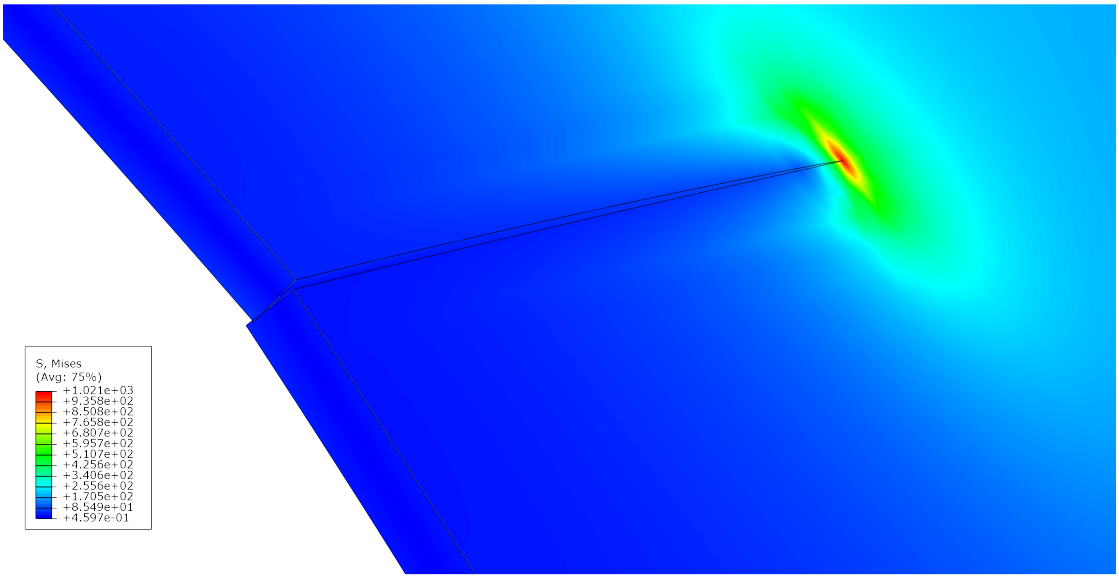


Figure 7.12: von Mises Stress on the crack zone, cut perpendicular to the Z-axis.

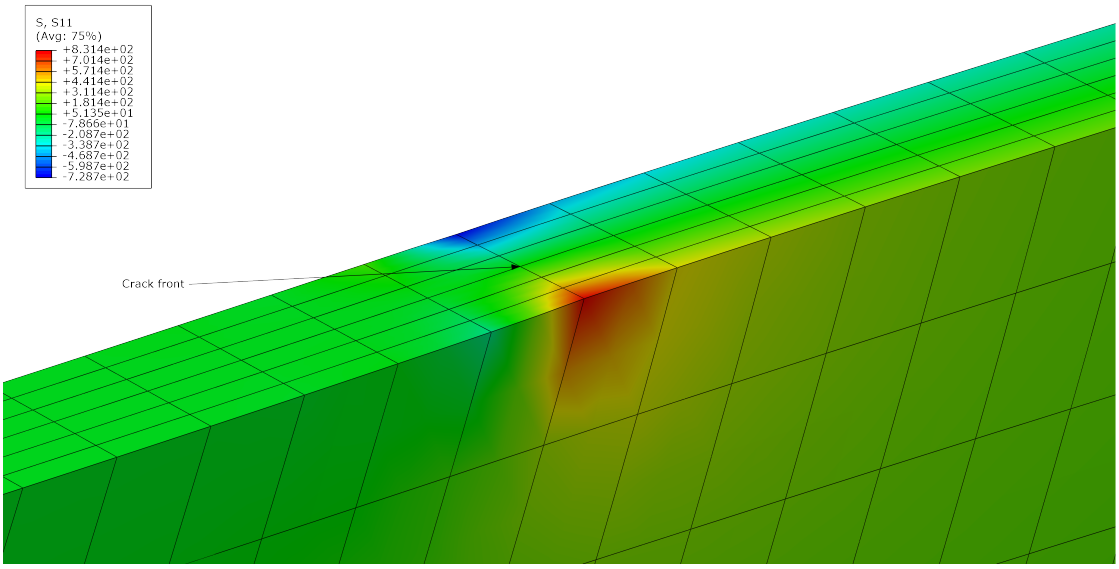


Figure 7.13: Stress normal to the crack plane.

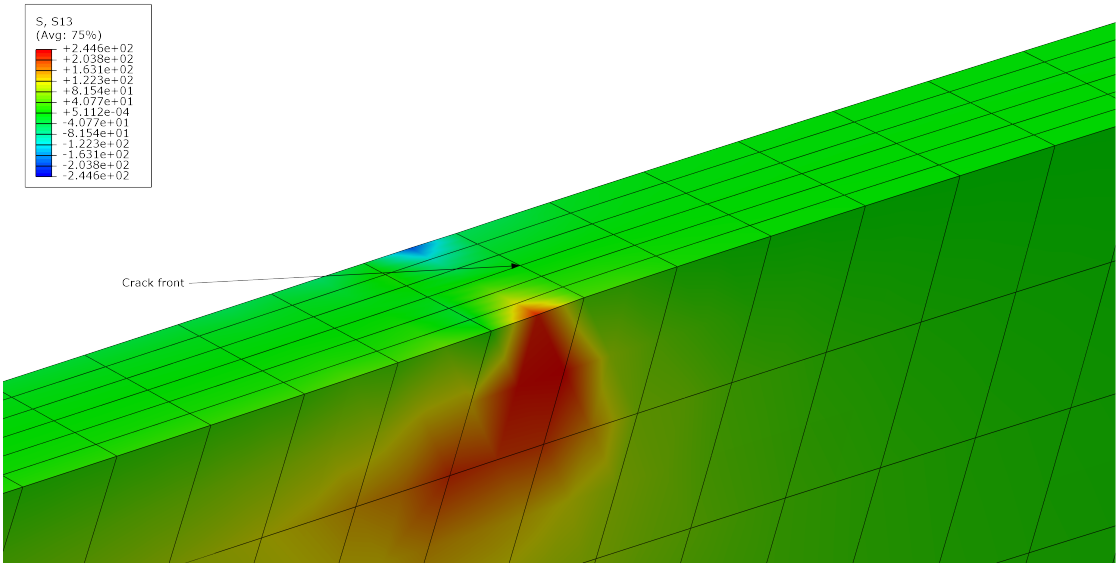


Figure 7.14: In-plane shear stress perpendicular to the crack front.

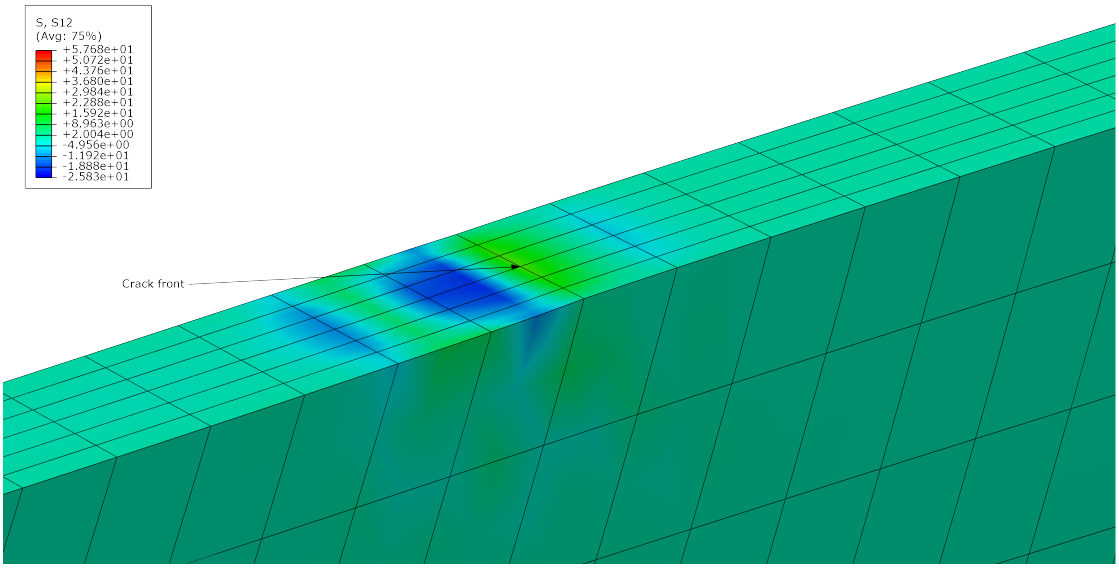


Figure 7.15: In-plane shear stress parallel to the crack front.

To better understand the evolution of the SIF along the thickness, these were graphically represented. Also, and since *Abaqus* does not provide reliable values for the crack front ends, linear regressions were fit to the points retrieved. Figures 7.16 to 7.18 show these graphics, providing better information to draw conclusions about the different values extracted.

Observing the fitted lines, trends mentioned above for mode I and II become clear, and small differences between linear and quadratic element regression lines are found. Graphics show that SIF values extracted using quadratic elements present visible fluctuations around the fitted line (correlation is slightly worse in these cases). This is visible, for instance, on the $K_{II}$ along thickness plot (Figure 7.17). For mode III, both element types yield fluctuating $K_{III}$ values, although quadratic elements exacerbate this behaviour. However, average $K_{III}$ values, around which the plots seem to fluctuate, only differ about 8% (Table 7.1), justifying the use of these average values. Also, and since $K_{III}$ average value is roughly 20 times lower than $K_I$ maximum value, its influence on crack behaviour was considered of minor importance. Therefore, any error associated with the use of average values is not of great concern.

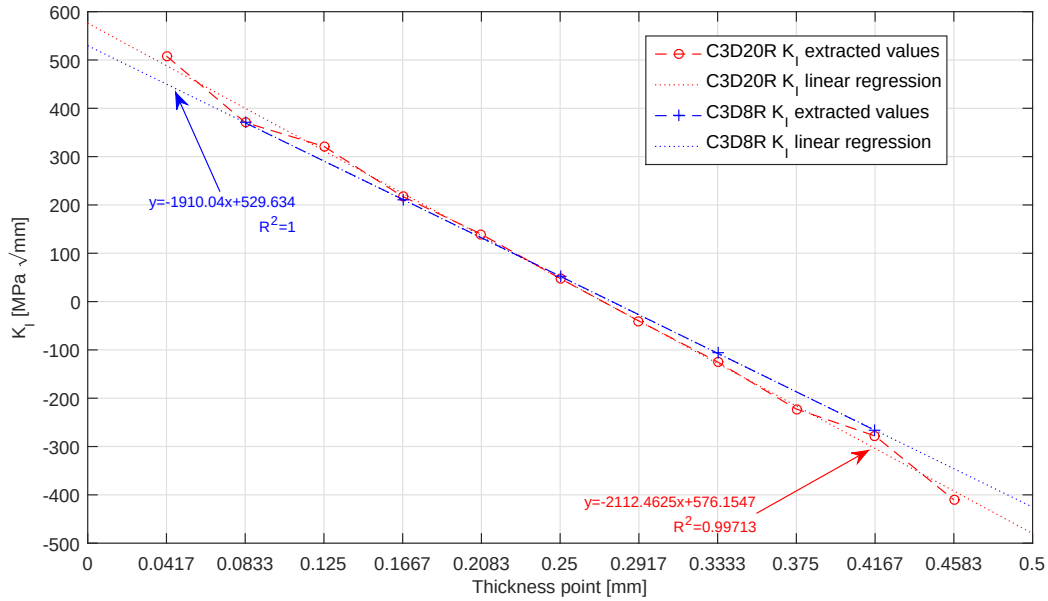


Figure 7.16: $K_I$ along thickness for both element types and fitted lines.

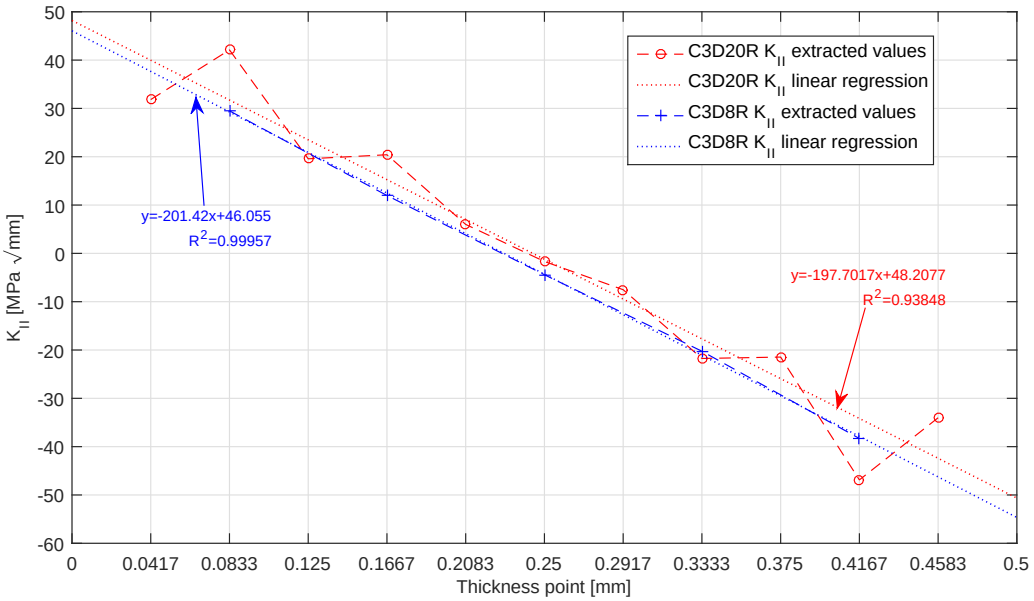


Figure 7.17: $K_{II}$ along thickness for both element types and fitted lines.

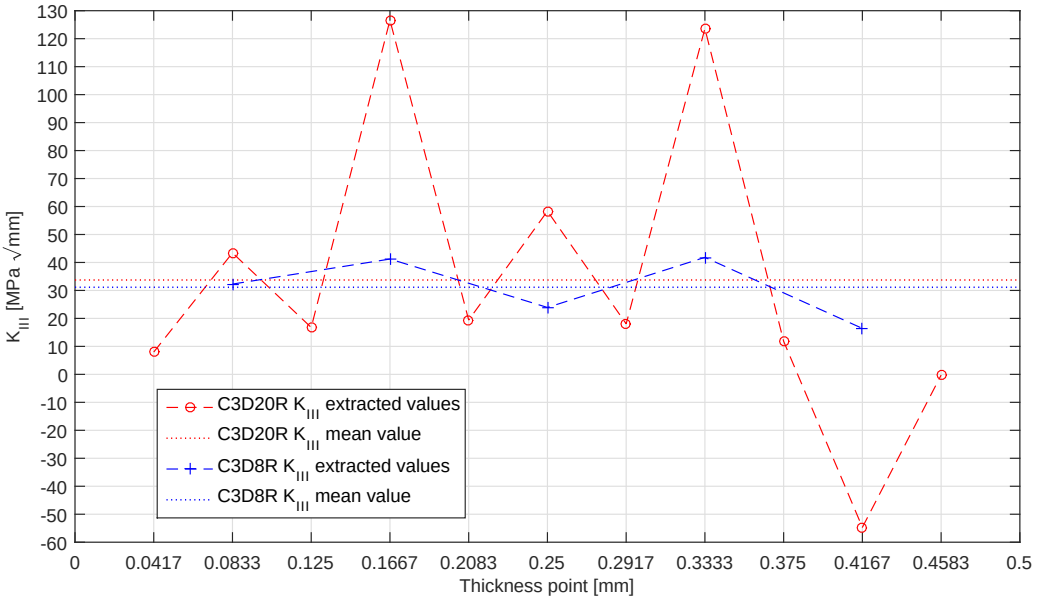


Figure 7.18: $K_{III}$ along thickness for both element types and mean values.

Some remarks in order to sum up this first study:

- It can be concluded that SIF values extracted using *Abaqus* J-Integral approach show only minor differences due to element type.

- *Abaqus* retrieves negative $K_1$ values for the crack tip zones under compressive normal stresses. These values have no physical meaning and will only be used for line fitting.

- It was shown that, for mode I and II, linear regressions provide good correlation, thus validating the use of this technique to extract SIF values for the crack front ends.

- For mode III, the $K_{III}$ values extracted fluctuated significantly. This behaviour was unpredicted, as it does not match the shear stress field aspect that drives crack opening mode III (Figure 7.15).

- However, it was shown the average $K_{III}$ values for both element types are close and low in comparison with the $K_I$ maximum value, therefore minimizing possible errors arising from this simplification.

### 7.3.2 Stress Intensity Factor versus Crack Length

To understand the crack propagation behaviour, it is important to obtain the curve of the SIF values for several crack lengths. As mentioned before, this was done by simulating cracks with increasing lengths and extracting SIF values for each case. Based on the conclusions of section 7.3.1, linear elements were used, since this type of element provided results faster and with better convergence (the latter being the chief reason for the choice).

SIF values were extracted along the thickness for each model. Using linear regression, lines were fitted to $K_I$ and $K_{II}$ values, and the exterior, interior and middle surface SIFs were calculated. Recalling again the conclusions of section 7.3.1, for mode I, only positive SIF values were plotted, and for mode III, average values were used. Figures 7.19 to 7.21 show the evolution of the SIFs with the increase of the crack length $2a$, and enable the analysis of the behaviour of this group of cracks.

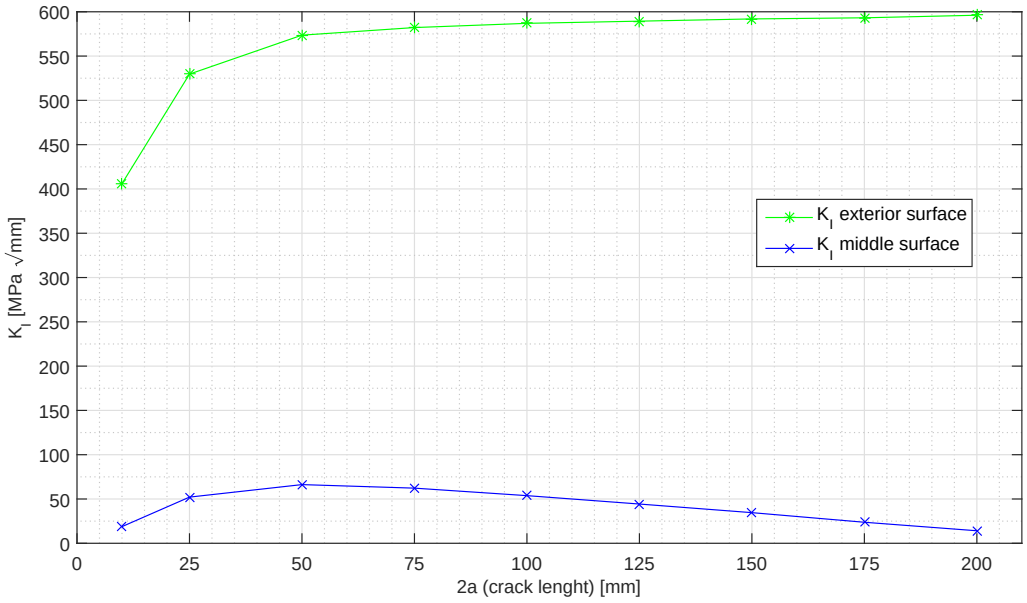


Figure 7.19: $K_I$ versus crack length.

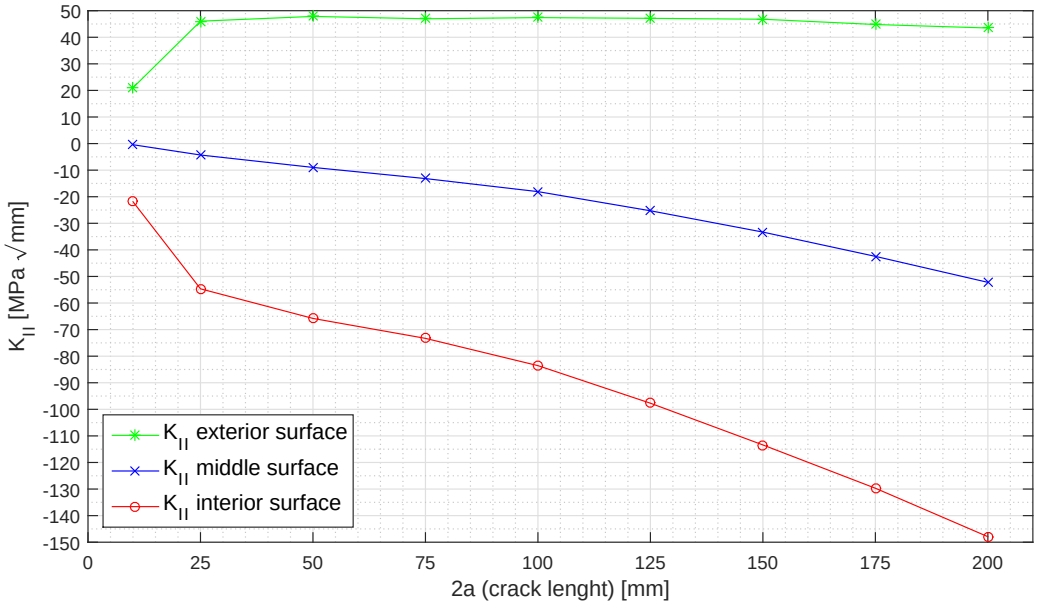


Figure 7.20: $K_{II}$ versus crack length.

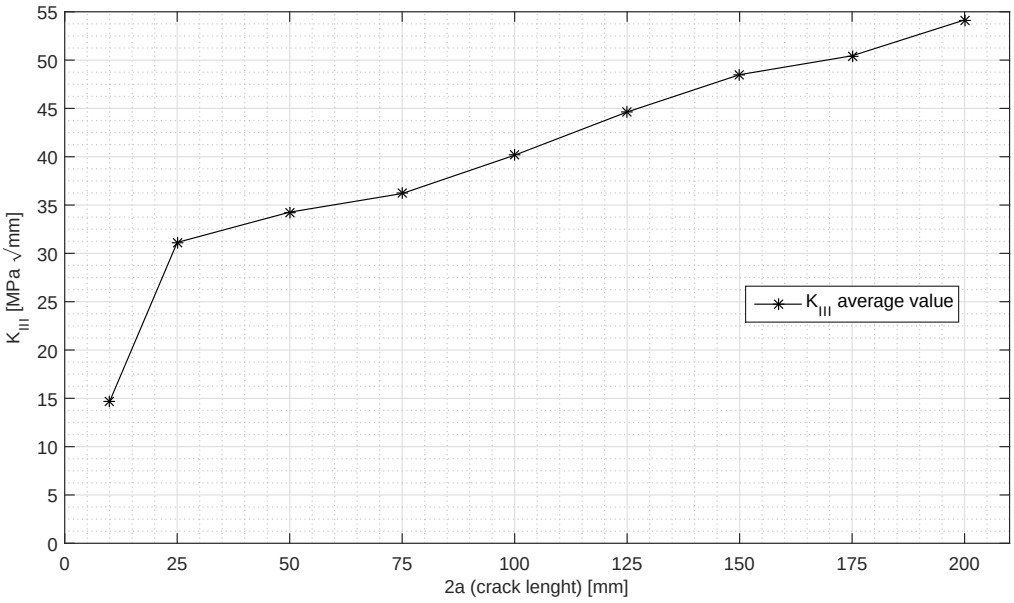


Figure 7.21: $K_{III}$ versus crack length.

The first conclusion taken from these three Figures is that mode I is the predominant opening mode in this location. In fact, for each crack length and in the exterior end of the crack front, for instance, values of $K_I$ are at least 10 times greater than those of $K_{II}$ and $K_{III}$.

Concerning the SIF values, it is interesting to note that $K_I$ values tend to stabilize after a certain crack length. This is contrary to the what happens on the basic fracture mechanics case of the infinite plate with a central crack and subjected to a remote uniform tensile stress. In this case, $\lim_{a\to\infty} K_I = \infty$. However, this behaviour is found on a infinite strip, of width $b$, containing a longitudinal crack and subjected to a certain stretch in the vertical direction. This problem as been studied and mentioned by several authors (Knauss 1966; Rice 1967; Fichter 1967; Isida 1971; pp. 88-89, Murakami, 1987; pp. 17.1-18.3, Tada et al., 2000; pp.130-133, Kundu, 2008). It has been shown that, for the same vertical stretch, the SIF values stabilize and even tend to lower values when the ratio $a/b$ increases sufficiently (Isida, 1971).

### 7.3.3 Stress Intensity Factor versus actuation

A last study was conducted for this first crack configuration, to understand the how the SIFs values during the morphing action. The model used, containing a crack with length $2a = 25$ mm, was the same used on section 7.3.1. Accordingly, the same mesh was

used, with 6 elements along the thickness.It was chosen to keep the linear mesh, since it provided good results.

Five simulation steps were used to mimic the increasing horizontal input on the lower arms of the compliant mechanism from 1 to 5mm. The 0mm displacement condition was not simulated, since it is the unloaded original state which would yield, necessarily, null SIF values. For each step, the SIF values along the thickness were retrieved. These will not be shown as it would require 15 graphics (3 modes times 5 steps) that would add little information to that given by Figures 7.16 to 7.18. For each case, linear regression were used to fitted to the points and the SIF values on both ends and the middle of the crack front were calculated. The mentioned linear regressions provided very good correlation, with the minimum coefficient of determination being $R^2 = 0.99955$.

The evolution of the 3 modes SIFs is shown on Figures 7.22 to 7.24. Lines were fitted using linear regressions, which again provided near perfect correlation. Mode III was the exception, but this is due to the use of average values and correlation is, nevertheless, quite good. Therefore, the present results show a linear elastic behaviour, as expected given the use of linear elastic FEM software.

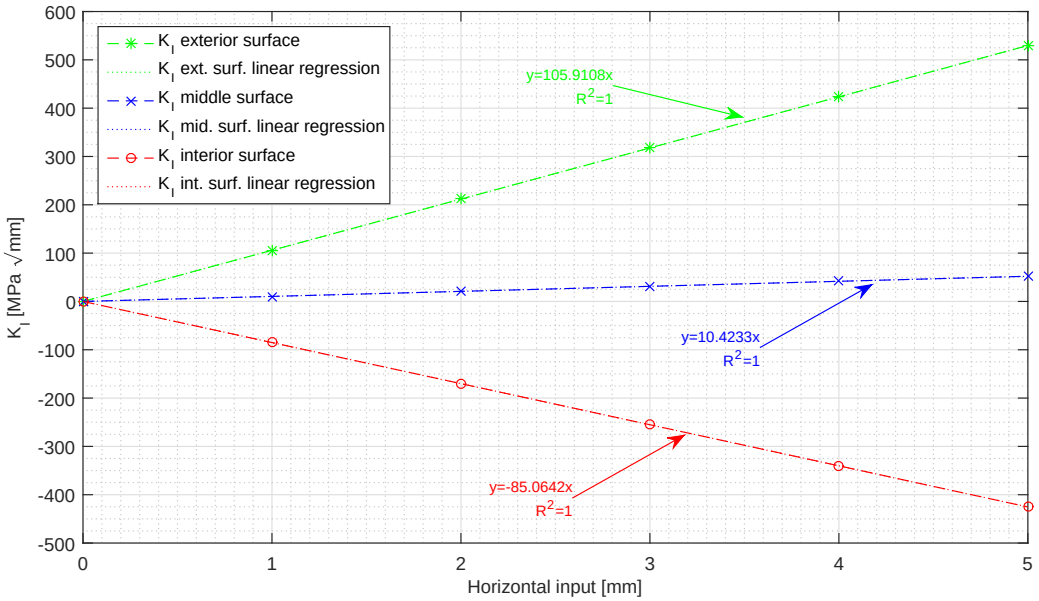


Figure 7.22: $K_I$ versus horizontal input, $2a = 25$ mm.

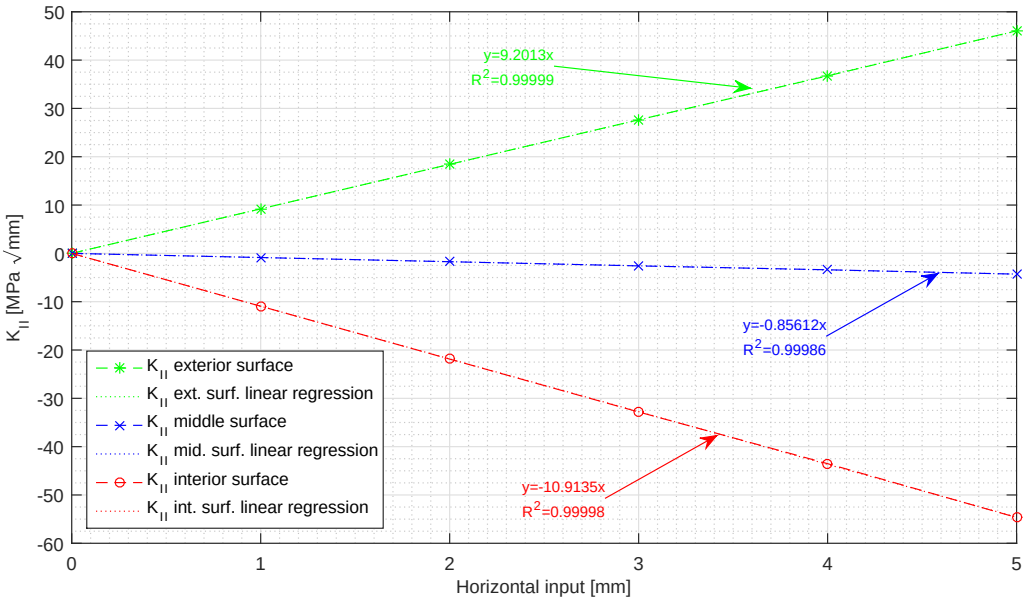


Figure 7.23: $K_{II}$ versus horizontal input, $2a = 25$ mm.

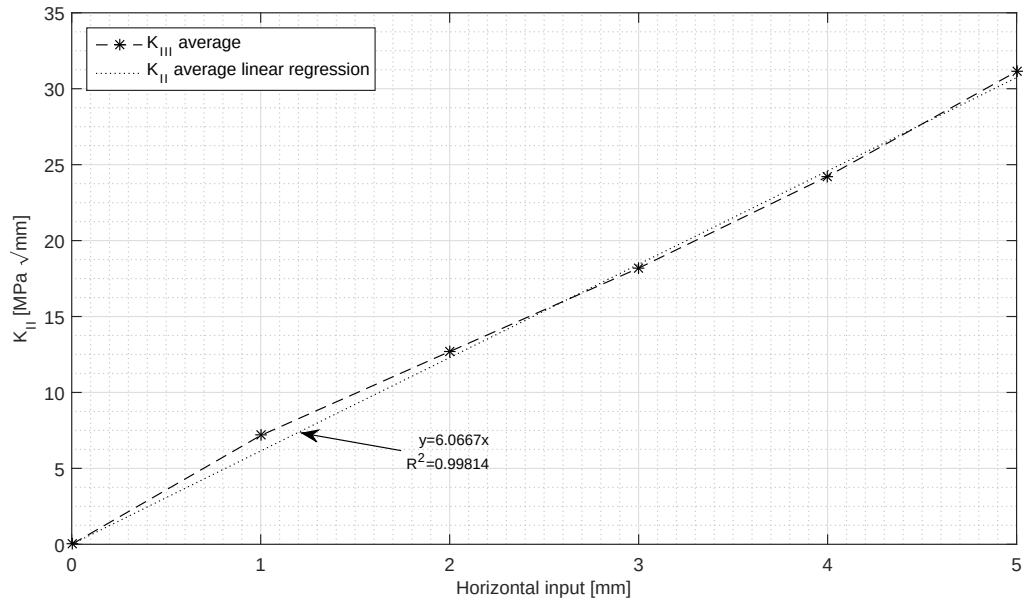


150

or150 or

Figure 7.24: $K_{III}$ versus horizontal input, $2a = 25$ mm.

## 7.4 Second Crack Location

The second crack simulated was located at 49% of the perimeter (Figure 7.25). SIF evolution along thickness was again studied, and SIF values were extracted for the crack lengths used on the last section.

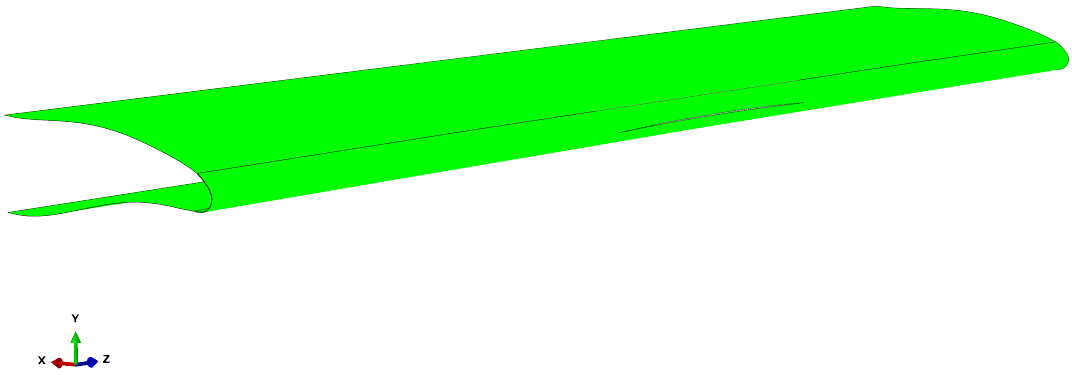


Figure 7.25: Second crack location. Amplified deformed shape (2x) for $2a = 200$ mm.

### 7.4.1 Stress Intensity Factor along Thickness

As done in section 7.3.1, a model containing a crack with length $2a = 25$ mm was used. This time, simulations were run quadratic elements and 6 elements along the thickness ($t = 0.5$ mm). Quadratic elements were chosen since linear elements did not provide convergent values. Also, due to the curvature of this location, careful meshing was needed until acceptable convergence was achieved. As mentioned before, *Abaqus* User's Manual states that "obtaining accurate contour integral results for a crack in a three-dimensional curved surface can be quite cumbersome" (Dassault Systèmes, 2016).

Figures 7.26a and 7.26b represent the deformed shape of the leading edge cracked zone, as done for the first crack. For this case, the bulging effect is more pronounced on the upper crack half.

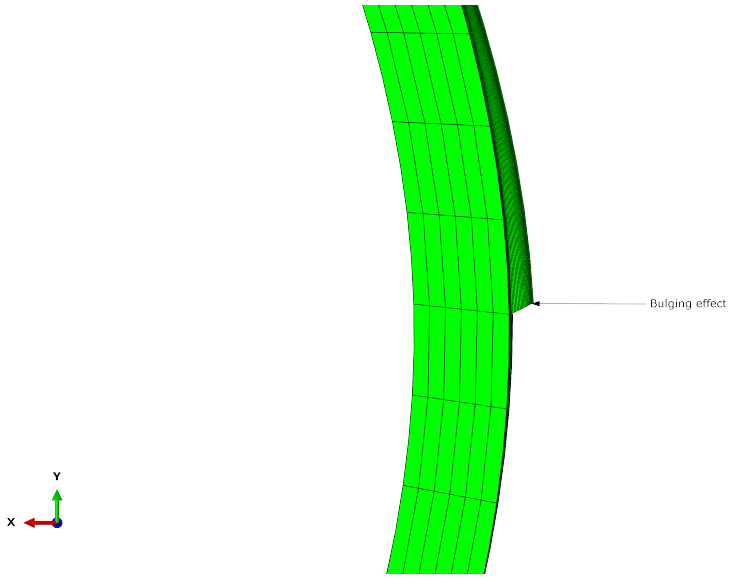


(a)

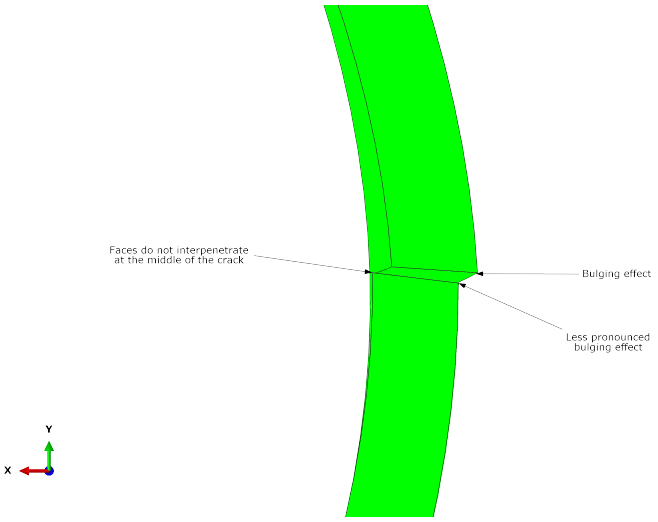


(b)

Figure 7.26: Deformed shape of the crack zone.

The SIF values along the thickness were recorded, and again the values for crack line extremities were not considered. 11 values were recorded, from the exterior to the interior of the skin. The relevant stress fields were again plotted using a zoom on the crack, cut by a plane perpendicular to crack at its half-length, and are shown on Figures 7.27 to 7.30.

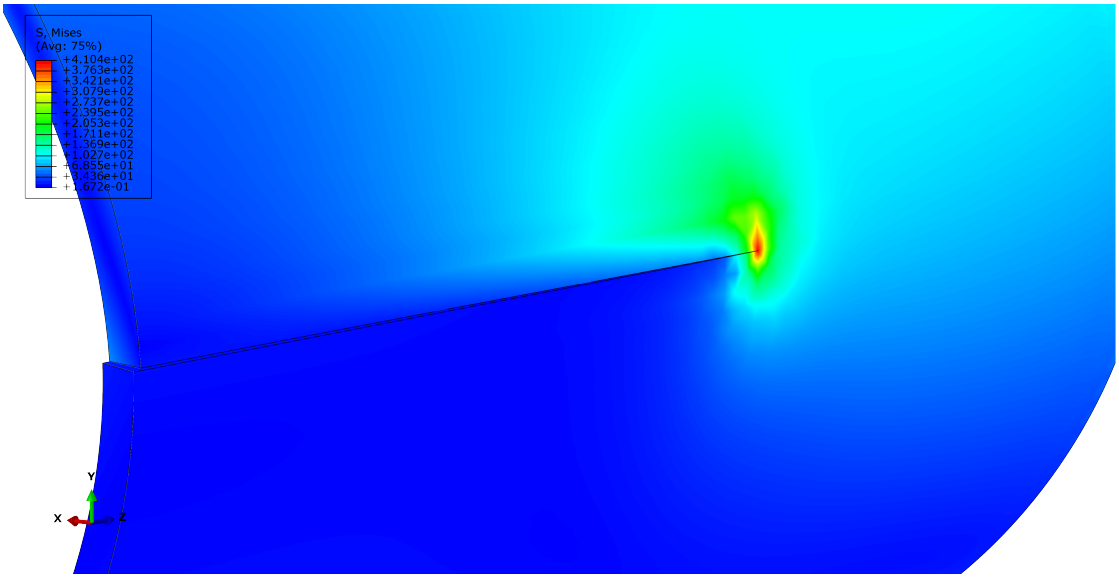


Figure 7.27: von Mises stress on the second crack zone, cut perpendicular to the Z-axis.

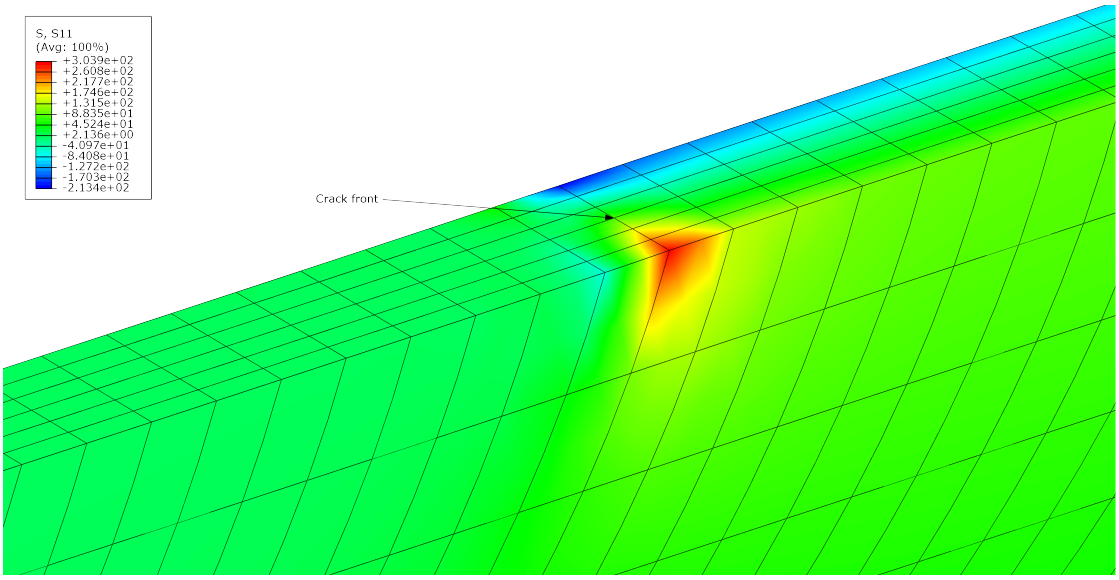


Figure 7.28: Stress normal to the second crack plane.

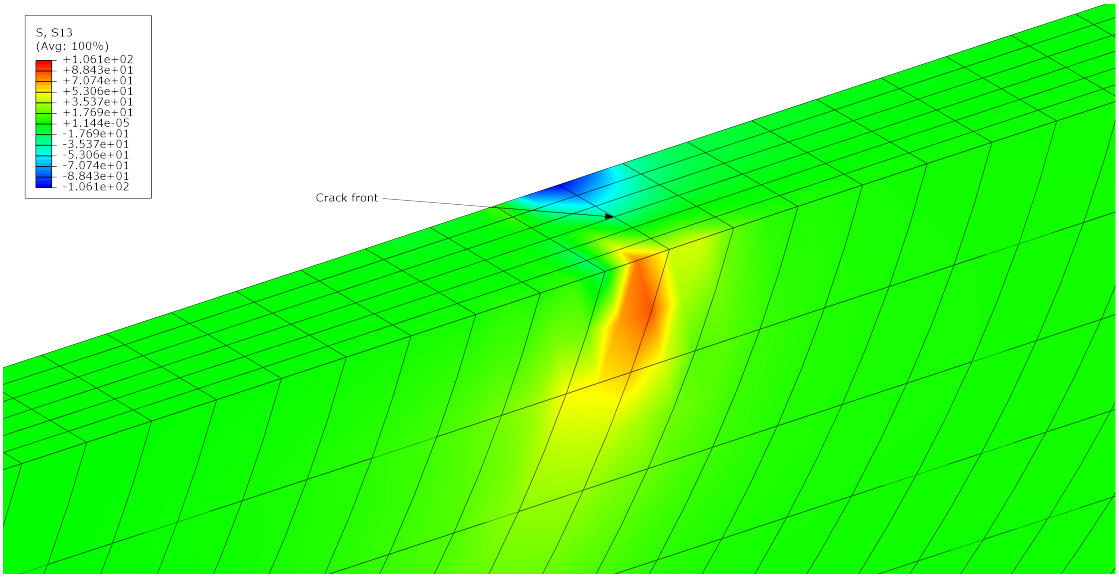


Figure 7.29: In-plane shear stress perpendicular to the second crack front.

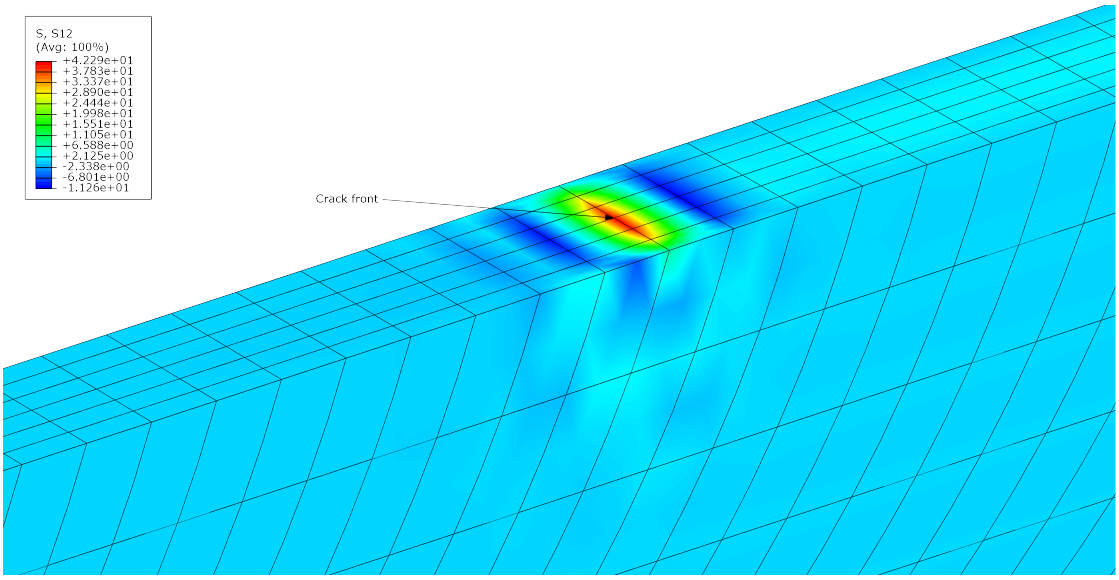


Figure 7.30: In-plane shear stress parallel to the second crack front.

These plots of the stress field plots show some similarities with those of the first case. Bending of the skin is again noticeable but, on this case, the compressive normal stresses are lower than the tensile ones This means that the bending neutral surface is not the middle surface but one nearer the inside of the skin (Figure 7.28). Thus, negative $K_I$ values occur on a smaller region, located closer to the interior zone. This is shown on Figure 7.31. Comparing the values from the graphic of this Figure with those from Figure 7.16, it can be concluded that, for this location, mode I is less severe.

S13, the shear stress on the crack plane and perpendicular to the crack front, relevant for crack mode II, does not show symmetry along the crack front. S13 absolute maximum (on the crack front) is situated on its the most interior node, where values are negative. Values gradually increase outwards, yielding positive $K_{II}$ values for the exterior zone (Figure 7.32). This can be attributed to the bulging effect being less distributed between the upper and lower surface: the material in the inside zone of the skin and immediately above the crack front stretches in the longitudinal direction to follow the bulging of the top half of the crack. However, the material in the inside zone of the skin and immediately below the crack front lower only needs to follow a less bulged surface. As a result, the shear stresses generated are higher than those of, for instance, the first case studied. It will be seen that this is aggravated be the increase of the crack length, leading to higher absolute values of $K_{II}$.

Regarding the intensity of mode II, and comparing the values from the graphic of Figure 7.35 with those from the graphic of Figure 7.20, it can be concluded that, for this crack position, mode II is more severe than for the first location, and its overall significance increases. Comparison of $K_{II}$ values with those of $K_I$ (Figure 7.34) show a increased significance of mode II on the crack front.

Concerning mode III results interpretation, one must analyse S12 (Figure 7.30), the shear stress on the crack plane an perpendicular to the crack front. This stress field presents symmetry about the middle surface, and a maximum (on the crack front) at middle of the skin thickness. However, SIFs values extracted present significant fluctuation but do not reflect these observations, as shown by Figure 7.33. For this reason, again the average value was presented and used for comparison.

The SIF values extracted for the nodes along the thickness were graphically represented, and linear regressions were fit to those points. Figures 7.31 to 150 or7.33 show these plots and trends mentioned above for mode I and II become clear, although some fluctuations occur, perfectly noticeable on the $K_{II}$ along thickness plot (Figure 7.32, note that these fluctuations seem to follow a pattern).

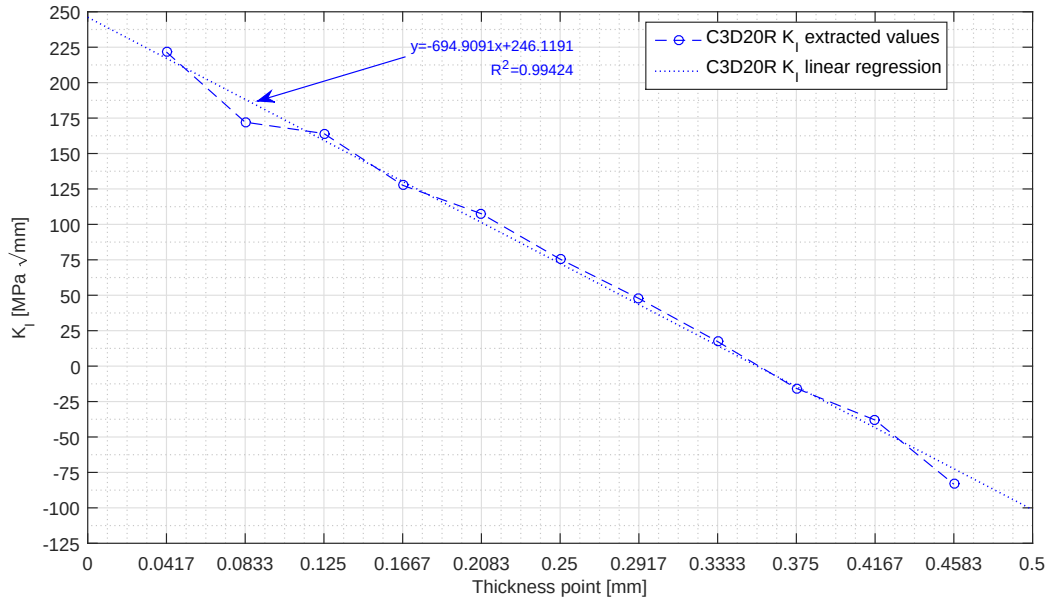


Figure 7.31: $K_I$ along thickness and fitted line.

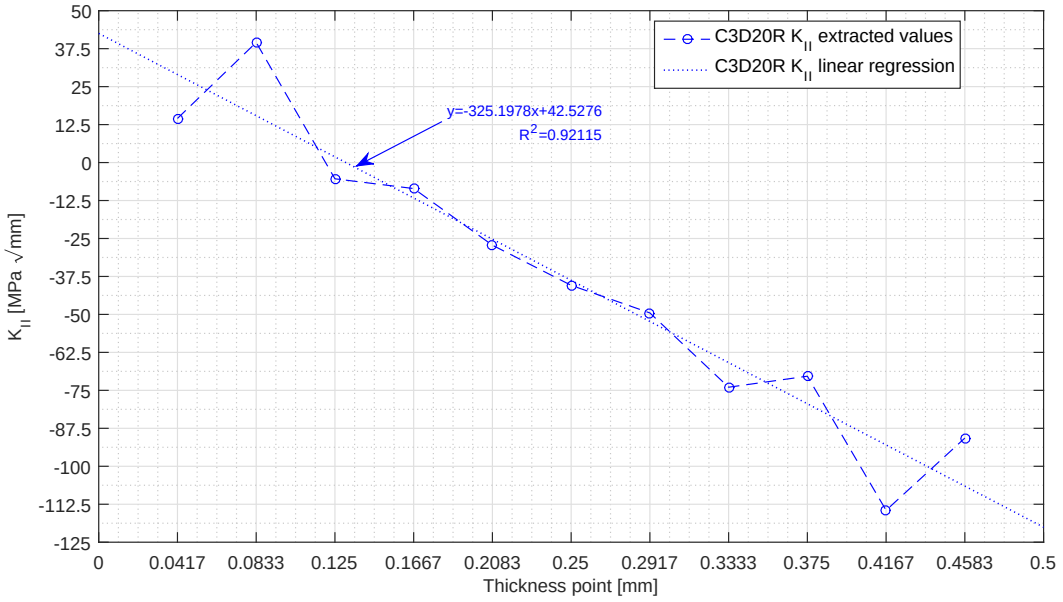


Figure 7.32: $K_{II}$ along thickness and fitted line.

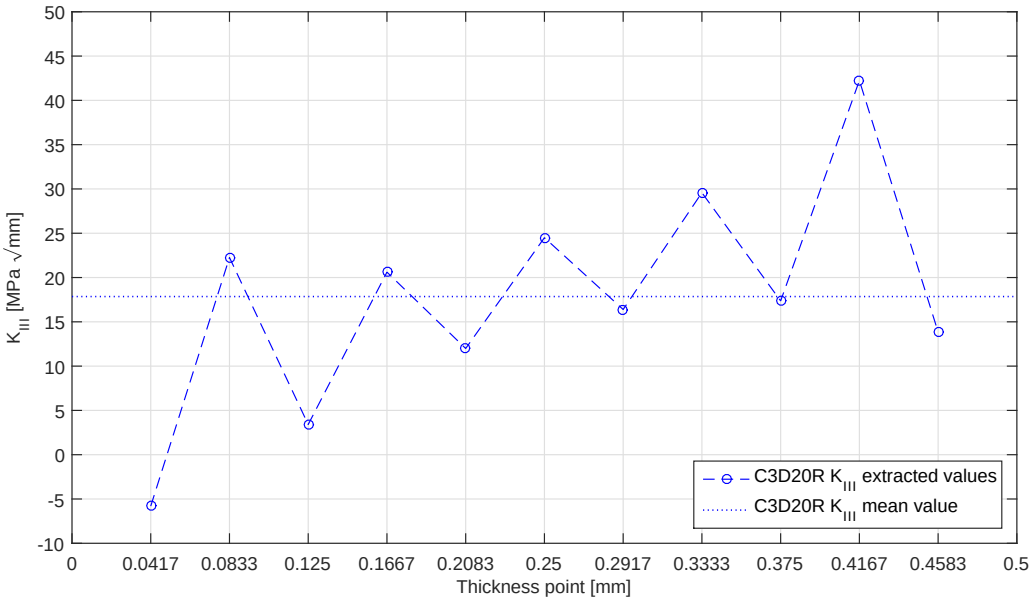


Figure 7.33: $K_{III}$ along thickness and mean value.

Summarising the conclusions of this study:

- Mode I for this crack location was found to be less intense than for the first case.
- On this location, the neutral bending surface is shifted to the interior of the skin (in compression), thus leading to less negative $K_I$ values.
- Bulging effect is more pronounced on the upper part of the crack zone. This could in part explain the asymmetry found on $K_{II}$ distribution.
- Mode II presence is more pronounced in this location, and its relevance compared to Mode I increases in this case.
- Similarly to what happened for the first crack location, $K_{III}$ values along thickness extracted significantly fluctuated, and therefore the average value was considered.
- Mode III is still of low relevance when compared with the other crack opening modes.

### 7.4.2 Stress Intensity Factor versus Crack Length

Cracks with increasing lengths located at 49% of the airfoil perimeter were modelled and SIF values extracted for each case. 20-noded quadratic brick elements with reduced integration (C3D20R) were used, as these element provided results with better convergence. The same procedure as Section 7.3.2 was carried out: only positive $K_I$ values were plotted; linear regressions were used to obtain the exterior, interior and middle surface mode I and II SIFs, and mode III average SIFs were considered. Figures 7.34 to 7.36 show the evolution of the SIFs with the increase of the crack length $2a$ for the second group of cracks.

The analysis of Figure 7.34 shows, at first sight, a behaviour similar to that found for the first case: $K_I$ values tend to stabilize after a certain crack length. Also, starting with a crack length of 100 mm, $K_I$ is positive for all locations, meaning that the crack front is completely in tension through the thickness, However, for this crack location, mode I is not as intense as for the previous one.

Figure 7.35 leads to different conclusion from those derived to the first case studied. For the second location, mode II gains importance, and for the larger cracks, on the inside end of the crack front, the absolute value of $K_{II}$ is superior to that of $K_I$. This may be explained by the exacerbation of the bulging effect. However, one must bear in mind that a crack length of 200 mm is an exaggeration, used with academic purposes only and that hardly would be found on a real situation.

Concerning mode III and Figure 7.36, and relying on the SIF values, though they do not show a coherent evolution, it can be said that this mode also suffer a slight increase on its overall presence. Bulging can play a part on this, as it induces a "scissoring" effect on the crack. However, it is wise to admit that the values extracted are not completely without errors, since convergence for mode III was difficult. Therefore, these values, although being the best obtained, must be seen with some caution.

A final remark, concerning the results obtained on section 7.1 and shown on Figure 7.7 and their comparison with those obtained in this Section. Although not numerically equal, the $K_I$ and $K_{II}$ values obtained for the shell elements and those obtained here for the middle surfaces seem to follow the same trend, and are of the same magnitude order. Considering that middle surface SIF values are considerably lower than those for the other surfaces, this proves that using solid elements was a good decision.

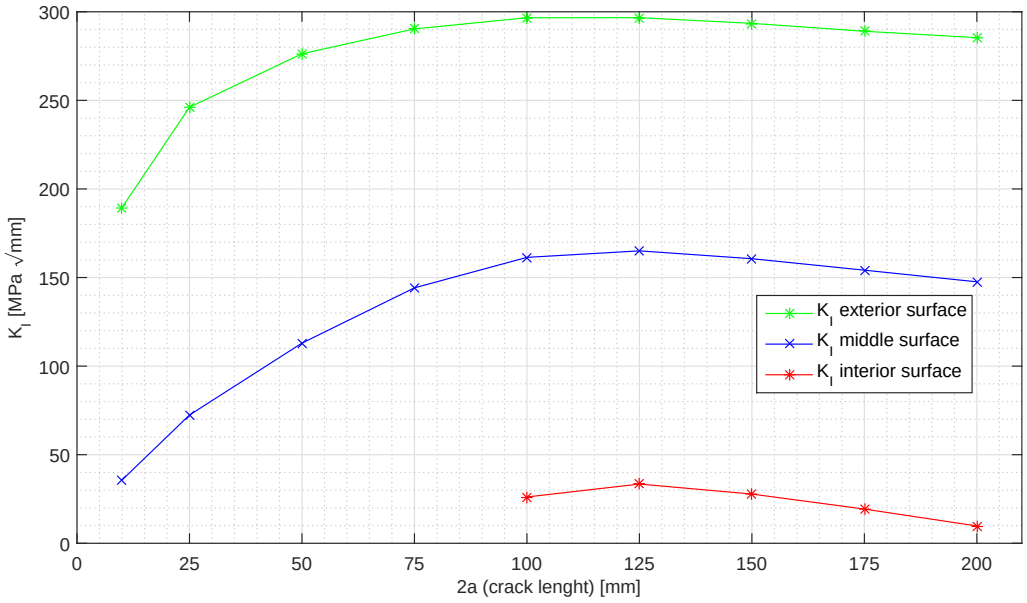


Figure 7.34: $K_I$ versus crack length.

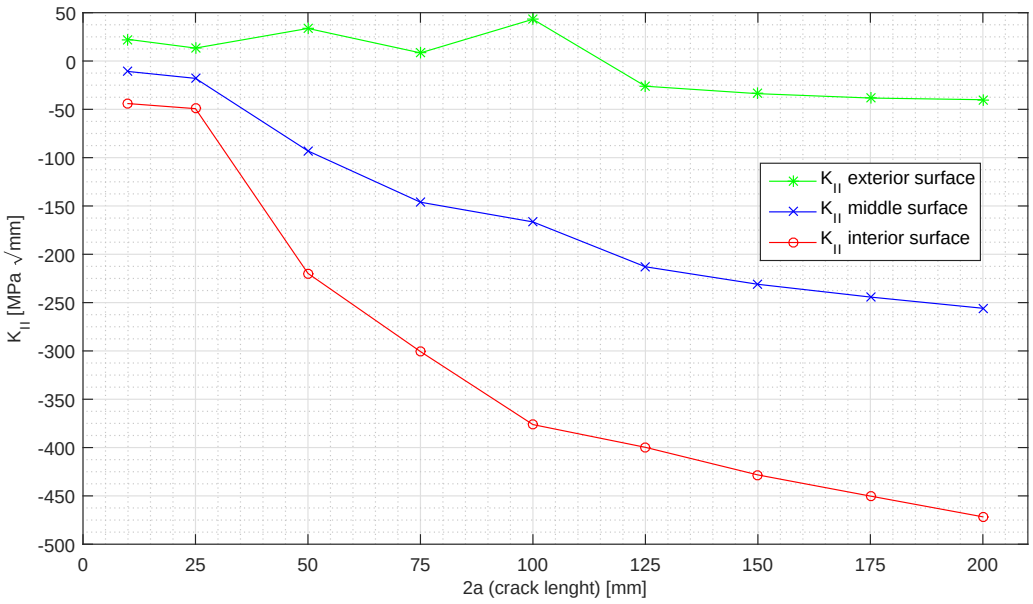


Figure 7.35: $K_{II}$ versus crack length.

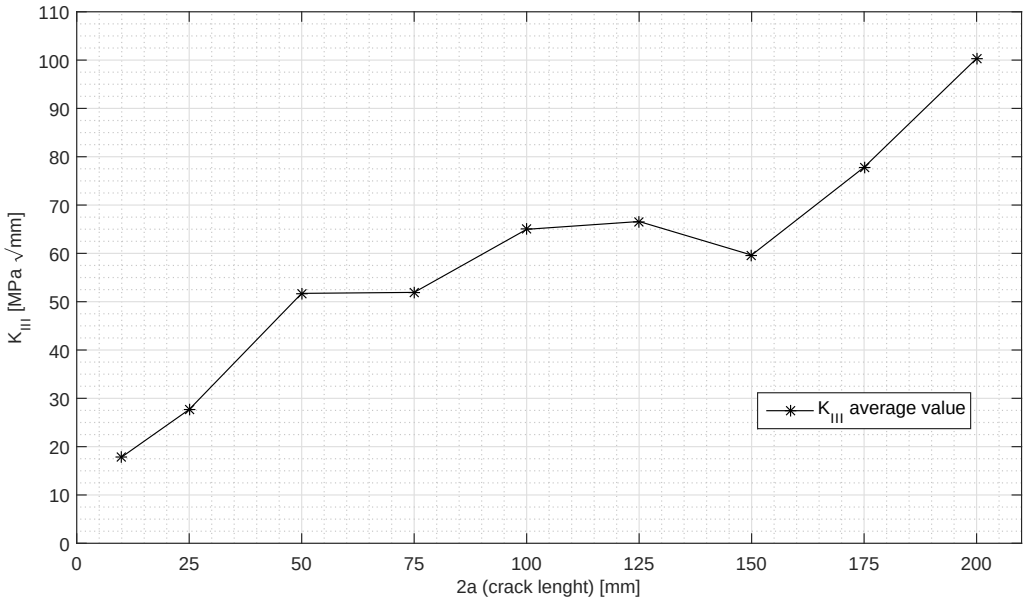


Figure 7.36: $K_{III}$ versus crack length.

## 7.5 Third Crack Location

The third crack location simulated was located at 46% of the perimeter (Figure 7.37). Likewise the previous locations, SIF evolution along thickness was studied, and SIF values were were extracted for several crack lengths.

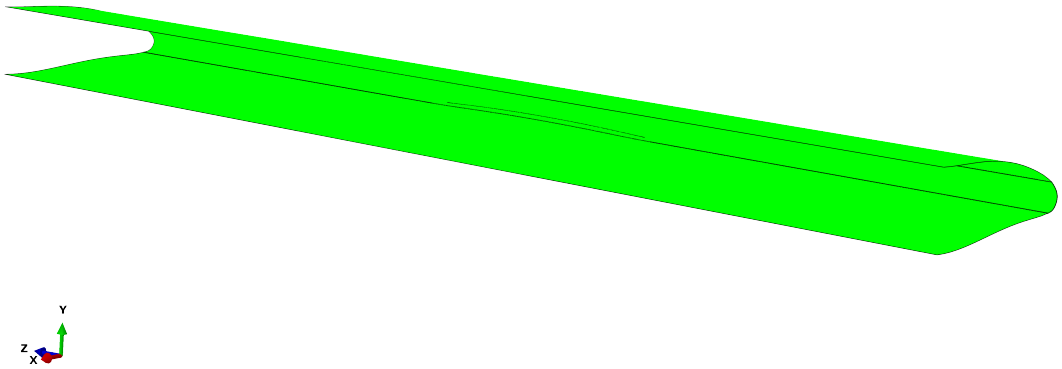


Figure 7.37: Third crack location. Inside view of the deformed shape for $2a = 200$ mm.

### 7.5.1 Stress Intensity Factor along Thickness

For this study, again a model containing a crack with length $2a = 25$ mm was used. Similarly to the second location, only quadratic elements provided convergent values. 6 elements along the thickness were used, and SIF values along for their nodes were registered, excluding the values for crack line end. Figures 7.38a and 7.38b represent the deformed shape of the leading edge cracked zone, as done for the previous cases.

Interestingly, for this case, bulging affects differently the upper and lower crack halves. The first shows the behaviour seen before, with a very small bulging to the exterior of the skin. On the other hand, the lower half shows a noticeable bulge to the interior. However, the overall bulging is less significant than on the previous case.

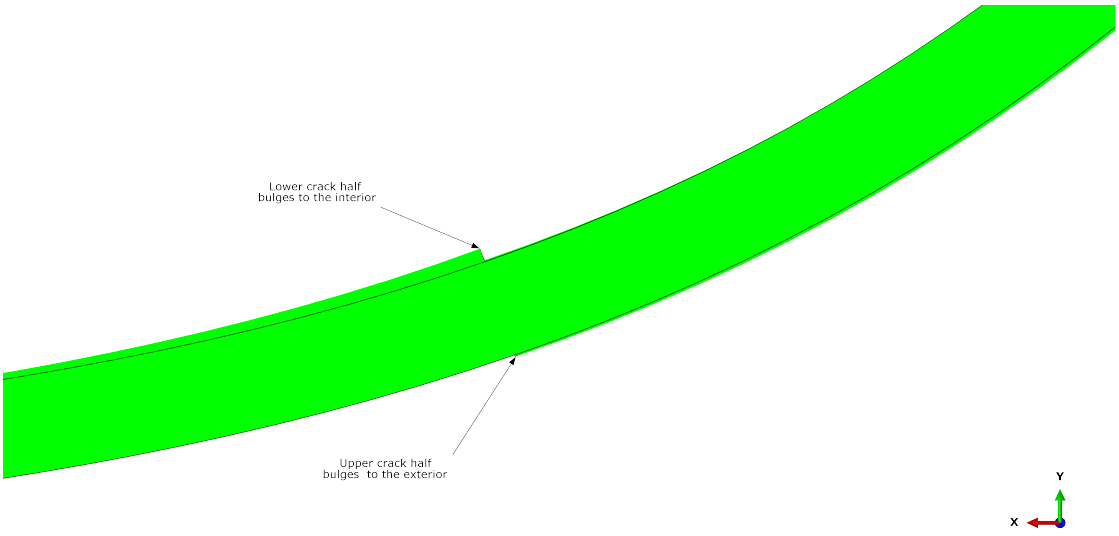


(a)

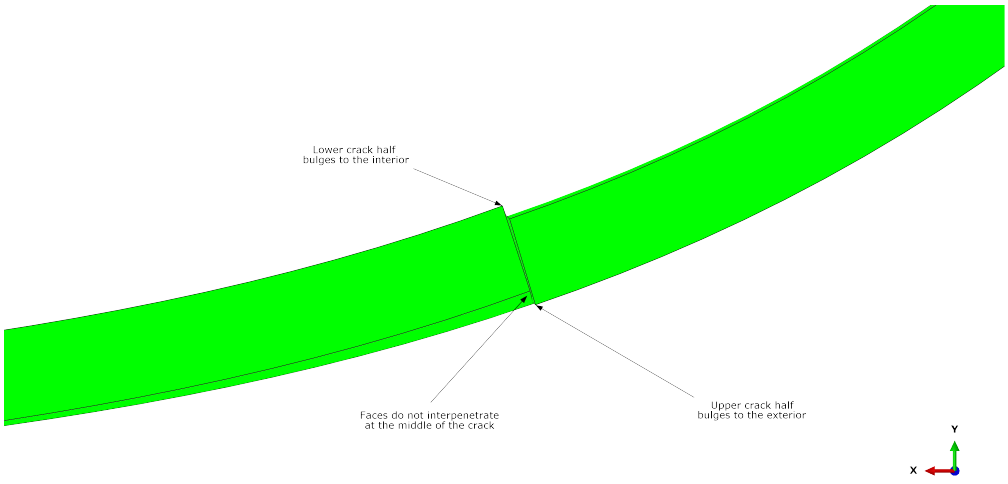


(b)

Figure 7.38: Deformed shape of the crack zone.

Due to this different bulging behaviour, the relevant stress fields on the crack zone were, this time, plotted over a zoomed cut by the upper (less bulged) crack face. This was due to ensure that the stress fields were easily comparable, since previously the stress field were plotted on the crack plane with the more bulged half "removed". The stress fields are shown on Figures 7.39 to 7.42.

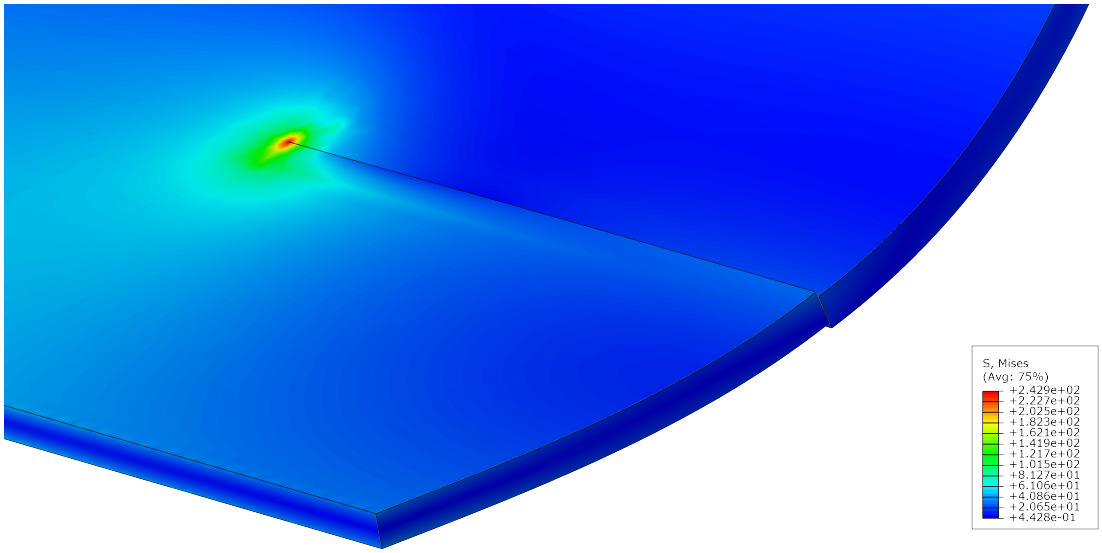


Figure 7.39: von Mises stress on the third crack zone, cut perpendicular to the Z-axis.

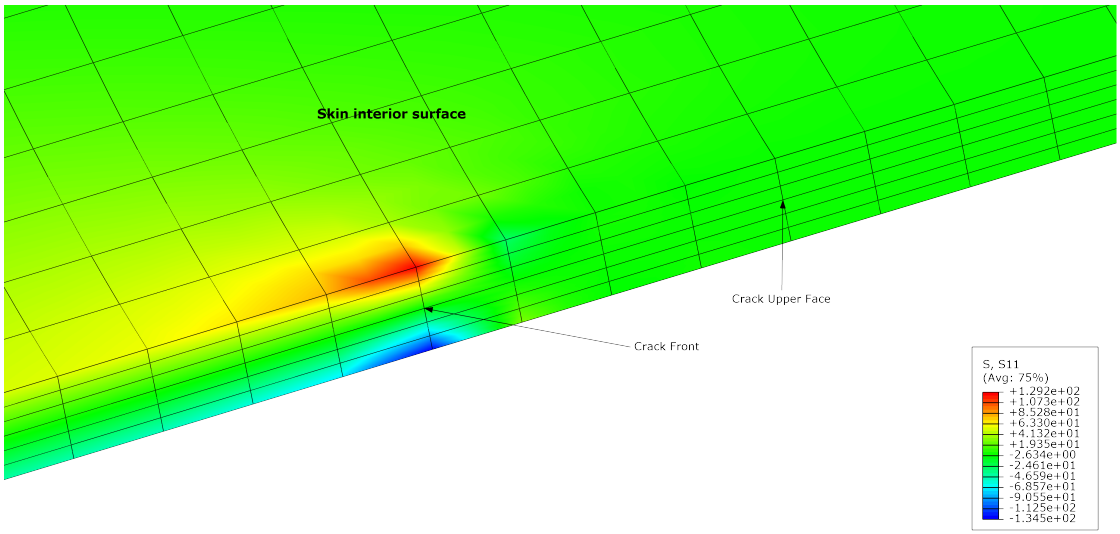


Figure 7.40: Stress normal to the third crack plane.

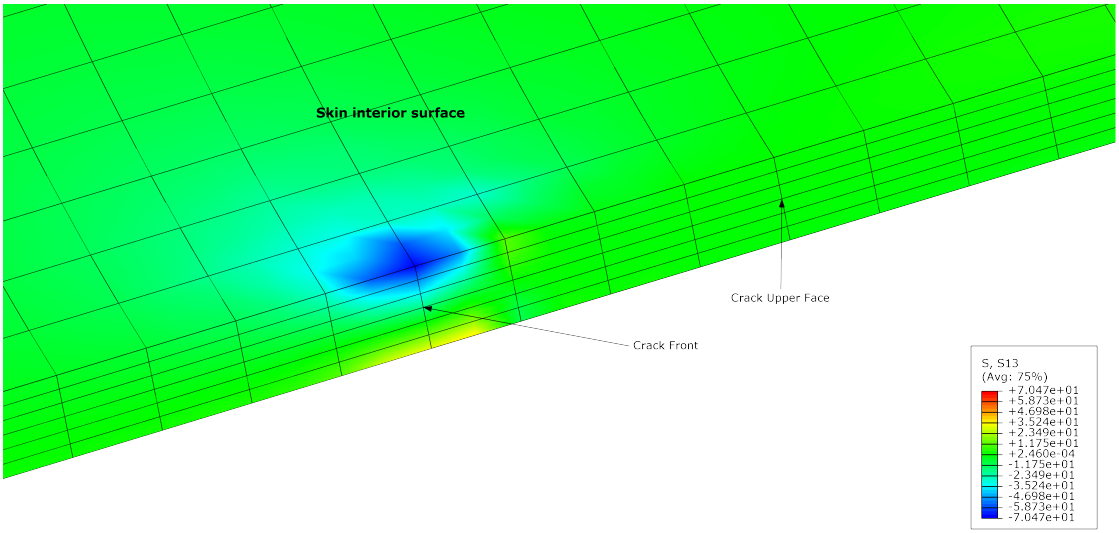


Figure 7.41: In-plane shear stress perpendicular to the third crack front.

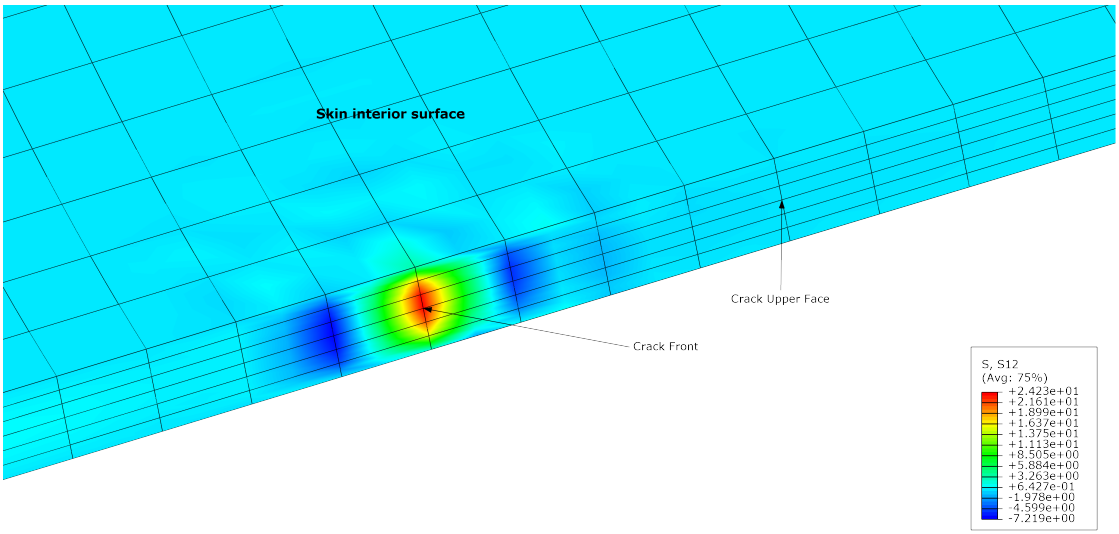


Figure 7.42: In-plane shear stress parallel to the third crack front.

Figure 7.40 shows that, at this location, the bending behaviour of the skin has changed, and now the interior face is the tensioned one, the exterior face being under

compression. It can be said that the neutral bending surface is approximately coincident with the middle thickness, as the maximum compressive and tensile normal stresses absolute values are very close. These considerations mean that $K_I$ distribution along the thickness will vary from negative on exterior to positive on the interior surface, and its absolute values will be fairly symmetric about the middle thickness point. This is shown on Figure 7.43. A comparison of the values from this graphic with those from Figures 7.16 and 7.43 shows that this is the less severe crack configuration, concerning mode I.

Regarding mode II, S13 plot shows a similar behaviour to the second case. Its absolute maximum along on the crack front is on the most interior node. Here values are again negative, and increase outwards, yielding positive $K_{II}$ values for the exterior zone (Figure 7.44). Bulging can again account for this, but its effect is less severe than in the second case, leading to a less intense S13 stress field. However, this is again aggravated by the increase of the crack length, leading to higher absolute values of $K_{II}$ on the interior zone (Figure 7.44). It must be noted that, since the bulging was more pronounced on the lower crack, forcing it to the interior, the stresses fields mentioned are on plotted on the same crack half, but on the crack half less affected by bulging for all cases. However, the only difference when seeing the crack plane from one side or another would be the sign convention.

The shear stress field S12 (Figure 7.42), relevant for mode III, is remarkably similar to that of the previous case (Figure 7.30). Once again, symmetry about the middle surface is found, as well as maximum at middle of the crack front). Nevertheless, and as before, SIFs values extracted largely fluctuate but do not show a relation with the stress field. On the contrary, the higher peaks occur near the crack line ends, as shown by Figure 7.45. This can be due to the proximity to the free surface, where *Abaqus* fails to obtain reliable results, or due to some difficult on defining the contours in these areas. The latter would also explain the fluctuations of $K_{II}$ on the same locations. Once more, these uncertainties led to the use of the average $K_{III}$ value.

Graphics representing the SIF values registered for each crack node are presented on Figures 7.43 to 7.45. As before, linear regressions were fit to the data retrieved, showing the trends mentioned predicted for mode I and II become clear and the mentioned fluctuations.

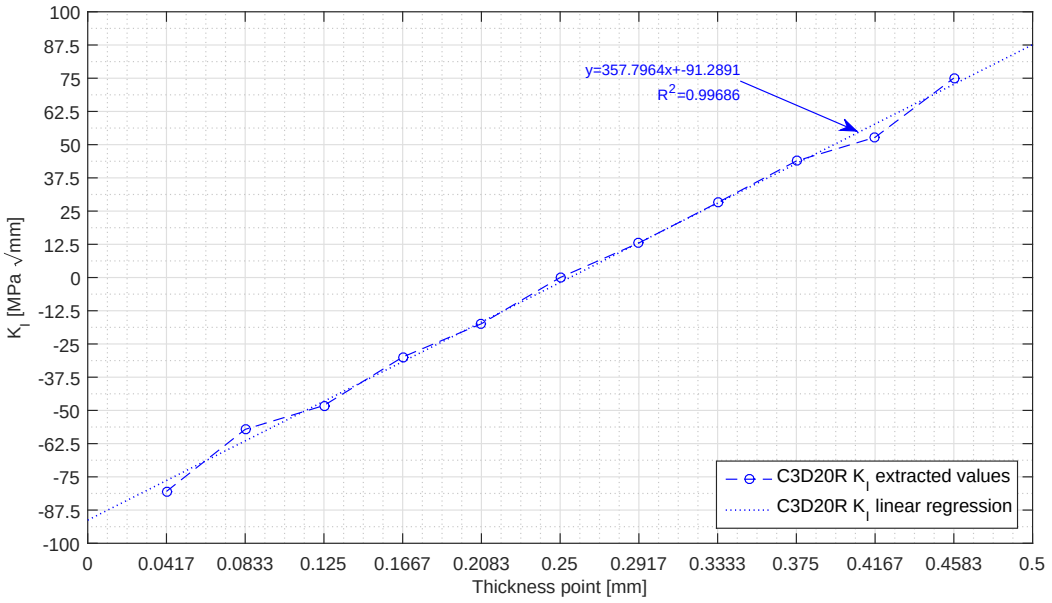


Figure 7.43: $K_I$ along thickness and fitted line.

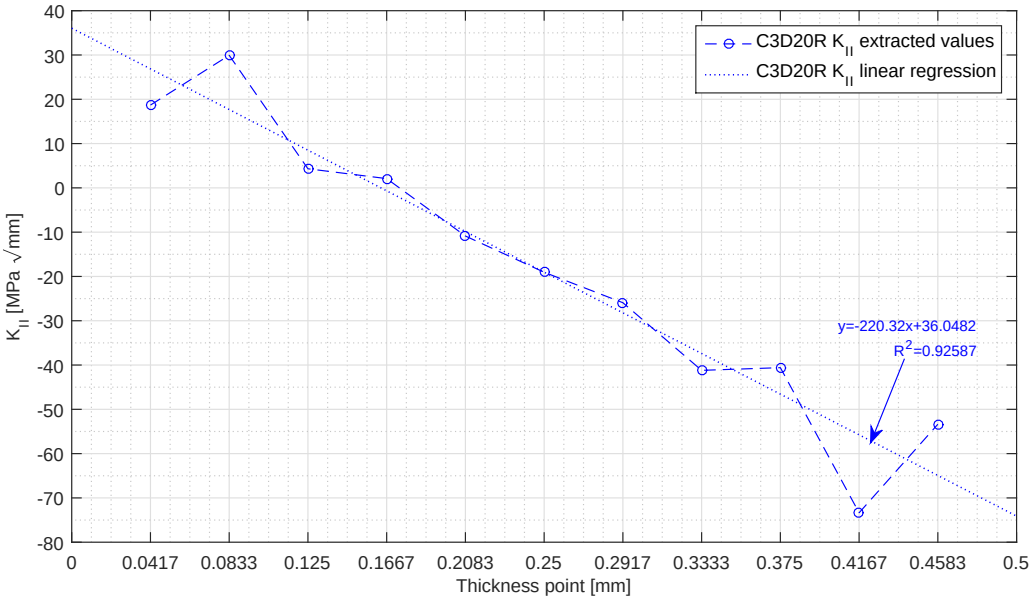


Figure 7.44: $K_{II}$ along thickness and fitted line.

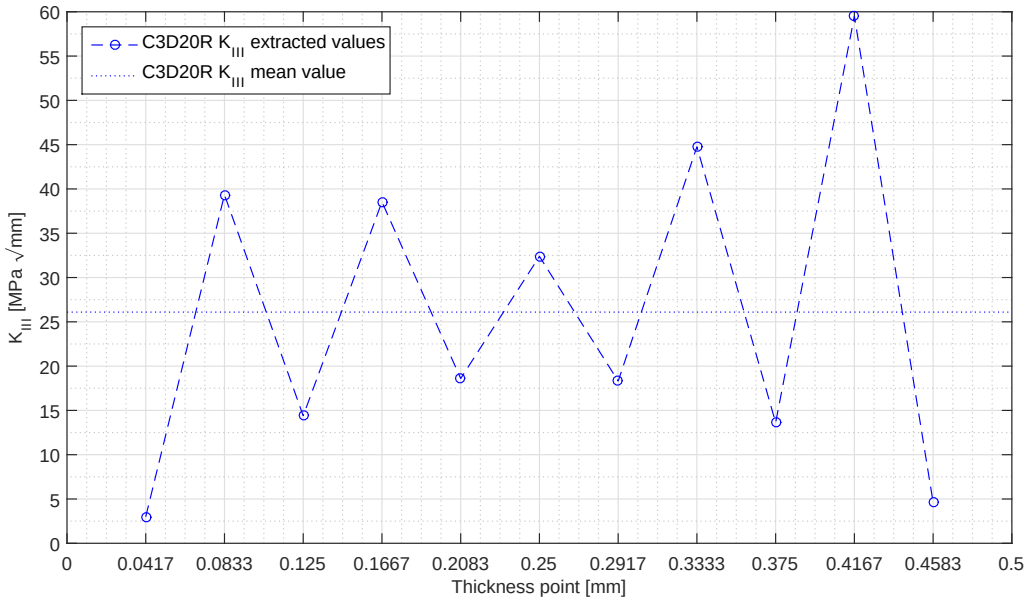


Figure 7.45: $K_{III}$ along thickness and mean value.

Summing up the conclusions of this study:

- This crack location yields the less severe SIFs for mode I and II.
- For this crack configuration, the compressed and tensioned surfaces are the opposite from the previous configurations. Tension occurs inside the skin, and compression outside.
- The bending neutral surface is coincident with the skin's middle surface, meaning that the crack front in under compression on its outside half.
- The lower half of the crack zone bulges to the interior, contrarily to the upper part of the crack zone and to what was observed in the previous cases. This can mean that bulging is influenced by normal stress, and the material tends to be shifted to the tensioned side.
- Mode II is relevant, when compared to Mode I.
- $K_{III}$ values along thickness showed again significant fluctuation, justifying once more the used of the average value
- Mode III intensity, compared with the other crack opening modes, gains some relevance on this case.

### 7.5.2 Stress Intensity Factor versus Crack Length

This study was carried out exactly as described in 7.4.2, the sole difference being the location of the growing cracks. These were modelled at 46% of the airfoil perimeter. The results for this crack location are shown on Figures 7.46 to 7.48.

It was concluded in the last section that, at this location, the stress state of the skin near the crack resembled less those of the first and second case. Figure 7.46 shows a different behaviour to those previously found, as $K_I$ steadily increases with the increase of the crack length. This behaviour is more usual: it is found in a myriad of fracture mechanics problems, starting with the traditional infinite plate with a central crack.

Concerning mode I severity, however, this location yields the lowest SIF values. The same cannot be said for mode II, since the corresponding SIFs, depicted on Figure 7.47, show a behaviour and values similar to those found on the second case. This means that mode II is, at least, as important as mode I, for this crack configuration. For instance, when $2a$ increases sufficiently, the absolute values of $K_{II}$ are superior to those of $K_I$. Again, exaggerated crack lengths such as 200 mm must be seen as a theoretical case only.

Average SIFs for mode III are shown on Figure 7.48. In contrast to the previous case, a curve with no discrepancies was found. It can be said that, although not the principal crack opening mode in this case, mode III is not residual, specially taking in account mode I SIFs. It may seem that $K_{III}$ tends to stabilize for larger cracks, but this cannot be affirmed without reserves. Only with values for larger (and unrealistic) cracks could this be determined for sure.

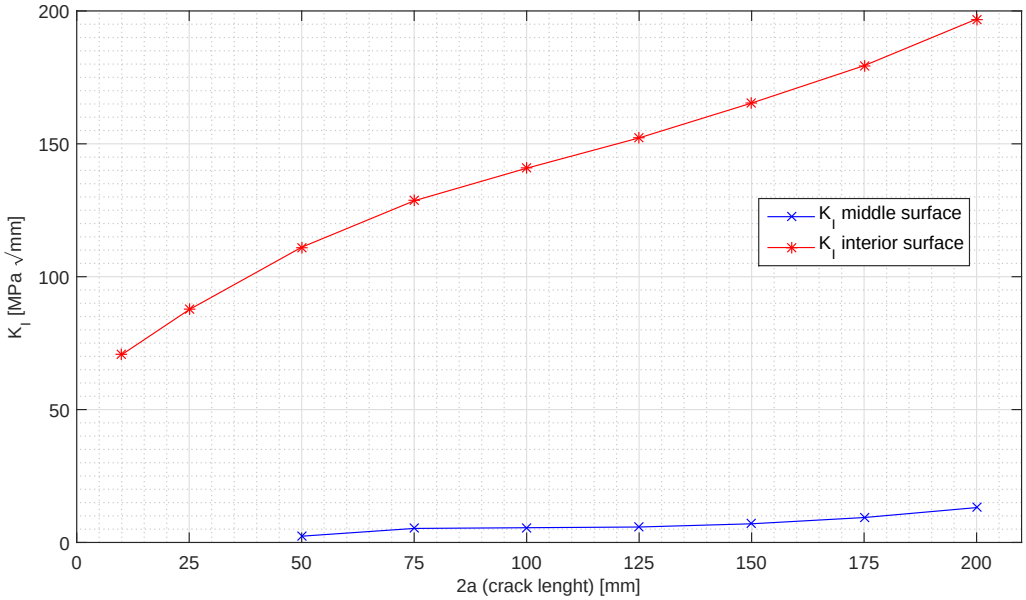


Figure 7.46: $K_I$ versus crack length.

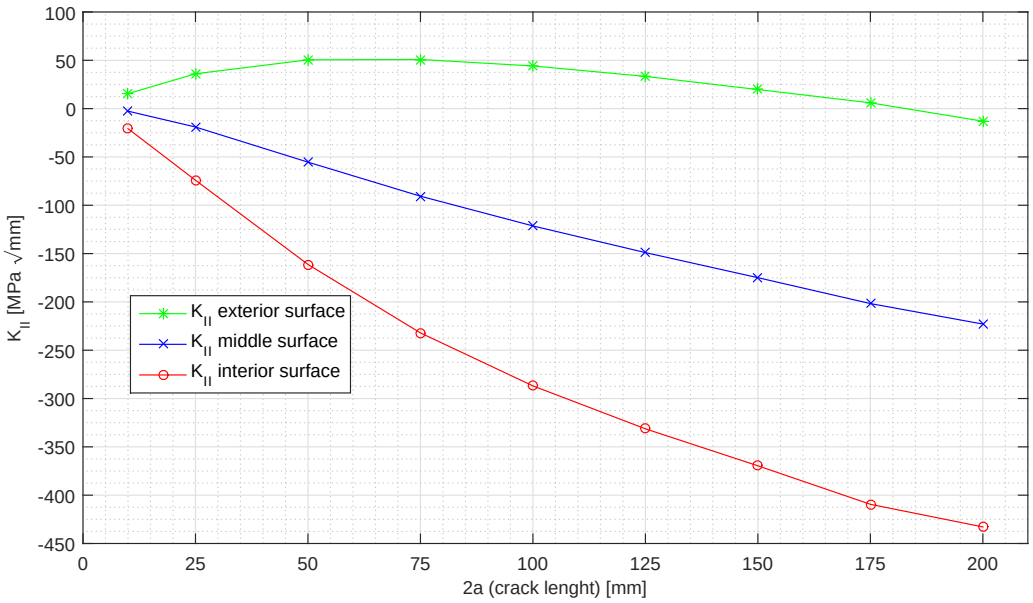


Figure 7.47: $K_{II}$ versus crack length.

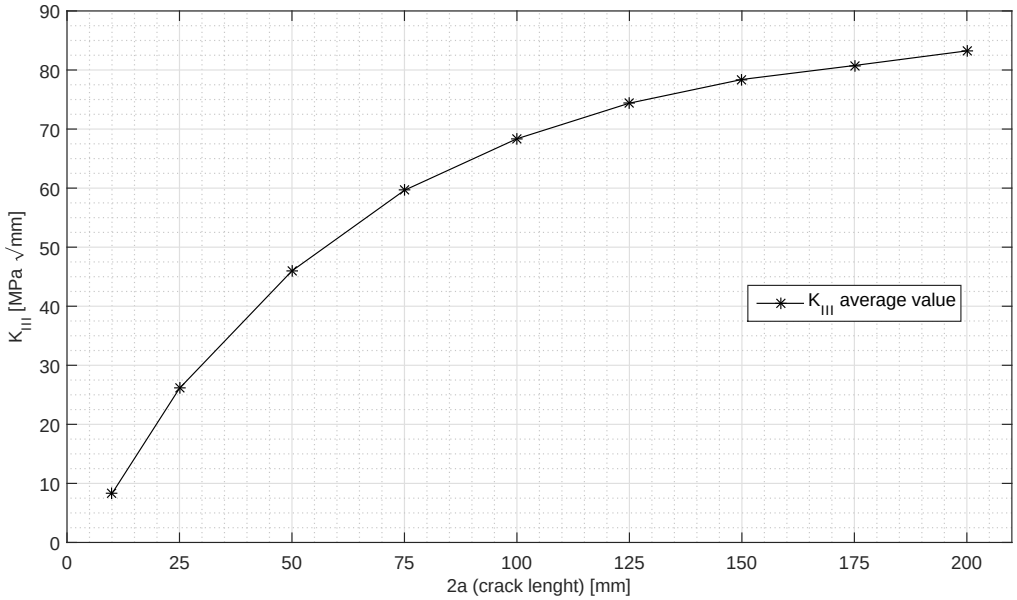


Figure 7.48: $K_{III}$ versus crack length.

# Chapter 8

# Modelling of Oblique Cracks

The present chapter will describe the creation of models of the wing leading edge skin containing through cracks not parallel to the skin surface generatrix. The effect of the inclination angle will be accessed, and a comparison between two methods of SIF extraction will be done. Finally, a model contemplating contact between the crack faces will be briefly considered.

## 8.1 Crack Modelling

Having studied the behaviour of several longitudinal cracks, the logical step to take was to understand the effect of crack inclination on its behaviour. For this purpose, the mixed element model was used and the 49% airfoil perimeter crack was chosen. This location was selected since its distance from the solid elements patch limits made less difficult the partitioning process needed to define the crack geometry and to refine and conform its local mesh.

A crack with $2a = 10$ mm was simulated, and four inclination angles $\alpha$ were simulated: $\alpha = 0°$, $\alpha = -15°$, $\alpha = -30°$ and $\alpha = -45°$ (rotations over the X-axis considered on Figure 1.2). Definition of the crack geometry presented some challenges. As done in the previous chapter, the crack fronts were intended to be normal to the skin surface. This was to ensure that the crack front lengths reflected the true thickness of the skin This is crucial when studying crack behaviour along thickness. However, and for a angled crack on a curved surface, this means that the cracked surface is no longer contained in a plan, but in a curved surface. This placed some modelling problems, not only on crack definition, but also on mesh conformation. Therefore, modelling only 3 cracks (since the 0° crack was already modelled) was a rather time consuming and cumbersome process.

To achieve the crack front perpendicularity and resulting crack curved surface mentioned above, the following procedure was used: first, the two vertical auxiliary planes which where to contain the crack fronts were defined, as well as two other planes used to create partitions conformed to the crack. The position of these planes was calculated for each case, in order to obtain an inclined crack length of $2a = 10$ mm .

Next, a plane centred with the original 0° crack and inclined by $\alpha$ was defined, and its

intersections with the vertical planes were used to define the crack front exterior points, and points on the auxiliary planes used to mesh conformation. This was done twice more, for two inclined parallel planes above and below of the first one, so that all necessary points on the exterior skin surface were defined.

The third step was to project these points on the corresponding normal locations of the interior skin surface, therefore obtaining all the points necessary to partition the solid element patch. These partitions were done resorting to the *Abaqus* feature of partitioning using a n-sided patch. This creates a partition by connecting the given points using the shortest path considering the available surfaces. Therefore, the crack front perpendicularity to the surfaces is ensured (since these are parallel), and the curved crack surface, constantly perpendicular to the surfaces, is also obtained.

For each case, adjustments were made when deemed necessary. Also, due to the curved nature of the surface, the modelled crack angles deviated slightly from the intended. However, these deviations were considered acceptable, given the curvature of the leading edge and inherent difficulties.

The modified Virtual Crack Closure Technique (mVCCT) was used to extract the SIF values. This was decided after several attempts to use *Abaqus* J-integral which did not achieve convergence, even after extreme mesh refinements (and consequent long computation times). However, it will be seen that this provides the opportunity to compare both approaches and conclude on their validity and applicability to this problem.

The use of mVCCT requires nodal forces at the crack front. After different approaches were attempted, this was achieved by creating a separate part for the lower crack half and tying its trough thickness faces to the original patch faces, with exception for the crack zone face. Compatibility and correct positioning of the two parts was assured by creating the second part from the first and removing all but the zones of interest. The crack opening was enabled by the existence of untied zones, which defined the crack faces. The nodal forces were extracted using *Abaqus* results visualization module, which allows to create free body cuts concerning the intended elements and provides the nodal reaction forces on the desired crack coordinate system. The displacements were also retrieved for the same coordinate system, and the procedure explained on Section 4.3.4 was used to obtain the Strain Energy Release Rate $G$ and, consequently, the Stress Intensity Factors $K$.

## 8.2 Crack with 0° inclination

### 8.2.1 Introductory remarks

The first crack was modelled without inclination. In fact, this was the same crack as that studied in Section 7.3.1, only with a smaller crack length. This model was based on the one created for that crack location, but modified accordingly to the procedure mentioned above. The interest of restudying this crack is to evaluate and understand possible differences between the mVCCT and *Abaqus* J-integral approach. Also, the influence of mesh refinement and element type was assessed during this study.

Recalling the previous chapter, it was found the interpenetration of the upper and lower face of the crack occurred. This is a result of the bending of skin, creating a compressed zone on the interior part of crack front being studied. It was found that *Abaqus* extracted negative values of $K_I$ for these nodes, which were considered without physical meaning. However, as will be seen in a while, mVCCT provided both negative and positive $K_I$ values this zone, the latter being the more usual. This behaviour lead to the existence of a inflection point on the plot of $K_I$ along the thickness. This incongruence is due to the interpenetration of the faces and the nodal force and displacement values associated with it, in conjunction with the discrete nature the FEM. Consider, for instance, the mVCCT for solid linear elements: relative displacement between the, supposedly, upper and lower nodes is calculated. If nodes reside in a penetrating area, this value will be negative. Being the corresponding crack front node in compression, a negative force will also be recorded, leading to a $G_I$ that seemingly indicates energy release and a therefore a positive $K_I$ value. On the transition zone, and due the FEM discretization, the little distance between the nodes where displacements and forces are recorded can lead to a negative force on the crack front but a positive relative displacement or vice-versa, explaining the existence of some negative $K_1$ values before returning to "false" positive ones. This reasoning can also be extrapolated to the quadratic elements, with the due changes. Therefore, and knowing beforehand the existence of a compression zone, results were analysed with increased critical spirit, and corrected on a case-by case basis: the inflection point was found and the following $K_I$ values accordingly corrected. Figure 8.1 shows an example of the nodal forces retrieving process, with a positive Z force where compression occurs (S11 is the stress normal to crack plane).

Inflection points also appeared on when analysing the values of $K_{III}$, and the explanation can be extrapolated from the one given for mode I. It was found the values of the relative X-axis displacements changed sign at a certain thickness node, meaning that the scissoring action was inverted at the point. However, nodal x-forces changed sign at the same or close node, meaning that the $G$ sign was not changed, since it results from the multiplication between the nodal forces and relative displacements. Again, as for mode I, some "false" positive or negative values. Therefore, a careful analysis was performed to discover the inflection point. Values were corrected taking into account the sign of the corresponding nodal force or forces (positive $K_{III}$ for positive nodal X-forces).

Another remark concerns the axis used by both *Abaqus* J-integral approach and mVCCT. It was found that, for $K_{II}$ disregarding the absolute value of the results ob-

tained, signs were opposite depending on the method used. This indicates that, while on mVVCT the X-axis points outwards the crack and Y-axis points to the interior of the skin, for *Abaqus* J-Integral this system is rotated 180° around the Z-axis (normal to the crack plane). Consequently, J-Integral approach extracted values were adjusted accordingly to ensure an easy and effective comparison.

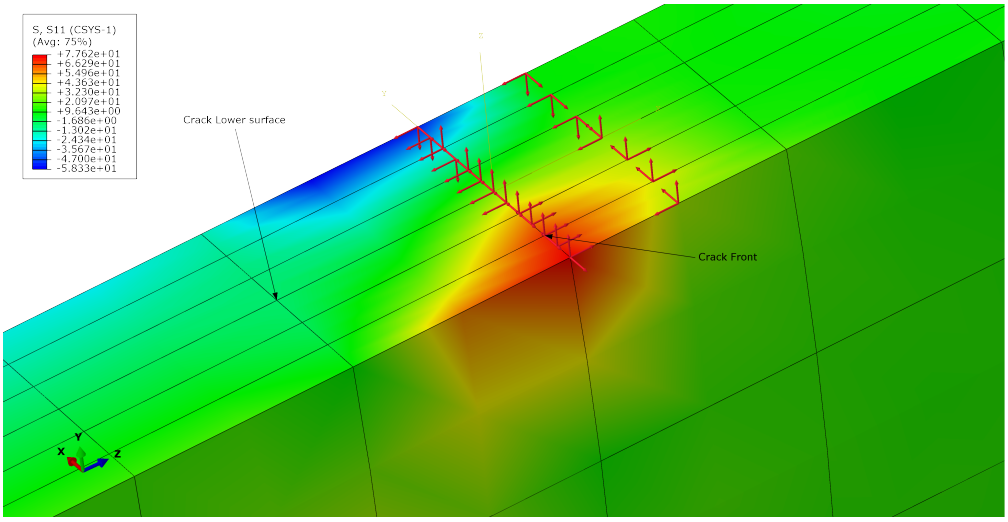


Figure 8.1: Example of nodal force extraction.

### 8.2.2 Element Type Comparison

To understand the influence of the element type on the the SIFs extracted values, both quadratic and linear solid elements models previously mentioned were used. The motivation for this study was not only the differences found on Chapter 6 (although these revealed low interference on the results show on Chapter 7), but also the fact the mVCCT usage is easier and faster for linear elements, thus reducing the manual post-processing time

For this study, 6 elements were used along the thickness. This result, for each mode, in 13 SIF values for the quadratic elements mesh and 7 SIF values for the linear elements mesh. Taking in account what was said in the previous Section, inflection points for mode I and III were discovered, This can be shown approximately, for mode I by plotting the vertical displacements the of the nodes immediately after the crack front (referred to crack coordinates system), thus obtaining a "vertical cut" of the crack on that position. For mode III, a "horizontal cut" using the X-displacements is used. Figures 8.2 and 8.3 show these plots with values retrieved from the quadratic mesh. It can be concluded that inflection occurs at around 0.375 mm of thickness for mode I, which is between thickness nodes 9 and 10. For mode III, this happens between 0.125 mm and 0.167 mm of thickness, which is between node 5 and 6.

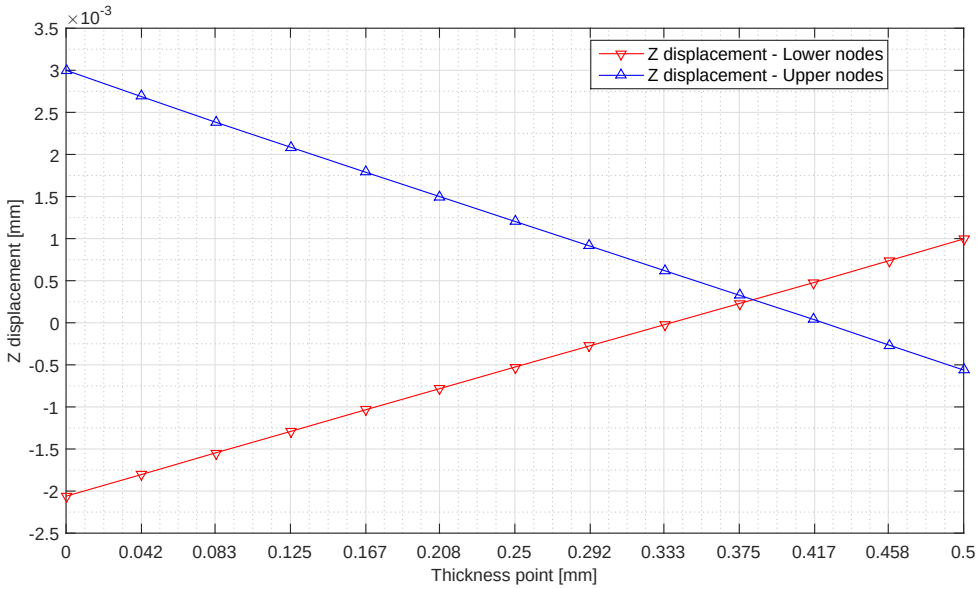


Figure 8.2: Nodal Z displacements of the first node line of the cracked zone.

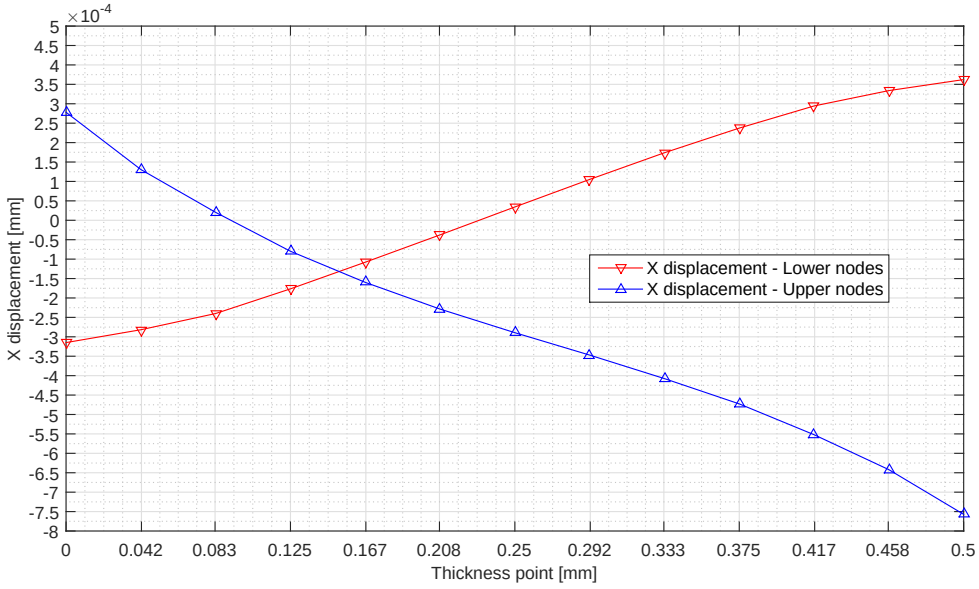


Figure 8.3: Nodal X displacements of the first node line of the cracked zone.

The results obtained using both element types and 6 thickness elements are shown in Figures 8.4 to 8.6. It seems that SIF values extracted for the three crack modes do not show substantial variation due to the element type. The erroneous values for mode I and III, mentioned in the previous Section, become clear. For instance, uncorrected $K_I$ values for the last 2 (linear elements) or 4 (quadratic elements) nodes are positive and its know that these locations are known to be under compression. Nevertheless, results extracted using both meshes show the same pattern and similar values.

Another observation that derives from all three graphics is that the absolute values of the SIFs for the nodes immediately next to the the skin surface are always higher than those of the SIFs for the nodes on the skin surface. This is an effect of the skin free surface, and was not noted on the previous chapter since values for these nodes were not available and were extrapolated.

To achieve the same along thickness resolution as with the 6 thickness elements quadratic mesh (which has mid-side nodes), a linear mesh using 12 thickness elements was created and SIFs values extracted. Results (also on Figures 8.4 to 8.6) present the same trends as those shown before, although some differences appear on the $K_{II}$ plot. Nevertheless, it can be affirmed that these results validate the use of the 12 thickness elements linear mesh. Results from Section 8.3.1 will confirm this affirmation. Since results are more promptly extracted by the mVCCT using linear elements, 12 thickness element meshes will be used from now on, except where stated.

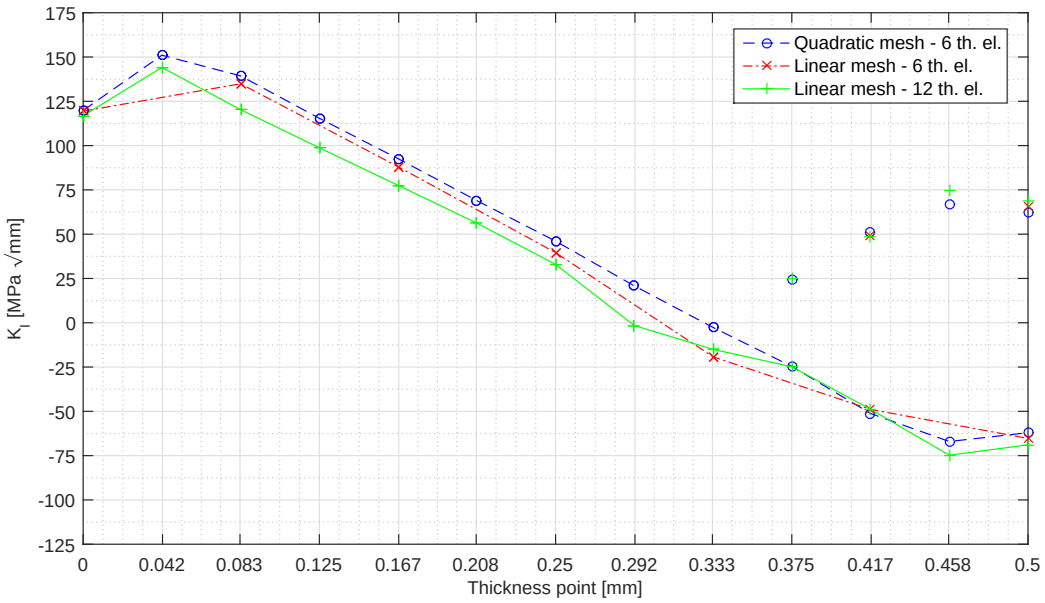


Figure 8.4: Comparison of $K_I$ extracted values for the three meshes.

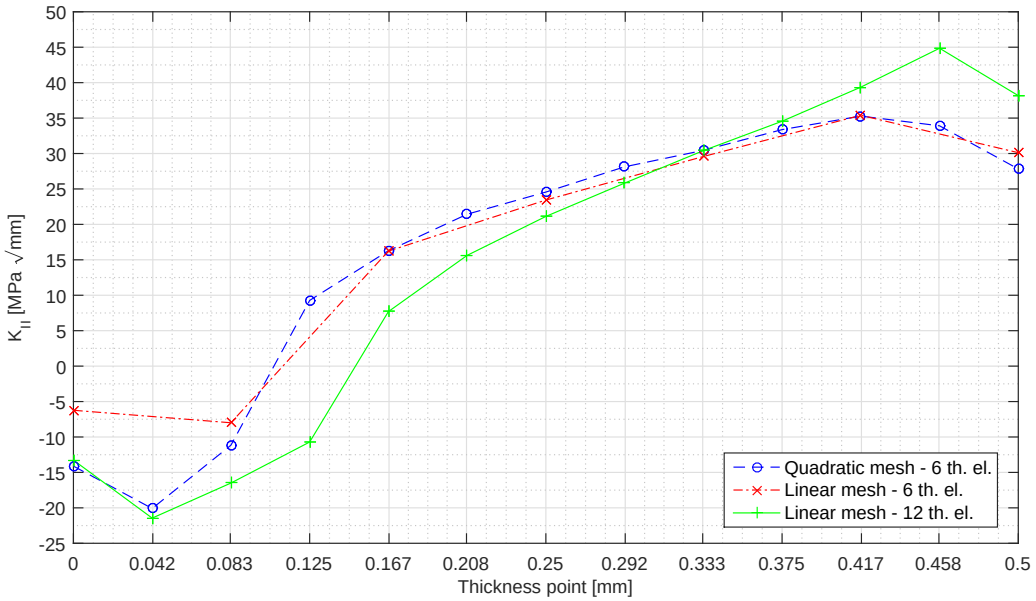


Figure 8.5: Comparison of $K_{II}$ extracted values for the three meshes.

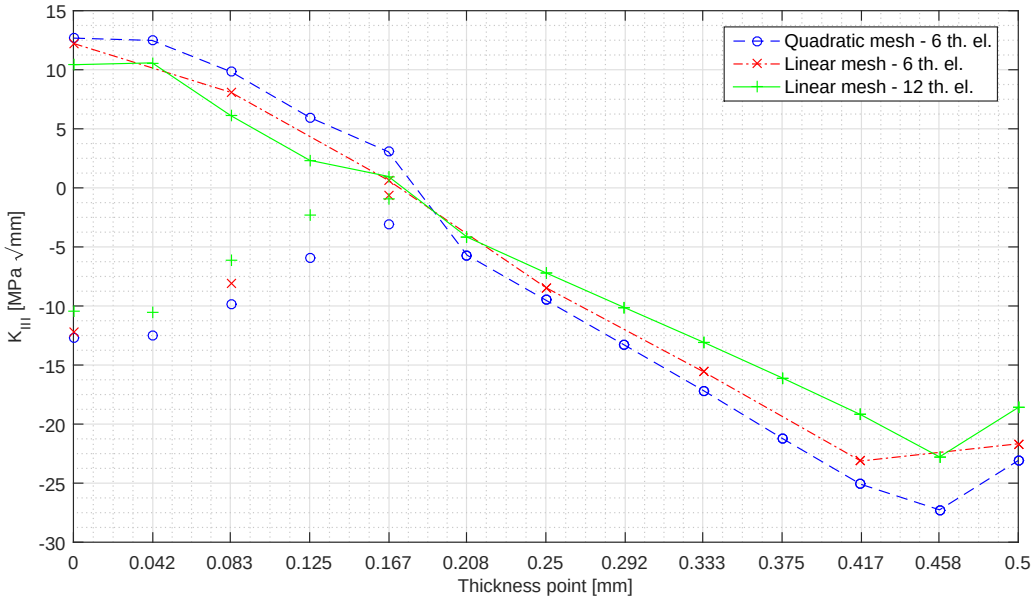


Figure 8.6: Comparison of $K_{III}$ extracted values for the three meshes.

### 8.2.3 mVCCT and *Abaqus* J-Integral Comparison

Since results extracted using both mVCCT and *Abaqus* J-Integral were available, these were compared. This served not only to access if results weren't being affected by systematic errors of the SIF extraction technique, but also to better understand the differences between the techniques used during this work. One should bear in mind that, given all the difficulties and constraints found during this work, a perfect match should not be expected. However, it is interesting to conclude that different techniques yield similar results. In fact, when compared, the SIF values obtained using both techniques show acceptable differences and similar trends, as shown in Figures 8.7 and 8.8. These result from adding the SIF values obtained via J-Integral to Figures 8.4 to 8.6.

Regarding mode I, results from both techniques show a complete correlation. Even if the uncorrected mVCCT $K_I$ values were plotted, those could be seen as "mirroring" those extracted using J-Integral. For mode II, although the same trend is present in all four data series, some differences on values arise. This could be explained by the fact that *Abaqus* calculates and takes into consideration the direction of the maximum tangential stress when extracting $K_{II}$ values, while in the mVCCT this direction is assumed to be the same of the crack. Nevertheless, mVCCT SIF extracted values can be used as a safe estimate, since they tend to be, in absolute value, greater than those extracted using J-Integral.

Although correlation was found on mode I and II, Figure 8.9 shows that the same does not hold true for mode III. In fact, the sawtooth shaped plot of the values extracted using *Abaqus* J-Integral approach does not resemble the clear pattern plotted using the mVCCT extracted values. The only similarity that can be indicated is between the absolute SIF values extracted using mVCCT for the crack front ends and the absolute average value calculated from *Abaqus* extracted values. This seems to be an *Abaqus* deficiency, but explanation could be found for this discrepancy after researching both literature and *Abaqus* User's Manual, which lacks any specific reference to $K_{III}$ extraction errors. However, this discrepancy will be accepted and taken as a minor issue. This is based in two assumptions: First, that the *Abaqus* extracted $K_{III}$ average absolute value, although not providing information of the along thickness mode III behaviour, of seems to indicate the order of magnitude of its intensity. Second, and based on this, that mode III is of relative low importance compared to mode I and II, as shown in the previous Chapter.

A final remark concerning the comparison between these two techniques. It is interesting to note that SIF values for the crack front end extracted using both techniques are affected by proximity from the free surface, although in completely different manners. For *Abaqus* J-integral approach, values from different contours show no convergence and show a rapid increase from contour to contour. On the other side, values extracted using mVCCT tend to be slightly inferior to those from the next interior node.

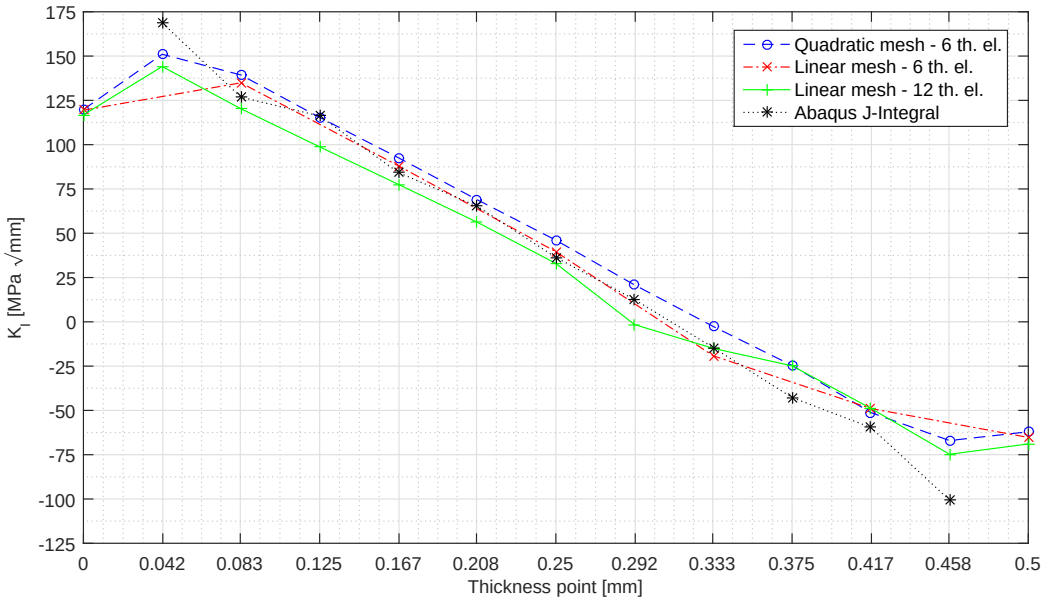


Figure 8.7: Comparison of $K_I$ extracted values using mVCCT and J-Integral.

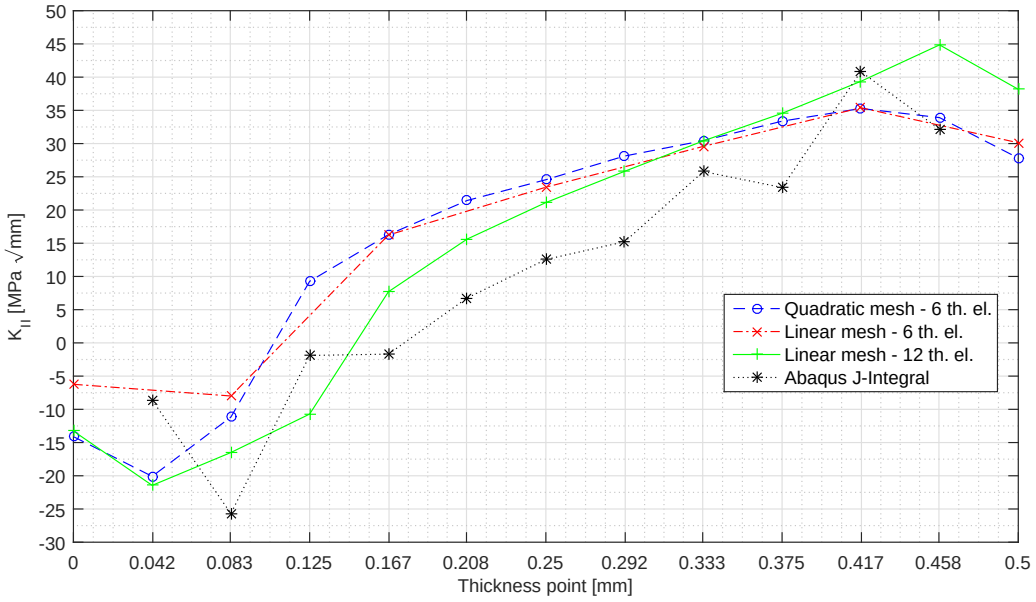


Figure 8.8: Comparison of $K_{II}$ extracted values using mVCCT and J-Integral.

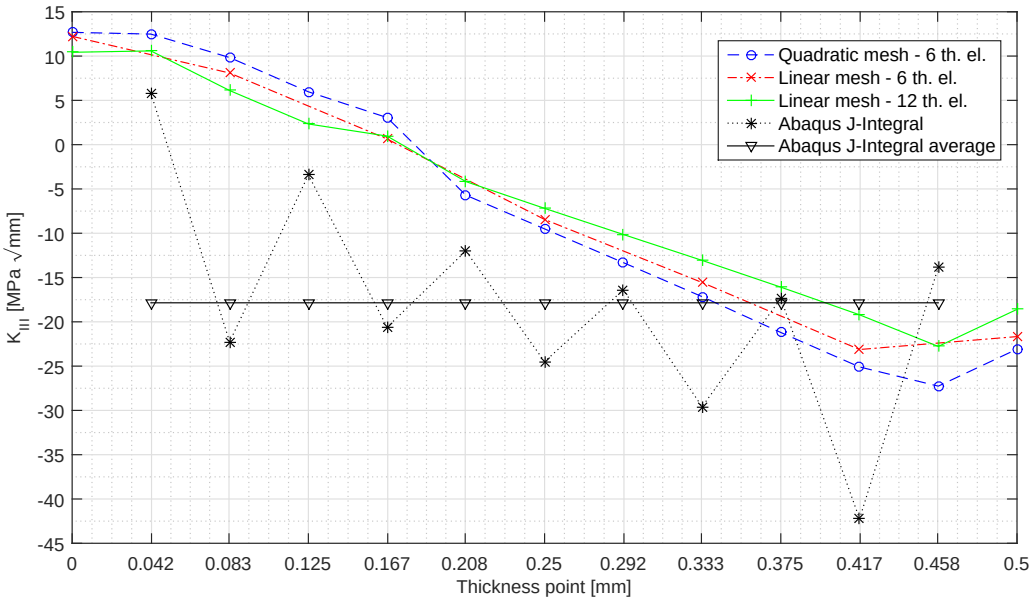


Figure 8.9: Comparison of $K_{II}$ extracted values using mVCCT and J-Integral.

## 8.3 Crack with -15° Inclination

The second crack was modelled via the process described on Section 8.1 and using a angle $\alpha = -15°$ . Modelling inclined cracks means that symmetry is no longer present on the model, and therefore the two crack fronts must be studied, since they are subjected to different stress fields. From now on, the crack tip located above the original 0° location will be named the upper crack front. Accordingly the crack tip below that location shall be named lower crack front. In this study, SIF values were extracted using the mVCCT for both crack front. Also, the influence of mesh refinement and element type was again assessed during this study, this time for the upper crack front.

Figure 7.3 shows the von Mises stress field on the crack zone.

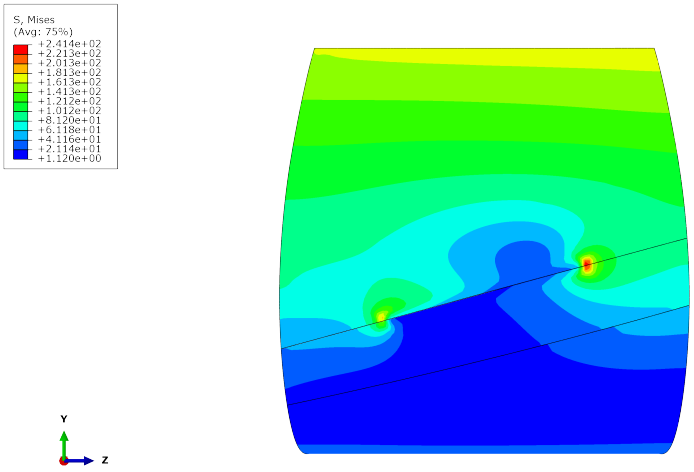


Figure 8.10: von Mises stress field on the crack zone, $\alpha = -15°$.

### 8.3.1 Upper Crack Front: Results and Element Type Comparison

The first step in this study was to understand the position of the inflection points for mode I and III. This was done analysing the corresponding displacements retrieved from a quadratic mesh of 6 thickness elements. For mode I, this point was found to be at 0.300 mm of thickness, between node between the eight and ninth node. For mode III, inflection was predicted to happen at around the same location. Using this information, $K_I$ and $K_{III}$ values for the nodes after these were accordingly corrected.

As done on Section 8.2.2, SIFs were extracted using 6 thickness elements linear and quadratic meshes, and 12 thickness elements linear meshes. Figures 8.11 to 8.13 illustrate the results for the three cases.

Analysing these plots, and concerning the element type influence, it becomes clear that, for a 6 thickness elements mesh, linear elements yield slightly lower SIF absolute

values. This is particularly noticeable for mode I (Figure 8.11). However, and using the SIFs extracted using quadratic elements as a reference, this error is minimised when using a 12 thickness elements linear mesh. Figure shows that the same holds true for mode II, even tough that, for this mode, differences due to the 6 thickness elements mess were not significant. Mode III SIFs ultimately prove that the refined linear mesh provides results with only slight differences.

Various observation not concerned with element type must be made. Different changes were observed for the inflection points positions: the inflection point for mode I has shifted towards the exterior, meaning that compression in the occurs in a larger crack region than for the the horizontal case. Contrarily, mode III inflection point was shifted towards the interior. These shifts were accompanied by corresponding changes on the SIFs evolution along the skin thickness. $K_I$ minimum value (negative) became lower (more negative), denoting the increased compression. However, its maximum value suffered only a low decrease. For mode III, the opposed happened, and an increase was observed on the maximum $K_{III}$ value. Mode II SIFs along the thickness suffered noticeable alterations, both on extreme values and range. In fact, $K_{II}$ minimum became positive, and its maximum decreased, thus showing less variation of mode II intensity along the thickness. Consequently, mode II became of less importance when compared with the horizontal case.

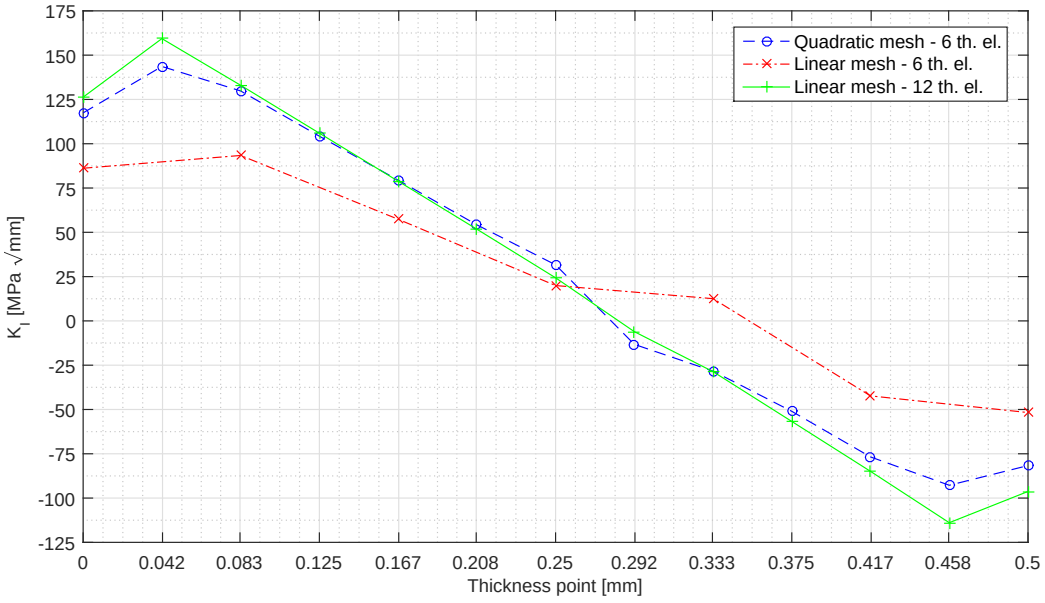


Figure 8.11: Comparison of $K_I$ extracted values for the three meshes.

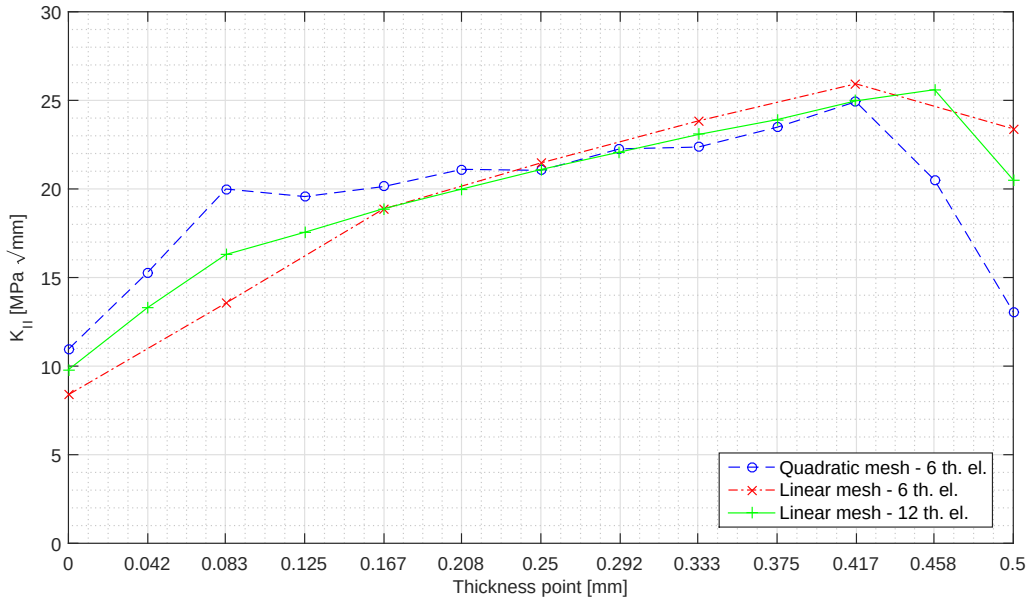


Figure 8.12: Comparison of $K_{II}$ extracted values for the three meshes.

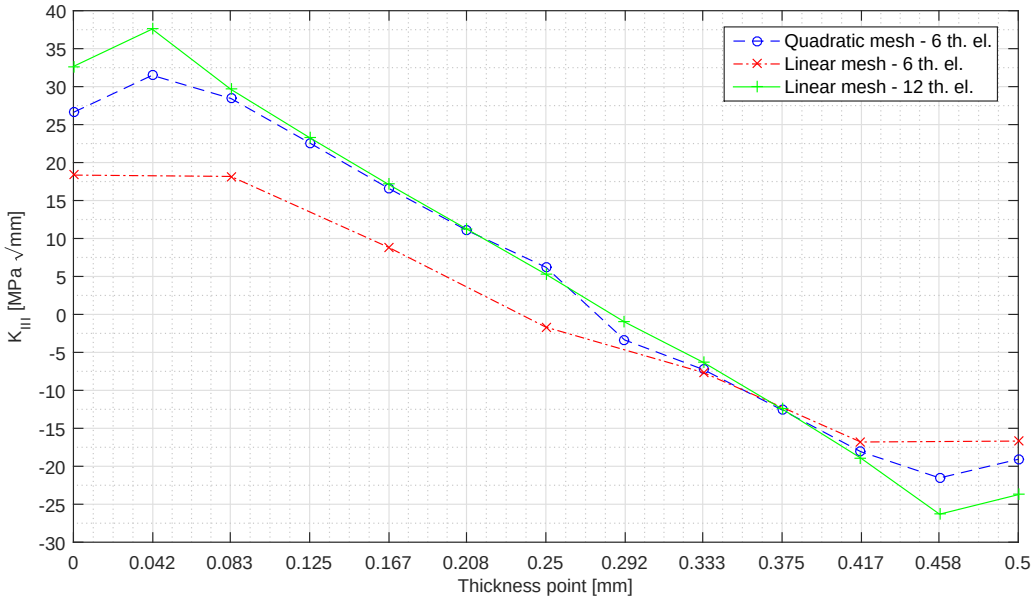


Figure 8.13: Comparison of $K_{III}$ extracted values for the three meshes.

### 8.3.2 Lower Crack Front

Following the procedure used on the previous Section, and using a 12 thickness elements linear mesh, the inflection points for where determined. For mode I, this point is located near node number 9, at about 0.333 mm of thickness. For mode III, and based on the X-axis displacements, this point seemed to be right before the second node. However, and considering that X-axis nodal force on the second node was also positive, this was considered the inflection point, located at about 0.042 mm. This choice was also based on the free surface effect, which has been present in all the previous plots.

Results of the SIF extraction are shown on Figures 8.14 to 8.16. Its interesting to notice that, although for mode I, the lower crack front inflection point is nearly at the same thickness that for the upper one, this is not true for mode III, in fact, this inflection point is almost on the exterior surface (i.e. nearly is not present). Also, its clearer that while the SIFs for each mode present similar trend as those present on the upper front, their absolute values are lower than. Therefore, it can be concluded that this crack front is less loaded than the upper one, meaning that the critical front for a crack inclined by $\alpha = -15°$ is the upper crack front.

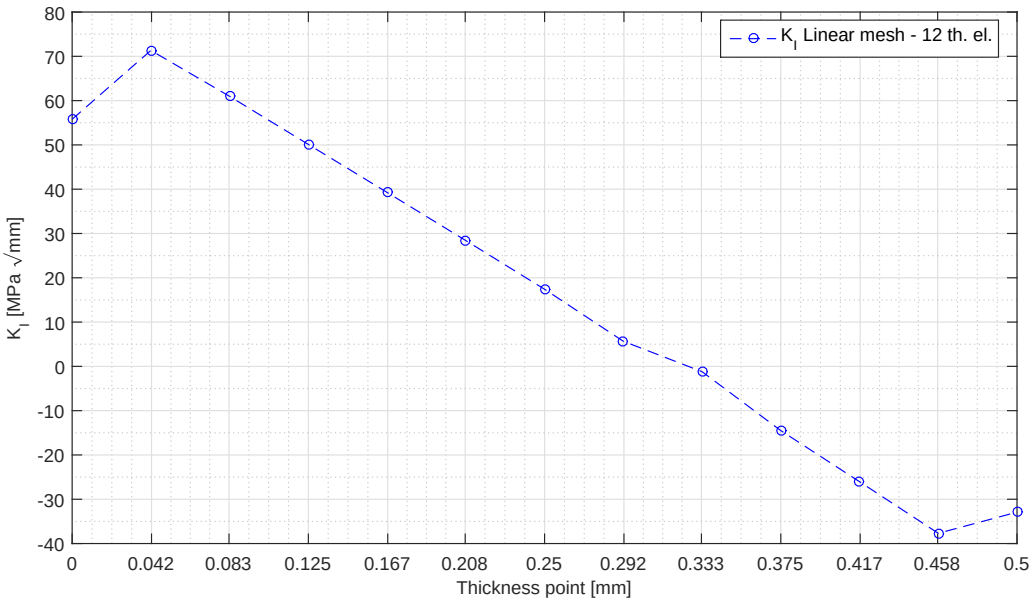


Figure 8.14: $K_I$ along thickness for the 15° crack lower front.

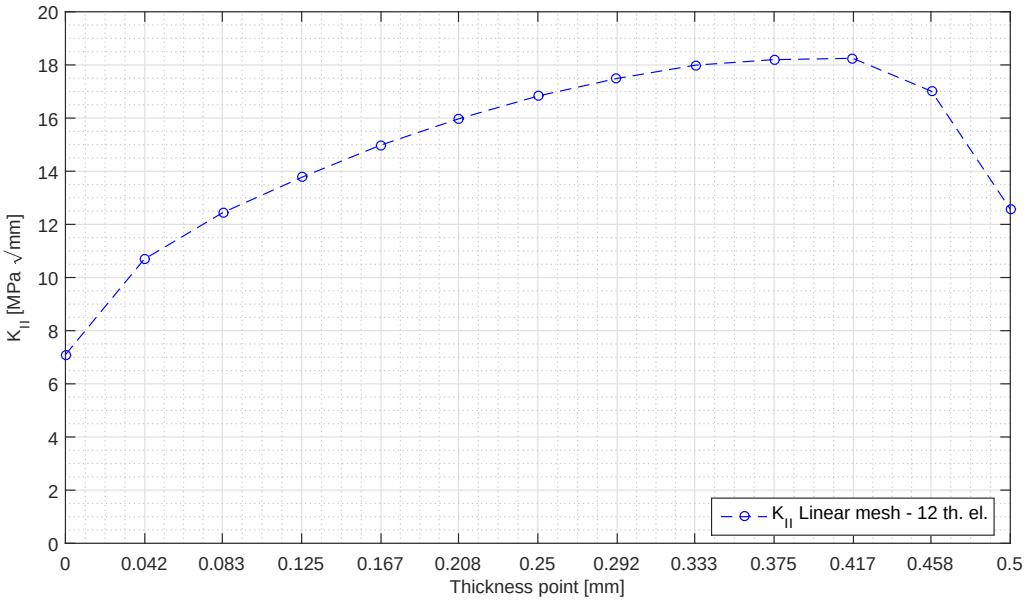


Figure 8.15: $K_{II}$ along thickness for the 15° crack lower front.

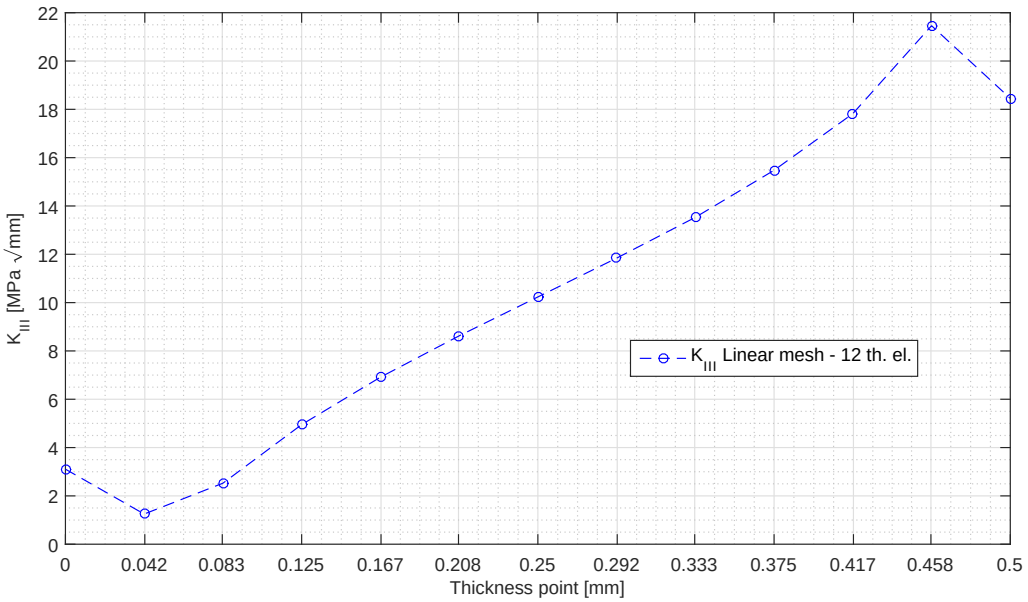


Figure 8.16: $K_{III}$ along thickness for the 15° crack lower front.

## 8.4 Crack with -30° Inclination

A third crack was modelled in the same fashion as the previous ones, using an inclination angle of $\alpha = -30°$ . Again, the two crack fronts were studied, but a new consideration was made. Until this point, all the cracks modelled and described on this and the previous chapters revealed an interpenetrating behaviour. This, while not being realistic, was considered as compression, being reflected on results. Their analysis, interpretation and adjustment was performed with due attention and caution, so that valid conclusions could be drawn. Nevertheless, and in the final stages of this work, it was considered of interest to simulate contact between the crack faces, and understand its effect on the results. This can be considered a more realistic approach to reality. However, modelling and simulating contact is not straightforward, and extends the computation times. This was one of the reasons why contact was not simulated when extracting SIFs via *Abaqus* J-integral approach.

As a result of this new consideration, two sets of SIFs will be presented for each mode: with or without contact modelled. It is interesting to note that for the models with contact modelling, the presence of inflection points and the necessity of finding them was greatly reduced and facilitated. This is logical, since these inflection points were the points where, for mode I, it was assumed that the crack faces contacted. As will be shown, this results in a visible change on shape of the "cuts" plotted using the nodal displacements of the first node line of the cracked zone changed.

Figure 8.17 shows the von Mises stress field on the crack zone.

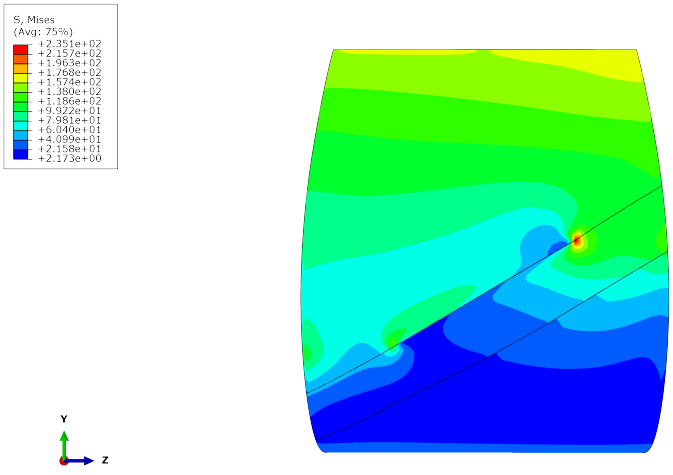


Figure 8.17: von Mises stress field on the crack zone, $\alpha = -30°$.

### 8.4.1 Upper Crack Front

Considering the crack modelled without contact, the inflection point for mode I was located at about 0.230 mm, between the 6 and 7 nodes of the crack front. This means that the compressed area has extended further in the exterior direction, and a larger portion of the crack front is expected to have negative $K_I$ values. For mode III, this point is located at approximately 0.300 mm, near node 8 and at roughly the same location as for the crack inclined by 15°.

If one considers contact, a different behaviour occurs. In this case, for the the vertical displacements its more appropriate to name the point of interest as the contact point. This point occurs, considering the Z-axis nodal forces, between nodes 8 and 9, at about 0.300 mm of thickness. This means that the crack front portion under tension increase by near 25%. For mode III, however, no significant change on the position of the inflection point was found. To better illustrate the differences found, Figure 8.18 shows the "vertical cuts" comparison for both cases.

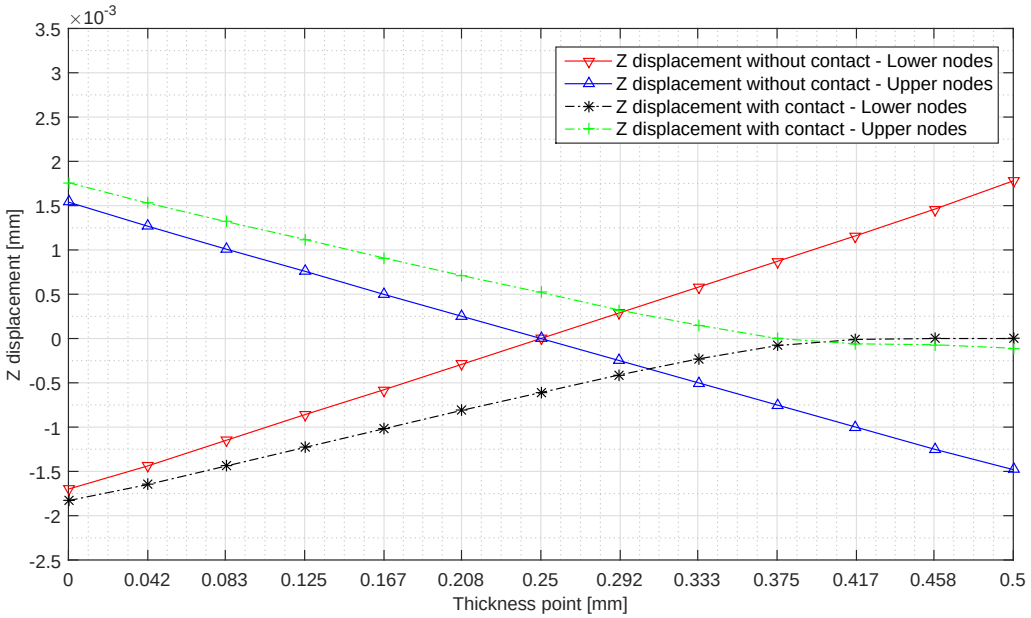


Figure 8.18: Comparison of the nodal Z displacements of the first node line of the cracked zone.

The results obtained with and without considering contact of the crack faces are shown on Figures 8.19 to 8.21. Analysing first the results for the crack modelled without contact, as predicted, a larger portion of the crack front presents negative $K_I$ values. Therefore, $K_I$ minimum value presents a more negative value, while the its maximum value decreased, due to the shift of the bending neutral surface to the interior of the wing

skin, at this crack front location. Mode II SIFs range also decreased, leading to a more uniform $K_{II}$ distribution along the thickness. The same observations can be made for mode III. It should also be noted that, while the intensity of the three modes shows an overall decrease, the trends observed for the upper crack fronts for $\alpha = 0°$ and $\alpha = -15°$ still can be observed for this crack. However, it seems that increasing inclination leads to the less pronounced trends, specially for mode II and III, and to an overall less severe stress field on the crack front.

Considering now the results obtained for the crack modelled with contact, several differences are found on both SIFs values and their variation along the thickness of the skin. It is clear that mode I SIFs are affected by this new consideration, with a increased $K_I$ maximum value. This is probably due to the surface contact acting as "lever", thus increasing the tension on the open portion of the crack. Some negative $K_I$ values appear, but these can be considered residual, and that derive from using *Abaqus* default contact tolerance. Should this value be reduced, SIF values would probably approach zero for the contact zone, but with a penalty computation time. Mode II is also affected, and although $K_{II}$ range is not significantly altered, mode II intensity is slightly higher when considering contact. For mode III, both $K_{III}$ absolute maximum and minimum increase, therefore increasing mode III intensity.

Based on these observations, it can be concluded that results obtained when contact is modelled show a crack front stress state appears to be more close to the reality. For the predominant mode I, t the percentage difference is at around 18%. Therefore, this should not invalidate the results previously presented, but lead to caution when using them, for instance, on fatigue life prediction calculations.

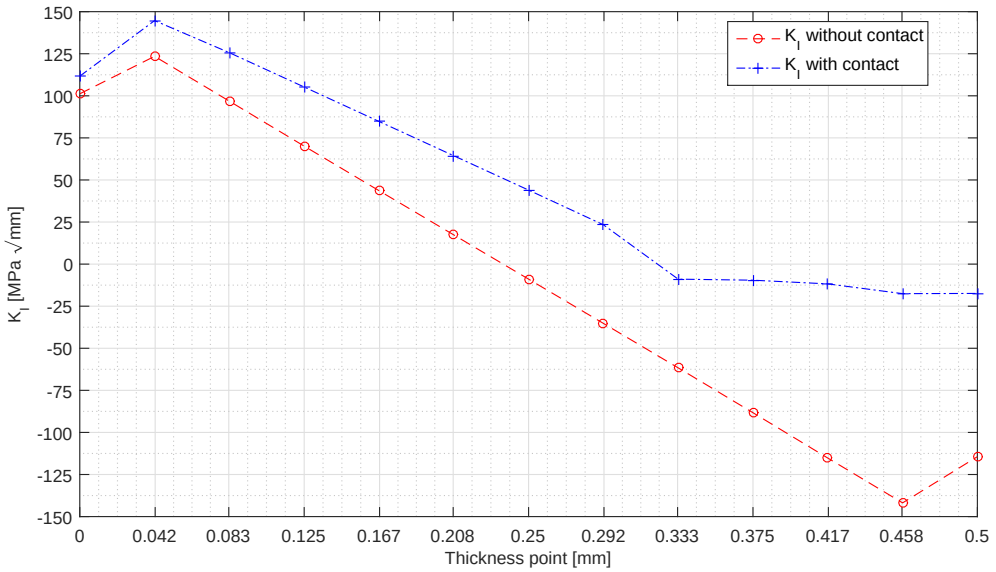


Figure 8.19: Comparison of $K_I$ values for the models with and without contact.

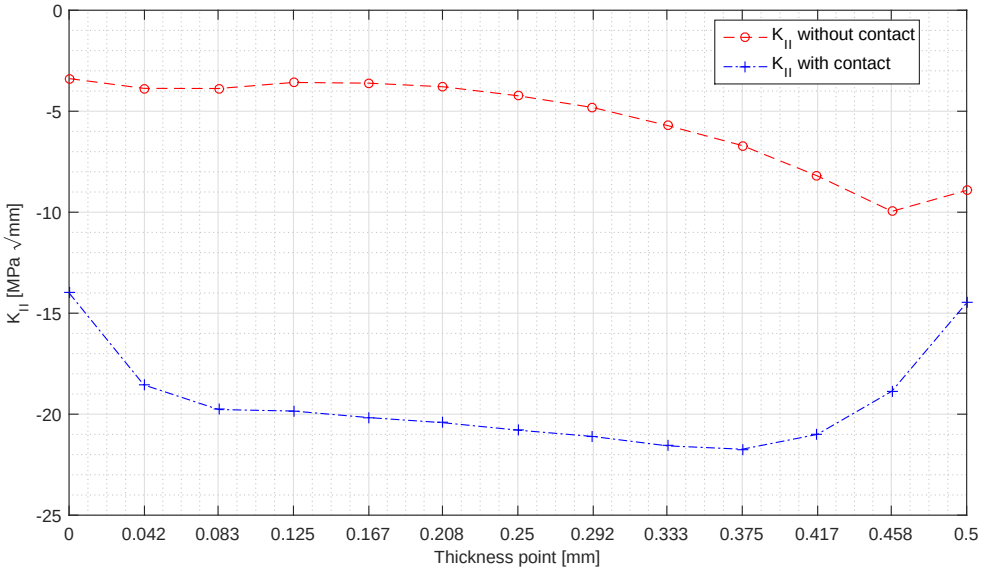


Figure 8.20: Comparison of $K_{II}$ values for the models with and without contact.

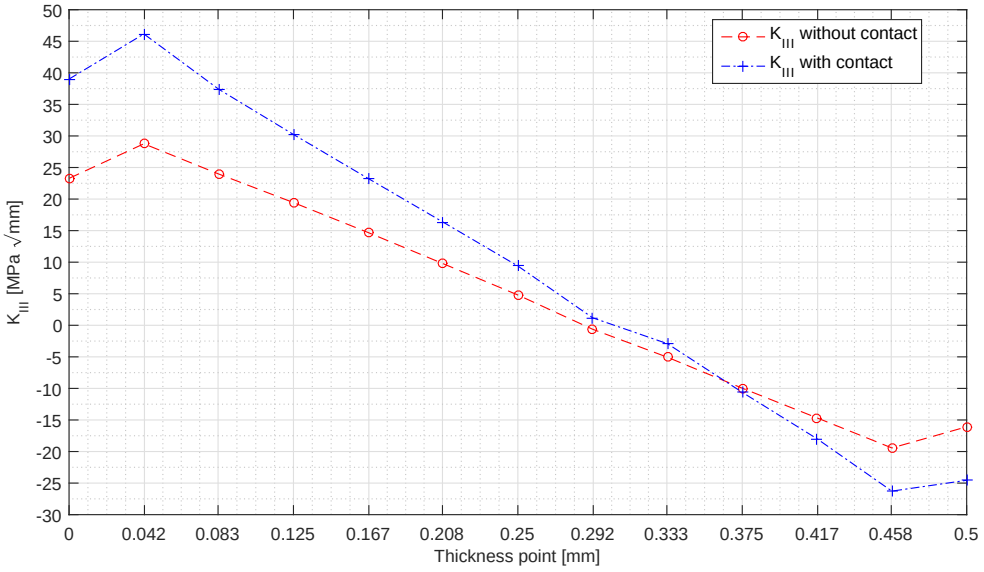


Figure 8.21: Comparison of $K_{III}$ values for the models with and without contact.

### 8.4.2 Lower Crack Front

The lower front was also analysed in the same manner as the upper one. For the contactless model, the inflection point of $K_I$ was found slightly before node 8, at about 0.290 mm of thickness. For mode III, a behaviour similar to that found on the lower tip of the -15° crack occurred, and the inflection point was located between the first and second nodes, at about 0.040 mm thickness. This conclusion can be questioned since no free surface effect was found. However, the difference has little significance. For the model contemplating contact, for mode I the relevant point was located just before node 11, at 0.410 mm. No inflection was found to occur for mode III.

Trends similar to those found for the lower tip of the last crack ($\alpha = -15°$) are visible in Figures 8.22 to 8.24 for all modes, when comparing the correspondent curves for models without contact. However, the absolute values of the SIFs maximum and minimum do not decrease, as happened between the 0° and -15° cracks. On the contrary, some increase is noticeable, tough the plot shapes remain the same. Regarding the SIFs for the model with contact, the SIFs were affected in the same manner of those from the upper crack tip, yielding again a more severe stress state. Nevertheless, for both models, the conclusion is that the lower crack front is subjected to a less intense loading, as previous found for the lower front of the $\alpha = -15°$ crack.

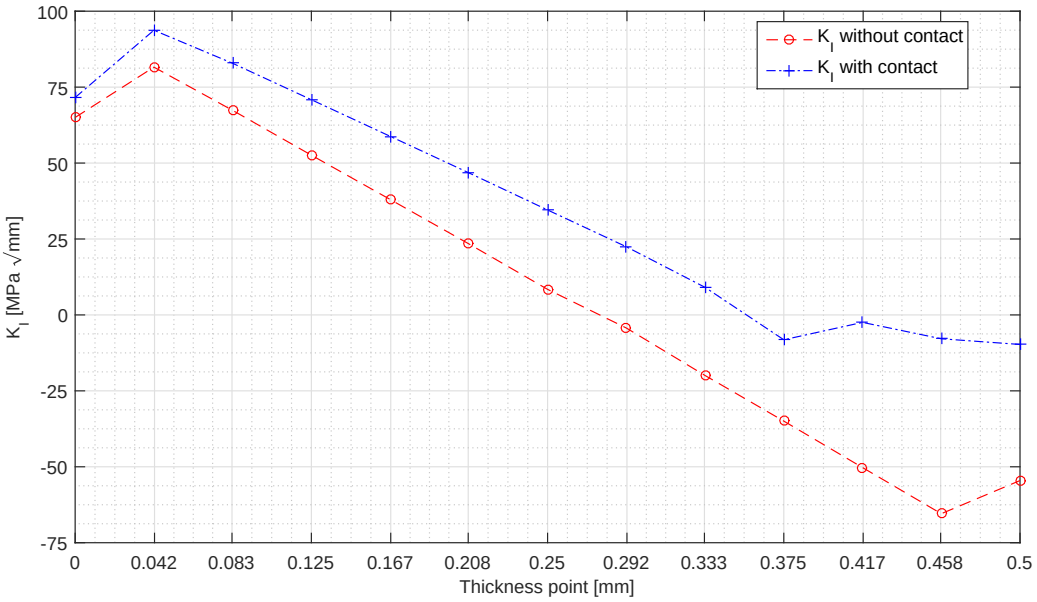


Figure 8.22: Comparison of $K_I$ values for the models with and without contact.

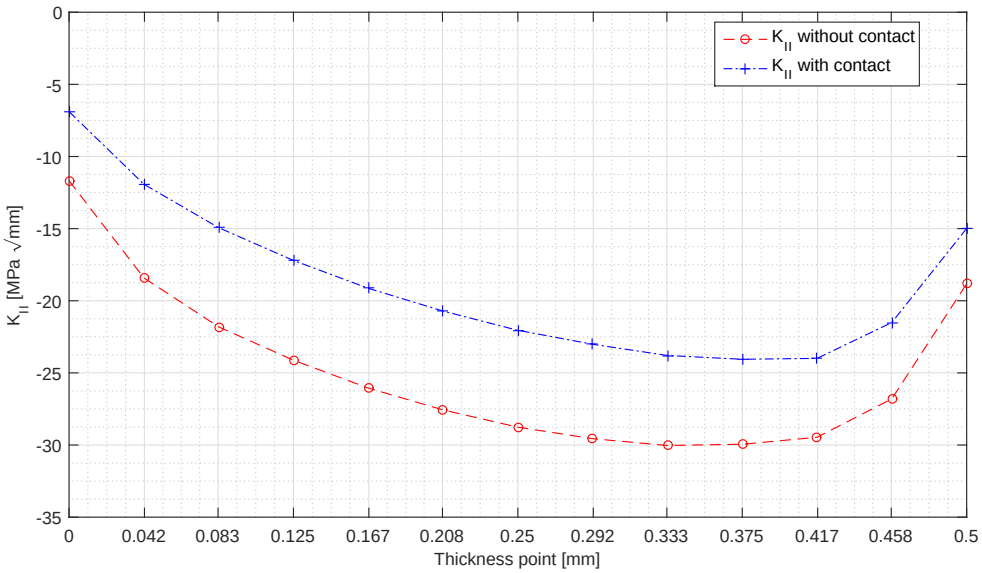


Figure 8.23: Comparison of $K_{II}$ values for the models with and without contact.

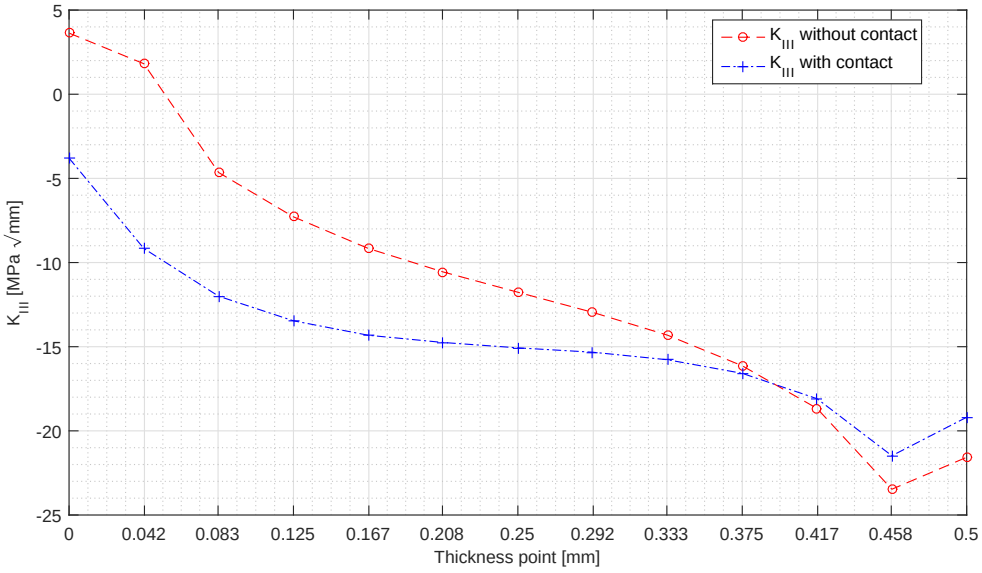


Figure 8.24: Comparison of $K_{III}$ values for the models with and without contact.

## 8.5 Crack with -45° Inclination

A final crack with $\alpha = -45^{o}$ was modelled. This crack was modelled following the steps mentioned on Section 8.1 as close as possible. Due the increased influence of the leading edge skin curvature, some adaptations, including the use of auxiliary points for further partitioning steps, were necessary to achieve a crack length of $2a = 10$ mm and an adequate mesh. The contact problem was as done on the previous Section, and the corresponding SIFs were extracted.

Figure 8.25 shows the von Mises stress field on the crack zone.

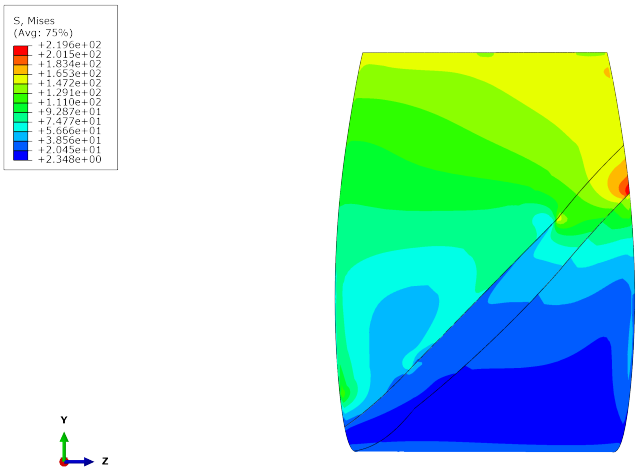


Figure 8.25: von Mises stress field on the crack zone, $\alpha = -45°$.

### 8.5.1 Upper Crack Front

A pattern following the previous crack not considering contact was noticed when finding the inflection point for mode I. This point was located between 0.125 mm and 0.167 mm, which is between nodes 4 and 5. This shows a pattern of increasing compression zone, which has been a constantly observed for increasing inclination angles. For mode III, there was no inflection point, meaning that $K_{III}$ values will always have the same value. This did not follow a pattern, since for mode III the inflection point had been constant in the two previous crack configurations.

The crack modelled with contact showed, for mode I, a contact point between 0.333 mm and 0.375 mm (nodes 9 and 10), which means a decrease on the compressed zone compared to the last crack with the same contact definition. The same shift towards the exterior happened to the inflection point for mode III, whose inflection point was located between nodes 5 and 6, corresponding to 0.208 mm and 0.250 mm.

The plots of SIFs extracted for this crack front are shown on Figures 8.26 to 8.28, and again the same trends are visible: the $K_I$ line shifts downwards along the $K$ axis, and $K_{II}$ and $K_{III}$ absolute minimum and maximum values decrease, thus reducing the corresponding SIFs range. Therefore, this inclination yields a yet lower stress field on the upper crack front. Concerning mode II, it should be noted that modelling contacted yielded a somewhat different SIF distribution, a behaviour that was only found for this mode and crack configuration. Results were double checked and no error was found. Yet, no explanation occurs for this behaviour.

Regarding the model contemplating contact, again a more severe state on the crack front is found, when comparing to the model without contact. However, when making the correspondent comparison between cracks modelled with contact, the same pattern of decreased severity against an inclination increase is found.

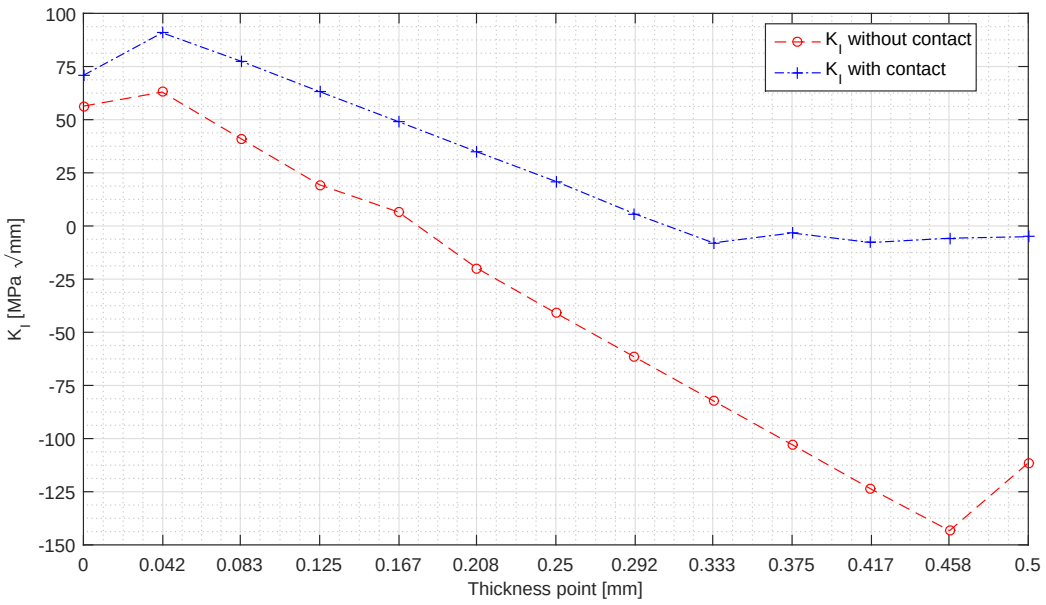


Figure 8.26: Comparison of $K_I$ values for the models with and without contact.

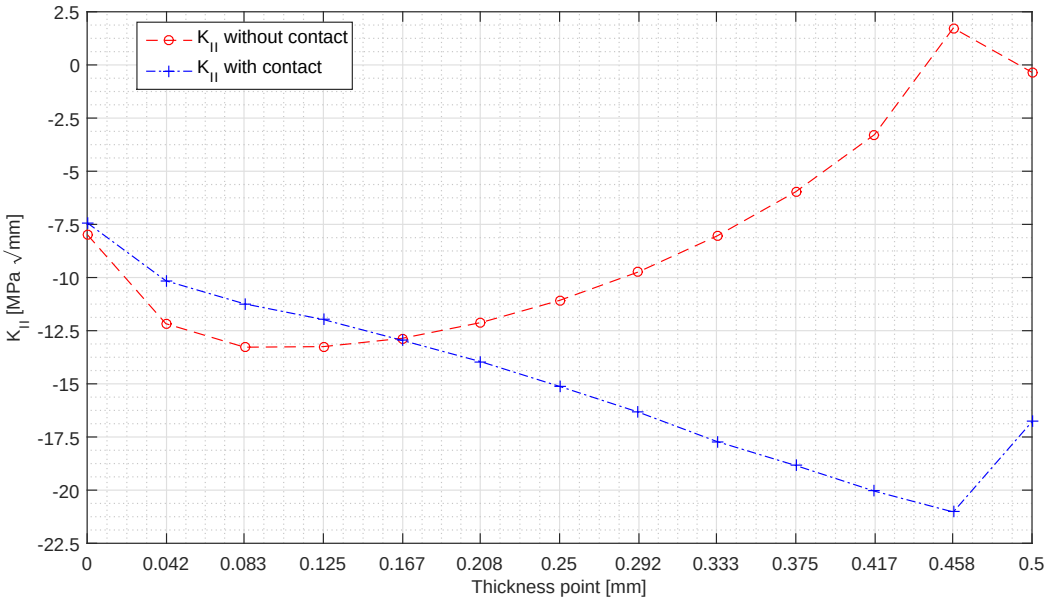


Figure 8.27: Comparison of $K_{II}$ values for the models with and without contact.

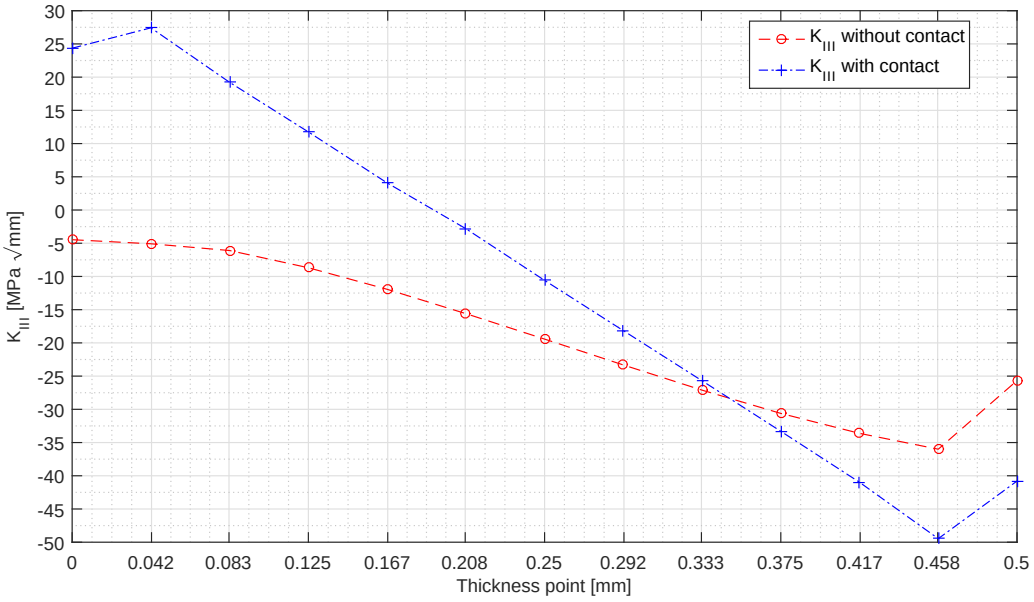


Figure 8.28: Comparison of $K_{III}$ values for the models with and without contact.

### 8.5.2 Lower Crack Front

The analysis of the lower crack front revealed a completely different mode I and III behaviour. At the zone where this crack front is located, the bending state of the skin is already inverted, and this was reflected on the crack behaviour. Regarding the model without contact, the inflection point was located at approximately 0.220 mm. However, the compression-tension transition occurred inwards the skin, and not outwards as on all previous cases. For mode III, the transition happened between nodes 11 and 12, but the $K_{III}$ signs were again inverse from what was previously studied. For the model with contact the last 3 thickness nodes seemed to be under tension. However, $K_I$ values were residual at these nodes, meaning that, for this model, mode I is barely present. Concerning mode III, and as verified for the 30° crack lower front, no inflection point was found. Although $K_{III}$ for this case presented opposite sign when compared to the last crack, these values were also very low. One could conclude that only mode II was present, but it must be remarked that its intensity, while higher than the other modes, was also low, thus revealing that the lower front of this last crack is under a very low load state.

Results for this crack front are plotted on Figures to 8.29 to 8.31.

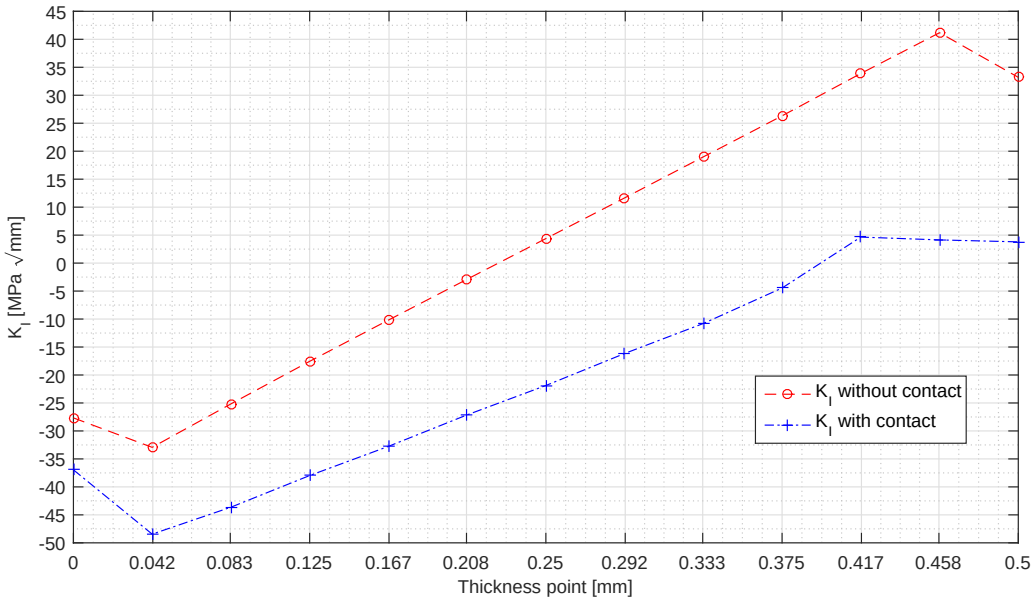


Figure 8.29: Comparison of $K_I$ values for the models with and without contact.

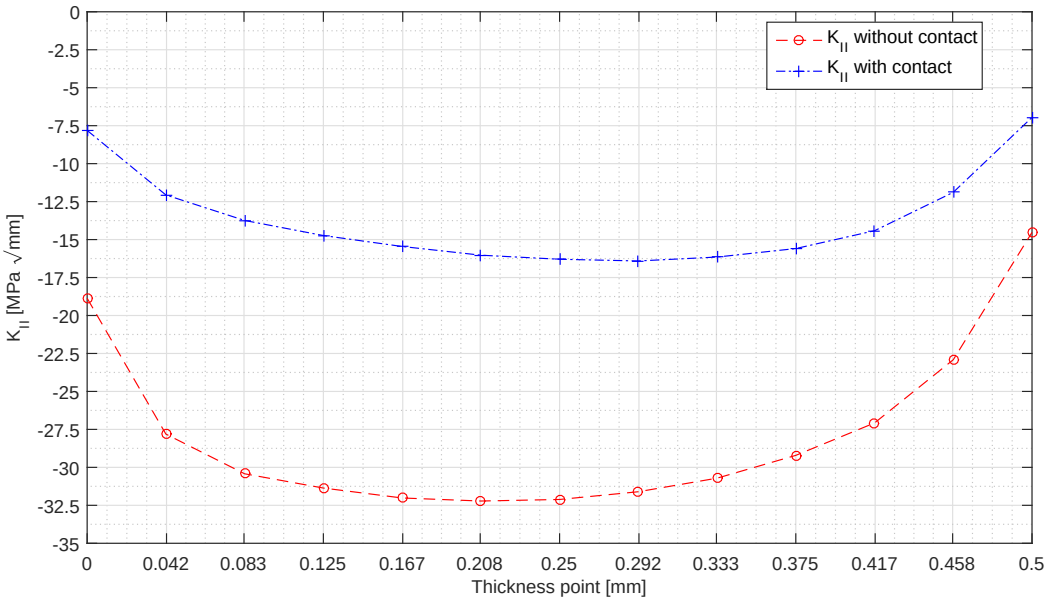


Figure 8.30: Comparison of $K_{II}$ values for the models with and without contact.

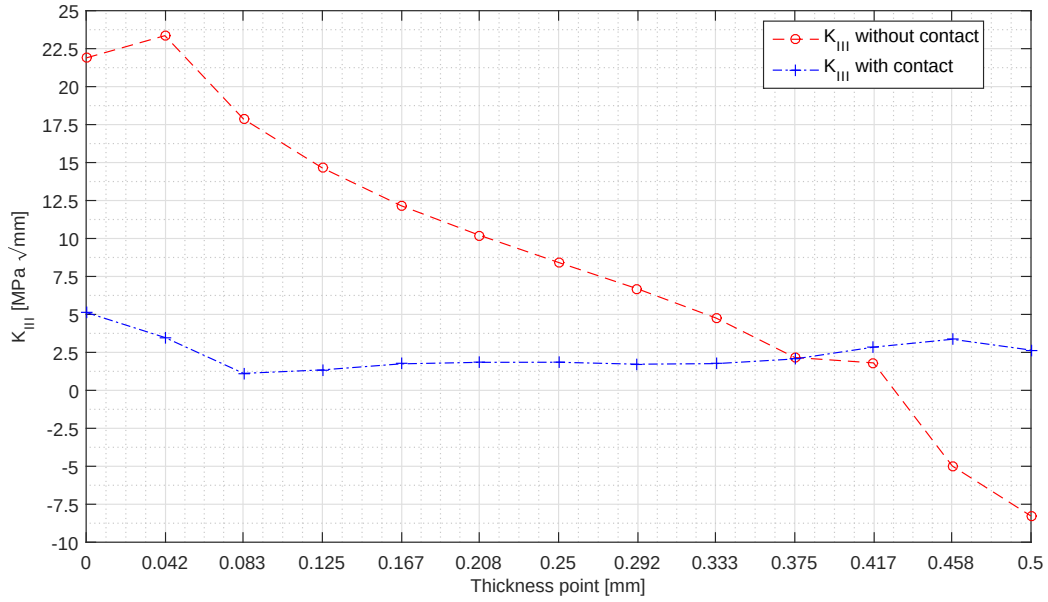


Figure 8.31: Comparison of $K_{III}$ values for the models with and without contact.

## 8.6 Final comparison

To provide the reader a final overview of the inclination effect on the SIFs, the SIFs maximum and minimum values (without contact) were plotted as a function of the absolute inclination angle $\alpha$. This can be seen on Figures 8.32 to 8.34.

Summarizing the results, it can be said that:

- Inclination angle tends to yield a greater compression region on the both crack fronts, resulting in lower $K_I$ values on the tensioned zones.
- Between 30° and 45° and for the lower crack, the compression zone shifts to the exterior surface and the tension zone to the interior one.
- Results are accordingly affected: $K_I$ maximum value for 45°occurs in the inside zone of the skin. Modes II and III also show alterations.
- With reserves for mode III and for mode II on the lower crack front, increasing angles yield lower crack front stress fields.
- Contact plays a role on the crack behaviour, yielding different deformed crack shapes and altering SIFs distribution and each mode importance.

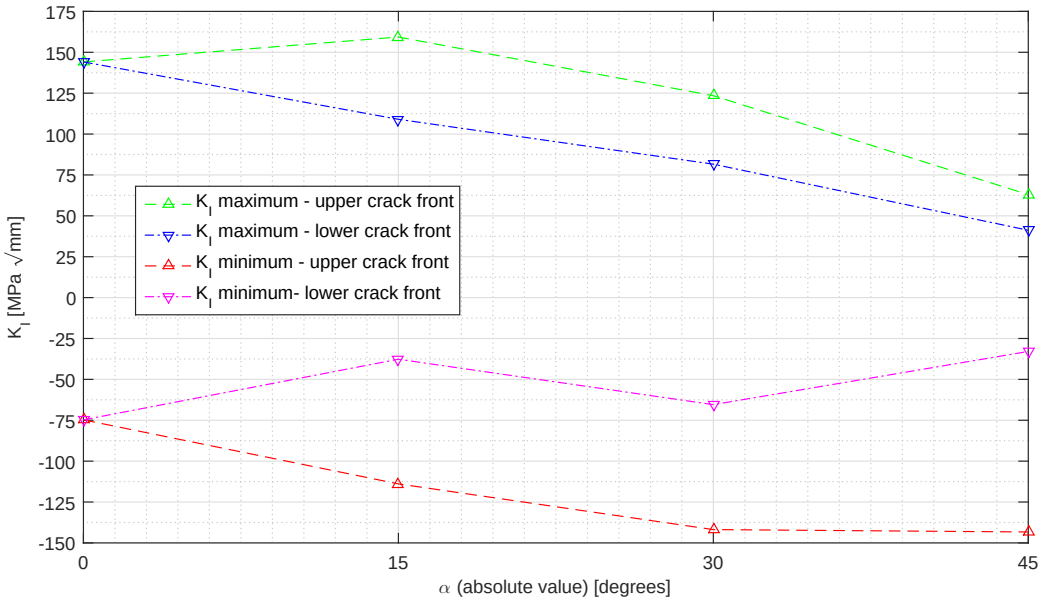


Figure 8.32: Evolution of $K_I$ maximum and minimum values.

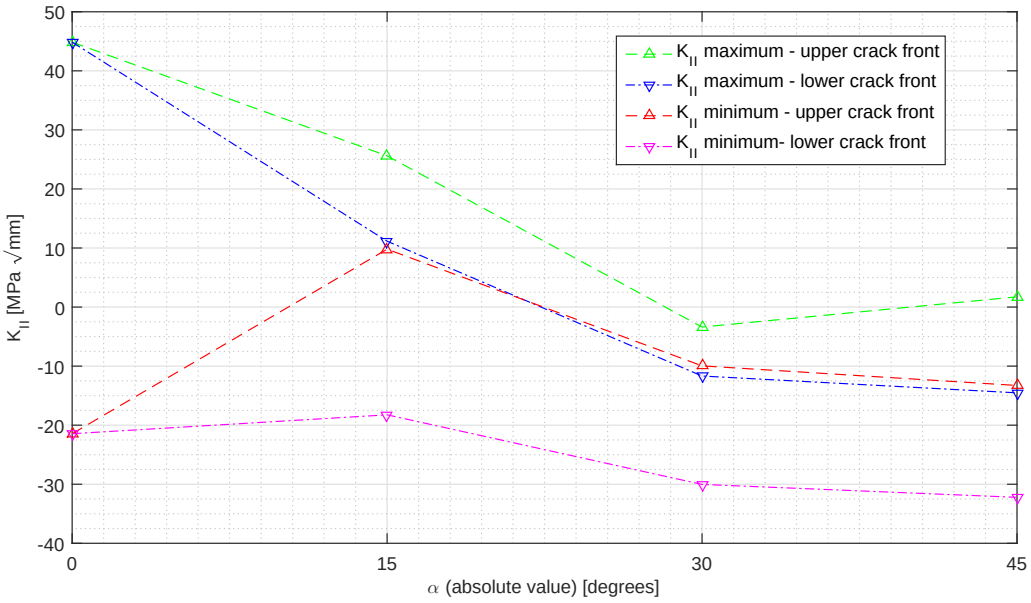


Figure 8.33: Evolution of $K_{II}$ maximum and minimum values.

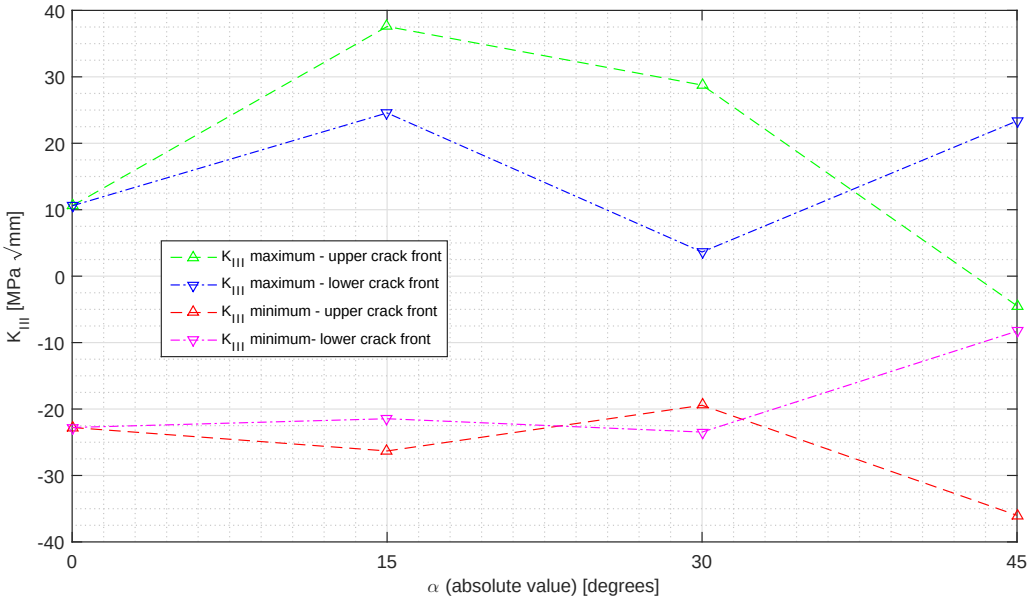


Figure 8.34: Evolution of $K_{III}$ maximum and minimum values.

# Chapter 9

# Estimation of the Fatigue Life

In this chapter, some concepts concerning damage tolerant design will be recalled, and an estimation of the crack propagation will be done. This will result of the numerical integration of the Paris Law, using the results from the previous chapter.

## 9.1 Equivalent Stress Intensity Factor Concept

The concept of stress intensity factor $K$ has been used throughout this work and was introduced on Chapter 4. On the the brief introduction to Fracture Mechanics principles made on that Chapter (Section 4.2), the relationship between $K$ and $G$, the Strain Energy Release Rate, was deduced for mode I (recall equation 4.5):

$$G_I = \frac{K_I^2}{E^*} \tag{9.1}$$

where

$$E^* = \begin{cases} E & for\, plane\, stress \\ \frac{E}{1-v^2} & for\, plane\, strain \end{cases}$$

However, and since mode I was not the only crack opening mode present on the studied cracks, it is important to extend this relationship to mode II and mode III. The same relationship is found for mode II (p.127, Broek, 1986, p.60, Anderson, 2005):

$$G_{II} = \frac{K_{II}^2}{E^*} \tag{9.2}$$

For mode III, this relationship is as follows:

$$G_{III} = \frac{K_{III}^2}{2\mu} \tag{9.3}$$

where $\mu$ is the shear modulus[a]. Bearing in mind that the relationship between the Young Modulus $E$ and the Shear Modulus $\mu$ is:

$$\mu = \frac{E}{2(1+\nu)} \tag{9.4}$$

equation 9.3 can be rewritten as:

$$G_{III} = \frac{K_{III}^2}{E}(1+\nu) \tag{9.5}$$

Therefore, the total Strain Energy Release Rate can be deduced from the above equations. Considering plane stress:

$$\begin{aligned} G = G_I + G_{II} + G_{III} &= \frac{K_I^2}{E} + \frac{K_{II}^2}{E} + (1+v)\frac{K_{III}^2}{E} \\ G &= \frac{1}{E}(K_I^2 + K_{II}^2 + (1+v)K_{III}^2) \end{aligned} \tag{9.6}$$

Using this equation, a equivalent SIF can be derived by similarity with Equations 9.1 or 9.2, for instance:

$$\begin{aligned} G = \frac{1}{E}(K_I^2 + K_{II}^2 + (1+v)K_{III}^2) &= \frac{K_{eq}^2}{E} \\ K_{eq} &= \sqrt{K_I^2 + K_{II}^2 + (1+v)K_{III}^2} \end{aligned} \tag{9.7}$$

The derivation of this formula for an equivalent SIF was based only on the relationship between $K$ and $G$ and on the assumption of plane stress. A version of this formula for plane strain is provided, for instance, on (Radaj, 2013). The same author discusses alternative formulations for an equivalent SIF, of increased extent and complexity. Nevertheless, the equation 9.7 will be used in this text in order to estimate the leading edge skin fatigue life.

## 9.2 Paris Law Integration

As mentioned on Chapter 4, the growth rate of a crack, during its stable-growth phase, can be predicted using the Paris Law. This law was presented on section 4.2.4 and is now recalled:

$$\frac{da}{dN} = C(\Delta K)^m \tag{9.8}$$

[a]The shear modulus is usually denoted by $G$. This is the current practice at FEUP, but was not followed to avoid confusion with Strain Energy Release Rate.

This equation provides information about the crack growth rate $da/dN$ for a certain $\Delta K$, and its integration can be used to calculate the number of cycles that lead to a certain crack length increase from $a_i$ to $a_f$:

$$N = \frac{1}{C}\int_{a_o}^{a_f} \frac{1}{(\Delta K)^m} da \tag{9.9}$$

The integral from equation 9.9 is easily calculated provided that a continuum SIF calibration is present, such as $K = Y\sigma\sqrt{\pi a}$, and consequently $\Delta K = Y\Delta\sigma\sqrt{\pi a}$. However, for the object of present study, and given the complex part geometry and loading conditions, no SIF calibration is available other than the discrete SIF data for obtained for certain crack lengths, $\Delta K = \{\Delta K_1, \Delta K_2, \Delta K_i, ..., \Delta K_n\}$. Therefore, a numerical integration technique is the only way to integrate equation 9.9 for this case.

Several numerical techniques exist. The trapezoidal rule was chosen since it is of simple use. Also, given the discrete nature of the data points retrieved, a more complicated method was deemed unnecessary. The trapezoidal rule is an approximation that considers the region under a graphic representation of a certain function $f(x)$ as trapezoid and calculates its area:

$$\int_a^b f(x)\,dx \approx (b-a)\left[\frac{f(a)+f(b)}{2}\right] \tag{9.10}$$

For the case being studied, $f(a)$ and $f(b)$ will be the SIFs values extracted for the crack lengths $a$ and $b$. Considering that the crack lengths studied are $\{a_1, a_2, a_i, ..., a_n\}$ (being $n = 9$ in this case), and applying the trapezoidal rule to calculate the integral between each pair of crack lengths, the number of cycles until $(a_n - a_{n-1})/2$[b] can be calculated by:

$$N = \sum_{i=i}^{n-1}\left[\left(\frac{1}{C\Delta K(a_i)^m} + \frac{1}{C\Delta K(a_{i+1})^m}\right)\frac{a_{i+1}-a_i}{2}\right] \tag{9.11}$$

Taken into account the equation 9.7, numerical integration will be done using:

$$\Delta K = K_{eq,max} - K_{eq,min} \tag{9.12}$$

In this case, $K_{I,min} = K_{II,min} = K_{III,min} = 0$, meaning that $K_{eq,min} = 0$[c]. Therefore:

$$\Delta K = K_{eq,max} \tag{9.13}$$

[b] This average value is due to the formulation of the numerical integration rule.

[c] $K_{min}$ and $K_{max}$ refers to the minimum and maximum SIF values during the loading cycle.

## 9.3 Equivalent SIF calculation for each Crack Location

The stress intensity factor calibrations mentioned in the last section were obtained on Chapter 7. These SIFs curves were obtained for through thickness cracks parallel to a generatrix of the skin surface, located at three different positions: 52%, 49% and 46% of the airfoil perimeter. It was found that, due to the bending of the skin, the crack opened only on the tensioned zone, and interpenetration (due to no contact consideration being done) of the crack faces occurred on the compressed zone. This resulted on negative $K_I$, which were disregarded.

Later, on Chapter 8, it was verified that modelling contact, while eliminating interpenetration, yielded, in general, SIFs of the same order of magnitude and trough thickness behaviour of models disregarding contact, . Therefore, it can be said that the SIF calibrations obtained, for each crack and each crack loading mode, on Chapter 7, can be used to provide an estimate of the leading edge skin fatigue part (considering, of course, these locations only).

Given that the concept of equivalent stress intensity factor was only introduced in the beginning of this chapter, it is necessary to calculate this value for each crack location and length. Considering that negative $K_I$ values will be disregarded, the $K_{eq}$ values will be calculated for the locations under tension. Moreover, since the SIF distribution is not uniform along the thickness, $K_{eq}$ will be calculated for the crack front end under tension, where the SIF values for all modes tend to be maximized. This means that the estimation of the fatigue life will be conservative.

For the first crack location, tension occurs on the exterior side of the skin. Consequently $K_{eq}$ was calculated for the exterior end of crack front. This calculation is presented, for each crack length $2a$, on table 9.1. Considering now the second crack set, the exterior end of the crack front is also under tension. Values of $K_{eq}$ were calculated accordingly and registered on table 9.2. Finally, $K_{eq}$ was calculated for the third set of cracks. In this case, tension is located on the interior zone of the skin. Values of $K_{eq}$ for this location can be found on Table 9.3.

To better illustrate the evolution of the equivalent SIFs versus crack length, their curves were plotted and are shown on Figure 9.1. It can be concluded that the first crack location is, between the three configurations studied, the critical one, yielding the most severe crack front stress field. It is also visible that, for this and the second crack configuration, the SIF stabilization trend observed for mode I is reflected on $K_{eq}$. This can be seen as a proof of mode I predominance for these cracks. On the other side, the third crack configuration shoes a continuous increase trend, similar to that of mode II for this location (refer to table 9.2). This confirms that mode II gains importance on the third crack location.

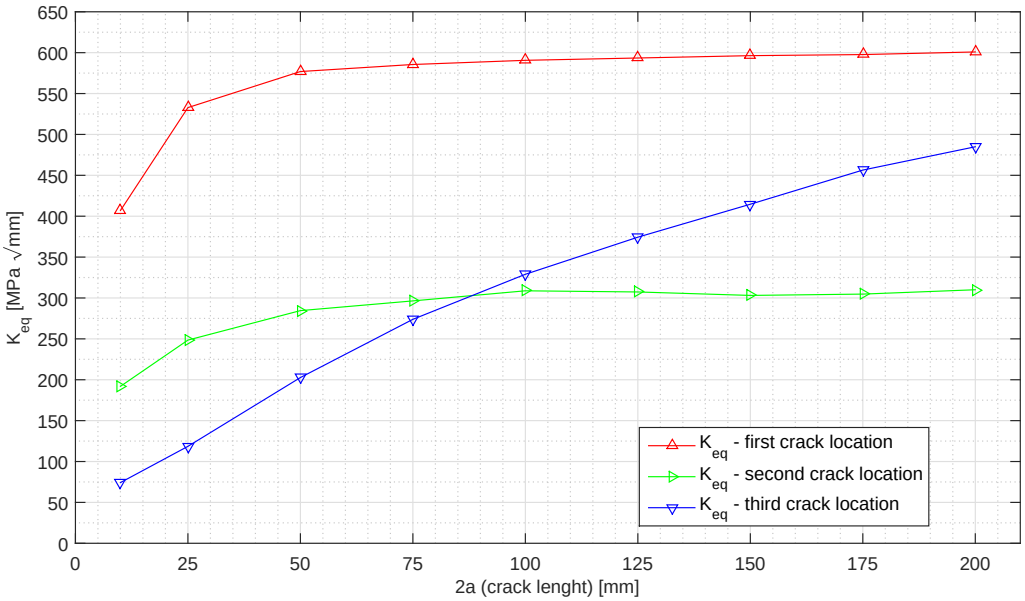


Figure 9.1: $K_{eq}$ versus $2a$ for the three crack positions.

Table 9.1: $K_{eq}$ calculation for the first crack.

| $2a$ | $K_I$ | $K_{II}$ | $K_{III}$ | $K_{eq}$ |
|---|---|---|---|---|
| 10 | 406.0 | 21.0 | 14.7 | 406.9 |
| 25 | 529.6 | 46.1 | 31.1 | 532.8 |
| 50 | 573.6 | 47.9 | 34.3 | 576.9 |
| 75 | 582.2 | 47.0 | 36.2 | 585.5 |
| 100 | 587.0 | 47.4 | 40.2 | 590.6 |
| 125 | 589.4 | 47.1 | 44.6 | 593.5 |
| 150 | 591.9 | 46.8 | 48.5 | 596.3 |
| 175 | 593.2 | 44.8 | 50.4 | 597.7 |
| 200 | 596.1 | 43.5 | 54.2 | 600.9 |
| [mm] | $MPa\sqrt{mm}$ | | | |

Table 9.2: $K_{eq}$ calculation for the second crack.

| $2a$ | $K_I$ | $K_{II}$ | $K_{III}$ | $K_{eq}$ |
|---|---|---|---|---|
| 10 | 189.5 | 22.4 | -10.8 | 191.2 |
| 25 | 246.1 | 42.5 | -38.8 | 253.6 |
| 50 | 276.3 | 33.7 | -93.0 | 297.9 |
| 75 | 290.3 | 8.4 | -146.1 | 334.8 |
| 100 | 296.6 | 43.2 | -166.5 | 354.8 |
| 125 | 296.7 | -26.1 | -212.9 | 384.2 |
| 150 | 293.5 | -33.8 | -231.1 | 395.8 |
| 175 | 289.0 | -38.3 | -244.3 | 403.2 |
| 200 | 285.4 | -40.0 | -255.9 | 410.1 |
| [mm] | $MPa\sqrt{mm}$ | | | |

Table 9.3: $K_{eq}$ calculation for the third crack.

| $2a$ | $K_I$ | $K_{II}$ | $K_{III}$ | $K_{eq}$ |
|---|---|---|---|---|
| 10 | 70.7 | -20.7 | 8.3 | 74.2 |
| 25 | 87.6 | -74.1 | 26.1 | 118.5 |
| 50 | 111.1 | -161.2 | 46.0 | 202.7 |
| 75 | 128.6 | -232.1 | 59.6 | 273.9 |
| 100 | 140.8 | -286.9 | 68.4 | 329.0 |
| 125 | 152.2 | -331.3 | 74.4 | 374.3 |
| 150 | 165.3 | -369.6 | 78.4 | 414.7 |
| 175 | 179.4 | -409.4 | 80.8 | 456.4 |
| 200 | 196.9 | -432.9 | 83.2 | 484.9 |
| [mm] | $MPa\sqrt{mm}$ | | | |

## 9.4 Fatigue life estimation

The previous sections section provided both the tools and the data necessary for an estimation of the fatigue life, with exception of the Paris law parameters. These depend on material and $R$ ratio, which is, in this case, $R = 0$. However, this loading ratio poses experimental difficulties, and most testing in order to retrieve Paris law constants is done for $R = 0.1$ or higher. Consequently, this value was considered when picking these parameters from literature.

Three aluminium alloys of common aeronautical use were chosen: alloy AA2024-T35, alloy AA2198-T8 and alloy AA6056-T6. Their Paris law constants are presented in Table 9.4.

Table 9.4: Paris law parameters for the Aluminium alloys considered

| Alloy | $C$ | $m$ | Source |
|---|---|---|---|
| AA2024-T351 | $2.85 \times 10^{-12}$ | 2.94 | (Golestaneh et al., 2009) |
| AA2198-T8 | $1.21 \times 10^{-11}$ | 2.71 | *NASGRO software* |
| AA6056-T6 | $1.36 \times 10^{-11}$ | 2.74 | (Moreira et al., 2010) |

To ensure the applicability of Paris law, the $\Delta K$ range should be comprehended between $\Delta K_{th}$ and $K_c$. Literature was consulted and, although values for the above mentioned alloys were not specifically mentioned, $\Delta K_{th}$ values between approximately 63 $MPa\sqrt{mm}$ to 94 $MPa\sqrt{mm}$ were found to be common for aluminium alloys. Concerning $K_c$, mentioned values were about ten times higher: 800 $MPa\sqrt{mm}$ and above (John et al., 2003; Suresh, 1998; Smith, 1979a). It can be concluded that the equivalent SIF calibration obtained for the three crack locations is within this limits. Thus, Paris law can be used to estimate the fatigue life.

Using each alloy parameters and the equivalent SIF calibration for each crack, numerical integration of the Paris law was performed. Results are presented for each crack alloy on Figures 9.2 to 9.7 and for each crack location on Figures 9.8 to 9.10. These are plots of the final crack length $2a_f$ in function of the number of loading cycles. These results indicate that first and second cracks are much more severe than the third crack. Regarding the aluminium alloys considered, AA6056-T6 yielded the least favourable results. This is in accordance the parameters presented on Table 9.4, since AA6056-T6 has the higher $C$ parameter of the three alloys studied. Since this parameter is the slope of the stable crack growth curve, obviously crack growth is easier on this alloy.

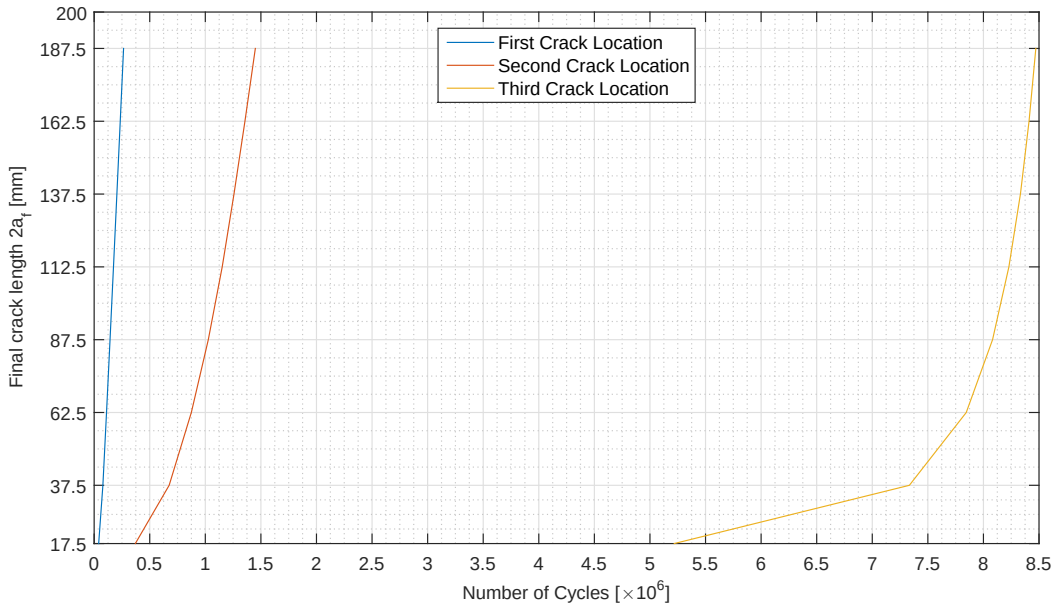


Figure 9.2: Final crack length $2a_f$ for a given number of cycles N, alloy AA2024-T351.

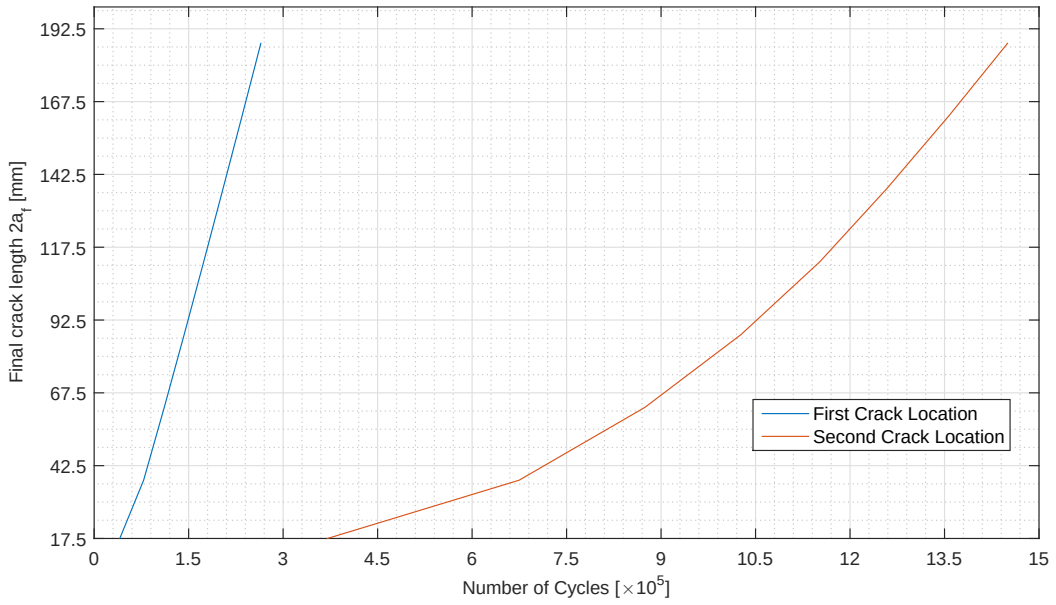


Figure 9.3: Zoom of Figure 9.2 for the first two crack locations.

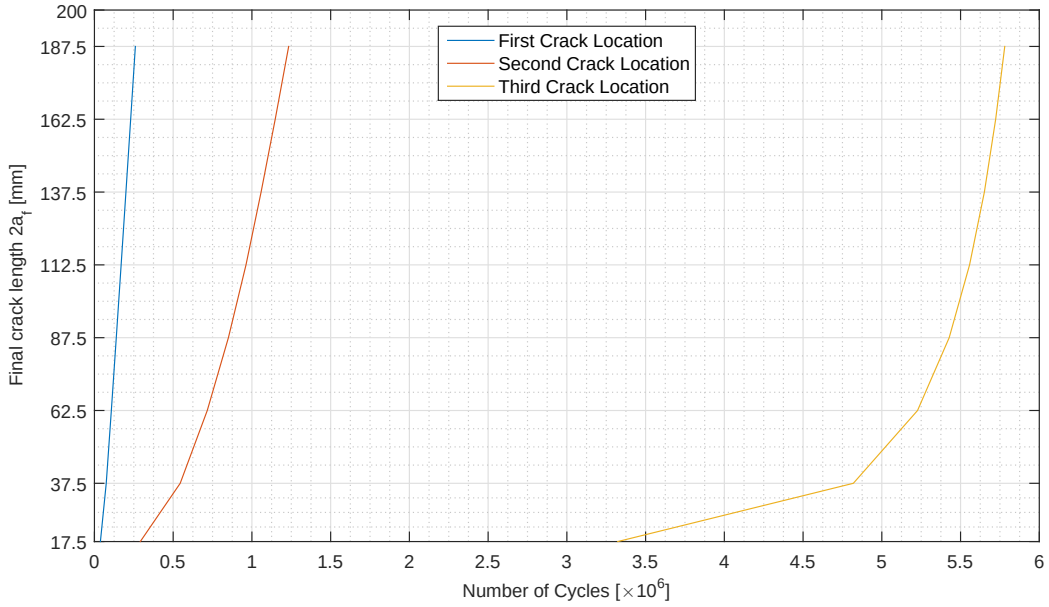


Figure 9.4: Final crack length $2a_f$ for a given number of cycles N, alloy AA2198-T8.

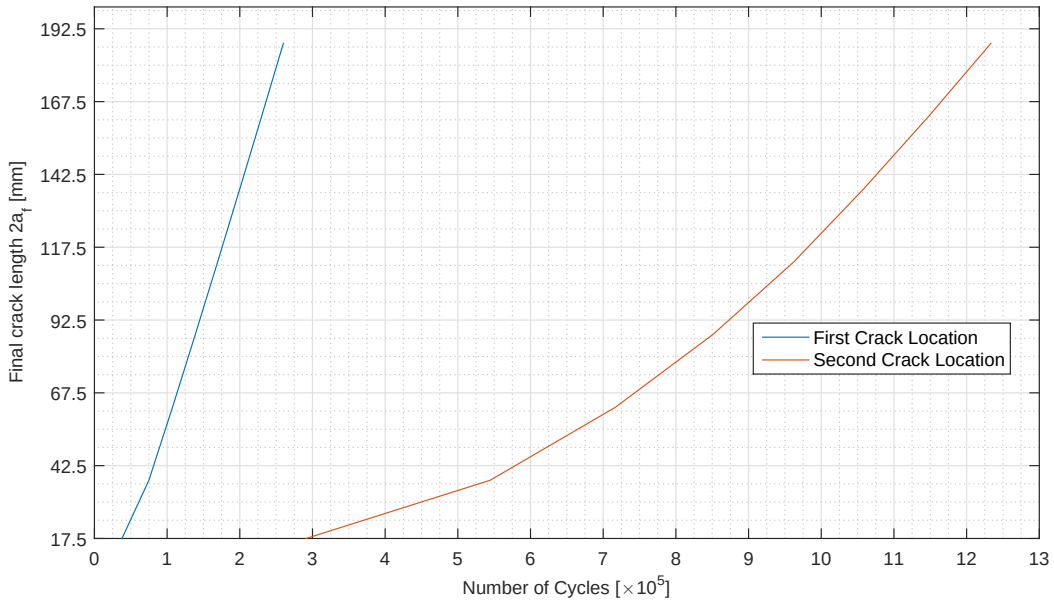


Figure 9.5: Zoom of Figure 9.4 for the first two crack locations.

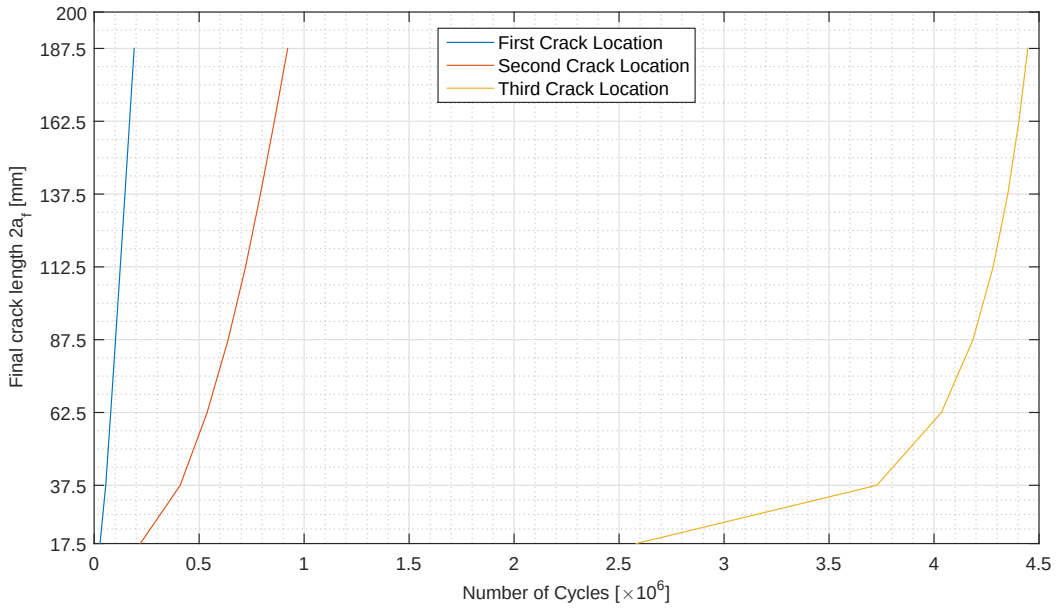


Figure 9.6: Final crack length $2a_f$ for a given number of cycles N, alloy AA6056-T6.

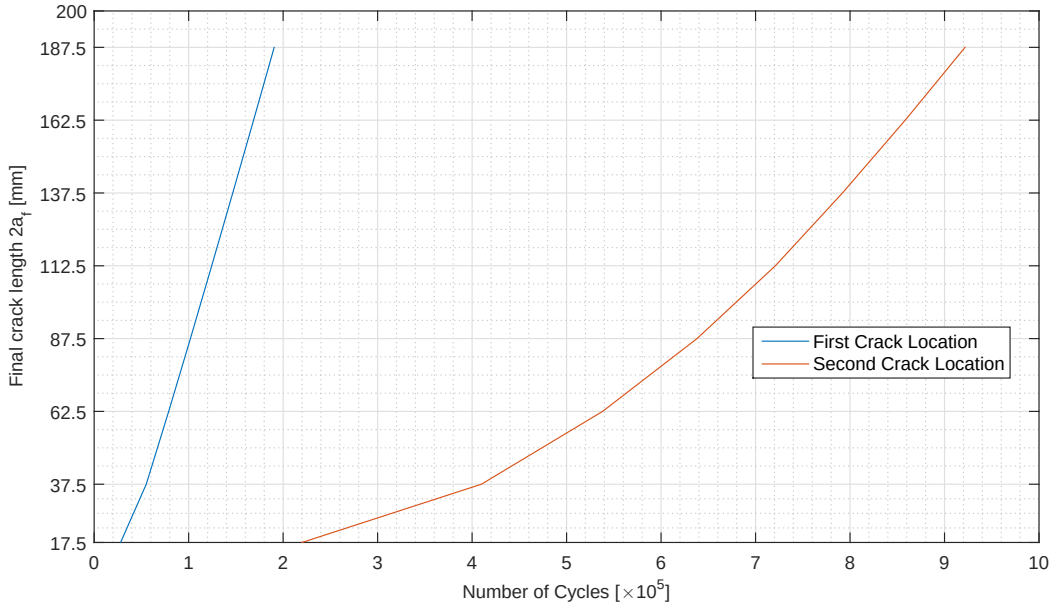


Figure 9.7: Zoom of Figure 9.6 for the first two crack locations.

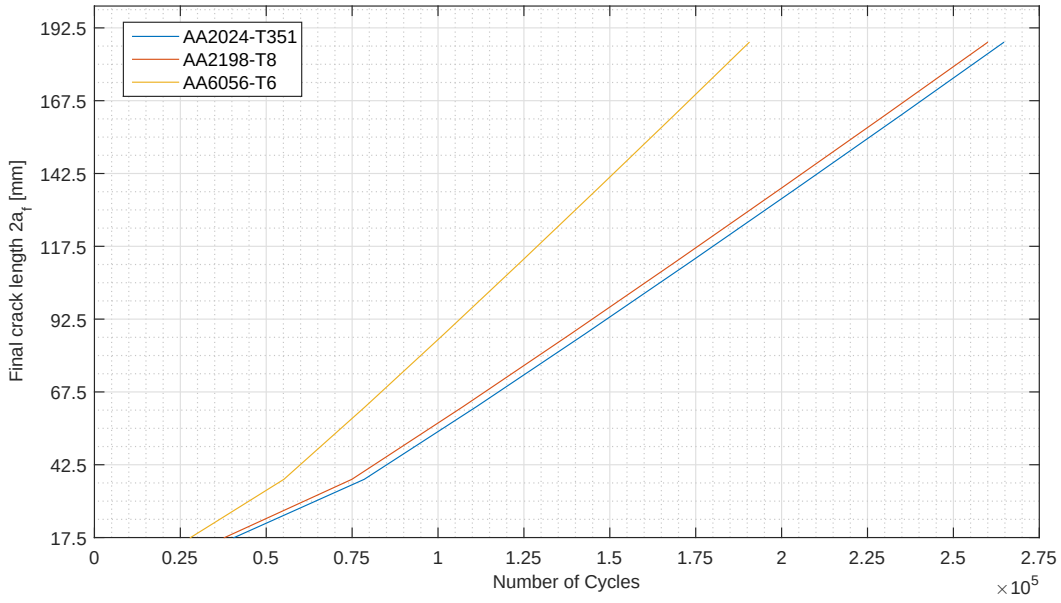


Figure 9.8: Final crack length $2a_f$ for a given number of cycles N, first crack location.

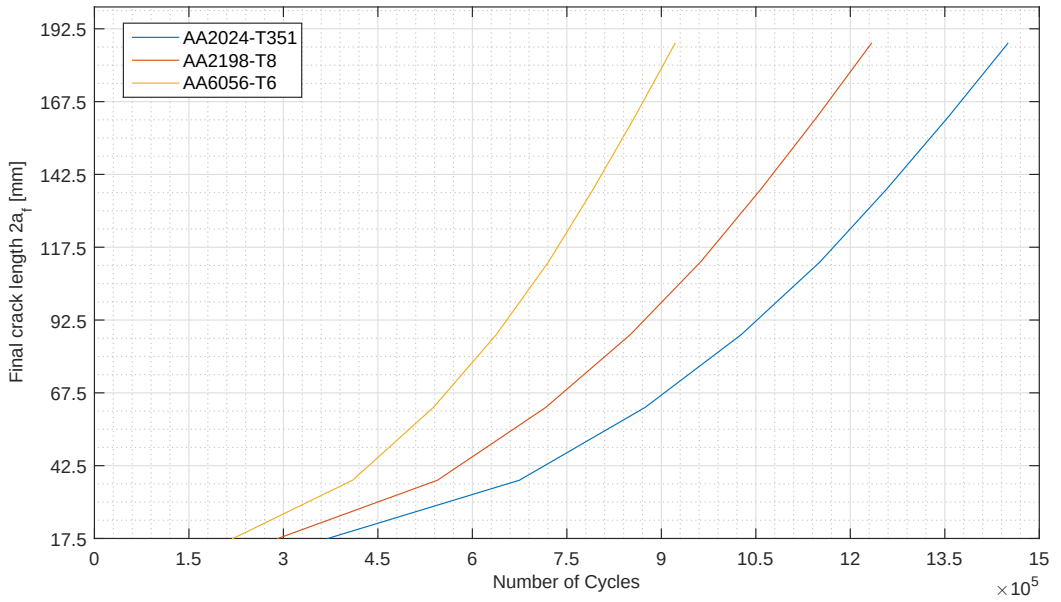


Figure 9.9: Final crack length $2a_f$ for a given number of cycles N, second crack location.

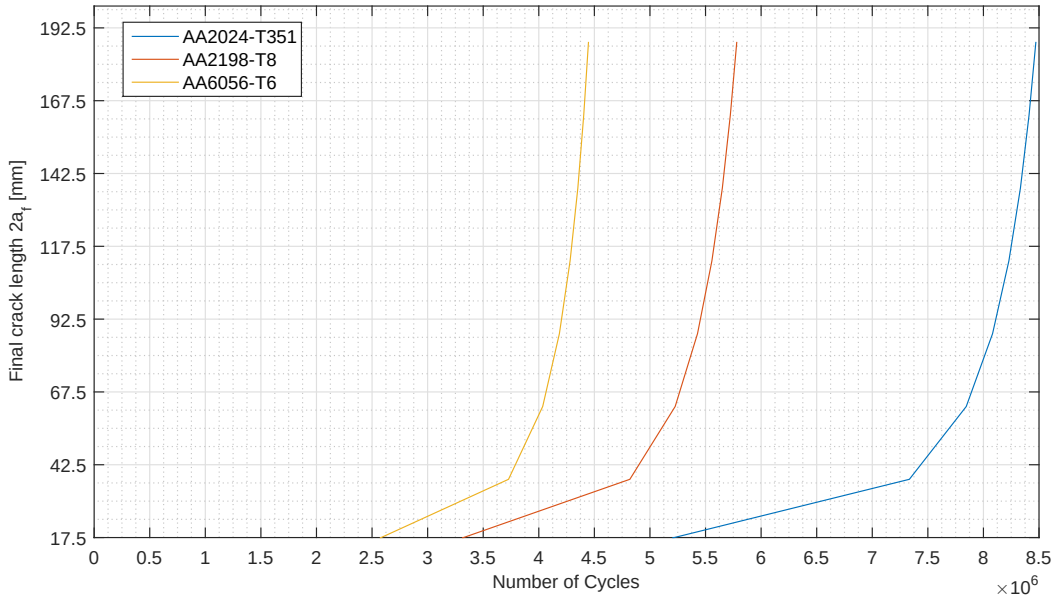


Figure 9.10: Final crack length $2a_f$ for a given number of cycles N, third crack location.

To finalize this study, the results presented should be critically analysed. Concerning the initial assumed crack length, $2a = 10$ mm, it is worth nothing that this value of the same order of those prescribed by the United States Air Force (p.1.3.9, Miedlar et al., 2002): 0.25 inches, or 6.35 mm, to structural details with thickness inferior to 0.125 inches, or 3.175 mm (the case of the wing skin studied). Regarding the worst case registered, it should be noted that, even if a crack was to reach $2a = 200$ mm, which was predicted to happen after 175000 morphing cycles, it was also predicted that, for this configuration, after a certain crack length, the equivalent SIF tended to stabilize or decrease, decreasing the danger posed by this crack to the structural integrity of the wing skin. The same happened to the second most severe crack.

The third crack location, even being the less severe, should be given some attention: equivalent SIF for this configuration tends to increase steadily, and this crack can is compressed on the outside, meaning that it is less detectable. Therefore, if this concept is to be materialized, it seems wise to recommend, accordingly, an inspection plan thought not only with the most severe location in mind, but also for this one.

Finally, it should be noted that only three locations were studied, out of hundreds that could be considered realistic. Bearing in mind this, the results presented should be taken as indicative.

# Chapter 10

# Conclusions and Future Work

## 10.1 Conclusions

- Morphing leading edges pose interesting and complex design challenges that cross many fields of science and engineering, from materials science to the theory of control, passing by applied mechanics and aerodynamics.
- Most of the research in this area is focused on UAVs and composite and advanced non-traditional materials.
- The morphing structure actuation plays a major role in achieving the intended morphing. The use of compliant mechanism, which prevents backlash, creates design problems. Dealing with this problems may involve function-tailored materials.
- The nature of the morphing actions can generate fatigue problems. In composite materials, interlaminar fracture and debonding can pose a problem.
- Although these materials are becoming increasingly present even on passenger aircraft, traditional materials such as Al alloys still are the choice for a significant part of these structures. In the Boeing 787, which uses 50% composites, leading edge structures are mostly made from Aluminium alloys.
- Therefore, morphing structures built of Aluminium alloy should be subjected to a damage tolerance analysis.
- Modelling of the morphing leading edge structure was not a straightforward problem. The uncertainties about diverse constructive details of this assembly lead to several simplifications that may have a noticeable effect on the results of the study.
- Abaqus is one of the most useful and powerful tools for finite element analysis. Nevertheless, one must bear in mind that any software only provides correct results if correct inputs are made. Mistakes can be easily made, and their implications on the results can render these useless.

- Therefore, FEM modelling using Abaqus requires practice, background knowledge and extensive consultation of the user's manual, in order to achieve realistic models and reasonable results. Critical mind is crucial when creating and analysing FEM models.

- However sophisticated and powerful, Abaqus built in capabilities also have deficiencies. As a consequence, users must be aware that, sometimes, results of Abaqus FEM analysis are only a step towards the intended objective.

- Crack modelling on Abaqus can be a cumbersome and time consuming task, again requiring a strong understanding of the implications that each modelling choice has on results accuracy or computational time, for instance.

- Concerning Fracture Mechanics, Abaqus provides diverse tools based on different approaches. Nevertheless, during this work, it was proven that these techniques have their application limits. It was verified that, for mode III, Abaqus J-Integral approach should be used with many reserves. It was also verified that this approach is of limited use on curved surfaces.

- The morphing action simulated during this study yielded a bending state of stress in the leading edge skin. This stress state leads to rather uncommon crack behaviour, with compression on certain regions of the crack front and crack faces.

- Crack modelling showed that, from all the three crack locations considered, compression occurred and lead to the extraction of negative mode I SIFs.

- This was accompanied by interpenetration of the crack fronts, which has no physical meaning. Later on the work, it was shown that modelling contact greatly reduced this.

- Concerning crack locations, it was found that the location at 52% of airfoil perimeter of the leading edge presents the higher severity, and is likely to be the damage initiation location, as a result of unnoticed bird strike, impact with foreign object or other reasons.

- Nevertheless, it was shown that the crack located at 46% of the airfoil perimeter is compressed on the skin exterior zone. If a crack was to exist and propagate, even slowly, its presence could remain unnoticed for a long period.

- Three different locations were considered for cracks parallel to the wing surface generatrix (longitudinal direction). For all locations studied, mode I was found to be preponderant. Accordingly, crack propagation was judged to occur on the longitudinal direction. Mode II and, to a lesser extent, mode III were also present, and consequently the latter affirmation involves an approximation and is made with reserve.

- Oblique cracks were also simulated, centred at the same location as the more severe longitudinal ones. Inclination created new modelling and analysis problems, due to the curved nature of the skin surface. Abaqus J-integral approach was unable to extract acceptable SIF values.
- mVCCT was used for these cases. A comparison for the longitudinal crack was made between mVCCT and Abaqus J-Integral: results showed good agreement.
- mVCCT application is also not straightforward due to the interpenetration of crack faces verified, leading to the need to perform a case by case results adjustment.
- Concerning the crack inclination, it was found that this yielded less severe stress fields on the crack fronts. This can be related to the less severe crack longitudinal locations studied, since inclination shifted the crack fronts to areas closer to that location. Also, inclination led to changes in the crack opening behaviour.
- Contact was simulated for the last four FEM analysis and, for mode I, SIF was found to be 18% higher. Also, contact simulation led to alterations on mode II and mode III behaviour.
- For the most severe crack scenario considered, and for a skin manufactured using common aeronautical Aluminium alloys, the fatigue life was estimated to be in the order of $1.75 \times 10^5$ cycles.

## 10.2 Suggestions for future work

- Other skin materials, metallic and composite, should be studied.
- Optimization of skin thickness, as a function of location, may facilitate the achievement of a desired aerodynamic profile.
- Fatigue behaviour of the actuation mechanism should be also studied, particular in the sections subjected to high bending and tensile stresses.
- Other locations should be considered for the initial damage, since they may prove to yield a shorter fatigue life.
- Also, other damages could be considered, such as bolt and rivet holes and resulting stress concentrations.
- Contact should be considered in future analysis of structures under the same bending loading.
- Experimental validation of the effects of mode II and mode III on fatigue crack growth should be performed.
- Other morphing structures, more suitable for single or twin aisle aircraft, could be studied.

# Bibliography


Abbott, I. and A. von Doenhoff (1959). *Theory of Wing Sections, Including a Summary of Airfoil Data*. Dover Books on Aeronautical Engineering Series. Dover Publications.

Abdulrahim, M. and R. Lind (2006). Using avian morphology to enhance aircraft maneuverability. In *AIAA Atmospheric Flight Mechanics Conference and Exhibit*, Guidance, Navigation, and Control and Co-located Conferences. American Institute of Aeronautics and Astronautics.

AFWAL-TR-88-3082, A.-A. . (1988). AFTI/F-111 Mission Adaptive Wing Briefing to Industry.

Agarwal, R. K. (2012). *Review of technologies to achieve sustainable (green) aviation*. INTECH Open Access Publisher.

Aircraft Engineering (1954). Aero-isoclinic wing and all-moving wing-tips: Some account of the short sherpa and the considerations which have led to its design. *Aircraft Engineering and Aerospace Technology 26*(1), 18–18.

Ajaj, R. M., C. S. Beaverstock, and M. I. Friswell (2016). Morphing aircraft: the need for a new design philosophy. *Aerospace Science and Technology 49*, 154–166.

Anderson, J. (1989). *Introduction to Flight*. McGraw-Hill series in aeronautical and aerospace engineering. McGraw-Hill.

Anderson, J. (2011). *Fundamentals of Aerodynamics*. McGraw-Hill series in aeronautical and aerospace engineering. McGraw-Hill.

Anderson, T. L. (2005). *Fracture mechanics: fundamentals and applications*. CRC Press.

Atkinson, R., W. Winkworth, and G. Norris (1962). *Behaviour of skin fatigue cracks at the corners of windows in a Comet I fuselage*. HM Stationery Office.

Barbarino, S., O. Bilgen, R. M. Ajaj, M. I. Friswell, and D. J. Inman (2011). A review of morphing aircraft. *Journal of Intelligent Material Systems and Structures 22*(9), 823–877.

Barbarino, S., R. Pecora, L. Lecce, S. Ameduri, L. De Rosa, et al. (2011). Airfoil structural morphing based on sma actuator series: numerical and experimental studies. *Journal of Intelligent Material Systems and Structures*, 1045389X11416032.

Barnett, D. and R. Asaro (1972). The fracture mechanics of slit-like cracks in anisotropic elastic media. *Journal of the Mechanics and Physics of Solids 20*(6), 353–366.

Barter, S., J. Clayton, and G. Clark (1993). Aspects of fatigue affecting the design and maintenance of modern military aircraft. *International Journal of Fatigue 15*(4), 325–332.

Bartley-Cho, J. D., D. P. Wang, C. A. Martin, J. N. Kudva, and M. N. West (2004). Development of high-rate, adaptive trailing edge control surface for the smart wing phase 2 wind tunnel model. *Journal of Intelligent Material Systems and Structures 15*(4), 279–291.

Bertin, J. and R. Cummings (2009). *Aerodynamics for Engineers*. Pearson international edition. Pearson/Prentice Hall.

Blueprints (2016). Panavia Tornado Blueprint, http://drawingdatabase.com/panavia-tornado.

Bolonkin, A. and G. B. Gilyard (1999). Estimated benefits of variable-geometry wing camber control for transport aircraft. Technical report, NASA Scientific and Technical Information (STI) Program Office.

Bonnema, K. and S. Smith (1988). AFTI/F-111 mission adaptive wing flight research program. In *AIAA Flight Test Conference, 4 th, San Diego, CA*, pp. 155–161.

Brocks, W. and I. Scheider (2001). Numerical Aspects of the Path-Dependence of the J-Integral in Incremental Plasticity. How to calculate reliable J-values in FE analyses. Technical Note GKSS/WMS/01/08. Internal report, Institut für Werkstofforschung, GKSS-Forschungszentrum Geesthach.

Broek, D. (1986). *Elementary engineering fracture mechanics* (4th revised edition ed.). Martinus Nijhoff Publishers.

Bubert, E. A., B. K. Woods, K. Lee, C. S. Kothera, and N. M. Wereley (2010). Design and fabrication of a passive 1d morphing aircraft skin. *Journal of Intelligent Material Systems and Structures 21*(17), 1699–1717.

Burnelli, V. (1933, July 11). Aircraft. US Patent 1,917,428.

Cesnik, C. E., H. R. Last, and C. A. Martin (2004). A framework for morphing capability assessment. *AIAA Paper No. AIAA-2004-1654*.

Chen, J. and H. Pan (2013). Stress intensity factor of semi-elliptical surface crack in a cylinder with hoop wrapped composite layer. *International Journal of Pressure Vessels and Piping 110*, 77–81.

Courtin, S., C. Gardin, G. Bezine, and H. B. H. Hamouda (2005). Advantages of the j-integral approach for calculating stress intensity factors when using the commercial finite element software abaqus. *Engineering Fracture Mechanics 72*(14), 2174–2185.

Dassault Systèmes (2016). *Abaqus 2016 Documentation Collection.*

Dayyani, I., H. H. Khodaparast, B. K. Woods, and M. I. Friswell (2014). The design of a coated composite corrugated skin for the camber morphing airfoil. *Journal of Intelligent Material Systems and Structures*, 1045389X14544151.

Dayyani, I., A. Shaw, E. S. Flores, and M. Friswell (2015). The mechanics of composite corrugated structures: a review with applications in morphing aircraft. *Composite Structures 133*, 358–380.

Drela, M. (1989). Xfoil: An analysis and design system for low reynolds number airfoils. In *Low Reynolds number aerodynamics*, pp. 1–12. Springer.

Elzey, D. M., A. Y. Sofla, and H. N. Wadley (2003). A bio-inspired high-authority actuator for shape morphing structures. In *Smart structures and materials*, pp. 92–100. International Society for Optics and Photonics.

Falcão, L., A. A. Gomes, and A. Suleman (2011). Aero-structural design optimization of a morphing wingtip. *Journal of Intelligent Material Systems and Structures 22*(10), 1113–1124.

Faruk, O., A. K. Bledzki, H.-P. Fink, and M. Sain (2014). Progress report on natural fiber reinforced composites. *Macromolecular Materials and Engineering 299*(1), 9–26.

Fichter, W. B. (1967). Stresses at the tip of a longitudinal crack in a plate strip. Technical report, NASA Langley Research Center.

Gabor, O. Ş., A. Simon, A. Koreanschi, and R. M. Botez (2015). Improving the uas-s4 éhecal airfoil high angles-of-attack performance characteristics using a morphing wing approach. *Proceedings of the Institution of Mechanical Engineers, Part G: Journal of Aerospace Engineering*, 0954410015587725.

Gao, H., M. Abbudi, and D. Barnett (1992). Interfacial crack-tip field in anisotropic elastic solids. *Journal of the Mechanics and Physics of Solids 40*(2), 393–416.

Georgiadis, S., A. J. Gunnion, R. S. Thomson, and B. K. Cartwright (2008). Bird-strike simulation for certification of the Boeing 787 composite moveable trailing edge. *Composite Structures 86*(1), 258–268.

Gilbert, W. W. (1981). Mission adaptive wing system for tactical aircraft. *Journal of Aircraft 18*(7), 597–602.

Golestaneh, A. F., A. Ali, and M. Zadeh (2009). Modelling the fatigue crack growth in friction stir welded joint of 2024-t351 al alloy. *Materials & Design 30*(8), 2928–2937.

Gomez, J. C. and E. Garcia (2011). Morphing unmanned aerial vehicles. *Smart Materials and Structures 20*(10), 103001.

Gordon, Y., E. Gordon, and B. Gunston (2000). *Soviet X-planes*. Midland Pub.

Grandt, A. (2003). *Fundamentals of Structural Integrity: Damage Tolerant Design and Nondestructive Evaluation*. John Wiley & Sons.

Griffith, A. A. (1921). The phenomena of rupture and flow in solids. *Philosophical transactions of the Royal Society of London. Series A, containing papers of a mathematical or physical character 221*, 163–198.

Grigorie, T. L., A. V. Popov, and R. M. Botez (2012). *Fuzzy logic control of a smart actuation system in a morphing wing*. INTECH Open Access Publisher.

Hedayati, R. and M. Sadighi (2015). *Bird Strike: An Experimental, Theoretical and Numerical Investigation*. Elsevier Science.

Houghton, E. and P. Carpenter (2003). *Aerodynamics for Engineering Students*. Elsevier Science.

Isida, M. (1971). Effect of width and length on stress intensity factors of internally cracked plates under various boundary conditions. *International Journal of Fracture Mechanics 7*(3), 301–316.

Janssen, M., J. Zuidema, and R. Wanhill (2004). *Fracture Mechanics, second edition*. Taylor & Francis.

Jha, A. K. and J. N. Kudva (2004). Morphing aircraft concepts, classifications, and challenges. In *Smart structures and materials*, pp. 213–224. International Society for Optics and Photonics.

John, R., K. Jata, and K. Sadananda (2003). Residual stress effects on near-threshold fatigue crack growth in friction stir welds in aerospace alloys. *International Journal of fatigue 25*(9), 939–948.

Kintscher, M. and M. Wiedemann (2013). Design of a smart leading edge device. In *Adaptive, tolerant and efficient composite structures*, pp. 381–390. Springer.

Kintscher, M., M. Wiedemann, H. P. Monner, O. Heintze, and T. Kühn (2011). Design of a smart leading edge device for low speed wind tunnel tests in the european project sade. *International Journal of Structural Integrity 2*(4), 383–405.

Knauss, W. G. (1966). Stresses in an infinite strip containing a semi-infinite crack. *Journal of Applied Mechanics 33*(2), 356–362.

Knott, J. (1973). *Fundamentals of fracture mechanics*. Butterworth-Heinemann Limited.

Kroo, I. (1997). Aircraft design: Synthesis and analysis, http://adg.stanford.edu/aa241/AircraftDesign.html.

Krueger, R. (2002). The Virtual Crack Closure Technique: History, Approach and Applications. ICASE Report No. 2002-10. Technical report, Institute for Computer Applications in Science and Engineering (ICASE).

Kundu, T. (2008). *Fundamentals of fracture mechanics*. CRC Press.

Lafountain, C., K. Cohen, and S. Abdallah (2009). Camber controlled airfoil design for morphing uav. In *47th AIAA Aerospace Sciences Meeting Including The New Horizons Forum and Aerospace Exposition*, pp. 211–218.

Lafountain, C., K. Cohen, and S. Abdallah (2012). Use of xfoil in design of camber-controlled morphing uavs. *Computer Applications in Engineering Education 20*(4), 673–680.

Lilienthal, O. (2001). *Birdflight as the Basis of Aviation: A Contribution Towards a System of Aviation, Compiled from the Results of Numerous Experiments Made by O. and G. Lilienthal*. American aeronautical archives. Markowski International Pub.

Loftin, L. K. (1985). *Quest for performance: The evolution of modern aircraft*. Scientific and Technical Information Branch, National Aeronautics and Space Administration.

Mathew, A. P., K. Oksman, and M. Sain (2005). Mechanical properties of biodegradable composites from poly lactic acid (PLA) and microcrystalline cellulose (MCC). *Journal of applied polymer science 97*(5), 2014–2025.

Mattioni, F., A. Gatto, P. Weaver, M. Friswell, and K. Potter (2006). The application of residual stress tailoring of snap-through composites for variable sweep wings. In *Proc. 47th AIAA/ASME/ASCE/AHS/ASC Structures, Structural Dynamics, and Materials Conf.(SDM)*.

McGowan, A.-M. R., D. D. Vicroy, R. C. Busan, and A. S. Hahn (2009). Perspectives on highly adaptive or morphing aircraft.

Mcknight, G., R. Doty, A. Keefe, G. Herrera, and C. Henry (2010). Segmented reinforcement variable stiffness materials for reconfigurable surfaces. *Journal of Intelligent Material Systems and Structures 21*(17), 1783–1793.

Merriam-Webster Dictionary (2016). "Morph", http://www.merriam-webster.com/dictionary/morph.

Miannay, D. (1997). *Fracture Mechanics*. Mechanical Engineering Series. Springer New York.

Miedlar, P. C., A. P. Berens, A. Gunderson, and J. Gallagher (2002). Analysis and support initiative for structural technology (ASIST) delivery order 0016: USAF damage tolerant design handbook: guidelines for the analysis and design of damage tolerant aircraft structures. Technical report, DTIC Document.

Može, P. (2016). Lecture 12.13: Fracture mechanics applied to fatigue, http://www.fgg.uni-lj.si/~/pmoze/esdep/master/wg12/l1300.htm.

Moreira, P. M. G. P., P. M. S. T. de Castro, S. M. Tavares, and V. Richter-Trummer (2010, 3). Characterization of fatigue crack growth rate of aa6056 t651 and t6: Application to predict fatigue behaviour of stiffened panels. In *Advanced Materials Forum V*, Volume 636 of *Materials Science Forum*, pp. 1511–1517. Trans Tech Publications.

Morgado, J., M. Abdollahzadeh, M. Silvestre, and J. Páscoa (2015). High altitude propeller design and analysis. *Aerospace Science and Technology 45*, 398–407.

Morgado, J., R. Vizinho, M. Silvestre, and J. Páscoa (2016). XFOIL vs CFD performance predictions for high lift low Reynolds number airfoils. *Aerospace Science and Technology 52*, 207–214.

Murakami, Y. (1987). *Stress intensity factors handbook, volume 1*. Pergamon.

NASA (2009). F-111 Advanced Fighter Technology Integration.http://www.nasa.gov/centers/dryden/multimedia/imagegallery/F-111AFTI/EC85-33205-07.html.

Naval Air Training Command (1988). *Fundamentals of aerodynamics, CNATRA P-202*.

Olson, S. et al. (2013). *Educating engineers: Preparing 21st century leaders in the context of new modes of learning: Summary of a forum*. National Academies Press.

Paris, P. C., M. P. Gomez, and W. E. Anderson (1961). A rational analytic theory of fatigue. *The trend in engineering 13*(1), 9–14.

Parker, H. (1920). The Parker variable camber wing, NACA Technical Report 77. Technical report, National Advisory Committee for Aeronautics.

Perera, M. and S. Guo (2009). *Optimal Design of a Seamless Aeroelastic Wing Structure*. Structures, Structural Dynamics, and Materials and Co-located Conferences. American Institute of Aeronautics and Astronautics.

Perera, M., Y. He, and S. Guo (2010). Structural and dynamic analysis of a seamless aeroelastic wing. In *Proceedings of the 51st AIAA/ASME/ASCE/AHS/ASC structures, structural dynamics, and materials conference*.

Pickering, K. L., M. A. Efendy, and T. M. Le (2016). A review of recent developments in natural fibre composites and their mechanical performance. *Composites Part A: Applied Science and Manufacturing 83*, 98–112.

Piercy, N. (1947). *Aerodynamics*. English Universities Press.

Previtali, F. and P. Ermanni (2012). Performance of a non-tapered 3d morphing wing with integrated compliant ribs. *Smart materials and structures 21*(5), 055008.

Radaj, D. (2013). *Extended Stress Intensity Factor Concepts*, pp. 101–265. Berlin, Heidelberg: Springer Berlin Heidelberg.

Radestock, M., J. Riemenschneider, H. P. Monner, and M. Rose (2014). Structural optimization of an uav leading edge with topology optimization. *DeMEASS Design, Modelling and Experiments of Advanced Structures and Systems*.

Radestock, M., J. Riemenschneider, H. P. Monner, and M. Rose (2015). Experimental Investigation of a Compliant Mechanism for an UAV Leading Edge. *Proceedings of the 7th ECCOMAS Thematic Conference on Smart Structures and Materials, SMART 2015*.

Raither, W., E. Furger, M. Zündel, A. Bergamini, and P. Ermanni (2014). Variable-stiffness skin concept for camber-morphing airfoils. *Journal of Intelligent Material Systems and Structures*, 1045389X14546780.

Raymer, D., A. I. of Aeronautics, and Astronautics (1992). *Aircraft Design: A Conceptual Approach*. AIAA education series. American Institute of Aeronautics and Astronautics.

Ricci, S., A. Scotti, and M. Terraneo (2006). Design, manufacturing and preliminary test results of an adaptive wing camber model. In *47th AIAA/ASME/ASCE/AHS/ASC Structures, Structural Dynamics, and Materials Conference 14th AIAA/ASME/AHS Adaptive Structures Conference 7th*, pp. 1–12. Newport, Rhode Island.

Rice, J. C. (1967). Discussion: "Stresses in an Infinite Strip Containing a Semi-Infinite Crack" (Knauss, W. G., 1966, ASME J. Appl. Mech., 33, pp. 356–362). *Journal of Applied Mechanics 34*(1), 248–249.

Rice, J. R. (1968). A path independent integral and the approximate analysis of strain concentration by notches and cracks. *Journal of Applied Mechanics 35*(2), 379–386.

Rodriguez, A. R. (2007). Morphing aircraft technology survey. In *45th AIAA aerospace sciences meeting and exhibit*.

Rooke, D., D. Cartwright, and G. B. M. of Defence (1976). *Compendium of Stress Intensity Factors*. Her Majesty Stationery Office.

Rudd, J., T. Hsu, and H. Wood (1979). Part-through crack problems in aircraft structures. In *Part-Through Crack Fatigue Life Prediction*. ASTM International.

Rybicki, E. F. and M. Kanninen (1977). A finite element calculation of stress intensity factors by a modified crack closure integral. *Engineering Fracture Mechanics 9*(4), 931–938.

Sadraey, M. (2012). *Aircraft Design: A Systems Engineering Approach*. Aerospace Series. Wiley.

Schijve, J. (2009). Fatigue damage in aircraft structures, not wanted, but tolerated? *International Journal of Fatigue 31*(6), 998–1011.

Seigler, T. M., D. A. Neal, J.-S. Bae, and D. J. Inman (2007). Modeling and flight control of large-scale morphing aircraft. *Journal of Aircraft 44*(4), 1077–1087.

Sforza, P. (2014). *Commercial Airplane Design Principles*. Elsevier Science.

Shih, C., B. Moran, and T. Nakamura (1986). Energy release rate along a three-dimensional crack front in a thermally stressed body. *International Journal of Fracture 30*(2), 79–102.

Smith, R. (1978). An introduction to fracture mechanics for engineers: Part i: Stresses due to notches and cracks. *International Journal of Materials in Engineering Applications 1*(2), 121–128.

Smith, R. (1979a). An introduction to fracture mechanics for engineers part ii: Using the stress intensity factor to characterise fracture and fatigue crack growth. *International Journal of Materials in Engineering Applications 1*(4), 227 – 235.

Smith, R. (1979b). An introduction to fracture mechanics for engineers: Part iii: Elastic/plastic fracture mechanics and energy methods. *International Journal of Materials in Engineering Applications 1*(6), 316–322.

Smojver, I. and D. Ivančević (2010). Numerical simulation of bird strike damage prediction in airplane flap structure. *Composite structures 92*(9), 2016–2026.

Sofla, A., S. Meguid, K. Tan, and W. Yeo (2010). Shape morphing of aircraft wing: Status and challenges. *Materials & Design 31*(3), 1284 – 1292.

Sruthi, A., B. Rajesh, M. Soumya, S. Apurva, K. Kumar, S. Y. Ali, A. Reddy, and A. Nadar (2015). A brief study, research, design, analysis on multi section variable camber wing. *Int. Journal of Engineering Research and Applications* (5).

Stephens, R., A. Fatemi, R. Stephens, and H. Fuchs (2000). *Metal Fatigue in Engineering*. A Wiley-Interscience publication. John Wiley & Sons.

Stiffler, G. L. and J. A. Tershin (1967, December). United States Patent 3356550: Chemical milling of aluminum alloys.

Strelec, J. K., D. C. Lagoudas, M. A. Khan, and J. Yen (2003). Design and implementation of a shape memory alloy actuated reconfigurable airfoil. *Journal of Intelligent Material Systems and Structures 14*(4-5), 257–273.

Sun, J., Q. Guan, Y. Liu, and J. Leng (2016). Morphing aircraft based on smart materials and structures: A state-of-the-art review. *Journal of Intelligent Material Systems and Structures*, 1045389X16629569.

Suo, Z. (1990). Singularities, interfaces and cracks in dissimilar anisotropic media. In *Proceedings of the Royal Society of London A: Mathematical, Physical and Engineering Sciences*, Volume 427, pp. 331–358. The Royal Society.

Suresh, S. (1998). *Fatigue of materials*. Cambridge University Press.

Tada, H., P. Paris, and G. Irwin (2000). *The Stress Analysis of Cracks Handbook*. Wiley.

Talay, T. A. (1975). *Introduction to the Aerodynamics of Flight*, Volume 367. Scientific and Technical Information Office, National Aeronautics and Space Administration.

The Aviation History Online Museum (2013). A Wing and a Prayer, http://www.aviation-history.com/boeing/b17tail.html.

Thill, C., J. Etches, I. Bond, K. Potter, and P. Weaver (2008). Morphing skins. *The Aeronautical Journal 112*(1129), 117–139.

Thorpe, J. (2003). Fatalities and destroyed civil aircraft due to bird strikes, 1912-2002. In *International Bird Strike Committee, 26th Meeting. Warsaw, Poland*.

United States Air Force (1943). Close-up of the damage to Boeing B-17F-5-BO (S/N 41-24406) All American III, http://media.defense.gov/2006/Jun/01/2000554804/-1/-1/0/060517-F-1234S-006.JPG.

United States Air Force (2015). Republic XF-91 Thunderceptor, http://www.nationalmuseum.af.mil/Visit/MuseumExhibits/FactSheets/Display/tabid/509/Article/195745/republic-xf-91-thunderceptor.aspx.

Valasek, J. (2012). *Morphing aerospace vehicles and structures*. John Wiley & Sons.

van der Horst, S., J. E. van de Wiel, C. S. Ferreira, and N. R. García (2016). Flow curvature effects for vawt: a review of virtual airfoil transformations and implementation in xfoil. In *Proceedings of the 34th Wind Energy Symposium*. American Institute of Aeronautics & Astronautics.

Vocke, R. D., C. S. Kothera, B. K. Woods, and N. M. Wereley (2011). Development and testing of a span-extending morphing wing. *Journal of Intelligent Material Systems and Structures*, 1045389X11411121.

Vos, R., Z. Gurdal, and M. Abdalla (2010). Mechanism for warp-controlled twist of a morphing wing. *Journal of Aircraft 47*(2), 450–457.

Wang, F. and Z. Yue (2010). Numerical simulation of damage and failure in aircraft windshield structure against bird strike. *Materials & Design 31*(2), 687–695.

Weiss, P. (2003). Wings of change: Shape-shifting aircraft may ply future skyways. *Science News 164*(23), 359–359.

Weisshaar, T. A. (2006). Morphing aircraft technology-new shapes for aircraft design. Technical report, DTIC document.

Weisshaar, T. A. (2013). Morphing aircraft systems: historical perspectives and future challenges. *Journal of Aircraft 50*(2), 337–353.

Wereley, N. M. and F. Gandhi (2010). Flexible skins for morphing aircraft. *Journal of Intelligent Material Systems and Structures 21*(17), 1697–1698.

Wikipedia (2006). Mikoyan-Gurevich MiG-23, https://en.wikipedia.org/wiki/Mikoyan-Gurevich_MiG-23.

Wikipedia (2009a). General Dynamics F-111 Aardvark, https://en.wikipedia.org/wiki/General_Dynamics_F-111_Aardvark.

Wikipedia (2009b). Vougt F-8 Crusader, https://en.wikipedia.org/wiki/Vought_F-8_Crusader.

Wikipedia (2014). Makhonine Mak-10, https://en.wikipedia.org/wiki/Makhonine_Mak-10.

Wikipedia (2015). Airbus A380, https://en.wikipedia.org/wiki/Airbus_A380.

Wikipedia (2016a). All American (aircraft), https://en.wikipedia.org/wiki/All_American_(aircraft).

Wikipedia (2016b). Flap (aeronautics), https://en.wikipedia.org/wiki/Flap_(aeronautics).

Wikipedia (2016c). Igo Etrich, https://en.wikipedia.org/wiki/Igo_Etrich.

Wikipedia (2016d). Leading-edge slats, https://en.wikipedia.org/wiki/Leading-edge_slats.

Wikipedia (2016e). NASA AD-1, https://en.wikipedia.org/wiki/NASA_AD-1.

Wikipedia (2016f). Otto Lilienthal,https://en.wikipedia.org/wiki/Otto_Lilienthal.

Wildschek, A., T. Havar, and K. Plötner (2010). An all-composite, all-electric, morphing trailing edge device for flight control on a blended-wing-body airliner. *Proceedings of the Institution of Mechanical Engineers, Part G: Journal of Aerospace Engineering 224*(1), 1–9.